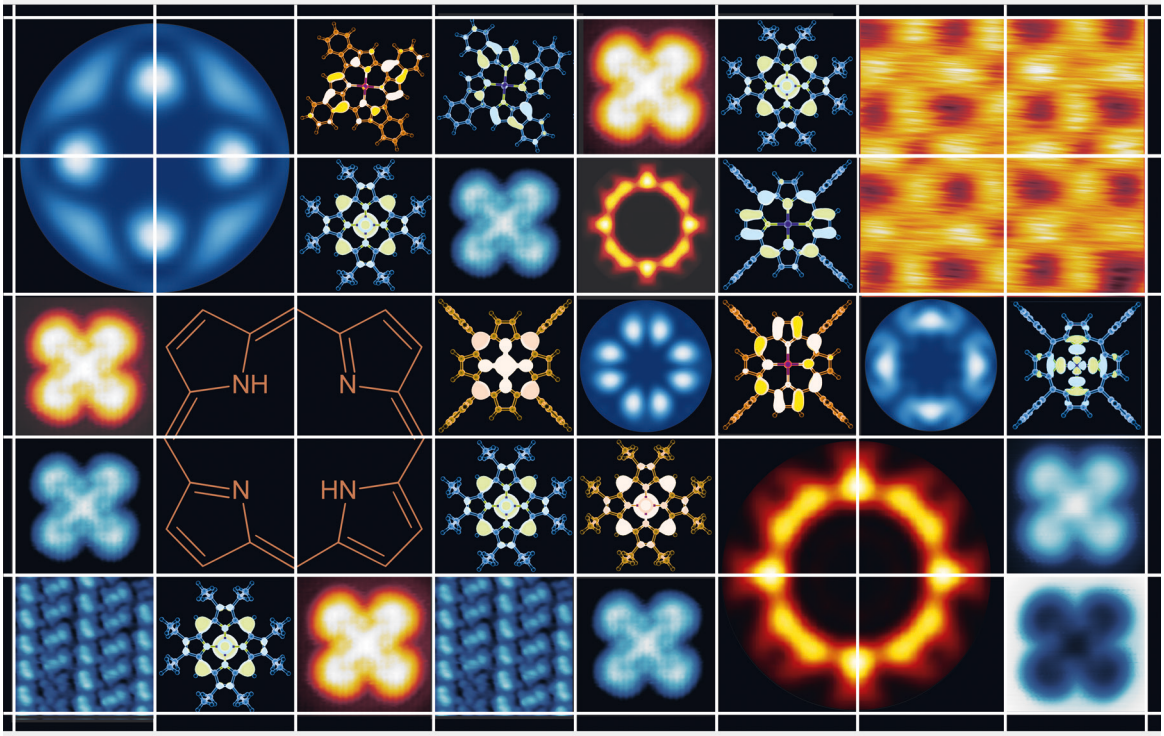

Activating molecular magnetism by controlled on-surface coordination

Iulia Cojocariu

Information
Band / Volume 91
ISBN 978-3-95806-674-8

Mitglied der Helmholtz-Gemeinschaft

JÜLICH
Forschungszentrum

Schriften des Forschungszentrums Jülich
Reihe Information / Information Band / Volume 91

Forschungszentrum Jülich GmbH
Peter Grünberg Institut (PGI)
Elektronische Eigenschaften (PGI-6)

Activating molecular magnetism by controlled on-surface coordination

Iulia Cojocariu

Schriften des Forschungszentrums Jülich
Reihe Information / Information Band / Volume 91

ISSN 1866-1777 ISBN 978-3-95806-674-8

Bibliografische Information der Deutschen Nationalbibliothek.
Die Deutsche Nationalbibliothek verzeichnet diese Publikation in der
Deutschen Nationalbibliografie; detaillierte Bibliografische Daten
sind im Internet über http://dnb.d-nb.de abrufbar.

Herausgeber und Vertrieb:	Forschungszentrum Jülich GmbH Zentralbibliothek, Verlag 52425 Jülich Tel.: +49 2461 61-5368 Fax: +49 2461 61-6103 zb-publikation@fz-juelich.de www.fz-juelich.de/zb
Umschlaggestaltung:	Grafische Medien, Forschungszentrum Jülich GmbH
Druck:	Grafische Medien, Forschungszentrum Jülich GmbH
Copyright:	Forschungszentrum Jülich 2022

Schriften des Forschungszentrums Jülich
Reihe Information / Information, Band / Volume 91

D 464 (Diss. Duisburg, Univ., 2022)

ISSN 1866-1777
ISBN 978-3-95806-674-8

Vollständig frei verfügbar über das Publikationsportal des Forschungszentrums Jülich (JuSER)
unter www.fz-juelich.de/zb/openaccess.

Living is easy with eyes closed
Misunderstanding all you see

The Beatles

Contents

Zusammenfassung

Das anhaltende Interesse an der Erforschung metallorganischer Komplexe ergibt sich aus den nachgewiesenen vielseitigen Anwendungsmöglichkeiten, wie beispielsweise Gassensorik, Speichermedien und heterogene Katalyse sowie Einzelmolekülmagnete. Die grundlegenden Eigenschaften, die das Molekül benötigt, um diese Funktionen zu erfüllen, können bereits im Molekül selbst vorhanden sein, oder seine Funktionalisierung kann genutzt werden, um die gewünschten Anforderungen zu erfüllen. In diesem Zusammenhang dient die Funktionalisierung der Moleküle an der Oberfläche als Mechanismus zur Stabilisierung der koordinierten Metallionen in katalytisch und magnetisch aktiven Zuständen.

Die Bedeutung der vorliegenden Arbeit liegt in der Untersuchung der Faktoren, die den Magnetismus und die katalytische Aktivität an der organisch-metallischen Grenzfläche steuern, wobei als organisches Molekül ein Übergangsmetallporphyrin oder -phthalocyanin gewählt wird.

Der erste bekannte Faktor, der die Eigenschaften der molekularen Filme beeinflusst, ist die Oberfläche. Die entscheidende Bedeutung der Substratwahl wird durch die Kombination verschiedener eingebetteter Übergangsmetallionen, die sich durch eine unterschiedliche elektronische Konfiguration auszeichnen, und verschiedener Metalloberflächen, nämlich Gold, Silber und Kupfer, die eine zunehmende Oberflächenreaktivität aufweisen, demonstriert. Indem verschiedene Grenzflächen einem externen Liganden, Stickstoffdioxid, ausgesetzt werden, wird gezeigt, dass nur die mit Kupfer gebildete Grenzfläche die notwendigen Eigenschaften zur weiteren Manipulation der elektronischen und magnetischen Eigenschaften des Metallkerns durch axiale Ligandenwechselwirkung beibehält.

Ein weiterer wichtiger Faktor bei der Funktionalisierung von organischen Grenzflächen ist die Veränderung der Molekülperipherie und -struktur. Ein Beispiel hierfür ist die Einführung stark elektronenziehende Gruppen in das Metallphthalocyanin, und es wurde die Möglichkeit der Realisierung gut definierter p-n-Heteroübergange aufgezeigt.

Ein weiterer etablierter Ansatz zur Strukturmodifikation ist die molekulare Planarisierung, die durch eine temperaturinduzierte Cyclodehydrierungsreaktion an der Oberfläche hervorgerufen wird. Diese Umwandlung ermöglicht es, die Unverzichtbarkeit der molekularen Flexibilität für den Einsatz dieser Grenzflächen als NO_2-Sensoren zu definieren. Im Fall von Metallphthalocyaninen, die in ihrer ursprünglichen Form planar sind, wird jedoch gezeigt, dass, obwohl keine Wechselwirkung mit dem undissoziierten Dioxid besteht, die Molekül-Substrat-Grenzfläche bei der Spaltung von NO_2 aktiv ist und die Stabilisierung verschiedener magnetischer Zustände dennoch möglich ist.

Synopsis

The enduring interest in the study of metallorganic complexes emerges from the demonstrated multi-faced applications, which range from gas sensing to memory storage, and heterogeneous catalysis, as well as single-molecule magnets. The fundamental properties required for the molecule to achieve these functions can already be intrinsically present in the molecule itself, or its functionalization can be exploited to meet the desired requirements. In this regard, on-surface molecular functionalization serves as a mechanism to stabilize the chelated metal ions in catalytically and magnetically active states.

The importance of the present thesis results from the investigation of the factors guiding magnetism and catalytic activity at the organic-metal interface, where the organic molecule is chosen to be a transition metal porphyrin or phthalocyanine.

The first well-known factor influencing the properties of the overlayer is the surface. The cruciality of the substrate choice will be demonstrated by combining different embedded transition metal ions, characterized by a different electronic configuration, and several metal surfaces, *i.e.* gold, silver, and copper, possessing an increasing surface reactivity. By exposing various interfaces to an external ligand, nitrogen dioxide, it is demonstrated that only the interface formed with copper retains the necessary properties for further manipulating electronic and magnetic properties of the metal core through axial ligand interaction.

Another important factor identified in the view of organic interface functionalization is the modification of molecular periphery and structure. An example of this is the introduction of strongly electron withdrawing groups in the metal phthalocyanine, and the possibility of realizing well-defined heterostacked p-n junctions is demonstrated.

A distinct established approach for structural modification is found in molecular planarization induced by an on-surface temperature-induced cyclodehydrogenation reaction. This transformation allows us to define the indispensability of molecular flexibility for employing these interfaces as NO_2 sensors. However, in the case of metal phthalocyanines, which are planar in their pristine form, it is shown that although there is no interaction with the undissociated dioxide, the molecule-substrate interface is active in NO_2 cleavage and the stabilization of different magnetic states is still achievable.

Introduction

In the last two decades, considerable efforts have been made to stabilize and control the spin and oxidation states in metal ions at the nanoscale in order to design devices with novel functionalities and improved performance. This offers prospects for enhancing the reactivity of single-atom catalysts [1], developing new strategies for efficient gas separation in metal-organic frameworks [2], building single-atom magnets capable of storing information [3], as well as realizing spin-based logic operations [4].

One way to stabilize metal ions and to prevent their local magnetic moment from decreasing or being quenched by the interaction with the substrate [5], is to cage them into a ligand field through their lateral unsaturated coordination bonds. This can be achieved using molecular ligands, *e.g.* cyano- or carboxylic-molecular terminations, as demonstrated for Fe, Ni and Mn ions forming 2-dimensional high-spin metal-organic networks [6–10]. An alternative route is to incorporate the metal ion in a tetrapyrrolic macrocycle, which represent the core of porphyrins and phthalocyanines [11,12], allowing one to stabilize the metal in different spin configuration states.

Being the central metal ion accessible from both sides of the molecular plane, coordination can proceed in multiple ways. In an adsorbed phase, the first coordination site is saturated by the interaction with the underlying substrate, which can induce changes in the chemical, electronic and magnetic properties of the central atom. The additional coordinational site of the central metal ion, which points out of the surface, can be involved in the interaction with external ligands, leading to changes in the metal ion electronic and magnetic properties. The competition between surface and axial ligand coordination is the on-surface analog of the trans-effect, commonly encountered in coordination chemistry. The so-called *surface trans-effect* is a concept extended to on-surface studies allowing for the understanding of electronic and magnetic properties in adsorbed porphyrins and phtalocyanines in the presence of external ligands.

The molecular degrees of freedom open up numerous viable pathways to modify the electronic, magnetic and catalytic properties of porphyrins and phthalocyanines. Molecular versatility derives primarily from the potential of incorporating within the macrocycle various metal ions characterized by a different electronic and spin configuration. In this respect, the electronic structure of the metal is the first central factor in inducing a magnetic moment in the molecule. In addition to this, the choice of the substrate allows for tuning the strength of molecule-surface interactions and activating the central metal ion towards axial ligand coordination.

The purpose of this thesis is to explore some of the factors standing behind the modification in the electronic and magnetic properties observed upon molecular functionalization. Subject of study are porphyrins and phthalocyanines containing metals belonging to the first transition row (Fe, Co, Ni) supported on coinage metal substrates.

The thesis structures as follows. In **Chapter 1** the description of the overall properties of metal-containing porphyrins and phthalocyanines is give together with a recap on the current state-of-the-art on substrate-supported metallorganic compounds. Particularly, information on the energy level alignment, on transition metal complexes and on the surface trans-effect is given to better follow the subsequent discussion.

In **Chapter 2** are given the basic concepts of the techniques employed here. The properties of metal-supported metal porphyrins and metal phthalocyanines are monitored with several photoemission and absorption spectroscopies, complemented by micro- and mesoscale analytic methods, Scanning Tunneling Microscopy (STM) and Low Energy Electron Diffraction (LEED), respectively. Synchrotron-based X-ray Photoemission Spectroscopy (XPS) and Angle-Resolved PhotoEmission Spectroscopy (ARPES) are employed for chemical and electronic characterization. In function of excitation light polarization Near Edge X-ray Absorption Spectroscopy (NEXAFS) and X-ray Magnetic Circular Dichroism (XMCD) are used for structural and magnetic characterization of the supported molecular layers. In addition, the coordination geometry of the axial ligand is studied with Infrared Reflection-Absorption Spectroscopy (IRAS).

The role of the substrate on the properties of flexible Co and Ni-containing porphyrins is unraveled in **Chapter 3** with the aim of developing a method for controlling and tuning the catalytic and magnetic properties of the chelated metal ion using an on-surface coordination approach. In particular, the most common coinage metal substrates, Cu(100), Ag(100) and Au(111), characterized by a decreasing surface reactivity, are here investigated. The study focuses mainly on the metal tetraphenylporphyrins, but a brief overview on the role of the molecular periphery is given by comparing cobalt tetraphenylporphyrin with cobalt octaethylporphyrin. The *surface trans-effect* is investigated by exposing the different metallorganic systems to a strongly oxidizing gas, NO_2. At the end of the chapter, the study of the alkali metal doping of nickel and cobalt tetraphenylporphyrin on Au(111) highlights the importance of the molecular conformation in defining the molecular properties.

By inducing planarization *via* a surface-assisted cyclodehydrogenation reaction, the role of the molecular conformation in the catalytic reactivity is tested in **Chapter 4**. Metal octaethylporphyrins and metal tetraphenylporphyrins undergo cyclodehydrogenation on silver. On copper, while for metal octaethylporphyrin the reaction takes place smoothly, in the case of nickel tetraphenylporphyrin, the strong interface pinning and the close-packed assembly induced by the phenyl groups do not allow us to observe such reaction, urging a different approach to elicit the ring-closure reaction. The possibility of coordinating planar systems with axial ligands is tested by exposing them to NO_2.

In **Chapter 5** information elaborated in the two previous experimental chapters is extended to the metal phthalocyanine family. The possibility of changing the electronic and magnetic properties in nickel and iron phthalocyanine is investigated at the interface with Cu(100). Special attention is paid to the latter, which shows the possibility of stabilizing three different spin configurations *via* ligand coordination.

Finally, in **Appendix 1** the possibility of constructing p/n junctions from the appropriate stacking of iron phthalocyanine and its fluorinated form is shown.

A systematic study has been performed for the different interfaces studied here. Changes induced on the alignment of molecular levels following surface deposition are investigated by both ARPES, combined with Photoemission Tomography (PT), and NEXAFS. Adsorption geometry and molecular order are characterized by STM, LEED and PT, moving then to the core of interest,

the properties of the central metal ion. Its oxidation and spin state is accessed by means of XPS and NEXAFS, the latter often supported by theoretical predictions based on density functional theory. For selected systems, XMCD measurements allowed us to access the magnetic information contained in the central metal ion. Interaction with the external ligand, NO_2, is tracked by a combination of different spectroscopic techniques, XPS and NEXAFS primarily, and, in some particular cases, STM, IRAS and XMCD.

Chapter 1

On-surface functionalization

In the situation where electronic device miniaturization with *top-down* approaches is reaching a saturation limit, *bottom-up* approaches emerge as a promising solution strategy to overcome the limit [13]. Organic molecules represent one of the most promising class of materials in this sense and their use in nano-fabrication methods presents some key advantages [14]. Besides their nanometer size, the formation of self-assembled structures opens up new possibilities for engineering long-range ordered, low-dimensional molecular frameworks, thus offering a promising prospect for electronic device miniaturization [15–17]. Moreover, through molecular synthesis chemistry, different functional groups can be substituted, allowing one to introduce and control new properties of the molecule [18].

Aromatic organic molecules such as porphyrins and phthalocyanines can be deposited in the monolayer regime on single crystal surfaces in ultra high vacuum and geometrically ordered structures can be obtained from this procedure [11]. The unsaturated molecular macrocycle brings synthetic tailorability for these chemical systems thanks to the presence of different positions in which functional groups can be substituted [19]. By varying the composition and geometry of these molecules, it is possible to control their structural, bonding, transport, and optical properties.

Taking advantage of the flexibility in choosing the substituents, in combination with the presence of active sites of interactions with metals, this kind of molecules can be used to fabricate two-dimensional arrays of metallic centers with nanometric spacing. This makes them promising candidates for applications in emerging fields like spintronics and molecular electronics, as building blocks for molecular-based devices with controllable and tunable properties [6,20], for novel metal–organic architectures in solid-state chemistry and in molecular engineering [19,21–26] as well as to form patterned surfaces for catalytic, magnetic, optoelectronic, and sensing materials [27–34].

Several metals can be efficiently coordinated within the molecule macrocycle, forming metal porphyrins and metal phthalocyanines [12,35–42]. Recent developments in the field of surface magnetism, with the possible applications of some paramagnetic metal-organic macrocycle molecules as switchable elements in molecular spintronic devices [43–45], have generated much interest into the structural and magnetic properties of these molecules [23,46–67].

1.1 Energy level alignment at the metal–organic interface

Metal-organic interfaces are pivotal in molecular electronics as their properties define the charge injection and transport through the device [68]. The formation of an interface dipole by the adsorption of metallorganic molecules on metallic surfaces is influenced by the interaction of the macrocycle and central metal atom with the substrate, and has a significant impact on charge injection barriers [69]. Charge transfer due to molecule-substrate hybridization effects, the push-back effect involving interaction of molecular electron cloud and metallic substrate electron density, and back donation of charge density from molecule to substrate leading to charge redistribution are all processes that can influence energy level alignment at the molecule-substrate interface [70].

The nature of the central metal atom and substituent groups has a great impact on the chemical reactivity, stability, and character of frontier molecular orbitals of the metallorganic molecules [12]. As a result, selecting the proper metallorganic molecule and substrate provides a plethora of alternatives for controlling and manipulating the electronic and magnetic properties of molecular thin films. Depending on the substrate and molecule, different processes may govern the overall energy level alignment and charge injection barriers at the interface. However, no unified model exists to explain all the possible factors. As a result, each molecule-substrate system must be investigated using a multi-technique approach to obtain the largest amount of information about the system.

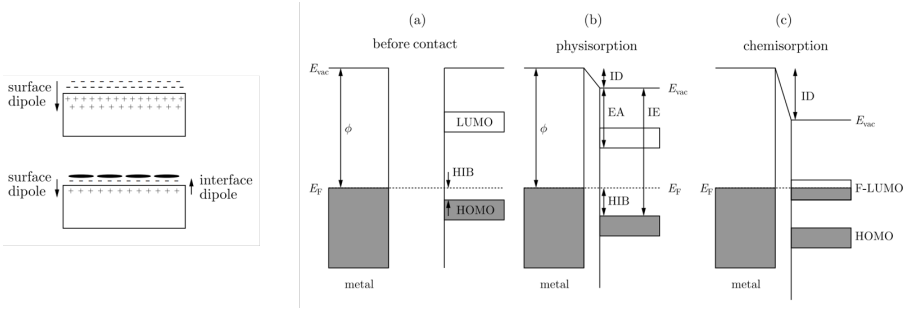

Figure 1.1: (left) Principle of the push-back effect. Upon adsorption of molecules the surface dipole is reduced compared to a clean metal substrate, while an interface dipole is created. Energy level alignment at the metal-organic interface. (right) (a) DOS of a metal and molecule before contact, showing the highest occupied molecular orbital (HOMO), lowest unoccupied molecular orbital (LUMO), and the hole injection barrier (HIB). (b) For physisorbed molecules, the push-back effect creates an interface dipole (ID), which lowers the vacuum level E_{vac} and thereby the effective work function. The HIB is increased. Different electronic quantities are introduced, which can be influenced possibly by the energy level alignment, namely ionization energy (IE) and electron affinity (EA). (c) Hybridization of molecular and metal orbitals can change the electronic structure of the molecule significantly. For the displayed example, a charge transfer from the metal to the molecule fills partially the former (F-) LUMO, and the molecule thus becomes conducting.

The strength of the molecule-substrate interaction is a key criterion for categorizing interfaces, leading to two different adsorption regimes, physisorption and chemisorption.

The first factor to consider is a fundamental property of the metal substrate, the work function, defined by the surface electrostatic potential and the bulk chemical potential. When molecules adsorb on metallic substrates in the monolayer regime, the work function changes dramatically.

Different factors contribute, such as (i) the "push-back" effect [71], which lowers the electron density at the metal surface (ϕ_{met}), (ii) an attractive surface potential, ϕ_{pol}, which induces polarization effects within the molecules, (iii) the intrinsic dipole moment of the organic molecule (ϕ_{dip}), (iv) charge transfer between the two interacting subsystems, *i.e.* hybridization at the metal-molecule interface, and (v) the chemical bond formation (ϕ_{chem}). Considering all these contributions, the total work function variation ($\Delta\phi$) can be written in first approximation as:

$$\Delta\phi = \Delta\phi_{\text{met}} + \Delta\phi_{\text{pol}} + \Delta\phi_{\text{chem}} + \Delta\phi_{\text{dip}}$$

The interaction at the interface induces an electron density redistribution within the adsorbate, which is linked to significant changes in molecular orbitals. This electronic rearrangement can results in a partial charge transfer between the adsorbate and adsorbant. The direction of the electron charge transfer is controlled by the chemical potentials, with the charge flowing from the species with higher chemical potential to the one with the lower chemical potential.

Having in mind the central role of the surface dipole in defining the properties of adsorbed molecules, it becomes clear that the introduction of a buffer layer at the metal-organic interface can have a strong impact on the energy level realignment. The presence of such a buffer layer can notably influence the charge transfer across the interface, push-back effect and hybridization.

In addition to this, energy alignment at the interface is determined by the molecular ordering and, indeed, this factor can strongly influence the properties at the interface, *i.e.* in donor/acceptor layered heterostructures. Controlling the molecular ordering is therefore critical.

1.2 Transition metal complexes on surfaces

Metal porphyrins and phthalocyanines, as previously mentioned, have caught the interest of scientists due to their intriguing electronic and magnetic properties [72]. These molecular thin films have shown potential in thin-film organic field-effect transistors (OFETs), organic light-emitting diodes (OLEDs), and organic photovoltaic devices [73]. Because of the importance of these applications, much attention has been paid to the various factors influencing charge carrier mobility and light harvesting ability of molecular thin films.

Since there are many conceivable porphyrins and phthalocyanines, only the families studied in this thesis are presented below (see Figure 1.2).

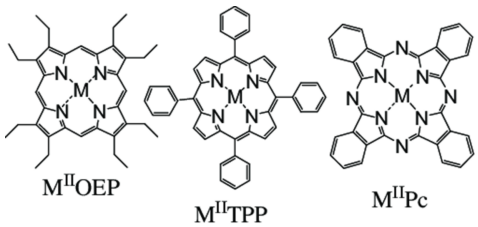

Figure 1.2: Schematic representation of metal tetraphenylporphyrin, metal octaethylporphyrin and metal phthalocyanine molecules.

The porphyrins' parent compound is the porphin, a planar heteromacrocycle with D_{2h} sym-

metry. The π-conjugated system contains 18 electrons, and thus is an aromatic system following Hückel's rule ($4n$+2). The electron delocalization within the molecule leads to the molecular planarity and to a strong molecular stability. When peripheral substituents are added to the porphin, a new class of compounds is taken into account, the porphyrins, characterized by increased stability compared to their parent compound.

Metal tetraphenylporphyrins. Tetraphenylporphyrins are substituted porphyrins with four phenyl groups in the *meso* position (5,10,15,20-Tetraphenyl porphyrin).

The introduction of phenyl groups can lead to significant on-surface changes in the geometry of the macrocycle itself. Due to steric repulsions between the hydrogen atoms in the *ortho* positions of the phenyl rings and adjacent hydrogen atoms at the porphin core, the *meso* phenyl substituents are not co-planar with the macrocycle. The sterical hindrance leads also to a considerable barrier for the rotation of the phenyl. The twisting of the *meso* substituents is in synergy with the porphyrin-core saddling: when, for example, coerced by packing forces, the phenyls rotate towards the porphyrin plane, the pyrrole rings can alleviate the steric hindrance by tilting away to a saddled conformation. STM studies for the adsorption of FeTPP, CoTPP on Ag(111) confirm the presence of a saddle–shaped molecular conformation [74]. Such adsorption-induced structural deformations are strongly influenced by the molecule-substrate interaction.

The non-planarity is central in many biological functions [75], and also in non-biological applications, like supramolecular chemistry and catalysis. Moreover, a structural deviation reduces symmetry from the ideal D_{4h} and can introduce changes in the physical and electronic structure.

Metal octaethylporphyrins. Another category of porphyrin molecules are the metal octaethylporphyrin molecules substituted with eight peripheral ethyl groups. Ethyl groups can adopt different orientations in order to minimize steric hindrance and to obtain an energetically stable configuration [76]. Nevertheless, the flexibility of the ethyl substituents allows the preservation of the macrocycle planarity. In addition, a different filling of the central metal atom can notably impact the frontier molecular orbitals (MOs) energy level alignment, thereby influencing the interaction of porphyrin molecules with the underlying substrate. The ordering and interfacial electronic properties of metal octaethylporphyrins molecules adlayers are influenced by molecular conformation and intermolecular interactions.

Although metal porphyrins have structural similarity with phthalocyanines, these two classes of molecules differ in their macrocycle for the number of nitrogen atoms, which notably impacts the overall properties of the molecule. In addition, metal porphyrins with peripheral ethyl and phenyl groups exhibit more flexibility as compared to the more rigid phthalocyanine molecules. Indeed, tetraphenylporphyrins can adopt different molecular conformations. These factors strongly influence the interaction of tetrapyrrolic complexes with the underlying substrate, notably impacting the molecular electronic and magnetic properties.

Metal phthalocyanines. Metal phthalocyanines belong to the category of planar and fully conjugated complexes of molecules. Similar to porphyrins, phthalocyanines also exhibit strong light-absorption properties in the visible region as well as thermal stability attributable to the conjugated π-system. In contrast to porphyrins, however, phthalocyanines are not found in nature. These molecules possess good photo-stability and easily form ordered molecular assemblies upon deposition on metallic substrates. Therefore, these molecules are an attractive choice for novel electronic devices such as thin film transistors, organic light-emitting diodes, and organic photovoltaic and liquid crystalline materials [77].

The introduction into the tetrapyrrolic macrocycle of a transition metal provides access, for all of the aforementioned metal porphyrins and phthalocyanines, to molecular magnetism.

1.3 Coordination of axial ligands and *surface trans-effect*

Functionalization of surfaces on the nanoscale is the key to designing novel catalysts, sensors, and other devices that are based on the interaction of an active surface with the surrounding medium. Since they combine a structure-forming element (the porphyrin framework) with an active site, usually the coordinated metal center, metal porphyrins and similar planar metal complexes are particularly well-suited for this task.

When metal tetrapyrroles are adsorbed on metal surfaces, the porphyrin plane is usually parallel to the surface, and one of the two axial coordination sites is occupied by the underlying surface, which can act as an unconventional axial ligand and influence the electronic structure (and thus chemical reactivity) of the metal center [31, 63]. The remaining axial site represents a reactive center with potential catalytic [78–80], or sensor functionality [81–87]. For example, cobalt(II) tetraphenylporphyrin (CoTPP) supported on TiO_2 proved to be an efficient catalyst for the reduction of NO and NO_2 with CO or H_2 [78,88,89]. Since neither the unsupported CoTPP nor TiO_2 are active alone, there must be some synergistic interplay between CoTPP and the underlying surface, inducing the catalytic activity. It was proposed that the modification of the electronic structure of the Co ion, caused by electron transfer from the TiO_2 support, is responsible for the catalytic activity [78]. This underlines that the reactivity of the metal center can be influenced by changing the chemical nature of support or metal ion and by adjusting the distance between the two [31].

Metalloporphyrin monolayers or thin films have also been employed as sensors [81–87]. Recently, a monolayer of a substituted zinc porphyrin has been reported as the active element in an electric sensor for the detection of nitrogen bases such as pyridine. [87]. The coordination of the N bases to the metal center leads to changes in the drain current. Suitable for repeated use due to the reversible coordination of the N bases, this sensor detects amounts below one femtomole and can be rapidly restored by exposure to light, possibly because of photoinduced cleavage of the coordination bond.

Chapter 2

Methods

The underlying concepts of the experimental techniques used in this work are summarized in this chapter. As all of these methods are well-established and extensively discussed elsewhere in the literature, only the basics that are required to understand the results of this thesis will be introduced. At first, the techniques based on the photoemission process, *i.e.*, photoemission tomography (PT) and x-ray photoemission spectroscopy (XPS), are introduced. Then, techniques based on absorption due to excitation of electrons from core levels, *i.e.*, near-edge x-ray absorption fine structure spectroscopy (NEXAFS), x-ray magnetic circular dichroism (XMCD), are discussed. After that, infrared reflection absorption spectroscopy (IRAS) will be introduced, which exploits the absorption of light in the IR regime due to the excitation of molecular vibrations. Low energy electron diffraction (LEED) and Scanning tunneling microscopy (STM), which relies on the tunneling of electrons from (to) the surface to (from) the tip, will be discussed subsequently.

2.1 Photoemission spectroscopy

Photoemission spectroscopy is a well-established and widely employed tool for investigating the electronic properties of metal-organic interfaces. The basic principle of this technique relies on the photoelectric effect, which, from a historical point of view, was discovered in 1887 by Hertz [90] and later explained by Einstein in 1905 by including the quantum nature of light in the description [91]. When the light used to probe the sample has enough energy to promote electrons into the vacuum, photoemission occurs. The electrons then travel with a certain kinetic energy, which can be derived using the following equation:

$$E_{kin} = h\nu - E_{bin} - \phi \tag{2.1}$$

where E_{kin} is the kinetic energy of the photoemitted electrons as measured by the instrument, $h\nu$ is the photon energy, E_{bin} is the binding energy of the electron measured relative to the chemical potential and ϕ is the work function for the specific surface of the material, which in real measurements includes a small correction by the instrument's work function because of the contact potential. Work function represents the minimal energy needed for promoting an electron to the vacuum level.

In photoemission experiments, the photon energy has to be chosen in accordance with the

binding energy range of the electronic levels to be investigated. While valence band states are typically measured with UV light to enhance the photoemission cross section, x-ray light is required for core levels. These disciplines are generally referred to as ultraviolet photoemission spectroscopy (UPS) or valence band (VB) spectroscopy and x-ray photoemission spectroscopy (XPS), respectively, and will be introduced in the following. The measured intensity is usually plotted as a function of the binding energy in a photoemission spectrum, making the scale independent of the photon energy used during the acquisition. For solids, it is standard practice to position a zero at the Fermi energy, while the vacuum level energy is commonly used for gas-phase experiments.

Several models have been proposed to theoretically treat the photoemission process in experiments. Berglund and Spicer [92] developed in 1964 a phenomenological description in which the photoemission process is divided into three steps. Optical excitation between two Bloch states (initial and final), electron transport to the surface, and electron escape into the vacuum are all treated separately in this approach.

In the first step, an electron from the initial state $|i\rangle$ is excited to a final state $|f\rangle$ by a photon with the energy $h\nu$. The transition probability per unit time $\omega_{i\to f}$ can be described by Fermi's golden rule derived from time-dependent first-order perturbation theory [93]:

$$\omega_{i\to f} \propto \frac{2\pi}{\hbar} \underbrace{|\langle f|\Delta|i\rangle|^2}_{M_{i\to f}} \times \delta\left(E_\mathrm{f} - E_\mathrm{i} - h\nu\right) \tag{2.2}$$

where E_f and E_i are the energies of the final and initial state, respectively, and Δ is a small, time-dependent, perturbation. For the photon energies used in this work, the perturbation Δ, which describes the interaction of the electron and the electromagnetic field, can be written in the so-called dipole approximation leading to:

$$M_{\mathrm{i}\to\mathrm{f}} = |\langle f|\Delta|i\rangle| \approx \left|\left\langle f \left| \overrightarrow{A_0} \cdot \vec{p} \right| i \right\rangle\right| \tag{2.3}$$

where $\overrightarrow{A_0}$ is the vector potential describing the monochromatic radiation and $\vec{p}$ is the momentum operator of the photoelectron. By evaluating the combinations of initial and final states that lead to a non-zero transition matrix element in equation 1.2, the so-called dipole selection rules can be formulated. They can be used to infer the symmetry of the states involved in direct transitions [93].

The photoelectrons propagate in the solid after being excited, as described in the second step of the photoemission process. The transmitted photoelectrons go through elastic and inelastic scattering processes with electrons, phonons, and defects. The length that an electron can travel in a material without being inelastically scattered is called the electron inelastic mean free path, and it is determined by the kinetic energy of the excited electron. The mean free path for typical incident photon beams in the UV and soft X-ray range is in the order of a few nm, which can probe up to 10 atomic layers depending on the local atomic arrangement. Instead, inelastically scattered electrons produce a broad background with a quadratic dependence on the kinetic energy.

In the third step, the electron overcomes the surface barrier and escapes into the vacuum. Since the periodic potential present in the solid is broken upon surface crossing, the momentum component perpendicular to the surface is not conserved. When a photoelectron is emitted

from the surface, its energy-momentum dependence can be approximated with a free-electron dispersion. This allows one to rewrite the momentum conservation law in the system as:

$$\mathbf{k}_{\parallel} = \mathbf{k}_{x,\parallel} + \mathbf{k}_{y,\parallel} = \sqrt{\frac{2m}{h^2} E_{kin}} \cdot \sin(\theta) \tag{2.4}$$

$$\mathbf{k}_{\perp} = \sqrt{\frac{2m}{h^2} \left(E_{kin} \cos^2(\theta) + \mathrm{V}_0\right)} \tag{2.5}$$

where θ is the emission angle of the photoelectron, V_0 is the inner potential, a material intrinsic property corresponding to the lowest energy level of the valence band with respect to the vacuum level. As a result, the perpendicular component of the photoelectron momentum can be only empirically determined, whereas the parallel component can be directly determined from the kinetic energy and the polar emission angle [94]. Even though the three-step model is sufficient for the description of a wide range of phenomena, the decomposition into three separate incoherent steps is not always appropriate [95]. In this case, the one-step model, in which the three above-mentioned steps are described as a single quantum-mechanical process, is more accurate [96].

2.1.1 X-ray photoemission spectroscopy (XPS)

X-ray photoelectron spectroscopy (XPS) belongs to the family of photoemission spectroscopies in which electron population spectra are obtained by irradiating a material with a beam of X-rays. It is a surface-sensitive analytic technique that can retrieve valuable information from a material. XPS allows one to identify the elements present within a material (elemental composition) or that are covering its surface, as well as their chemical state, and the overall electronic structure and density of the electronic states in the material. XPS is a powerful measurement technique because it not only shows what elements are present, but also what other elements they are bonded to.

XPS, thanks to the high energy of X-ray photons, permits exploring the binding energies of the tightly bonded electrons of the matter, the core levels. This implies that after the emission of the photoelectron the system is in a core-hole excited state. The decay process involves an electron occupying a higher energy state that fills the core hole, leaving a shallower hole. This decay can follow a radiative path with emission of fluorescent light, or a non-radiative path with emission of a third electron, called Auger electron. These electronic levels are element specific, permitting the composition analysis of the sample. The XPS allows retrieving information about the stoichiometry of a sample by comparison of the signal intensities originating from the different elements. The abundance of different elements can be correlated to the intensity of the photoemitted peaks through their cross-section σ. This factor takes into account the probability of the transition upon illumination at certain wavelength. Following Hüfner [93], σ can be defined as the transition probability (see Eq. 2.2) normalized by the photon flux per unit of time and area.

Another value to consider into the quantitative XPS analysis is the inelastic mean free path which comes into the Lambert-Beer law [97], allowing for the estimation of the decay of the electron flux (I) passing through a layer:

$$I = I_0 e^{-\frac{d}{\lambda \cos \alpha}} \tag{2.6}$$

where I_0 is the non-attenuated flux, d is the thickness of the layer, α is the angle of emission

measured with respect to the surface normal, and λ is the inelastic mean free path (IMFP). The IMFP represents the thickness of a layer that reduces the flux to 1/e of its non-attenuated value. It can be calculated following the semi-empirical equation proposed by Seah and Cumpson [98]:

$$\lambda = 0.316a^2 \left\{ \frac{E_{kin}}{Z^{0.45}\left[\ln\left(\frac{E_{kin}}{27}\right)+3\right]} + 4 \right\} \tag{2.7}$$

where a is the lattice parameter, E_{kin} the kinetic energy of the electron and Z the mean atomic number of the compound. This factor is critical in determining the portion of the sample from which the signal is acquired, and it is what distinguishes XPS as a surface sensitive technique.

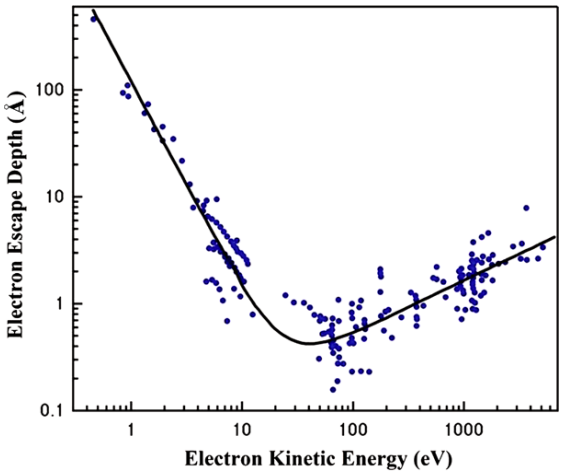

Figure 2.1: Universal curve of the electron inelastic mean free path.

Besides chemical composition and stoichiometry, XPS allows also the determination of the chemical state. Indeed, multiple chemical environments of a certain element within a molecule or an alloy can lead to different changes in the binding energies of a specific core level, commonly referred to as chemical shifts. However, changes in the binding energy could be caused both by initial and final state effects. While the first are reflecting changes in the chemical state and in the atomic environment, final state effects reflect photoemission-induced changes, *i.e.*, electronic relaxation, polarization or core-hole screening. Screening effects are strongly dependent on the distance between the molecule and the metal surface, for this reason their evaluation becomes crucial in the molecular monolayer regime, where the molecules are in direct contact with the metal substrate.

The XPS measurements in this work were carried out at the ALOISA and at the NanoESCA beamlines of the Elettra Synchrotron in Trieste, Italy. The beamlines will be introduced at the end of section 2.1.2 and 2.2.1, respectively.

2.1.2 Angle-resolved photoemission spectroscopy (ARPES)

Valence band (VB) spectroscopy, also known as ultraviolet photoelectron spectroscopy (UPS), is another valuable tool for the characterization of materials. As XPS, it is based on the photoelectric effect but, instead of probing the strongly bound core electrons, VB spectroscopy usually employs less energetic radiation to explore the valence band of the specimen. For molecules in the gas-phase or adsorbed on surface, this technique allows us to access the frontier orbitals in proximity of the vacuum level.

The resulting spectrum at the sample surface includes the following features: the onset of the photoemission signal at the Fermi edge, primary peaks associated with occupied frontier orbitals, a valence band from the metal substrate, and a sloping background caused by secondary electrons. Because of the improved energy and momentum resolution, reduced beam damage, and higher cross-section for excitation, the valence band is best investigated at lower energies (typically < 100 eV for ultraviolet). The typical photoemission spectrum has a sharp cutoff at E_{kin} = 0 that can be used to determine the sample work function [93]. It is important to note that in this evaluation the work function of the analyzer must be considered. Photoemission data in this thesis are presented using binding energies, recalculated from the Fermi level E_F of metal substrates, for the energy scale.

If an angle-resolved electron analyzer is utilized, *i.e.* using angle-resolved photoemission spectroscopy (ARPES), the parallel and perpendicular momenta of the outgoing electron are determined by:

$$k_{\parallel} = \sqrt{2m_e E_{\mathrm{kin}}/\hbar^2}\sin\theta \tag{2.8}$$

$$k_{\perp} = \sqrt{2m_e E_{\mathrm{kin}}/\hbar^2}\cos\theta \tag{2.9}$$

or further converting $K_{\parallel}$ into two cartesian components k_x and k_y:

$$k_x = k_{\parallel}\cos\phi \tag{2.10}$$

$$k_y = k_{\parallel}\sin\phi \tag{2.11}$$

where θ and ϕ are the polar and azimuth angles under which the electrons leave the surface, respectively. As mentioned before, unlike the wave vector components parallel to the surface, the perpendicular k_z component is not conserved when the photoelectrons are transmitted from the sample into the vacuum above. The full angular distribution of the photocurrent ($I(k_x, k_y)$), also known as a momentum map, can be acquired in one single image by using photoemission electron microscopy (PEEM).

One important consideration of using electron spectroscopy for surface analysis is the high surface sensitivity. In the kinetic energy range of interest, 10 to 100 eV, the mean free path λ for inelastic photoelectrons is only a few Ångstroms [93]. Therefore, photoemission spectroscopy is suited to probe the near-surface region, where the main contribution of the total photoemission intensity originates from. This also requires an atomically clean surface under ultra high vacuum (UHV) condition to avoid contamination.

Photoemission tomography (PT)

Common experimental methods for imaging molecular orbitals (MOs), *i.e.*, obtaining their distribution in real or reciprocal space, are either limited to very small molecules, *e.g.*, laser-aligned simple gas-phase molecules for imaging with ARPES, or highly demanding experimental conditions, *e.g.*, flat-lying molecules electronically decoupled from the substrate at cryogenic temperatures and in UHV for imaging with STM. Photoemission tomography (PT), an easy and robust technique for reconstructing MOs of adsorbed molecules and many other applications, is introduced as a powerful alternative in the following.

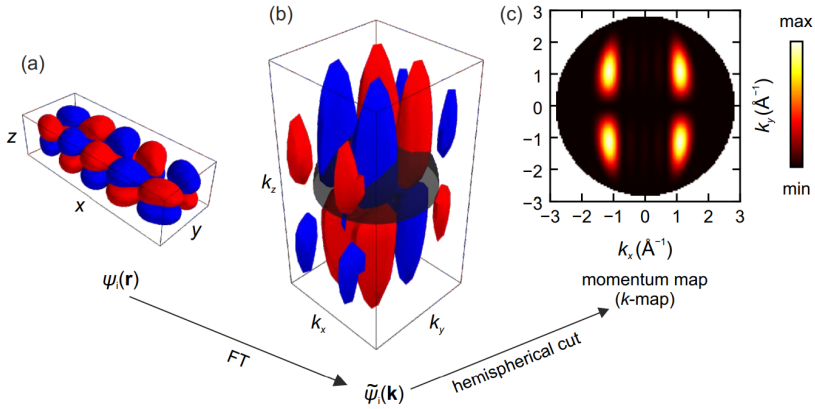

Figure 2.2: Relationship between the molecular orbital in real space $\Psi_i(\vec{r})$ and reciprocal space $\Psi_i(\vec{k})$ and the measured momentum maps (k-maps). (a) Calculated HOMO of isolated pentacene. x and y coordinates are parallel to the long and short molecular axis, respectively, and z is perpendicular to the molecular plane. (b) Fourier Transform (FT) of the pentacene HOMO. A hemisphere with radius $k = \sqrt{2m_e E_{\text{kin}}}/\hbar$ (E_{kin} = 30 eV) is shown in gray. (c) Absolute value of the HOMO FT on the hemisphere. Adapted from [99].

PT is a combined approach consisting of photoemission spectroscopy and density functional theory. In this technique, the Fourier-transformed electron densities obtained by DFT are used to characterize the features of momentum maps and understand the chemical structure of molecular adsorbate systems [100, 101]. Under certain assumptions [99], the molecular orbitals are visible in the valence band spectrum of molecule-single crystal interfaces, representing a fingerprint of a specific state. Exploiting this, PT can also be used to follow on-surface reactions.

Starting from Eq. 2.3, the photoemission current can be written as:

$$I\left(k_x, k_y; E_{\text{kin}}\right) \propto \sum_i \left| \left\langle \Psi_f\left(k_x, k_y; E_{\text{kin}}\right) \left| \overrightarrow{A_0} \cdot \vec{p} \right| \Psi_i \right\rangle \right|^2 \times \delta\left(E_{\text{f}} - E_{\text{i}} - h\nu\right) \tag{2.12}$$

which includes the sum over all initial state wave functions $|\Psi_i\rangle$ to the final state $|\Psi_f\rangle$, which contains the information about the direction ((k_x, k_y) and kinetic energy (E_{kin}) of the photoemitted electrons [99].

In PT, the evaluation of the transition matrix element can be further simplified by approximating the final state by a plane wave, $|\Psi_f\rangle = e^{i(\vec{k}\cdot\vec{r})}$. The matrix can be then rewritten as

$M_{i\to f} \propto \overrightarrow{A_0}\cdot\vec{k}|\langle\Psi_f|\Psi_i\rangle$ or:

$$M_{i\to f} \propto \left(\overrightarrow{A_0}\cdot\vec{k}\right)\int_{-\infty}^{\infty}\Psi_i e^{i(\vec{k}\cdot\vec{r})}d^3r. \tag{2.13}$$

Based on theoretical considerations, the plane-wave final-state approximation is expected to be valid for (i) π orbital emissions from large planar molecules, (ii) an experimental geometry in which the angle between the polarization vector $\overrightarrow{A_0}$ and the direction of the emitted electron $\vec{k}$ is rather small, and (iii) molecules consisting of many light atoms (H, C, N, O) [102].

Within this approximation, equation 2.12 can be rewritten as:

$$I\left(k_x,k_y;E_{\text{kin}}\right) \propto \left|\overrightarrow{A_0}\cdot\vec{k}\right|^2\left|\left(\mathcal{F}\left(\Psi_i\right)\right)\left(\vec{k}\right)\right|^2. \tag{2.14}$$

Within the plane-wave approximation the angle-resolved photoemission intensity is proportional to the square of the product of the Fourier Transform (FT) of the initial state wave function and the polarization factor $\overrightarrow{A_0}\cdot\vec{k}$ related to the experimental geometry. Applying FT on an orbital $\Psi_i(\vec{r})$ of interest, one can directly compare the measured photoelectron distribution (momentum map) with the intersection of its FT, $\Psi_i(\vec{k})$, and a hemisphere of radius $k=\sqrt{2m_e E_{\text{kin}}}/\hbar$ (Ewald sphere construction) [99]. Due to the fact that molecular orbitals could be sliced in the momentum space for a chosen kinetic energy E_{kin}, this experimental technique is referred to as "photoemission tomography".

NanoESCA beamline

The majority of the measurements reported in this thesis, including momentum maps, momentum-integrated valence band photoemission as well as part of the XPS spectra were acquired at the NanoESCA beamline of the Elettra synchrotron in Trieste, Italy, run by Peter Grünberg Institute 6 of Forschungszentrum Jülich. The endstation consists of an UHV setup with a commercially available NanoESCA PEEM, which has been modified as described in [103] and a separated chamber for in-situ preparation. Generally, the microscope can be operated in a direct and a momentum imaging mode. Momentum maps were collected to analyze the photoemission intensity in a lateral reciprocal space range of $k_x, k_y \in$ [-2.1, 2.1] Å^{-1}. In all the measurements here performed the sample was kept at a constant temperature of 90 K, achieving a total energy and momentum resolution better than 100 meV and 0.03 Å^{-1}, respectively.

2.2 Absorption spectroscopy

Another commonly used class of techniques in the investigation of metal-organic interfaces is based on the absorption of photons. Here, the kind of information one can gain depends on the employed photon energy and the polarization of the light. Here, we will first discuss NEXAFS and XMCD, where the absorption of light in the x-ray regime is measured. In this regime, the absorption is mainly caused by electronic excitations from core levels to unoccupied states. The subsequent section discusses IRAS, where the absorption of light in the infrared regime, caused by vibronic excitations, is detected.

2.2.1 Near-edge absorption spectroscopy (NEXAFS)

Near-edge X-ray absorption fine structure (NEXAFS) is an experimental technique developed during the 1980s to specifically study low-Z molecules (mainly constituted by H, C, N, O and F) adsorbed on surfaces. The main capabilities of this technique are the detection of specific bonds in molecules (*e.g.* C-H, C-C, C=C) and the determination of the bond lengths, but also the orientation of the molecule or functional groups on the surface as well as the orbitals involved in chemisorption processes. Low-Z molecules are particularly suitable to be studied with this technique due to their strong bond directionality which, combined with light polarization of NEXAFS, results in a strong dichroism for angle-dependent measurements. These kind of molecules have also a strong dependence of the bond length on its hybridization; this, combined with a large back-scattering cross section of the low-Z atoms, provides clear structure-sensitive resonances in the first 30 eV above the threshold [104].

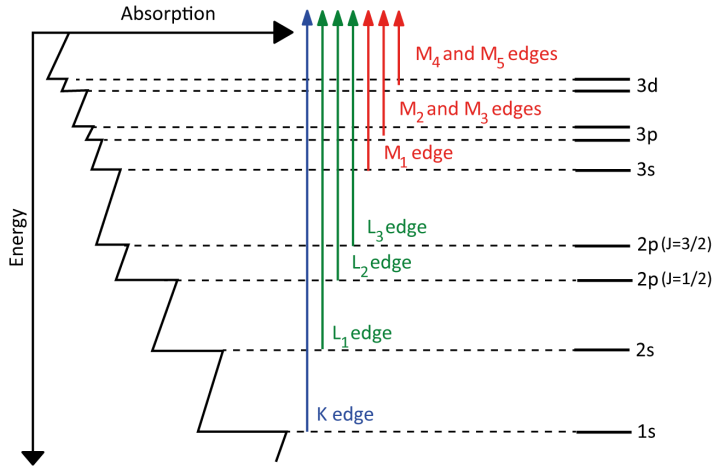

Figure 2.3: Schematic illustration of the transitions that contribute to XAS edges.

Experimentally, the X-ray energy is scanned through a specific atomic species threshold and the absorbed X-ray intensity is measured. In particular, as the photon energy is increased from below the absorption threshold of the probed atom, photoelectrons are excited from core levels by the absorbed X-rays. The created holes are then filled by Auger decay (which is dominant in the soft X-ray region over fluorescence) processes. As the photon energy is increased more, a photoemission peak is then observed. The intensity of the emitted primary Auger electrons, however, will follow the absorption cross-section of the atomic shell. In the so-called Auger electron yield (AEY) modality, the recorded intensity of the Auger peak is a direct measure of the X-ray absorption and, due to the small electron escape depth, is a highly surface sensitive technique ($\sim$1 nm). As they leave the sample, primary Auger electrons create many scattered secondary electrons which dominate the total electron yield (TEY) intensity. This is the most simple detection modality and consists of collecting electrons of all energies from the sample. The TEY cascade involves several scattering events and originates from an average depth, the electron sampling depth, of a few nanometers. Electrons created deeper in the material lose too much

energy to overcome the work-function barrier of the sample, thus not contributing to the TEY intensity. However, this detection technique suffers from the interference of photoemission peaks entering in the measured intensity. In the partial electron yield (PEY) variant, only electrons with a kinetic energy larger than a set threshold value are detected; by suitably choosing this threshold, the presence of photoemission peaks in the detected kinetic energy window over the spanned energy range can be avoided [104].

The fine structure of NEXAFS arises when the photoelectrons coming from the probed element are excited into unoccupied orbitals, so when the X-ray energy is tuned close to the ionization potential and electrons are excited just few electronvolts above the Fermi level. NEXAFS is element-specific because the X-ray absorption edges of different elements have different energies and are sensitive to the bonding environment of the absorbing atom. This results in a chemical shift similar to the case of XPS, but also with a considerably different fine-structure line-shape, thus allowing to achieve an higher sensitivity. Moreover, the major asset of NEXAFS is its polarization dependence.

When the electric field of a linearly polarized photon is aligned with the unoccupied orbitals into which electrons are excited, the intensity increases. This allows one to determine the orientation of these empty orbitals and thus the orientation of functional groups and simple molecules on the surface.

For the determination of geometry, it is necessary to measure NEXAFS spectra at two different angles of the polarization vector with respect to the surface, further simply addressed "polarization angle" or "polarization". On a threefold or higher symmetry surface, the two polarizations are obtained with the electric field of the radiation parallel or perpendicular to the substrate surface. In principle, a reliable theoretical calculation is requested for a correct attribution of measured peaks to MO with known geometry, but for many organic molecules it is also possible to compare the spectra with the ones obtained with known systems. For instance, molecules with aromatic rings or conjugated double bonds, are expected to show transitions to both σ* and π* empty orbitals which have opposite symmetry, and the π* unoccupied orbital lies lower in energy. The dependence of the probability of a transition on the mutual orientation between the orbital and the polarization vector can lead to dichroism between spectra taken at s and p-polarizations. If the geometry of the orbital is already known, this effect gives clues about the orientation of the molecule with respect to the surface.

In this regards, a useful relation that allows the determination of the molecular tilt angles (γ), obtained by following Stöhr's treatment [104] is:

$$\frac{I_p}{I_s} \propto \tan^2(\gamma) \tag{2.15}$$

where I_p and I_s are the transitions intensity in p and s polarization, respectively.

The XAS spectroscopies are classified on the basis of the shell from which the electron is excited, the most common one being the 1s or K-shell. For the purposes of this thesis, C and N K-edge spectra have been acquired. In order to obtain information on the state of the transition metals studied in each case, the focus was shifted instead to the L-edge. Metal L-edge absorption features take into account transitions whose origin corresponds to the $2s^2\ 2p^6$ shell (L-shell). The L_1 edge implies excitations of electrons from the 2s sub-shell, while both L_2 and L_3 edges arise from the spin-orbit splitting of the 2p sub-shell. Due to the nature of the L_1-edge XAS excitations, it offers little spectroscopic information; thus, when referring to the L-edge spectra of a first-row

transition metal complex, this usually indicates the $L_{2,3}$ ones. The $L_{2,3}$-edges imply $2p \rightarrow nd$ dipole-allowed transitions, which generate a $2p^{m-1}\ nd^{n+1}$ final configuration. The orbital angular momentum ($\ell = 1$) of the $2p^{m-1}$ core configuration couples with the spin angular momentum ($s = 1/2$) with the generation of the total angular momenta $j = 3/2$ and $j = 1/2$.

ALOISA beamline

NEXAFS and XPS spectra reported in this thesis were taken at the ALOISA beamline at the Elettra synchrotron. The spectra were measured in partial electron yield mode by means of a channeltron facing the sample, with an energy resolution of 80 meV [105]. The low-energy secondary electrons have been filtered out by means of a negatively polarized grid placed in front of the sample (230 V for the C edge, 370 V for the N edge, 500 V for the O K-edge, 670 V for the Fe L-edge, 740 V for Co L-edge, 820 V for Ni L-edge, 900 V for Cu L-edge). The orientation of the surface with respect to the linear polarization of the synchrotron beam was changed by rotating the sample around the beam axis while keeping a constant grazing angle of 6°. This scattering geometry allows one to change the linear polarization of the light from s to p without varying the illuminated area on the sample [106]. The raw data were normalized to the total photon flux and, in the case of spectra taken on the molecular layer, divided by the clean substrate signal.

2.2.2 X-ray magnetic circular dichroism (XMCD)

X-ray magnetic circular dichroism (XMCD) is a polarization effect in X-ray absorption spectroscopy (XAS) that was first proposed by Schütz and co-workers in 1987 [107], which allows for the determination of spin and angular momentum order in a sample. The remarkable feature of XAS is the direct coupling of the X-ray electric field to the charge and the X-ray angular momentum to the electron angular momentum and spin. The absorption processes are governed by electric dipole transitions that obey strict selection rules on angular momentum conservation and couple different core shells to specific valence shells. Spin-orbit coupling in these final states allows to be sensitive to the electronic spin in the absorption process.

Experimentally, the XMCD measurement technique is equivalent to NEXAFS, but, instead of linearly polarized photons, in order to be sensitive to the angular momentum, circularly polarized light is sent to the sample. Left and right circularly polarized photons possess opposite angular momenta which are transferred to the photoelectron excited from the core shell. The photoelectron then possesses a well defined angular momentum and, in a one-electron picture, one may view the empty valence shell as a detector of this momentum [108, 109].

The X-ray magnetic circular dichroism (XMCD) absorption intensity is defined as the intensity difference measured with left and right circularly polarized light.

Specific sum rules links this intensity to the size of the orbital and spin momenta of the empty valence states [110–112]. Similarly to the case of NEXAFS, angle dependent measurements in magnetic fields can determine the anisotropies of the orbital moment and of the spin density.

In the case of transition metals such as Fe, Co, and Ni, the absorption spectra for XMCD are usually measured at the L-edge, in which the incoming photon excite a 2p electron to a 3d state [113, 114].

The XMCD experiments in this work have been performed at the **X-Treme beamline**, located in the Swiss Light Source at the Paul-Scherrer Institüt in Villigen, Switzerland [115].

2.2.3 Infrared reflection–absorption spectroscopy (IRAS)

IR spectroscopy is a powerful tool not only to identify chemical species, but also to probe the molecular structure, orientation, or chemical interaction of adsorbates. Absorption of IR light in the range of 100 to 10 000 cm^{-1} excites molecular vibrations and rotations if certain selection rules are obeyed. A vibrational mode is IR-active and a transition from the initial to the final vibrational state occurs only if the electric dipole moment μ or one of its components μ_x, μ_y, or μ_z are unequal zero.

In order to investigate adsorbate interactions at metal surfaces, infrared reflection absorption spectroscopy (IRAS) is a commonly applied technique due to its sensitivity towards the molecular orientation. This sensitivity is a result of further selection rules that are elaborated in the following.

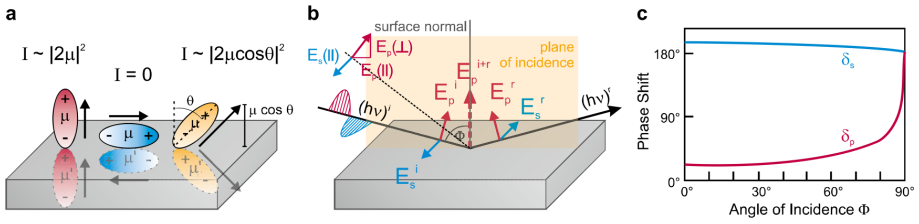

Figure 2.4: Schematic explanation of the MSSR (a), components of the electric field for s- and p-polarized light (b), phase shift as a function of the angle of incidence (c). Adapted from [116,117].

In IRAS, the high reflectivity of metal surfaces for IR light is exploited. On a metal surface, the electric field of an incident light beam interacts not only with adsorbate molecules, but also with the free electron gas in the metal. The same is valid for the dipole moment of the adsorbate, which induces an image dipole μ' in the metal. As the free electron gas redistributes based on the dipole charge of the adsorbed molecule, dynamic dipole moments of translations oriented in parallel to the metal surface cancel out and are therefore IR-inactive. A translation in the z-direction, on the other hand, generates an enhanced dipole moment. This phenomenon is commonly referred to as metal surface selection rule (MSSR) [117]. Furthermore, the MSSR can be employed to derive the molecular tilting angle of adsorbate molecules via a comparison of relative peak intensities obtained from IRAS and bulk spectra.

When IR light is reflected at a metal surface, the reflected beam experiences a phase shift. This phase shift is a function of the incident angle ϕ and the polarization of the light. Similar to the MSSR, electric field components of the incident and reflected beam that are oriented parallel to the metal surface interfere destructively, while electric field components perpendicular to the surface are strengthened [118]. The polarization of light is defined with respect to the plane of incidence. Whereas the electric field of p-polarized light is oriented in parallel, the electric field of s-polarized light is oriented perpendicular to the plane of incidence. Upon variation of the angle of incidence ϕ, the electric field components of s-polarized light are always oriented parallel to the surface leading to a constant phase shift of 180°and, as a result, destructive interference. The electric field of p-polarized light, on the other hand, consists of components oriented in parallel and perpendicular to the metal surface. Their contribution is dependent on the incidence angle ϕ. At angles of grazing incidence, the electric field is enhanced the strongest as constructive interference of the components oriented perpendicular to the surface is at its maximum [116]. Hence, the exclusive use of p-polarized light improves the signal-to-noise ratio in IRAS significantly.

The IRAS measurements were carried out at the Friedrich-Alexander-University Erlangen-Nuremberg, in the facilities of the **Interface Research and Catalysis** group (ECRC). The apparatus is equipped with various characterization and preparation tools described in [119].

2.3 Low energy electron diffraction (LEED)

Low energy electron diffraction (LEED) is a surface sensitive technique committed to the determination of structural properties in a solid. Since low energy electrons are used in LEED (typically 50 - 500 eV) their wavelength corresponds to the atomic lengths of almost all the materials, therefore being sensitive to the atomic arrangement. Low-energy electrons are also characterized by a limited inelastic mean free path, therefore limiting the probing depth to the first subsurface layers. Consequently, the inspection of a LEED pattern provides the means to study the surface lattice symmetry, the lattice constant and the presence of contaminants.

From a LEED experiment, qualitative and quantitative information about sample surface can be extracted. The qualitative analysis is performed by visual inspection of the electron diffraction pattern, being able to provide information on the size and symmetry of the surface unit cell.

2.4 Scanning tunneling microscopy (STM)

The experimental techniques introduced so far obtain spatially averaged information, as the signal originates from a macroscopic area of the surface, which contains many electronically or vibrationally excited molecules. STM is a widely employed tool that offers the possibility to resolve single molecules and even atoms, as lateral and vertical resolutions of 1 Å and 0.01 Å, respectively, can be reached [120].

When a metallic tip is approached to a conductive surface, a potential barrier due to the vacuum gap is present between the two objects. If a bias voltage is applied between them, and their distance is small enough, the electrons can tunnel across the potential barrier from the tip to the sample or *vice versa*, giving rise to a current flow between them, which is strongly dependent on the tip-to-sample distance: this phenomenon is called quantum tunneling.

The STM images are obtained by scanning the tip over an area (x, y) of the surface with sub-Ångstrom lateral resolution and recording the tip height z or the tunneling current I. Therefore, the recorded $(x, y; z(x, y))$ or $(x, y; I(x, y))$ data are displayed in a 2-dimensional plot.

The tip position is controlled via a piezoelectric tube in the (x, y) directions through the electrodes along the tube and in the z direction (tip height) through a feedback mechanism. Since the piezoelectric expansion/contraction is controlled with sub-angstrom precision in the (x, y, z) directions, the tip is scanned over an area of the surface with sub-angstrom resolution and high resolution images of the surface of interest can be obtained.

There are two modes of scanning in an STM (see Fig. 2.5):

• **constant height mode**: the tip is kept at a constant height (constant z) while scanning, and the tunneling current $I(x, y)$, which is recorded in every scan point, is color-coded to form the STM image $(x, y; I(x, y))$;

• **constant current mode**: during the scan, the tunneling current is kept constant by changing the tip height z by means of an electronic feedback system, and the STM image $(x, y; z(x, y))$ is formed by color-coding the tip height $z(x, y)$ at every scan point.

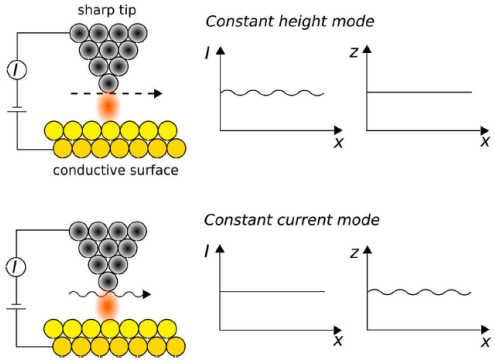

Figure 2.5: The two imaging modes in STM.

The information contained in an STM image is not simply the topography of the surface, because the tip is governed by the tunneling current, which depends not only on the geometrical position of the atoms at the surface, but also on the spatial distribution and the energy of the tip/sample electronic states available for the tunneling process.

Although STM has the great advantage to give real space atomic-resolution images of the surfaces, it lacks chemical sensitivity. However, thanks to technical and theoretical developments, the STM has evolved so that we can get information about the electronic properties of samples and adsorbates by Scanning Tunneling Spectroscopy (STS) [121, 122].

Following the Bardeen's formalism [123], and assuming a tip with a constant DOS, the first derivative of the tunneling current gives:

$$\frac{\mathrm{d}I}{\mathrm{d}V} \propto \rho_S \left(E_F - eV\right)$$

and thus it is possible to probe the DOS of the sample, or molecular states close to the Fermi level, through the tunneling current conductance.

The STM and STS experiments in this work were performed in collaboration with Dr. Alessandro Sala in the **Surface Structure and Reactivity at the Atomic Scale** (STRAS) laboratory in Trieste, Italy. The measurements were done with an Omicron LT-STM system at a sample temperature of 77 K.

Chapter 3

Stabilization of catalytically and magnetically active sites by on-surface coordination

When contacted to a substrate, the free molecule can drastically change its properties. In order to unravel the changes induced by the different metallic substrates investigated herein, first the molecules will be deposited on an inert substrate, where no interaction between the molecule and the substrate is expected. Different passivating procedures have been proposed in the past, here we will use the oxygen-passivated copper substrate that allow us to maintain the order of the layer and to study the free-standing properties of the molecule. In the following, we will model the chelated metal ion spin and oxidation state switching by tuning the strength of the molecule-surface interaction. Different metallic substrates, with decreasing reactivity, copper, silver and gold, are studied in this course. Moreover, the interaction with external axial ligands will be investigated with the aim of further tuning the magnetic and electronic properties of the molecular systems, in which the *surface-trans effect* plays a pivotal role. Two different porphyrin systems, namely nickel and cobalt tetraphenylporphyrin (TPP), are primarily considered. Finally, by replacing TPPs with OEPs, the role of the molecular periphery in the molecular properties will be explored. It will be shown that the molecular reactivity remains unchanged as long as the molecular flexibility is preserved on a substrate that activates the central metal. At the end of the chapter, alkali metal doping of the two metal tetraphenylporphyrins studied here will be presented. The crucial role of the molecular conformation in defining the metal reduction will be unraveled.

3.1 NiTPP on oxygen-passivated Cu(100): the free-standing reference

Due to its open structure, the tetrapyrrolic ring in metal tetraphenyl porphyrins can be strongly influenced by the coordination, either to the surface or to external ligands. To evaluate the molecule-substrate and inter-molecular interactions [39, 124, 125], reference data for free or weakly interacting molecules are required. Gas-phase molecules or powder samples, as well as thin molecular films, are commonly employed for this purpose. While the molecules are randomly

oriented in both gas-phase and powder samples, an ordered multilayer offers the advantage of probing the molecular orbitals with selective sensitivity to the orbital symmetry by means of NEXAFS measurements with different light polarizations.

In fact, σ^* and π^* absorption resonances are selectively measured by exploiting their dependence on the photon beam polarization. The electric field perpendicular (s-polarization) or parallel (p-polarization) to the incidence plane will yield different intensities (NEXAFS linear dichroism), according to the orientation of the orbitals involved in the excited electronic transitions [104]. In the case of planar aromatic compounds, a flat adsorption geometry yields the best discrimination of the symmetry selected unoccupied MOs. Unfortunately, even in the case of perfectly planar aromatic molecules, a fully coherent growth and a quasi-planar molecular orientation can be hardly achieved beyond the few-layer thickness limit, and only for few specific systems. In particular, epitaxial growth parallel to the surface can be achieved for 2D extended planar molecules like phthalocyanines [11,12,126,127], or when the substrate lattice offers a good matching with the molecular structure, such as sexi-thiophene on Au(110) [128] and pentacene on Ag(111) [129], Cu(110) [130], TiO_2(110) [131]. Neither of these conditions is achieved for hetero-cyclic molecules that contain substituents with high rotational freedom, like MTPPs. Based on these considerations, a first step in this direction was to exploit the anisotropic surface corrugation of rutile-TiO_2(110) to drive the oriented growth of both poly-conjugated aromatics [131–136] and porphyrins [137–140]. However, significant charge transfer may take place between large aromatic molecules and defects of the rutile surface [141]. In addition, a strong chemical interaction between the porphyrin tetrapyrrolic center and the titanium dioxide has been reported [142,143]. Alternative approaches for the decoupling of the organics from metal surfaces are based either on the intercalation of insulating layers [144] or on the passivation of the surface, *e.g.*, by graphene [145], Sn alloying [146] and oxidation [147,148]. In particular, it has been shown that, for an oxygen-modified copper surface, the covalent nature of the Cu–O interaction yields a strong localization of the surface electrons and inhibits the charge transfer from the metal to the organic overlayer [147,149,150]. Particularly, the $(\sqrt{2} \times 2\sqrt{2})$R45°-O-reconstructed Cu(100) surface, besides quenching the molecule-surface interaction, allows the preservation of an ordered layer, as confirmed by low-energy electron diffraction. Therefore, it can be employed as a template for reference systems to probe both symmetry and occupation of molecular orbitals. The effectiveness of this approach will be here demonstrated on the NiTPP molecule.

The valence band spectra of a NiTPP monolayer deposited on the bare Cu(100) and on the O-Cu(100) surfaces are presented in Figure 3.1a (top and bottom, respectively). On the bare copper surface, the VB spectrum exhibits two peaks, previously assigned to the gas-phase LUMO/+1 and LUMO+3. These are two π-type molecular orbitals that are partially filled as a result of the strong molecule-metal interaction [100].

When NiTPP molecules are deposited on the $(\sqrt{2}$ x $2\sqrt{2})$R45°-oxygen-reconstructed copper surface, however, the valence band peaks related to the LUMOs features vanish (see Figure 3.1a, bottom). This observation points towards a significant quenching of the charge transfer at the interface, as a result of the weakening of the interaction between the molecule and the copper substrate favored by the pre-adsorbed oxygen layer. These changes in the electronic structure have dramatic consequences also in the overall appearance of the NEXAFS spectra: while the charge transfer from the substrate to the organic film usually results in the partial or total quenching of the lower-energy NEXAFS features, due to the emptying of the starting molecular orbitals involved in the transitions, the quenching of the charge transfer allows the preservation of these

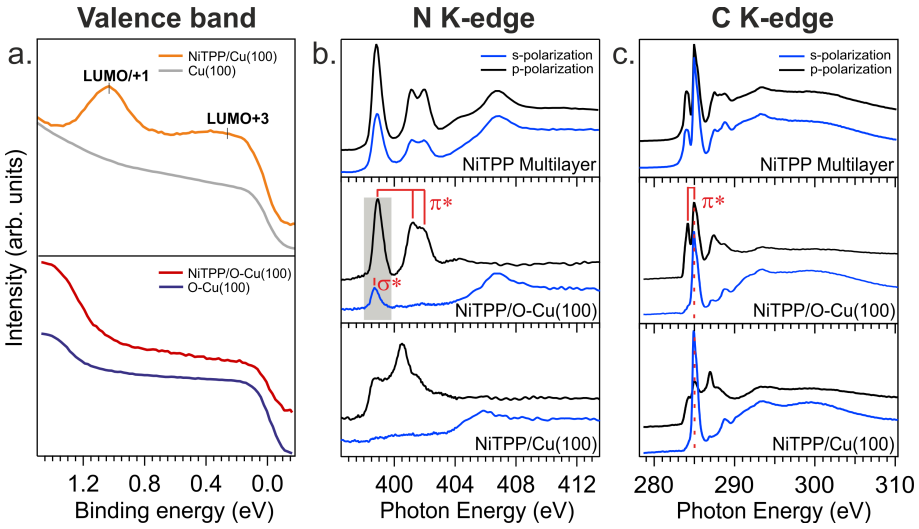

Figure 3.1: a) Valence band spectra of NiTPP on Cu(100) (blue curve) and on O-Cu(100) (black curve); the spectra of bare Cu(100) and O-Cu(100), green and red curve, respectively. b) N K-edge NEXAFS spectra of NiTPP multilayer and NiTPP monolayer deposited on bare and oxygen modified Cu(100) surface. c) C K-edge NEXAFS spectra of NiTPP multilayer and NiTPP monolayer deposited on bare and oxygen modified Cu(100) surface.

features. Moreover, the intensity of the absorption resonances depends on the number of available excitation channels and on the associated oscillator strength of the transitions [151], together with the angle between the electric field of the linearly polarized incoming light and the spatial orientation of the unoccupied MOs.

The nitrogen K-edge spectra of the NiTPP monolayer deposited on the bare (bottom) and oxygen-modified (middle) copper surface, together with the NiTPP multilayer (top), are compared in Figure 3.1b. The NEXAFS spectra of the NiTPP multilayer on Cu(100) do not show linear dichroism, suggesting a random molecular orientation in the organic layers. The lack of linear dichroism precludes the determination of the symmetry of the resonances, as well as the estimate of the oscillator strength of the transitions. Instead, strong linear dichroism is observed in the N K-edge spectra for the NiTPP monolayer on the bare and on the oxygen pre-covered Cu surfaces. In particular, the resonances dominating the p-polarization spectrum below the ionization threshold (∼404 eV) display opposite dichroism with respect to the broad resonance recorded in s-polarization above the ionization threshold. As a rule of thumb, the N *1s* ionization threshold separates the region of π*-symmetry resonance (below) from that of σ*-symmetry ones (above). Hence, the observed dichroism points to an adsorption orientation of the porphyrin macrocycle parallel or almost parallel to the surface in both cases.

The flat adsorption geometry of the macrocycle moiety is further confirmed by the dichroic behavior of the C K-edge spectra, both on the bare and on the oxygen pre-covered-Cu(100) substrates (see Figure 3.1c). Following a well-tested model analysis [39], the NEXAFS resonances at ∼284 eV are exclusively associated to the π*-symmetry LUMO states localized at the macrocycle ring, displaying large dichroism with a very small residual intensity in s-polarization, in full agreement with the observed behavior of the low energy N resonances. Instead, the intense

resonance at 284.9 eV is mainly ascribable to the transition to the π*-symmetry LUMO of the peripheral phenyl rings. The adsorption tilt angle (γ) of the phenyl rings with respect to the copper surface can be evaluated from the angle-dependent intensity ratios (I_s/I_p) of the resonance at 284.9 eV, following the equation $\gamma = \frac{1}{2} arctan^2(I_s/I_p)$ [106]. Using this approach, tilt angles of 69$\pm$5° and 52$\pm$5° have been derived for NiTPP on Cu(100) and O-Cu(100), respectively.

The charge transfer occurring at the NiTPP/Cu(100) interface strongly affects the intensity of the π* resonances and of the σ* feature as well: all low energy LUMOs are partially filled (and shifted). On the contrary, the close similarity between the resonance intensity and the shape of the multilayer spectra with that of the monolayer grown on the oxidized surface confirms the weak interaction of the latter substrate with the porphyrin array, which now allows us to disentangle the symmetry of the orbitals. On the oxygen modified system, the low energy features in the N K-edge spectra measured with p- and s-polarized light are related to π* (N *1s*→LUMO/LUMO+1 and LUMO+3) and to σ* (N *1s*→LUMO+2) resonances, respectively [152]. The latter transition from N *1s* to a mixed Ligand $2p_{x,y}$ - Metal $3d_{x^2-y^2}$ orbital falls close to the main π* symmetry resonance also in porphyrins and phthalocyanines coordinated to other metals, *e.g.*, Cu [106,153] and Co [154], where the precise energy position around the main π* transition depends on the specific metal element [155] and the local interaction with the substrate [156]. Because of its intrinsically low intensity, this σ* transition is hardly identified in disordered films [72,157]. Even in the case of homogeneously oriented multilayers, its intensity and energy position can be hardly evaluated, because of the overlap with the residual intensity of the large π* resonance in s-polarization due to the molecular tilt off from the surface. In the present case, the almost perfect parallelism of the porphyrin macrocycle to the surface allows us to perform a quantitative analysis of the lowest π* and σ* resonances at 398.95 eV and 398.75 eV, respectively (see Figure 3.1b, highlighted in gray). It has to be noted that the LUMO+2 associated to the σ* resonance does not yield any clear signature in the VB spectrum, but it is clearly observable in the NEXAFS spectrum. Remarkably, density functional theory calculations showed that the filling of this orbital is responsible for the reduction of the oxidation state of the Ni ion, from Ni(II) to Ni(I) [100,152].

3.2 Charge injection and spin switching at the metal-organic interface: NiTPP on Cu(100)

The valence band spectra of the NiTPP monolayer deposited on the bare and on the oxygen-passivated Cu(100) surfaces are presented in Figure 3.1a (top and bottom, respectively). As previously discussed, on the bare copper surface, the VB spectrum exhibits two peaks, assigned to the gas-phase LUMO/+1 and LUMO+3. These are two π molecular orbitals that are partially filled, as a result of the strong molecule-metal interaction [100].

When NiTPP molecules are deposited on the ($\sqrt{2}$ x $2\sqrt{2}$)R45°-oxygen-reconstructed copper surface, the valence band peaks related to the LUMOs features vanish. This observation points towards a significant quenching of the charge transfer at the interface, as a result of the weakening of the interaction between the molecule and the copper substrate favored by the pre-adsorbed oxygen layer. When fully decoupled from the substrate, the gas-phase oxidation state of the central metal ion is preserved, indeed for NiTPP/O-Cu(100) the nickel ion is in the +2 oxidation state (see Figure 3.2). Instead, when deposited on a strongly interacting surface, like the bare Cu(100) surface, where a strong charge transfer is taking place at the molecular-surface interface, the nickel

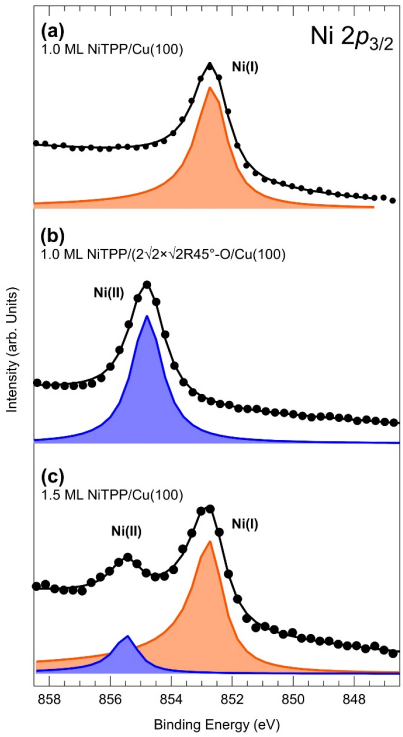

Figure 3.2: Ni $2p_{3/2}$ core level spectra collected at room temperature from: (a) 1.0 ML NiTPP/Cu(100); (b) 1.0 ML NiTPP deposited on the oxygen-precovered Cu termination; (c) 1.5 ML NiTPP/Cu(100); $h\nu$ = 1020 eV.

ion is reduced from Ni(II) to Ni(I) [100, 152]. The Ni *2p* XPS spectrum shows drastic changes between the monolayer deposited on the bare and on the oxygen modified copper. Indeed, a clear shift towards lower binding energies (around 2 eV) is observed in the case of NiTPP deposited on the bare copper surface. These differences support the stabilization of the nickel ion in two different oxidation states, namely Ni(II) for the NiTPP/O-Cu(100) and Ni(I) for NiTPP/Cu(100). At the Ni L_3-edge (see Figure 3.3a), the excitations from the occupied *2p* core levels to unoccupied *3d* valence states mostly contribute to the absorption spectrum of the incident light. Therefore, a change in the lineshape, as well as in the position of the absorption resonances, can provide information about the electronic structure of the nickel *3d* shell. The NEXAFS Ni $L_{3,2}$-edge of the NiTPP/O-Cu(100) interface shows a sharp feature having its centroid at 854.3 eV, plus a small satellite peak at 856.5 eV. The lineshape corresponds to a low-spin state for the Ni(II) in d^8 configuration. When contacted to the bare Cu(100) surface, the Ni $L_{3,2}$ edge recorded on the NiTPP monolayer shows the main adsorption resonance centered at 852.4 eV. This value is characteristic for the Ni(I) valence state and is associated with an $2p_{3/2} \rightarrow 3d_{x^2-y^2}$ transition. The single peak feature points towards a d^9 configuration with one hole in the nickel *3d* level.

The reduction of the central metal ion has strong effects on the overall properties of the molecular layer, starting from the electronic and magnetic properties and going to the catalytic

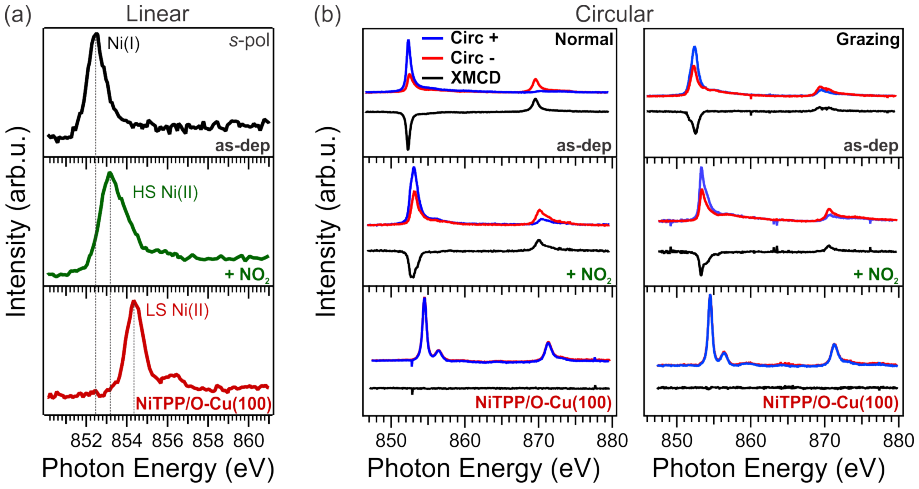

Figure 3.3: (a) NEXAFS spectra of the L_3-edges of the three systems, namely, from top to bottom, NiTPP/Cu(100), NiTPP/Cu(100) after a dose of 10 L of NO_2 and NiTPP/O-Cu(100). All the spectra were measured at room temperature. (b) Absorption spectra at the $L_{2,3}$-edge of left- and right-hand circularly polarized light and resulting XMCD signals for normal (left) and grazing (right) incidence. The spectra were acquired with an external magnetic field of 6.8 T and temperatures of 3 K. In order to ensure saturation of the NiTPP film, the system was exposed to 10 L of NO_2.

properties, as will be shown in the following. In order to follow the changes in the magnetic properties of the nickel ion, XMCD measurements were performed at the Ni L-edge. To check for magnetic saturation, the XMCD intensity at the L_3 edge was measured as a function of the applied magnetic field in the range between -6.8 T and 6.8 T (see Figure 3.4). The measurements are done by acquiring the TEY as a function of the applied magnetic field, at the energy of maximum XMCD and at the pre-edge where there is no XMCD contrast, in order to account for baseline drifts. The same measurement is repeated for different X-ray helicities in order to obtain the XMCD magnitude as a function of the applied field.

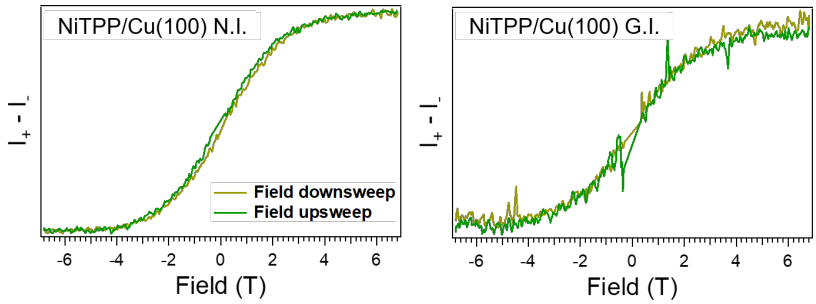

Figure 3.4: Magnetic hysteresis curves for NiTPP/Cu(100) measured at 3 K. Magnetic saturation is reached for normal (N.I., left panels) and grazing (G.I., right panels) photon incidence, respectively.

The absorption spectra acquired with left and right circularly polarized light at the L_3 and L_2 edges are depicted in Figure 3.3, together with the corresponding dichroic signal obtained by the

	Normal incidence	Grazing incidence
$m_{s,eff}$	$(1.64 \pm 0.09)\mu_B$	$(0.39 \pm 0.05)\mu_B$
m_l	$(0.22 \pm 0.02)\mu_B$	$(0.15 \pm 0.01)\mu_B$

Table 3.1: Resulting values for the effective spin moments and orbital moments of NiTPP/Cu(100) for normal and grazing incidence, respectively.

difference between spectra acquired with left and right circularly polarized light: $c_{minus} - c_{plus}$.

While the NiTPP molecule deposited on the O-Cu(100) surface does not show any XMCD signal, thus confirming the gas-phase LS d^8 configuration, the situation is completely different when the Ni porphyrin is in direct contact with the copper surface. Strong dichroism is present at the $L_{2,3}$ edge, suggesting an HS configuration. To obtain the effective spin moment and the orbital moment, a sum rule analysis has been performed. The calculated values of the sum rule analysis are shown in Table 3.1. Since the charge transfer at the NiTPP/Cu(100) interface leads to a change of the nickel oxidation state, we applied the same normalization for the isotropic absorption intensity over both edges as in Ref. [158].

By measuring in normal and grazing incidence, it is found that the effective spin moment ($m_{s,eff}$) is $(1.64 \pm 0.09)\mu_B$ and $(0.39 \pm 0.05)\mu_B$, respectively. Indeed, the values are similar to those of CuPc/Ag(100), where the Cu ion is also in a $3d^9$ configuration, *i.e.* $(1.67 \pm 0.08)\mu_B$ and $(0.35 \pm 0.08)\mu_B$ [159]. Thus, we conclude that the values agree with the previously reported magnitude and anisotropy of the spin-quadrupole coupling $<T_z>$.

In order to support our experimental observations and provide a detailed insight into the observed on surface molecular spin switching, numerical simulations based on density functional theory (DFT) were performed. DFT calculations reported in this section are performed in collaboration with Andreas Windischbacher and Prof. Peter Puschnig from the University of Graz, Austria. The projected density of states (PDOS) onto the different *3d* orbitals of the central Ni ion is shown in Figure 3.5.

For Ni(II)TPP on O-Cu(100) (see Figure 3.5a, bottom), the calculations confirm a gas phase-like $(d_{xy})^2$ $(d_{yz}, d_{xz})^4$ $(d_{z^2})^2$ $(d_{x^2-y^2})^0$ configuration with two holes and no unpaired electrons. Consequently, the *3d* orbital local magnetic density of states of Ni is equally distributed over the two spin-channels (spin $\uparrow$ and $\downarrow$, respectively). This results in a vanishing magnetic dipole moment (S = 0) and is in agreement with the absence of the XMCD signal. In contrast, upon the interaction of NiTPP with a clean Cu surface, charge transfer across the interface leads to the occupation of formerly unoccupied molecular orbitals [160]. This redistribution of electrons also enhances the electron density in the $d_{x^2-y^2}$ nickel orbital, ultimately resulting in the oxidation of the central nickel atom into a $(d_{xy})^2$ $(d_{yz}, d_{xz})^4$ $(d_{z^2})^2$ $(d_{x^2-y^2})^1$ occupation (see Figure 3.5a, top). Nickel then has one unpaired electron, and the system becomes paramagnetic with S = 1/2. The net magnetic moment gives rise to a magnetic dichroic signal at the Ni $L_{2,3}$-edge (Figure 3.3b, top).

Do the two systems show a different reactivity and can this be exploited to further tune the magnetic and electronic properties of the organic-metal interface? In order to test this, Ni(I)TPP and Ni(II)TPP 2D assemblies, stabilized on the bare and on the oxygen pre-covered Cu(100), respectively, were exposed to increasing doses of nitrogen dioxide (NO_2), which is a strongly oxidizing gaseous agent.

At room temperature (RT), both systems were exposed to increasing doses of NO_2 and the resulting changes in the molecular film were monitored by means of XPS. The photoemission

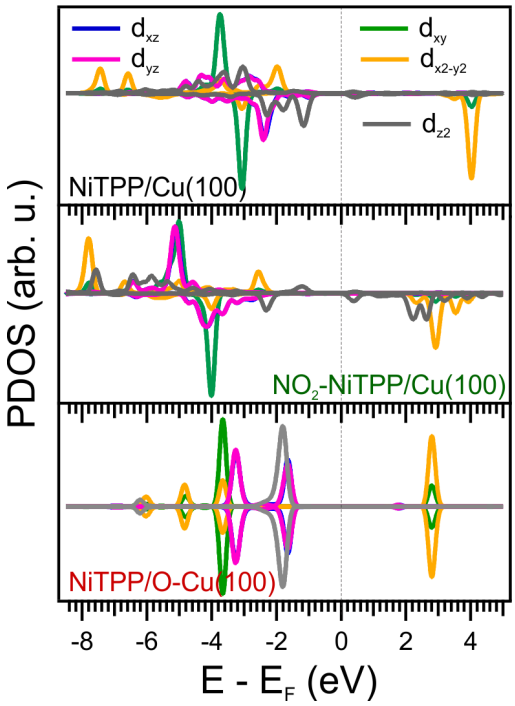

Figure 3.5: Calculated DOS projected onto the different d states of the central Ni atom for the majority and minority spin channels for the three interfaces, *i.e.* NiTPP/Cu(100), NO_2-NiTPP/Cu(100) and NiTPP/O-Cu(100).

spectra of the N *1s* core level shell before and after the exposure of the NiTPP/Cu(100) are shown in Figure 3.6a, top and bottom, respectively. The N *1s* spectrum of the pristine NiTPP on the copper surface shows a single peak at 398.6 $\pm$ 0.2 eV, as expected for the four chemically equivalent nitrogen atoms of the macrocycle [161]. After exposing the Ni(I)TPP/Cu(100) interface to NO_2, a new spectral feature appears at a binding energy of 402.5 $\pm$ 0.2 eV, while both the area and the BE of the pristine peak remain almost unaffected. Therefore, we tentatively assign this new component to the nitrogen atom of the NO_2 ligand that adsorbs at the NiTPP/Cu(100) interface at RT. Also the NEXAFS N K-edge measurements performed before and the NO_2 dose shows significant differences, suggesting the adsorption of the gaseous molecule to the nickel porphyrin.

The NEXAFS spectra of the Ni(I)TPP on Cu(100), acquired in p-polarization, show three feature A_N, B_N, and C_N at 398.7, 400.6, and 401.6 eV, respectively. They originate from the π^* resonances of the N *1s* $\rightarrow$ LUMO/LUMO+1 and LUMO+3 [160] and exhibit strong dichroism, thus vanishing in s-polarization spectra, which indicates a flat adsorption geometry of the porphyrin macrocycle. The strong interaction between the NiTPP and the Cu surface leads to the quenching of the resonance at 398.7 eV, whose intensity is reduced compared to the one observed for a molecular multilayer [160]. Upon exposure of the porphyrin film to NO_2, the NEXAFS spectrum measured with s-polarized light shows a new feature at 402.3 eV with a shoulder at 401.5 eV (labeled D_{NO_2}, in Figure 3.7b, bottom), which we associated to the π^* resonances of nitrogen dioxide [162, 163].

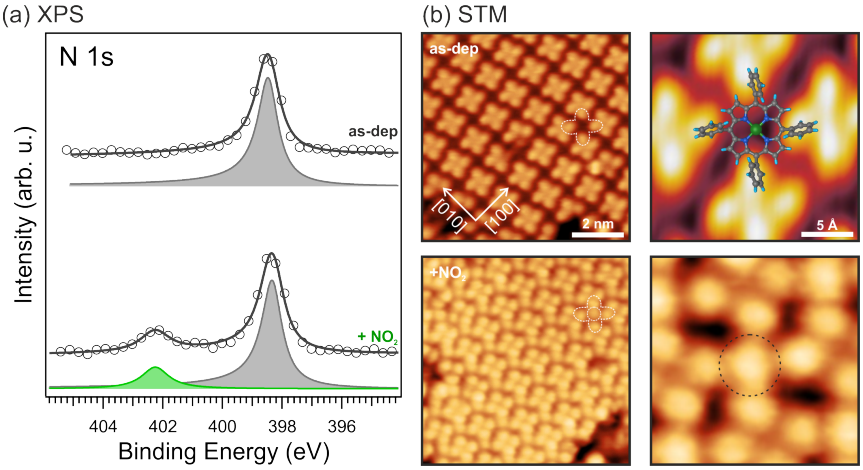

Figure 3.6: (a) N *1s* photoemission spectra ($h\nu$ = 1020 eV), together with their corresponding fits, of the as-deposited NiTPP/Cu(100) and after exposure to 10 L of NO_2, bottom and top, respectively. (b) STM images of NiTPP/Cu(100) before and after exposure to 10 L NO_2 acquired at 77 K, top and bottom, respectively. Image size 8x8 nm^2, tunneling parameters: as-deposited U = -1 V, I = 500 pA, after the NO_2 dose U = +1 V, I = 200 pA. On the right: close-up of the corresponding NiTPP/Cu(100) interface before and after the NO_2 dose. Image size 2x2 nm^2, tunneling parameters: as-deposited U = -1 V, I = 500 pA, after the NO_2 dose U = +1 V, I = 200 pA.

The same peak is almost absent in p-polarization, suggesting an upward geometry of the N-O bond. The position of the feature rising around 402.3 eV suggests the intactness of the NO_2 molecule upon adsorption.

To confirm the adsorption site of the ligand, scanning tunneling microscopy (STM) measurements have been performed before and after dosing NO_2 onto the NiTPP layer. The corresponding STM images are shown in Figure 3.6b, top and bottom panels, respectively. The STM appearance of the as-deposited NiTPP molecule is dominated by four bright features and a dark depression in the center (see Figure 3.6b, top right), associated with the four peripheral phenyl rings and the macrocycle core, respectively, as previously reported [147]. After exposure to NO_2, circular protrusions (circled in black) appear at the center of the NiTPP, replacing the depression at the macrocycle center (see Figure 3.6b, bottom right).

From large-scale STM images, it can be seen that such features appear on top of almost all the Ni sites (see Figure 3.8), and thus, in agreement with the XPS data, we can associate them with the NO_2 molecule bound to the nickel ion. Crucially, we also observe that a gentle annealing up to 390 K is sufficient to restore the NiTPP film (see Figure 3.9). The as-deposited NiTPP molecules (left) present a rounded protrusion at the center after exposure to 10 L of NO_2 (middle). After the annealing at 390 K (right) all NO_2 molecules are desorbed from the NiTPP molecules, restoring the dark depression at the macrocycle center, while the appearance of the lateral features related to the phenyl rings drastically changes. This phenomenon is associated to a flattening of the phenyl moiety upon sample annealing and will be discussed later (see Chapter 4). The flattening is in general not reversible, as the thermal treatment allows the molecule to reach a more stable adsorption configuration, however the flattening does not influence the magnetic and catalytic properties of the nickel ion; NO_2 can be re-adsorbed on NiTPP. Notably, in order to have a uniform

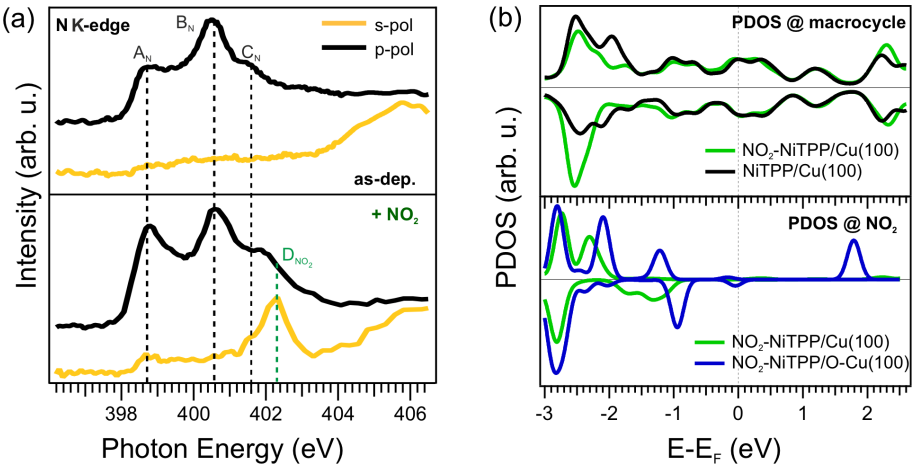

Figure 3.7: (a) Nitrogen K-edge adsorption spectrum for the NiTPP/Cu(100) interface before (top) and after (bottom) the exposure of 10 L of NO_2. (b) Top: PDOS of the macrocycle for the NiTPP/Cu(100) and NO_2-NiTPP/Cu(100) systems. Bottom: PDOS of the NO_2 molecule for NiTPP/Cu(100) and NO_2-NiTPP/Cu(100) systems.

NiTPP layer with all the phenyls in the final geometry, higher annealing temperatures, *i.e.* 470 K, are necessary [161].

Having established that NO_2 interacts with the Ni(I)TPP molecule, we demonstrate that the reduced oxidation state is crucial for the film reactivity by performing a similar experiment on a Ni(II)TPP layer. Notably, in contrast to Ni(I)TPP, no change in the N *1s* spectrum can be observed after dosing 20 L of NO_2 on the Ni(II)TPP layer (see Fig 3.10).

This suggests that the nickel is fully inert to nitrogen dioxide in the higher (Ni(II)) oxidation state, concluding that the choice of a proper substrate, which can reduce the chelated nickel ion, is crucial for the reactivity of the molecular layer.

To additionally characterize the interaction of NiTPP with Cu(100) and the adsorption behavior of NO_2, we performed IRAS experiments under UHV conditions. First, we monitored the deposition of a NiTPP multilayer (roughly 5 ML) on clean Cu(100) at 300 K *in-situ* by IRAS. In Figure 3.11 we show selected IRA spectra recorded during the uptake at different NiTPP coverages. In the multilayer spectra, the main bands appear at 3062, 3025, 1600, 1442, 1353, 1073, 1008, 800 and 752 cm^{-1}. According to the literature, we assigned the signals to specific modes, which are located predominately either at the central porphine macrocycle or at the phenyl rings [164–169]. The ATR reference spectrum of NiTPP is in good agreement with the multilayer IRA spectrum, confirming that the porphyrin is deposited without decomposition.

In the monolayer (ML) regime (marked in blue) most of the multilayer signals are present and have the same shape. However, there are some missing features, namely the bands at 3025, 1353 and 1008 cm^{-1}(marked in gray), which we ascribe to C-H stretching ν(C-H), combined stretching of C-C, C-N (and C-H) in the pyrrole units ν(C-N, C-C, (C-H))porphine, and in-plane deformation of the porphine $\delta_{ip,porphine}$. Since IRAS is sensitive to the adsorption geometry of adsorbates, changes between monolayer and multilayer spectra often indicate distinct orientations of the adsorbates near the surface. The reason is the metal surface selection rule (MSSR), which implies that only those modes are active in IRAS, which have a dynamic dipole moment that is

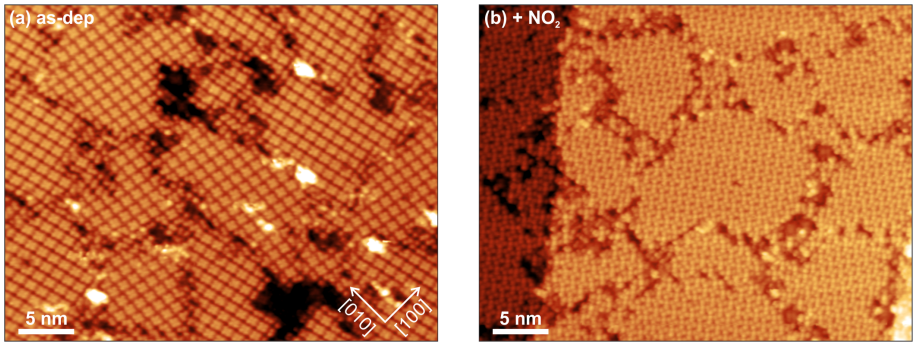

Figure 3.8: Large-scale STM images of NiTPP/Cu(100) before (a) and after (b) exposure to 10 L NO_2 acquired at 77 K. Image size 38.8 x 30 nm^2. Tunneling parameters: (a) U = +1 V, I = 500 pA, (b) U = +1 V, I = 200 pA.

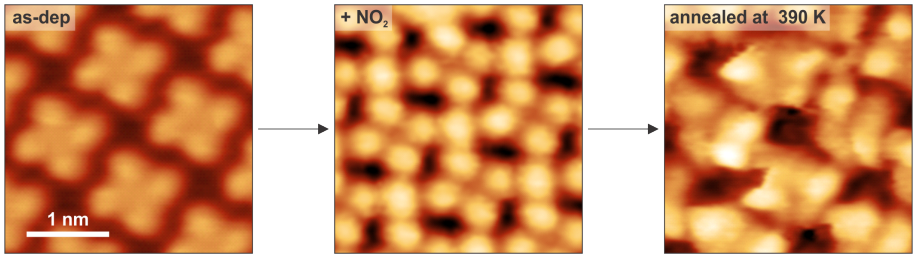

Figure 3.9: STM images of NiTPP/Cu(100) before (left) and after (middle) exposure to 10 L NO_2 and after annealing (right) up to 390 K. A single NiTPP molecule is framed with a dashed white square to guide the eye. All images are acquired at 77 K. Image size 3x3 nm^2. Tunneling parameters: (left) U = -1 V, I = 500 pA, (center) U = +1 V, I = 200 pA, (right) U = -1 V, I = 200 pA.

not parallel to the surface [116]. The vibration at 1008 cm^{-1}, for example, resembles deformations within the molecular plane and is not present in the monolayer spectrum. Thus, we conclude that the corresponding dynamic dipole moment is oriented largely parallel to the metal surface (see below for further details about the IR activity). This finding implies that the NiTPP is lying flat on the Cu(100) surface, in agreement with the adsorption geometries of MTPPs reported in the literature [37, 170–173] and with the DFT calculations in this work. As soon as the multilayer forms, the three missing signals rapidly gain intensity, which is in line with the loss of preferential orientation. These characteristic differences between the monolayer and multilayer spectra allow to estimate the porphyrin coverage directly from the IR spectra.

In contrast to classical IR spectroscopy, the dynamic dipole of a vibration must fulfill an additional selection rule for IRAS metals, namely the metal surface selection rule (MSSR). The MSSR states that components of the dynamic dipole moment which are parallel to the metal surface do not give rise to an absorption band. We now consider four IRA signal components of the NiTPP monolayer on Cu(100): the in-plane deformation vibrations of the porphine $\delta_{\text{ip, porphine}}$ (1008 cm^{-1}) and phenyl unit $\delta_{\text{ip, phenyl}}$ (1073 cm^{-1}) and the out-of-plane deformation modes of the porphine $\gamma_{\text{oop, porphine}}$ (800 cm^{-1}) and phenyl unit $\gamma_{\text{oop, phenyl}}$ (752 cm^{-1}). Since the flat-lying NiTPP has a molecular plane parallel to the underlying substrate surface, the porphine in-plane vibration is also parallel and thus IR inactive, whereas the out-of-plane vibration is strongly IR

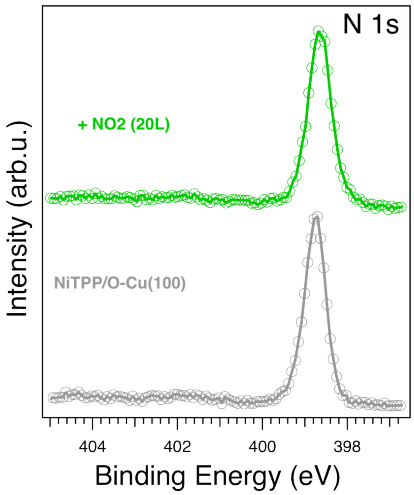

Figure 3.10: N *1s* spectrum ($h\nu$ = 515 eV) of NiTPP/O-Cu(100) before and after dosing 20 L of NO_2.

active (Figure 3.12a). Both deformation vibrations of the phenyl groups feature dynamic dipole components parallel and orthogonal to the surface. Thus, they are IR active, but less intense due to the loss of the parallel component (Figure 3.12b).

During the NO_2 uptake, all IR spectra are referenced to the background acquired on the as-prepared NiTPP. Thus, we observe only the changes which occur upon NO_2 exposure. We observe in Figure 3.13 the appearance of two signal components at 1320 and 800 cm^{-1} for the 1 ML NiTPP sample. According to the literature, NO_2 typically features three main vibrational fingerprints: an asymmetric O-N-O stretching band ν_{as}(ONO) in the 1600-1750 cm^{-1} range, a symmetric O-N-O stretching ν_s(ONO) in the 1200-1300 cm^{-1} and O-N-O bending δ(ONO) in the 750-800 cm^{-1} interval [174–177]. Thus, we assign our signals to the symmetric stretching mode ν_s(ONO) and at 800 cm^{-1} to the bending mode δ(ONO), respectively. However, we do not observe the asymmetric O-N-O stretching vibration. An explanation for the absence of this mode is the molecular orientation of the adsorbed NO_2 that creates a dynamic dipole, which is completely parallel to the surface and, therefore, forbidden by the metal surface selection rule [116].

Based on all the above observations, we propose an adsorption geometry where NO_2 binds to the Ni center through the central nitrogen atom. Here, the two oxygen atoms point upwards in a "V" shape configuration, leading indeed to an IR active ν_s(ONO) mode and to an IR inactive ν_{as}(ONO) mode (see Figure 3.13b).

Because of the fast (compared to the STM acquisition time) precession motion of nitrogen dioxide, this adsorption configuration gives rise to a time-averaged disc-shaped appearance of the NO_2 molecule in the STM topographic images instead of a two lobes protrusion [178].

In case of the multilayer samples there are weak features at 800 cm^{-1} upon NO_2 exposure, which have an s-shape or are pointing upwards. We attribute these features to bands of the NiTPP which experience small shifts as a result of reorientation or changes in intermolecular interaction.

In the next experiment, we prove that the enhanced reactivity is a true interfacial property. For this, we deposited NiTPP films of different thicknesses (1.0, 2.5 and 5.0 monolayers (ML)) atop

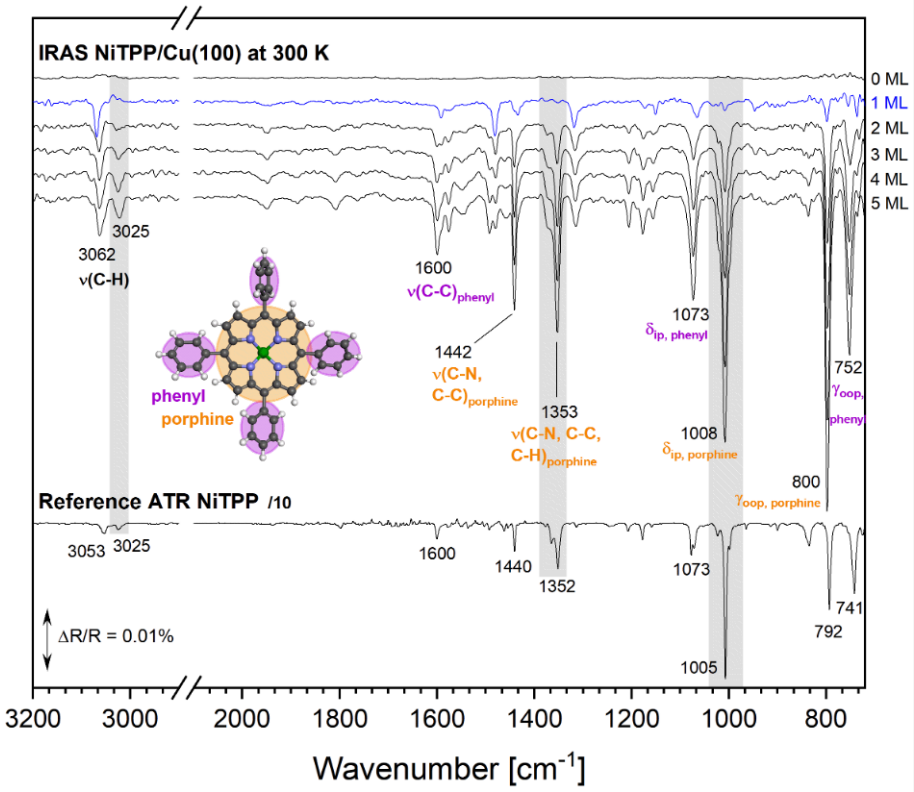

Figure 3.11: Top: Selected IRA spectra recorded during deposition of 5 ML NiTPP on Cu(100) at 300 K (ip = in plane, oop = out of plane). Bottom: Reference ATR IR spectrum of NiTPP.

Cu(100) and exposed them to different doses of NO_2. After each NO_2 uptake, we followed the changes at the interface by means of *in-situ* IRAS, which allows us to access the interface despite the thickness of the molecular layer.

For the different NiTPP film thicknesses, the features that appear upon NO_2 exposure are practically identical. However, the main difference between the three samples is the dose at which the NO_2 signal grows. One feature related to the adsorbed NO_2 is the peak at 1320 cm^{-1} which is associated with the symmetric stretching mode ν_s(ONO). The peak height of this component is plotted as a function of the NO_2 exposure in Figure 3.13c. We observe that for increasing film thickness, the required dose to form the adsorbed NO_2 species increases drastically, while the intensity of the corresponding mode at saturation, decreases. These findings suggest that the NO_2 diffuses through higher molecular layers and adsorbs on the Ni(I)TPP molecules of the first monolayer, while the Ni(II)TPPs, from the second layer on, are inert. This implies that the precise control of the molecular coverage is not fundamental for having an active interface, facilitating its practical implementation.

The changes induced in the nickel centers upon interaction with NO_2 are well evident also from the XPS Ni *2p* spectra recorded for increasing doses of NO_2.

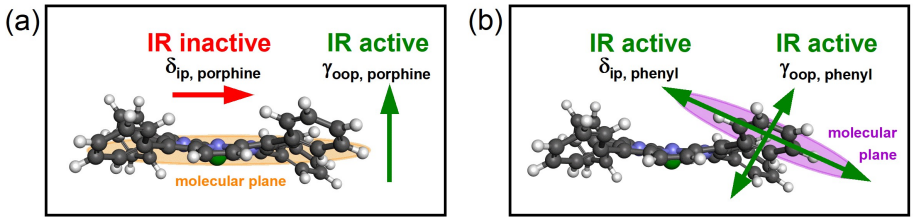

Figure 3.12: Model of the adsorbed NiTPP, orientation of the dynamic dipole moment for (a) $\delta_{\text{ip, porphine}}$ and $\gamma_{\text{oop, porphine}}$, (b) $\delta_{\text{ip, phenyl}}$ and $\gamma_{\text{oop, phenyl}}$ (ip = in plane, oop = out of plane).

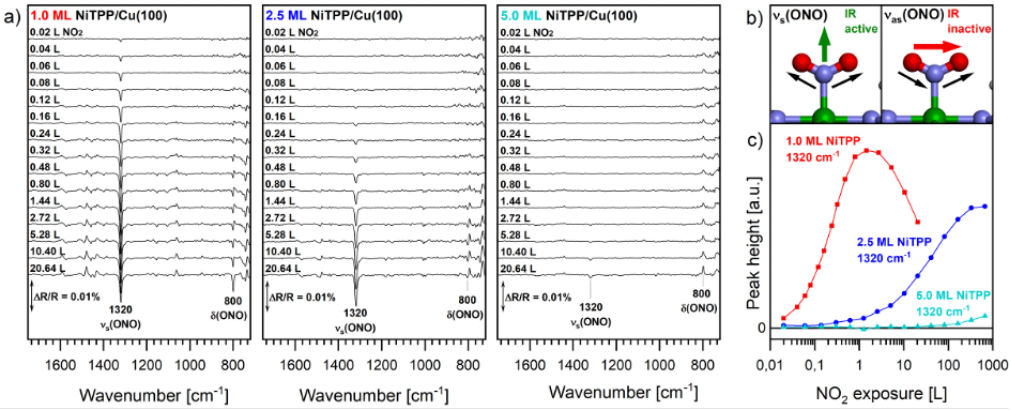

Figure 3.13: (a) IRA spectra of the NO_2 dosing on NiTPP/Cu(100) at 300 K for different NiTPP film thicknesses (1.0, 2.5 and 5.0 ML). (b) Schematic representation of the proposed NO_2 orientation when adsorbed on NiTPP and orientation of the dynamic dipole moment for ν_s(ONO) and ν_{as}(ONO). (c) Peak height of ν_s(ONO) as a function of the NO_2 exposure for different NiTPP film thicknesses.

While for the pristine molecular layer, the Ni *2p* spectrum is composed of a single peak at a binding energy of 852.9 $\pm$ 0.2 eV, which is specific for the Ni(I) ion (Figure 3.14, bottom), after the exposure of the NiTPP/Cu(100) to NO_2, a new feature appears at a BE of 854.6 $\pm$ 0.2 eV, while the Ni(I) component decreases substantially (Figure 3.14, top). This suggests that NO_2 binds directly to the Ni ion and the saturation of the metal porphyrin center is almost complete. The BE shift in the Ni $2p_{3/2}$ spectrum is associated with oxidation of Ni ion upon NO_2 coordination.

By combining the information provided by both N *1s* and Ni *2p* core levels, a semi-quantitative analysis can be carried out to exclude a multiple NO_2 adsorption at the same Ni site. Taking into account that every porphyrin has four nitrogen atoms and not all the NiTPP molecules host the external ligand, the areas between the two N *1s* components, one associated to the N atoms of the porphyrin and the other to the NO_2, can be compared. In doing so, photoelectron diffraction effects were neglected and a constant transmission of the analyzer at the corresponding kinetic energies was assumed. This yields a ratio close to 1:4 between the two peaks, suggesting that one single NO_2 molecule binds at the Ni center of every NiTPP.

After exposing the Ni(I)TPP layer to NO_2, the absorption spectrum changes drastically: the

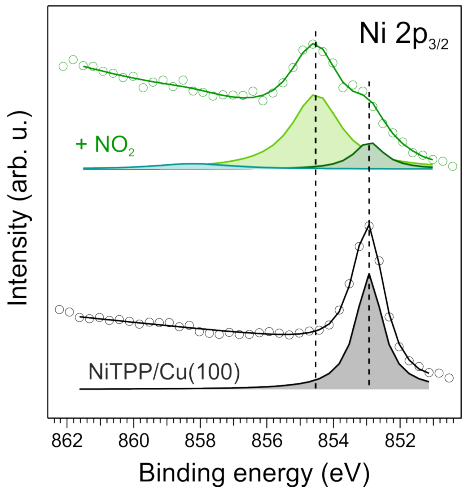

Figure 3.14: Ni *2p* photoemission spectra ($h\nu$ = 1020 eV), together with their corresponding fits, of NiTPP/Cu(100) before and after exposure to 10 L of NO_2.

main peak shifts towards higher photon energies (853.2 eV) with a pronounced shoulder at 854 eV and a new broad resonance appears at about 856 eV (Figure 3.3a, middle). Both the lineshape and the peak position suggest a re-oxidation of the nickel ion after coordination to the NO_2 ligand, Ni(I)→Ni(II) [179]. The shoulder at higher photon energy is a characteristic marker of the high spin (HS) configuration of nickel-containing complexes and metalloproteinase, where the Ni ion has two partially filled *3d* orbitals [179–182]. These conclusions are further supported by the changes in the Ni *2p* core-level spectra upon nitrogen dioxide exposure (see Figure 3.14). Clear differences can be observed between the spectra recorded on the Ni(II)TPP array on O-Cu(100) and after the NO_2 dose on the NiTPP/Cu(100) interface, pointing towards three different spin configurations (d^9, HS d^8, and LS d^8 for NiTPP/Cu(100), NO_2-NiTPP/Cu(100), and NiTPP/O-Cu(100), respectively). By exposing the NiTPP/Cu(100) interface to NO_2, a further change is observed in the XMCD (see Figure 3.3b, middle). The hysteresis curve recorded on the NiTPP/Cu(100) system after the dose to NO_2 confirms the magnetic saturation reached (see Figure 3.15).

The adsorption of nitrogen dioxide does not quench the magnetic moment at the Ni center, supporting the scenario depicted above, *i.e.* oxidation of the central metal ion from Ni(I) to Ni(II) followed by an HS transition.

The sum rule analysis performed on the NO_2-NiTPP/Cu(100) (see Table 3.2) yields an effective spin moment of $(2.76 \pm 0.2)\mu_B$. As in an HS d^8 and in a d^9 configuration the electrons in the energetically highest orbitals do not carry orbital angular momentum (*e.g.* orbitals), the values of the effective spin moment can, in a first approximation, be compared to the moments resulting from the spin-only formula. Indeed, with values of 1.73 μ_B and 2.83 μ_B for one and two unpaired electrons, respectively, they lie within the error of our measurements.

The experimental observations are also supported by the theoretical calculations. Indeed, through NO_2 coordination, the electronic structure of Ni changes once again, as revealed by the DOS projected onto the d-states (see Figure 3.5a, middle). The d_{z^2} states split and the spin ↓ part

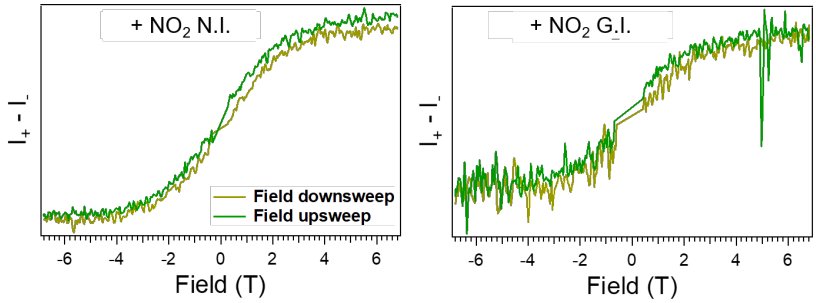

Figure 3.15: Magnetic hysteresis curves for NiTPP/Cu(100) after dosing 10 L of NO_2 measured at 3 K. Magnetic saturation is reached for normal (N.I., left panels) and grazing (G.I., right panels) photon incidence, respectively.

	Normal incidence	Grazing incidence
$m_{s,eff}$	$(2.76 \pm 0.2)\mu_B$	$(0.73 \pm 0.05)\mu_B$
m_l	$(0.29 \pm 0.05)\mu_B$	$(0.28 \pm 0.01)\mu_B$

Table 3.2: Resulting values for the effective spin moments and orbital moments of NO_2-NiTPP/Cu(100) for normal and grazing incidence, respectively.

shifts above the Fermi level (E_F). This corresponds, in first approximation, to a $(d_{xy})^2$ $(d_{yz}, d_{xz})^4$ $(d_{z^2})^1$ $(d_{x^2-y^2})^1$ configuration and, therefore, agrees well with the HS d^8 configuration suggested by the NEXAFS analysis. Indeed, also in this case, a clear XMCD signal can be observed, as expected for two unpaired electrons.

For the NO_2-NiTPP/Cu(100) system, the DFT optimized geometry shown in Figure 3.5b reveals that the nitrogen dioxide ligand only slightly influences the NiTPP adsorption structure. Surprisingly, the ligand-porphyrin complex remains highly interacting with the Cu surface, as proven by the fact that neither the geometric parameters nor the DOS projected on the macrocycle (see Figure 3.7b) are significantly altered by NO_2 adsorption. As a consequence, the massive charge transfer that populates the LUMOs, up to the LUMO+3, seems to be preserved. This is experimentally confirmed by the N K-edge NEXAFS spectra taken with s- and p-polarized light reported in Figure 3.7a. We observe only a moderate increase in the intensity of A_N and B_N, which suggests that the high charge transfer at the NO_2-NiTPP/Cu(100) interface is almost preserved, in good agreement with the DFT predictions. The macrocycle backbone is seemingly unaffected by NO_2 adsorption, thereby retaining its strong interaction with the Cu-surface. This leaves the Ni atom as the main interaction partner for NO_2. Calculations reveal that NO_2, which is acting as an additional ligand, increases the Ni-Cu surface distance by pulling the Ni atom $\sim$0.2 Å away from the surface towards the dioxide. The strong interaction of the porphyrin with the substrate seems to act as an energetic counterpart preventing further geometric changes induced by the so-called *surface trans-effect*. The latter is notably at work at other porphyrin/metal interfaces, where similar ligands with a strong donor/acceptor character, such as nitric oxide [54, 62] and ammonia [183, 184], lift the whole molecule away from the substrate surface.

The fact that the charge transfer at porphyrin/copper interfaces is not quenched upon NO_2 adsorption, further suggests that the switch of the spin state at the metal strongly relates to the gas uptake. As a test for this hypothesis, we have computed the NO_2-NiTPP complex on O-Cu(100),

where again the passivated surface causes gas-phase-like behavior. Note that the only purpose of this calculation is to understand the role of the exceptionally strong porphyrin-substrate interaction at the NiTPP/Cu(100) interface and that there was no NO_2 uptake of the NiTPP on the passivated surface observed at room temperature. In the bottom part of Figure 3.7b, we compare the DOS projected onto the NO_2 ligand of the complex on both surfaces.

As expected, we see a significant contribution above E_F in only one spin channel for NO_2-NiTPP on O-Cu(100), which accounts for the radical nature of NO_2. In contrast, this contribution is gone on the bare Cu surface. Analyzing the local magnetic moments, we notice that indeed any paramagnetic contributions come solely from the nickel atom. Thus, we conclude that there is an electron uptake by the NO_2, accompanied by oxidation of the nickel ion ($d^9 \rightarrow d^8$). Moreover, the additional electron density at the NO_2 ligand destabilizes the Ni d_{z^2} orbital to such an extent that the orbital splitting reduces sufficiently to form a high spin complex [100,160]. In summary, NiTPP on Cu(100) shows enhanced reactivity when exposed to NO_2. This behavior is not present in the gas-phase like NiTPP, obtained by depositing the molecule on a not interacting surface, in this thesis the O-Cu(100) surface, suggesting the pivotal role of the Ni(I) center in the activity towards NO_2 binding.

3.3 The role of spin and oxidation state in axial ligand coordination: CoTPP on Cu(100)

By doing a step back on the transition metal row, we go to CoTPP in which the cobalt ion is characterized by one electron less than nickel. This comparison will be crucial both for defining the similarities and differences induced by a different metal ion and for identifying the importance of oxidation state and unpaired spins in the reactivity of the MTPP. Indeed, while NiTPP has a d^8 electronic configuration in the gas phase, CoTPP has a d^7 configuration. In the present section, a comprehensive characterization of the CoTPP system deposited on bare and oxygen-passivated Cu(100) will be presented and then, similarly to what has been done for the NiTPP, the reactivity will be tested by exposing the system to NO_2. Moreover, by comparing the reactivity of CoTPP/Cu(100) and of CoTPP/O-Cu(100), the role of oxidation and spin state of the central metal ion in promoting the reactivity can be better elaborated.

A detailed comprehension of the changes induced by the surface in the supported CoTPP network may take advantage of a few words about the free molecule. Consistently with the presence of a LS Co(II) $3d^7$ central ion (S = 1/2), the CoTPP static magnetic moment is μ_s = 1.73 μ_B, while its effective magnetic moment is μ_e = 1.92 μ_B [185]. The square planar coordination of Co(II) in free CoTPP (D_{4h} symmetry [186]) lifts the five-fold degeneracy of the Co *3d* atomic orbitals (AOs) to generate a_{1g} (d_{z^2}), b_{1g} ($d_{x^2-y^2}$), b_{2g} (d_{xy}) and e_g ($d_{xz,yz}$) 3d-based MOs. The present ADF calculations, performed in collaboration with Dr. Silvia Carlotto and Prof. Maurizio Casarin from the University of Padova, Italy, confirm the higher stability (0.90 eV) of the LS state compared with the high spin (HS) one. LS energy levels lying in between -6.5 eV and -2.0 eV are displayed on the left side of Figure 3.16 together with 3D contour plots (CP) for Co 3d-based MOs. The inspection of the figure testifies that the unpaired electron is localized on the Co $3d_{z^2}$ orbital [187] (the lowest unoccupied MO (LUMO) corresponds to the Co $3d_{z^2}$-based β orbital), while the CoTPP highest occupied molecular orbital (HOMO) is the ring-based TPP-based $12a_{2u}$ MO (not shown). In a multilayer phase and when deposited on an inert substrate (here O-Cu(100)),

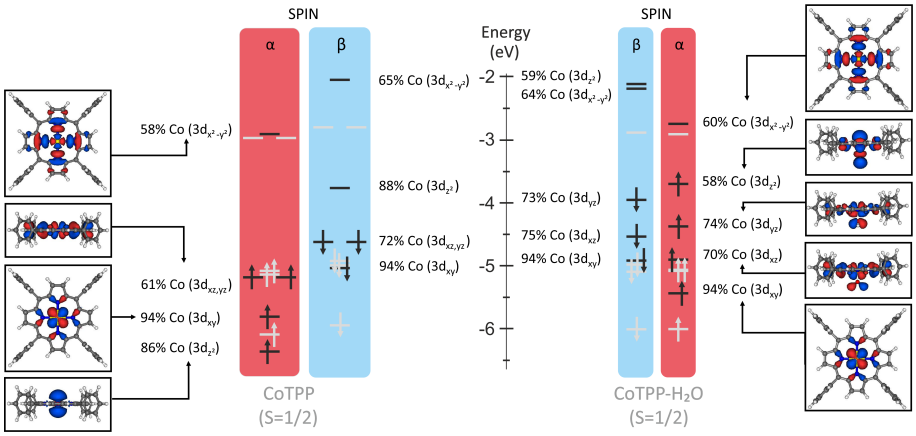

Figure 3.16: Energy level diagram associated to the LS CoTPP (left) and LS CoTPP-H_2O (right) species with a fixed Co-O distance at 1.6 Å (right) and optimized structures. Both α and β spins are reported. Black arrows indicate the occupied Co 3d-based α and β MOs (the relative percentage is also reported), whose 3D contour plots are displayed in the insets. The comparison between α and β spin occupation shows that the single unpaired electron is localized on the α Co $3d_{z^2}$ MO. Grey arrows indicate the occupied α and β TPP-based MOs. No unpaired electron is localized on the TPP fragment. Grey and white spheres are representative of C and H atoms, respectively.

the free molecule properties are preserved. This is well visible in N K-edge spectra acquired on the system CoTPP/O-Cu(100), when compared to the CoTPP/Cu(100).

Then, to get insight into the cobalt-based 3d MOs, the cluster approach has been extended to the CoTPP/O-Cu(100) system. The adoption of the molecular cluster approach to model a periodic system implies the saturation of the oxygen dangling bonds with hydrogen/pseudo-hydrogen atoms. The interaction of CoTPP with chemisorbed oxygen on the O-Cu(100) surface, which shows a $(\sqrt{2}x2\sqrt{2})R45°$ reconstruction, has been mimicked by considering an H_2O molecule directly bound to the Co ion. Literature data suggest that an H_2TPP monolayer grown on the oxygen passivated Cu(110) surface has an average height of 3.1 Å [188]; an inter-nuclear distance of 1.6 Å has been chosen for the Co-O bond in constrained optimization. Analogously to free CoTPP, the CoTPP-H_2O metal ion is a LS Co(II) with a single unpaired electron in the Co $3d_{z^2}$-based MO. Interestingly, the oxidation and spin states of the Co ion do not change by varying the Co-O inter-nuclear distances from 1.3 Å to 2.0 Å. Incidentally, the Co-N_{Py} bond lengths undergo a slight lengthening in CoTPP-H_2O (2.002 Å), as compared to free CoTPP (1.978 Å). Moreover, in the CoTPP-H_2O complex, the Co(II) ion is displaced out from the N_{Py} coordinative plane by 0.19 Å. The energy level diagram for CoTPP-H_2O is displayed on the right side of Figure 3.16. Even if neither the Co oxidation state nor its spin state change, the opposite is true when the single Co 3d-based MOs are considered. As expected, the most relevant perturbation, a strong destabilization, is experienced by the Co $3d_{z^2}$-based MO, which points directly toward the O atom and becomes the HOMO of the CoTPP-H_2O cluster (the energy destabilization for the spin α amounts to 2.68 eV). Moreover, the Co-contribution to this MO decreases from 86% to 58% (see corresponding 3D CP in Figure 3.16). As such, it is of some interest to point out that, as a consequence of their partial z character, Co $3d_{xz}$- and $3d_{yz}$-based orbitals are slightly destabilized as well, but they maintain their lone pair character (70% and 74%, respectively) (see Figure 3.16).

Analogous considerations hold for the Co $3d_{xy}$- and $3d_{x^2-y^2}$-based MOs.

So, similarly to the free molecule, CoTPP deposited on O-Cu(100) has a LS state with a single unpaired electron occupying the $3d_{z^2}$-based MO (Fig. 3.16, right panel). Such an unpaired electron in the molecular electronic structure has attracted great attention in coordination chemistry studies [53, 54, 62, 183] and it is also a key point in the present discussion. Upon deposition on a metal substrate, the molecular layer in direct contact with the surface can experience chemical changes induced by the charge transfer at the organic-metal interface. At variance with CoTPP/O-Cu(100), where the Co ion preserves the $3d^7$ configuration of the free molecule, Co(II) is expected to reduce to Co(I) on more reactive surfaces, which implies a $3d^8$ configuration with no unpaired electrons in 3d-based MOs [62, 189]. In order to confirm the stabilization of Co(I) and Co(II) oxidation states in the CoTPP monolayer deposited on the reactive Cu(100) and passivated O-Cu(100), respectively, we performed XPS at the Co *2p* core level (see Fig. 3.17a). The Co $2p_{3/2}$ spectrum of CoTPP deposited on O-Cu(100) shows a shape similar to that of the CoTPP multilayer [62, 190]. More specifically, the intensity maximum is peaked at 779.25 eV in binding energy and the spectrum displays the characteristic multiplet structure of LS Co(II) with one unpaired electron. On the other hand, the shape and BE (778.4 eV) of the CoTPP/Cu(100) Co $2p_{3/2}$ peak are similar to those reported for CoTPP/Ag(111) [62], suggesting the Co(II)→Co(I) reduction upon chemisorption of CoTPP on Cu(100).

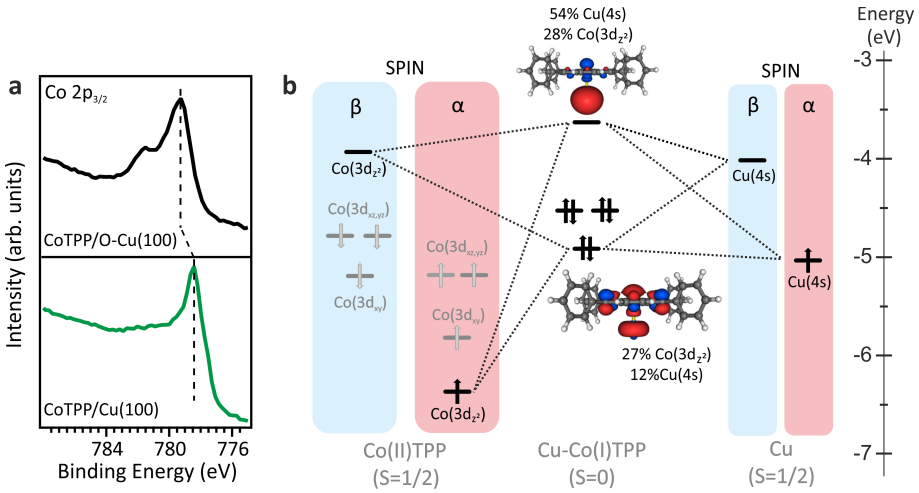

Figure 3.17: (a) Co $2p_{3/2}$ XPS core level spectra of CoTPP on bare (bottom panel) and oxygen-passivated (upper panel) Cu(100). (b) Energy level diagram for selected MOs, Co *3d* and Cu *4s*, for LS Cu-CoTPP. 3D plots displayed isosurfaces correspond to $\pm$ 0.03 $e^{1/2}$ $Å^{-3/2}$.

Further information about the interaction of CoTPP with the Cu(100) surface can be gained by means of DFT calculations (performed by Carlotto and Casarin). Previous results obtained by exploiting a periodical model [186, 189, 191] will be here extended by combining the molecular cluster approach [192, 193] with DFT-based calculations, which ultimately allows us to gain information about AOs and MOs in the metal-molecule complex [62, 194]. This approach has been used to correctly reproduce the magnetic properties of supported metal porphyrins and phthalocyanines [62, 195, 196]. Indeed, the molecular cluster approach has the great advantage

of accurately describing the oxidation and spin states of the central ion in metallorganics [197], and therefore, it is the best suited approach to investigate the Co metal ion chelated in the CoTPP molecule, involved herein in the axial coordination. The molecular cluster approach provides a quantitative analysis of the MOs and AOs formed upon interaction (giving information about the charge redistribution in the molecular cluster) and it stands at the basis of XAS simulations, which ultimately give a theoretical feedback on the metal spin state and the metal oxidation state modification.

Our calculation shows that both Cu(0) and Co(II) in the Cu-CoTPP cluster are characterized by the presence of a single unpaired electron occupying the Cu *4s* AO and the Co $3d_{z^2}$-based MO (see Figure 3.17b), and the molecular complex can be stabilized either in a LS (S = 0) or a high spin (HS) state (S = 1) configuration. As such, energy deviations (ΔE) from the Cu-CoTPP ground state (GS) reported in Fig. 3.18 clearly show the LS higher stability for Cu–Co distances smaller than 3.6 Å. A short inter-metallic distance appears then to favor the Co(II) + Cu(0) → Co(I) + Cu(I) on-surface redox reaction.

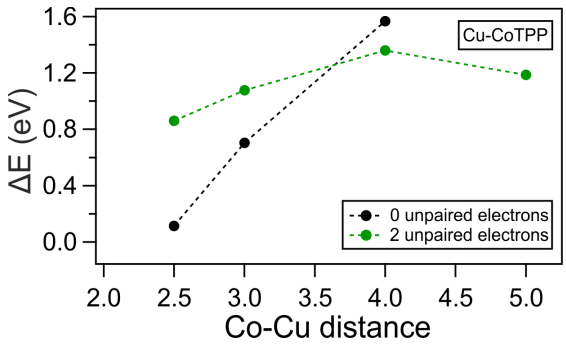

Figure 3.18: Energy variations of the optimized systems at different Co-Cu fixed distance and different spin state. 0 (LS) and 2 (HS) unpaired electrons are in black and green, respectively. They are expressed in eV and as a difference with respect to the most stable system: the 0 unpaired electrons with a Cu-Co distance of 2.5 Å. The 0 unpaired electrons calculation at Co-Cu = 5 Å does not converge.

Theoretical outcomes reported in Figure 3.17 strongly support the presence of a Cu(I)-Co(I)TPP cluster at a Co-Cu distance of 2.521 Å [189,191]; in fact, the (CoTPP + Cu) system is less stable than the Cu(I)-Co(I)TPP cluster by 1.04 eV. In particular, the charge transfer that causes the reduction of the cobalt is clearly visible on the MOs CoTPP-Cu compositions in Figure 3.17b: the fully occupied MO is mainly localized on the Co $3d_{z^2}$-based MO (27%), while the LUMO is localized (54%) on Cu *4s* MO. This confirms that the direct interaction of the CoTPP molecule with the copper substrate leads to the stabilization of a reduced Co(I), with no unpaired electrons in the valence states, contrary to the CoTPP/O-Cu(100) system, where the open-shell Co(II) state, characteristic of the free CoTPP molecule, is preserved. The present theoretical output is fully in agreement with the interpretation of the XPS data reported on Fig. 3.17a.

After stabilizing the Co chelated ion in the two desired configurations, namely, reduced Co(I) and open-shell Co(II) on bare and oxygen modified Cu(100) substrates, respectively, in the next step we elucidate the interplay between spin and oxidation state in the molecular reactivity towards axial ligands. To do so, both the CoTPP arrays have been exposed to a low dose of nitrogen dioxide at RT.

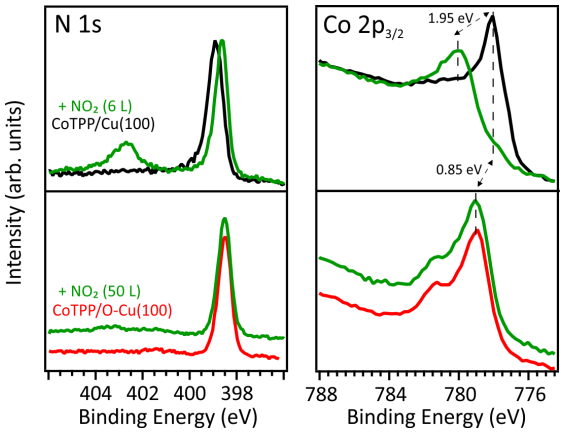

Figure 3.19: N *1s* and Co $2p_{3/2}$ core level spectra of CoTPP on bare and oxygen modified copper surfaces and after dosing of NO_2; doses are indicated.

The possible anchoring of the axial ligand to the Co ion in the Co(I)TPP and Co(II)TPP networks formed on the bare and oxygen-modified surfaces, respectively, was monitored by means of XPS. Both the Co $2p_{3/2}$ and N *1s* core-level spectra of Co(II)TPP deposited on the O-Cu(100) substrate remained unchanged after the exposure at RT to the NO_2 gas (see Figure 3.19).

This result indicates that the sole presence of an unpaired electron in the Co(II) ion may not be the key requirement for anchoring gas molecules to the metal-organic network, as previously discussed in the literature [53, 62], or, at least, it is not sufficient.

In contrast with the CoTPP/O-Cu(100) system, the Co $2p_{3/2}$ and N *1s* spectra of CoTPP deposited on the bare Cu(100) substrate show well-evident changes after the exposure of the metalloporphyrin network to NO_2. The N *1s* spectrum exhibits a new peak at 402.8 eV associated with NO_2 and a small energy shift to lower BE of the main peak associated with the tetrapyrrolic nitrogen atoms (see Figure 3.19). For what concerns the Co $2p_{3/2}$ spectrum, the intensity maximum is shifted by 1.95 eV to higher BE and a different distribution of satellites is observed after exposing the system to NO_2. This spectral behavior is consistent with the Co(I) oxidation induced by the interaction with the axial ligand and the formation of a Co–NO_2 bond. However, the Co $2p_{3/2}$ core level and the Co L-edge near-edge NEXAFS spectra of the Co–NO_2 system are different from the one of CoTPP/O-Cu(100) where the LS Co(II) is present (see Fig. 3.20). Hence, the stabilization of the Cu(100)/CoTPP–NO_2 complex probably leads to the Co(III) oxidation state.

To support these experimental observations and to provide a detailed insight into the stabilization of Co(III) ions in the metal porphyrin array, further DFT-based numerical simulations and additional NEXAFS simulations have been performed. The NO_2 interaction with the Co(I)TPP array has been modeled by exploiting the Cu-CoTPP-NO_2 cluster, whose constrained optimization has been carried out by assuming either 3 or 1 unpaired electrons and freezing the Cu–Co distance to 3 Å; *i.e.*, a value close to the one (2.93 Å) [186] optimized for the Cu–Co bond by means of DFT periodic calculations for similar interfaces. As such, it can be useful to anticipate that bond-length variations smaller than 0.1 Å do not significantly affect the modeled NEXAFS spectra reported herein. Thus, since the LS Cu-CoTPP-NO_2 cluster is more stable than the HS one by 1.06 eV, only

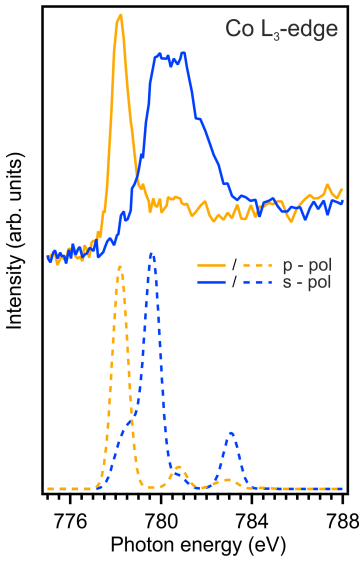

Figure 3.20: Measured and simulated Co L_3-edge NEXAFS spectra of CoTPP on the oxygen modified copper surface measured at p- and s- polarization of incoming light. To match the experimental data, the simulated spectra for CoTPP-H_2O (dashed line) are shifted by 2.3 eV and have a Gaussian broadening of 0.8 eV.

the former has been considered in the forthcoming discussion.

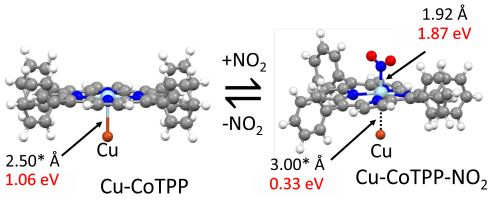

Figure 3.21: Optimized geometries of clusters associated with the transformations considered in the present work. Binding energies and bond lengths of Cu-CoTPP and Cu-CoTPP-NO_2 are described at BP86/TZVP level of theory. Both structures are in their LS states. Grey, white, orange, red, light blue and blue spheres are representative of C, H, Cu, O, Co and N atoms, respectively. Asterisks (*) refer to constrained optimization geometries.

Upon the formation of the Co–NO_2 bond, the energy of the Cu-Co bond decreases from 1.06 eV (Cu-CoTPP) to 0.33 eV (Cu-CoTPP–NO_2) (see Fig. 3.21). Our estimate of the Co–NO_2 bond energy (1.87 eV) in the Cu-CoTPP-NO_2 system is in good agreement with the value reported by Chang *et al.* [178, 198] for Cu(111)-supported CoTPP-NO_2 complexes (1.86 eV). Beside the recognition of the orbitals mainly contributing to the Cu–CoTPP–NO_2 interaction (Cu *4s* and Co $3d_{z^2}$ AOs and the NO_2 π^* MO), the analysis of the Cu-CoTPP-NO_2 electronic structure reveals that the singly occupied MO (SOMO) is strongly localized on the Cu *4s* AO. This suggests that the trans-effect induced by the NO_2 coordination implies the weakening of the Cu-Co interaction and the reduction of the Cu oxidation number to its original value (0). It has to be noted that

upon adsorption of CoTPP on the bare copper, the strong interaction between the Co ion and the surface, besides inducing the reduction to Co(I), could also introduce mechanical strain within the molecule. After the NO_2 trans-coordination to the supported CoTPP, the NO_2 being a stronger ligand than the copper surface, the Co-Cu distance increases of 0.5 Å, reducing possible molecular strains.

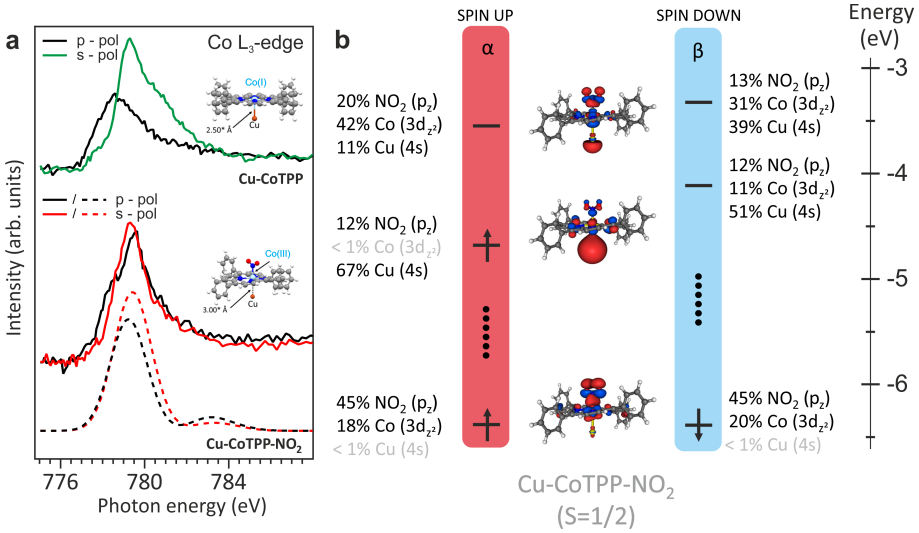

Figure 3.22: (a) Cu-CoTPP (top) and Cu-CoTPP-NO_2 (bottom) Co L_3-edge NEXAFS spectra for s- and p-polarizations and corresponding optimized geometries. To match the experimental data, the simulated spectra for Cu-CoTPP-NO_2 (dashed line) are shifted by 10.6 eV and have a Gaussian broadening of 2 eV. (b) Energy level diagram for selected molecular orbitals for LS Cu-CoTPP-NO_2 with a fixed Co-Cu distance (3 Å). Both α and β spins are reported. 3D plots displayed isosurfaces correspond to $\pm$ 0.03 $e^{1/2}$ $Å^{-3/2}$. Orbitals with a contribution below 1% are shaded. Vertical dots indicate that some levels, mainly localized on TPP fragment and/or Cu *3d* orbitals, are omitted. Grey, white, and yellow spheres are representative of C, H and Cu atoms, respectively.

The doubly occupied MO accounting for the Co-NO_2 bonding is mainly localized on NO_2 with a negligible Cu participation (see Fig. 3.22, right panel), while the Co $3d_{z^2}$ AO mainly contributes to the lowest unoccupied MO. As a whole, the NO_2 local electronic structure of the Cu-CoTPP-NO_2 cluster corresponds to a closed-shell with Cu in its elemental oxidation state and the octahedrally coordinated Co ion having a formal oxidation state +3 and a LS $3d^6$ electronic configuration with the $3d_{xy}$ and $3d_{z^2}$ as empty orbitals. As such, it has to be noted that Co(III), here observed in the surface-supported 2D metal-organic array, has been formerly described only for metal-organic complexes in solution [199]. Further information about the Co(III) stabilization at the metal-organic interface has been gained by recording, modeling and assigning the Co L_3-edge absorption spectra (see Figure 3.22a) after exposure of the CoTPP/Cu(100) interface to 6 L of NO_2. Clear differences can be observed in the spectra reported in Figure 3.22 with respect to the ones measured for CoTPP/O-Cu(100) reported in Figure 3.20.

Co L_3-edge spectra for s- and p-polarizations have been modelled by exploiting the optimized Cu-CoTPP-NO_2 cluster (see Figure 3.21) for which a LS state (1 unpaired electron) has been assumed. As already mentioned, $3d_{xz}$, $3d_{yz}$ and $3d_{x^2-y^2}$ orbitals for the $3d_6$ Co(III) species are

fully occupied, while the other MOs are empty and the Cu-CoTPP-NO_2 SOMO, as stated above, is strongly localized on the Cu *4s* AO. The lower excitation energy (EE) side of the single peak characterizing the modelled Co L_3-edge spectrum in p-polarization includes both $\Delta S = 0, +1$ electronic states. $\Delta S = 0$ states are generated by single electronic excitations from the Co *2p* orbitals to the Co-based d_{z^2} and d_{xy} virtual MOs (VMOs), while both Co-based and TPP-based VMOs are involved in electronic excitations generating $\Delta S = +1$ states. At variance to that, the higher EE side of the peak only includes $\Delta S = 0$ electronic states, which are determined by electronic transitions from the Co *2p* AOs to the Cu *4s*-based SOMO and Co-based VMOs. Only $\Delta S = 0$ states, mainly generated by Co *2p* $\rightarrow$ Co-based d_{xy} single electronic excitations, contribute to the s-polarized spectrum. The overall agreement between experimental and modeled spectra, in particular the energy position of the main peaks and the linear dichroic behavior observed in the spectra, fully supports the stabilization of the Co(III) species upon the interaction of the NO_2 ligand with the Co(I)TPP species stabilized on the Cu(100) substrate.

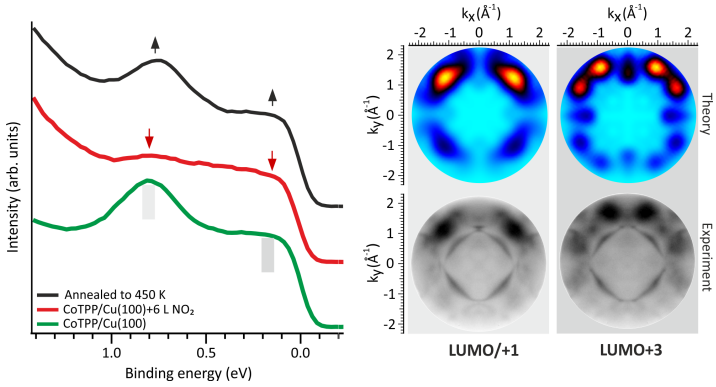

Figure 3.23: Left panel: Photoemission spectra of CoTPP/Cu(100), after NO_2 dosing and after annealing of NO_2-CoTPP/Cu(100) to 450 K. Right panel: Comparison between the measured momentum resolved photoemission maps at constant BE (0.15 eV and 0.80 eV, respectively) and the square modulus of the Fourier transform of the real space molecular orbitals (LUMO/+1 and LUMO+3).

The reversibility of the molecular-surface interaction and, accordingly, the Co(I) $\rightarrow$ Co(III) redox reaction has been tested here by annealing the NO_2-CoTPP/Cu(100) interface to 450 K under UHV conditions. The possible thermal desorption of NO_2 and restoring of the Co-Cu interaction has been monitored by valence band spectroscopy (see Figure 3.23). This, being an experimental technique sensitive to the changes in charge transfer and interaction strength at the metal-organic/metal interface, allows us to confirm the presence of the *surface trans-effect*, as suggested by calculations.

The valence band spectrum of the clean copper is dominated by the *sp*-band and has a rather featureless plateau, while the CoTPP/Cu(100) spectrum shows two prominent features at BEs of 0.15 eV and 0.80 eV. To clarify the origin of these features we measured momentum-resolved photoemission maps at constant BE and compared them with the square modulus of the Fourier transform (FT) of the real space MOs provided by DFT calculation [99], within the PT approach. Based on the excellent match between the experimental and theoretical data, the features at 0.15 eV and 0.80 eV BE can be assigned to the emissions from the gas-phase LUMO/LUMO+1 and the

LUMO+3, respectively. These molecular levels, delocalized over the entire molecular macrocycle of CoTPP, are filled due to the charge transfer occurring at the organic/metal interface, as a result of the strong anchoring of the Co ion to the copper substrate. As discussed above, in the Cu-CoTPP-NO_2 complex the Co-Cu interaction is weakened by the *surface trans-effect*, as evident from the quenching of the LUMOs features (see Figure 3.23). The annealing of the interface to 450 K induces the thermal desorption of the NO_2 ligand in the Cu-CoTPP-NO_2 complex, thus restoring the pristine interaction and the charge transfer between the copper surface and the CoTPP molecule. As a result, both LUMO states reappear in the valence band spectra. The Co $2p_{3/2}$ and N *1s* spectra further confirm the full reversibility of the Co(I) $\rightarrow$ Co(III) conversion (see Figure 3.24).

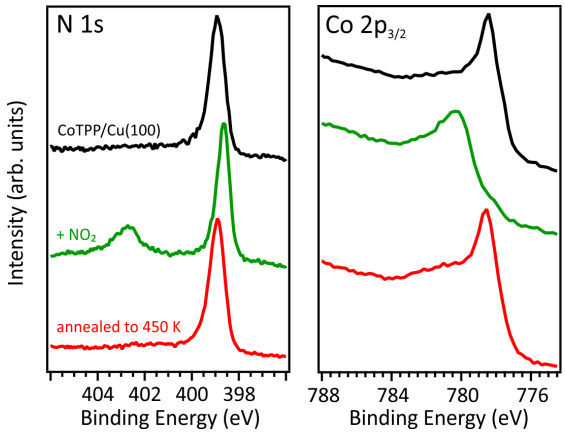

Figure 3.24: Top: N *1s* and Co $2p_{3/2}$ core-level spectra of CoTPP on Cu(100) and after dosing of NO_2; Bottom: after annealing of NO_2-CoTPP/Cu(100) interface to 450 K for thermal desorption of NO_2 ligand.

The data show that the Co-NO_2 chemical interaction is taking place on the CoTPP network supported by the copper electrode, where the Co ion is in a low and unusual oxidation state (I). Instead, this reaction has not been observed at the CoTPP/O-Cu(100) interface, where Co(II) ions have a LS state and a single unpaired electron in the valence shell. The *trans-effect* observed along the Cu-Co-N axis in the Cu-CoTPP-NO_2 complex suppresses the Cu-Co interaction, as confirmed by the valence band data, and stabilizes the Co(III) chelated ion in the metal-organic array. The Co(I) $\rightarrow$ Co(III) conversion is fully reversible, as the thermal-induced desorption of NO_2 taking place at 450 K restores the pristine Co-Cu interaction. Our experiment demonstrates that the on-surface reactivity towards axial coordination to the metal center of porphyrin 2D arrays is driven by the oxidation state, rather than by the presence of an unpaired electron in the d_{z^2} atomic orbital. Further, the reduction of the chelated metal by the *surface trans-effect* may be reversed by the axial coordination to NO_2 through a push-pull charge transfer mechanism. The combination of *surface trans-effect* and axial coordination to NO_2 allowed to manipulate the Co oxidation and spin states at room temperature. This is a key aspect for the generalization of the approach to ferromagnetic substrates, as well as for the practical use in molecular-based spintronic devices.

In conclusion, both NiTPP and CoTPP when interfaced with the Cu(100) substrate experience a strong charge transfer from the substrate, which leads to the partial filling up to LUMO+3 in both cases. This similarity is well visible in valence band and NEXAFS spectra. As a consequence

of the strong interaction with the substrate, both nickel and cobalt are reduced from the gas-phase oxidation state +2 to the oxidation state +1. These low valence states lead to the activation of the two systems towards the interaction with NO_2, a strong oxidizing gaseous species; however, the differences concerning the magnetic behavior and spin states in the two systems are considerable. While NiTPP is diamagnetic in the gas phase with a LS d^8 electronic configuration, and the coordination with the surface switches on the magnetism in the central nickel ion being now stabilized in a HS d^9 configuration, gas-phase CoTPP is paramagnetic with a LS d^7 configuration (unpaired spin localized on the $3d_{z^2}$) and the hybridization with the surface leads to a non-magnetic LS d^8 configuration. Differences between the two systems are also observed after the formation of the NO_2-MTPP-Cu complex. While after the coordination of NO_2 to the NiTPP molecule the central nickel ion is stabilized in a HS Ni(II) state, the CoTPP interaction with NO_2 leads to a non-magnetic Co(III) state. These differences are arising from a different interaction strength between the central metal ion and the copper surface, which induces a different *trans-effect*, that in the case of CoTPP leads to a bigger increase of the Co-Cu distance after the NO_2 coordination. Moreover, the presence of unpaired electrons in the M(II) ion is not sufficient for reactivity towards axial ligands.

Before investigating more deeply the role of the substrate in the modification of molecular properties, a brief overview on the role of molecular periphery will be given by studying the case of cobalt octaethylporphyrin (CoOEP) on the bare and oxygen-passivated Cu(100).

3.4 The influence of the porphyrin periphery: CoOEP on Cu(100)

The octaalkylporphyrins, which often occur in biological systems, represent another important class of substituted porphyrins. The substituents are typically attached to the β-positions of the pyrrole moieties, as for example in 2,3,7,8,12,13,17,18-octaethyl-porphyrin [200]. Contrary to the phenyl-substitued porphyrins, because of the conformational flexibility of the small peripheral ethylgroups, OEPs normally do not undergo significant adsorption-induced deformation.

Let's see now what are the properties of CoOEP upon deposition on the Cu(100) and on the O-Cu(100) surfaces. In order to determine the cobalt oxidation state in the CoOEP monolayer deposited on the reactive Cu(100) and passivated O-Cu(100), respectively, we performed X-ray photoemission spectroscopy at the Co *2p* core level (see Fig. 3.25 (right panel)). The Co $2p_{3/2}$ spectrum of CoOEP deposited on O-Cu(100) shows a shape similar to that of the CoTPP on the same passivated substrate, with an intensity maximum peaked at 779.25 eV in binding energy and a characteristic multiplet structure of LS Co(II) with one unpaired electron. On the other hand, the shape and BE (778.4 eV) of the CoOEP/Cu(100) Co $2p_{3/2}$ peak are similar to those observed for the CoTPP/Cu(100) system, suggesting the Co(II)$\rightarrow$Co(I) reduction upon chemisorption of CoOEP on Cu(100).

The stabilization of the cobalt ion in the Co(I) and in the LS Co(II) states on Cu(100) and on O-Cu(100), respectively, is also confirmed by the NEXAFS spectra acquired at the Co L_3-edge for the two systems (see Figure 3.25, right panel). Strong similarities with the CoTPP system are again observed in the overall appearence of the NEXAFS spectra, even though slight differences can be appreciated in the intensity of the spectrum acquired in p-polarization on the CoOEP/Cu(100) system. These differences probably result from different hybridization with the copper surface, in turn derived from different relaxation of the molecular structure once in contact with the metal

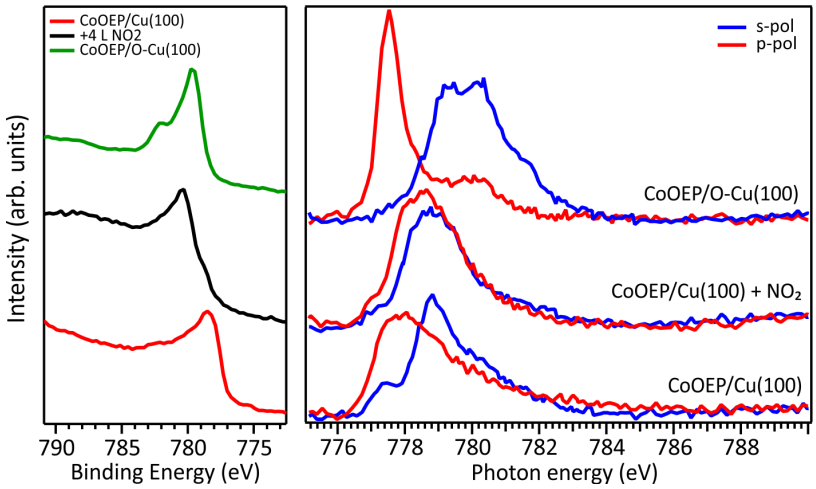

Figure 3.25: Left: Co $2p_{3/2}$ XPS core level spectra of CoOEP/Cu(100) before (red curve) and after exposure to 4 L of NO_2 (black curve), and on the oxygen-passivated Cu(100) (green curve). Right: Co L_3-edge of CoOEP/Cu(100) before (bottom) and after (middle) exposure to 4 L of NO_2, and of the CoOEP/O-Cu(100) system (top).

surface.

We are now going to study how the change of the molecular periphery, with the same oxidation state of the central metal, is going to change the molecular reactivity when exposed to NO_2.

In order to test the reactivity, both CoOEP/Cu(100) and CoOEP/O-Cu(100) interfaces have been exposed at room temperature to increasing doses of NO_2 and the N *1s* spectra have been acquired before and after the dose in order to track the possible adsorption of the gaseous species (see Figure 3.26). While no interaction is detected at the Co(II)OEP/O-Cu(100) interface, since neither changes in the Co *2p* spectrum nor the appearance of a new component in the N *1s* spectrum are observed for this system, the situation is different in the case of the Co(I)OEP/Cu(100) interface.

In this case, the exposure to NO_2 leads to the appearance of a peak at 402.8 eV associated with the NO_2 molecule. Also the N K-edge NEXAFS spectra acquired before and after the 4 L dose of NO_2 clearly indicate the adsorption of the new species at the interface, while preserving the flatness of the macrocycle. The interaction of the axial ligand with the cobalt center of the CoOEP molecule induces strong changes in the Co *2p* XPS and in the Ni L_3-edge NEXAFS spectra. The coordination of NO_2 induces the oxidation of the Co(I) species, leading to the stabilization of a Co(III) species in the NO_2-CoOEP/Cu(100) complex. The assignment of the oxidation state is strongly supported by the similarities observed with the spectra recorded for the NO_2-CoTPP/Cu(100) complex (see Section 3.3).

In conclusion, we have shown that by changing the nature of the *meso* substituents the molecular properties are not strongly affected, and, at least as far as the cobalt oxidation and spin states at the interface and reactivity towards NO_2 are concerned, CoTPP and CoOEP show the exact same behavior.

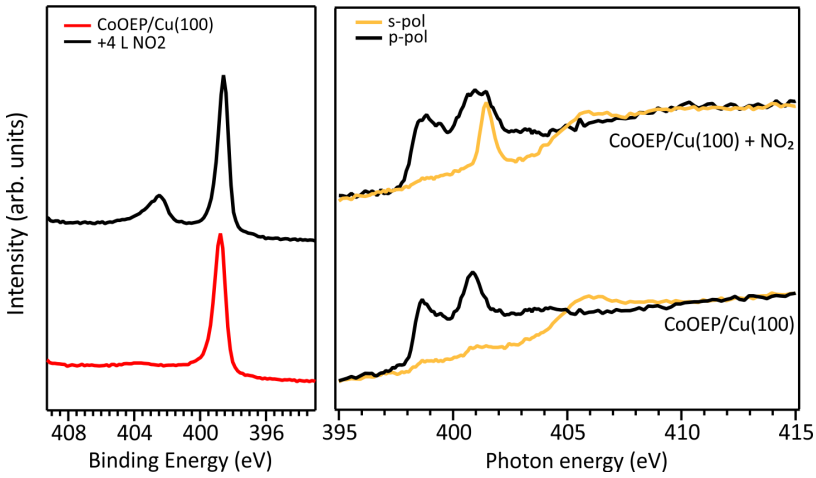

Figure 3.26: N *1s* XPS spectra (left) and N K-edge absorption spectra (right) of the CoOEP/Cu(100) interface before (top) and after (bottom) the exposure of 4 L of NO_2.

3.5 Impact of the substrate reactivity on the electronic structure and catalytic activity: NiTPP and CoTPP on Ag(100)

On the less reactive Ag(100) surface, the MTPP systems have a considerably different behavior. Upon anchoring to a metal substrate, TPP molecules can adapt their structural conformation to the local environment, deforming the macrocycle and/or reorienting the phenyl substituents. The final adsorption geometry results from the balance between the energy gain from the molecule-substrate interaction and the energy loss caused by the molecular deformation [12]. In particular, the saddle-shape deformation reduces the sterical barrier for phenyl rotation, which enables a smaller tilt angle of the phenyl rings relative to the metal surface. This conformational adaption has been already observed for CoTPP molecules adsorbed on the Cu(111) [38], Ag(111) [173] and Ag(100) [172] surfaces. CoTPP molecules adsorb on the Ag(100) surface kept at room temperature in two molecular conformations: saddle (A) and planar (B) (see Figure 3.27).

In the saddle conformation, the upward bending of two opposite pyrrole units results in two bright protrusions in the STM image, which are organized in molecular rows along the [110] crystal axis. Within two different molecular rows, the molecules have two different orientations, one rotated 90° with respect to the other. Instead, the planar molecules (B) have an approximately square shape, and the porphyrin's macrocycle is adsorbed parallel to the Ag(100) substrate. The planar conformation is randomly distributed within the porphyrin rows. CoTPP deposited on Ag(100) self-organizes into a nearly square unit cell with a length of 12.7 $\pm$ 0.2 Å, indicated by a red square in Figure 3.27a. Similar ordering has been found for other MTPPs on metal surfaces and is primarily driven by the intermolecular phenyl-phenyl interactions [100, 201]. In the STM data two domains, mirrored with respect to the [110] direction, are observed as a consequence of the four-fold symmetry of both substrate and CoTPP molecule. In the single domains, the phenyl-phenyl axes of CoTPPs are rotated by $\sim 4° \pm 5°$ with respect to the [1$\bar{1}$0] and [110] directions.

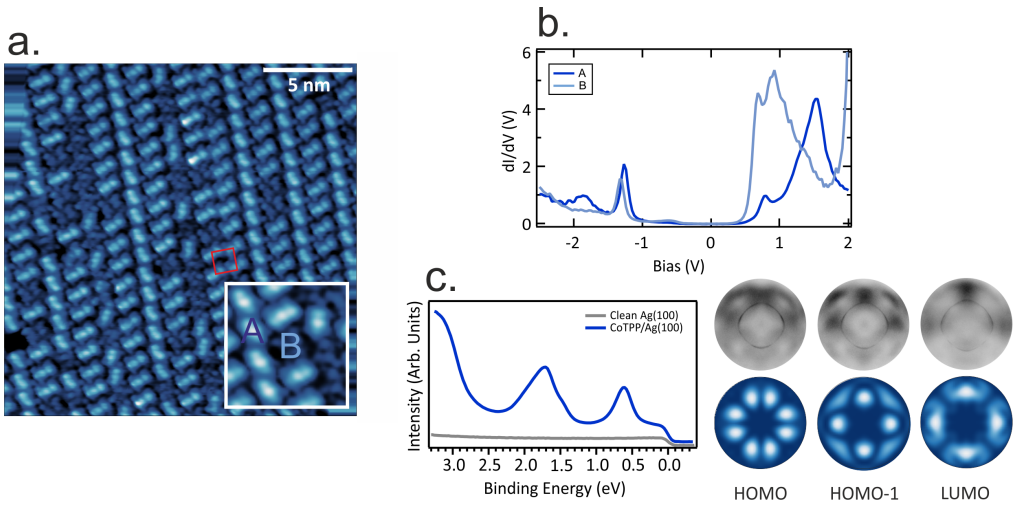

Figure 3.27: Self-assembly and electronic structure of CoTPP on Ag(100). (a) STM image of as-deposited molecular layer showing the two distinct molecules, labelled A and B. Images acquired at 77 K, tunneling parameters: U = -1.7 V, I = 0.5 nA. (b) STS spectra of the A and B species. The points at which the STS spectra were acquired are indicated in (a). (c) Valence band spectrum of CoTPP/Ag(100) and corresponding comparison between the measured momentum-resolved photoemission maps at constant BE (0.6 eV, 1.6 eV and 1.95 eV, respectively) and the square modulus of the Fourier transform of the real space molecular orbitals (LUMO, HOMO and HOMO-1).

In the next step, different spectroscopic techniques, specifically STS and PT, have been applied to study the electronic structure of the two different conformational forms of CoTPP self-assembled on the Ag(100) surface. While STS provides local information on the individual molecules, PT is sensitive to the energy level alignment over a larger scale within the molecular assembly. STS spectra were acquired on the two different conformers, A and B, observed in the STM images. Only the planar form (B) shows a peak located at -0.6 V bias, which is associated with charge transfer from the metal substrate to the former gas-phase LUMO states localized on the porphyrin's macrocycle. This peak is not present for the saddle-shaped molecular species (A). In the saddle conformation, the porphyrin plane is bent and the Co atom is situated closer to the substrate while the porphyrin's macrocycle is pushed away from the surface, thus reducing the surface interaction with the macrocycle moiety of CoTPP. The data show that the up-bending results in the quenching of the charge transfer from the silver substrate to the molecule. The peaks at -1.3 V and -1.85 V in the spectra measured for the A species, at this point, can be tentatively assigned to the HOMO and HOMO-1 orbitals. A rearrangement of the HOMO and HOMO-1 is observed in the spectra measured for the B species. Additionally, we observe strong changes in the spectra recorded at positive bias, suggesting that the charged species B has a different electronic level alignment concerning the unoccupied molecular orbitals (UMOs), compared to the uncharged molecular species A. In conclusion, the STM and STS data reveal that a stronger molecular-surface interaction takes place in the planar conformation species and it is accompanied by the charge transfer from the silver substrate to the porphyrin macrocycle, which results in the rearrangement of the HOMO and LUMO levels. This interaction is absent in the saddle forms. The CoTPP monolayer films consist of both negatively and neutrally charged species, similar to what was

recently reported for tetracene molecules self-assembled on an Ag(110) substrate [202].

To substantiate our tentative interpretation of the peaks observed in STS, in the following, we performed PT on the CoTPP monolayer self-assembled on the Ag(100) substrate. The valence band spectrum reported in Figure 3.27 shows the momentum-integrated photoelectron spectrum of the CoTPP/Ag(100) interface measured at 30 eV using p-polarized synchrotron radiation. Three prominent features are present in the CoTPP/Ag(100) spectrum, shoulders A and B are situated at 1.9 eV and 1.6 eV and peak C at 0.6 eV, while the valence band spectrum of the bare metal substrate shows a rather featureless plateau associated with the *sp*-bands of silver. To identify the origin of the molecular features observed in the CoTPP/Ag(100) spectrum the momentum maps at corresponding BE were measured and the results are presented in Figure 3.27. The experimental patterns have been compared with the square modulus of the FT of the frontier molecular orbitals in the real space, *i.e.*, HOMO-1, HOMO, and LUMO. In the simulated maps, the two rotational domains detected in the STM measurement have been taken into account. The best agreement between the simulated and measured maps shows that the CoTPP molecules are $4 \pm 5^{\circ}$ mirrored with respect to the [110] high symmetry direction of the substrate, in concordance with the STM data. Based on the excellent match between the experimental and theoretical data, the features at 1.9 eV and 1.6 eV BE, observed in the photoelectron spectrum of CoTPP/Ag(100) can be assigned to the emissions from the HOMO and HOMO-1, respectively, while the peak at 0.6 eV is attributed to the emission from the LUMO of the CoTPP. The occupation of the former LUMO, as previously mentioned, is associated with strong molecule-substrate interaction and this feature has been already observed in the STS spectra of the planar conformer. Moreover, taking into account the STS data, the B peak in the valence spectrum can be attributed to the saddle-shape conformation of the CoTPP molecule.

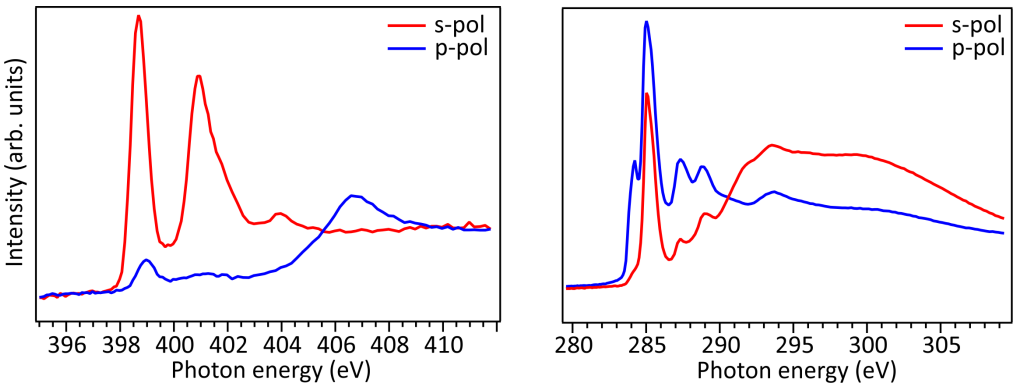

Figure 3.28: N K-edge and C K-edge NEXAFS spectra of CoTPP monolayer deposited on the Ag(100) surface.

The presence of the saddle-shaped configuration shows a clear fingerprint also in the N K-edge NEXAFS reported in Figure 3.28. Indeed, in the spectrum acquired in s-polarization, which is usually featureless when the macrocycle of the porphyrin lays parallel to the surface, a peak located at ∼399 eV is present, suggesting the distortion of the macrocycle moiety of the CoTPP molecule.

The C K-edge NEXAFS spectrum of the pristine CoTPP/Ag(100) interface is shown in the right panel of Figure 3.28. By determining the intensity ratio of the resonance at 285.05 eV in the

two polarizations, it is possible to define the average angle between the direction of the π^* orbitals of the phenyl moiety and the surface normal (tilt-off angle) [106]. A quantitative evaluation of the average tilt-off angle γ of the phenyl in CoTPP self-assembled on Ag(100) can be drawn according to the relation Is/Ip $\propto 1/2$ tg2γ, and it results to be $\sim 52^\circ \pm 3^\circ$. In a densely-packed monolayer, the early NEXAFS measurements performed for other metal TPP indicated that the phenyl groups are typically oriented at an edge-on angle with respect to the porphyrin macrocycle when bound to the metal substrate, rather than nearly perpendicular as in the gas-phase molecule.

The charge transfer at the MTPP/metal interface can alter the oxidation state of the chelated metal ion in the adsorbed molecule and, as a consequence, modify the magnetic properties in the organic array. In particular, while the porphyrin's macrocycle in the planar conformation form of CoTPP is charged by electron donation from the silver substrate, at the same time, in the saddle-shaped CoTPP this moiety remains uncharged. Therefore, the question that arises addresses the oxidation state of the chelated cobalt ion of these two conformers, where charged and uncharged porphyrin's macrocycles are stabilized on the surface. To investigate the Co oxidation state in the two different CoTPP conformations, namely saddle-shape and planar, we have performed XPS measurements at the Co $2p_{3/2}$ core-level.

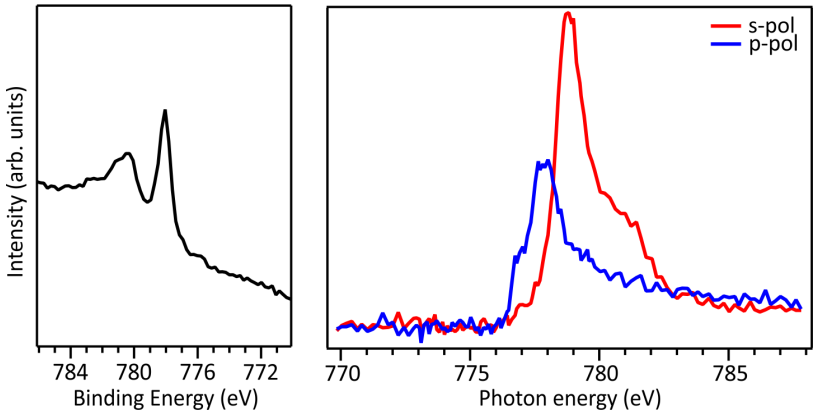

Figure 3.29: Co $2p_{3/2}$ XPS spectrum and Co L_3-edge K-edge NEXAFS spectra of CoTPP monolayer deposited on the Ag(100) surface.

In Figure 3.29, the Co $2p_{3/2}$ core-level spectra of CoTPP self-assembled on the Ag(100) substrate are shown. The XPS spectrum of CoTPP manifests a main line peaked at 778.2 eV and a broad satellite at higher BE with the maximum at 780.9 eV. To unravel the oxidation state of the chelated ion, we compare the present spectra with the one measured on the inert O-Cu(100) substrate, where the spectrum displays the characteristic multiplet structure of low spin Co(II) with one unpaired electron, as well as with CoTPP molecules self-assembled on the more reactive surface Cu(100), on which the Co(II) $\rightarrow$ Co(I) reduction is taking place (see Section 3.3). While the spectrum of Co(II) is peaked at 779.25 eV, in the spectra of CoTPP with the cobalt ion stabilized in the Co(I) configuration the sharp maximum is located at 778.4 eV. Looking closer to the XPS data reported in Figure 3.29, in particular spectral shape and energy position of the resonances, we can conclude that in both conformation forms, namely saddled and planar, of CoTPP self-assembled on Ag(100) substrate, the cobalt ion is stabilized in the formal Co(I) oxidation state.

The stabilization of the Co(I) state is also confirmed by the Co L_3-edge NEXAFS spectrum (see section 3.3 for comparison). However, appreciable differences can be observed in the intensity ratio between s- and p-polarization, suggesting smaller charge transfer from the less reactive silver substrate to the molecule compared to the highly interacting copper surface. Even though the central cobalt ion is in the formal oxidation state +1, it receives smaller charge transfer from the substrate, resulting in an oxidation state intermediate between +1 and +2, as evident in XPS from the different satellite structure at higher BEs.

How does this different reactivity of the substrate reflect in the reactivity of the CoTPP molecular layer? In order to test this, the molecular monolayer deposited on the Ag(100) has been exposed to increasing doses of NO_2 at room temperature.

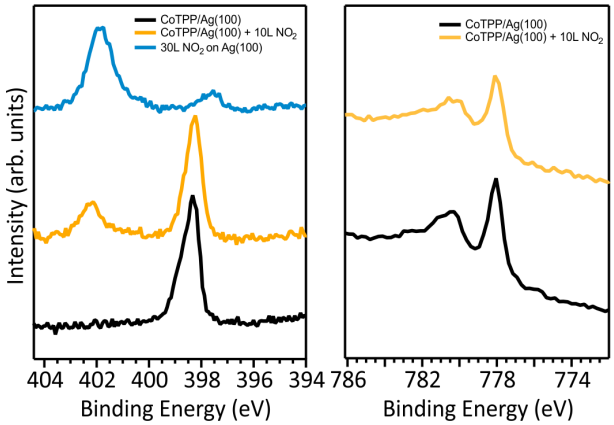

Figure 3.30: N *1s* and Co $2p_{3/2}$ XPS spectra before (red curve) and after (orange curve) exposing to 10 L of NO_2 the CoTPP/Ag(100) interface; blue curve in the N *1s* XPS spectrum corresponds to the 30 L NO_2 dose on the clean Ag(100) substrate.

After exposing the CoTPP/Ag(100) system to 10 L of NO_2 (see Figure 3.30), a new peak appears at binding energy 402.5 eV in the N *1s* spectrum. Based on this, one might think that NO_2 coordinates axially to the central metal also at the CoTPP/Ag(100) interface. However, no change in the Co $2p_{3/2}$ spectrum is observed after the appearance of this extra nitrosyl component, suggesting a different coordination site. One of the possible adsorption sites of NO_2 is the Ag(100) surface itself, and to test this possibility NO_2 was dosed directly on the bare metal surface. By exposing the Ag(100) substrate to increasing doses of NO_2 at RT, two new peaks appear in the N *1s* XPS spectrum, which can be attributed to the not dissociated NO_2 (BE 402.5 eV) and to the atomic nitrogen generated by the on-surface dissociation of nitrogen dioxide (BE 397.8 eV). Traces of oxygen on the Ag(100) surface are also detectable in the O *1s* (not reported here).

This interpretation is also supported by the N K-edge spectra measured after the NO_2 dose on the CoTPP/Ag(100) interface and on the bare Ag(100) surface (see Figure 3.31). After exposing the CoTPP monolayer on Ag(100) to NO_2 an intense peak located at 401.5 eV in photon energy appears in the spectrum acquired in s-polarization. This transition shows a clear fingerprint also in the spectrum acquired in p-polarization suggesting a random adsorption geometry of the NO_2 species (this was not the case on Cu(100), where the NO_2 was adsorbing on the cobalt sites with a defined orientation and, indeed, the ligand fingerprint was visible only in the s-polarized

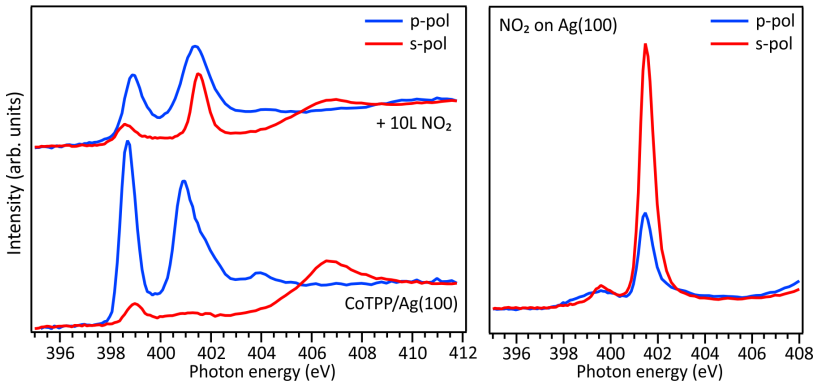

Figure 3.31: (a) N K-edge NEXAFS spectra before (bottom) and after (top) exposing to 10 L of NO_2 the CoTPP/Ag(100) interface. (b) N K-edge NEXAFS after exposing the bare Ag(100) to 30 L of NO_2.

spectrum). These extra features coincide with the ones rising after exposing the bare silver substrate to NO_2, confirming that the NO_2 adsorbs directly on the Ag(100) substrate when the CoTPP/Ag(100) interface is exposed to NO_2.

A similar behaviour is also observed in the case of the NiTPP monolayer deposited on the Ag(100) substrate.

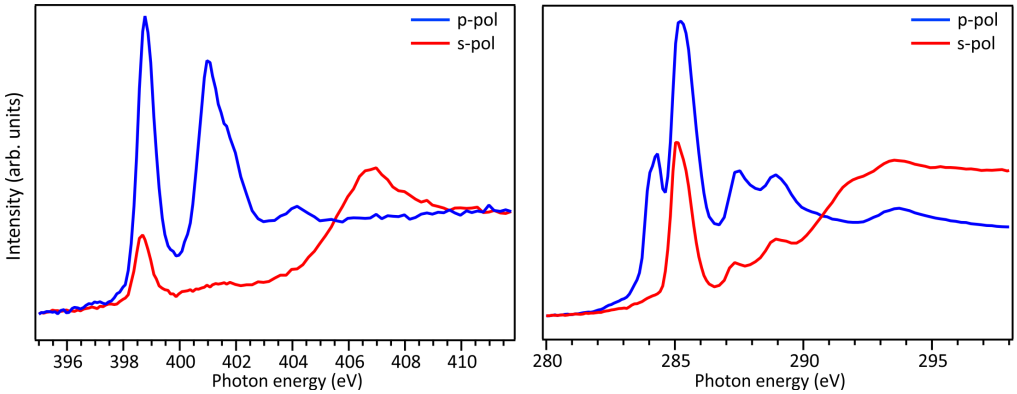

Figure 3.32: N K-edge and C K-edge NEXAFS spectra of NiTPP monolayer deposited on the Ag(100) surface.

Figure 3.32 includes the N K-edge and the C K-edge spectra acquired for the pristine NiTPP/Ag(100) system. The N K-edge NEXAFS spectra show strong similarities with the one acquired at the CoTPP/Ag(100) interface, suggesting the co-existence of planar and saddle shape conformers on the silver substrate. A quantitative evaluation of the average tilt-off angle γ of the phenyl in NiTPP self-assembled on Ag(100) can be drawn according to the relation Is/Ip $\propto 1/2$ tg2γ, where Is/Ip is the intensity ratio of the resonance at 285.05 eV in the two polarization, and it results to be $\sim 48^\circ \pm 3^\circ$. The conformational adaptation shows small deviations from the case of the CoTPP monolayer on Ag(100).

Major differences with respect to the CoTPP monolayer are observed in the oxidation state of

the central nickel ion. The Ni $2p_{3/2}$ XPS spectrum acquired at the NiTPP/Ag(100) interface shows a single peak centered at 855.4 eV. The position in binding energy suggests a Ni(II) oxidation state, but in order to exclude possible screening effects and to unequivocally determine the nickel oxidation state NEXAFS spectra were acquired at the Ni L_3-edge for the NiTPP/Ag(100) system. The absorption spectra confirms the presence of Ni(II).

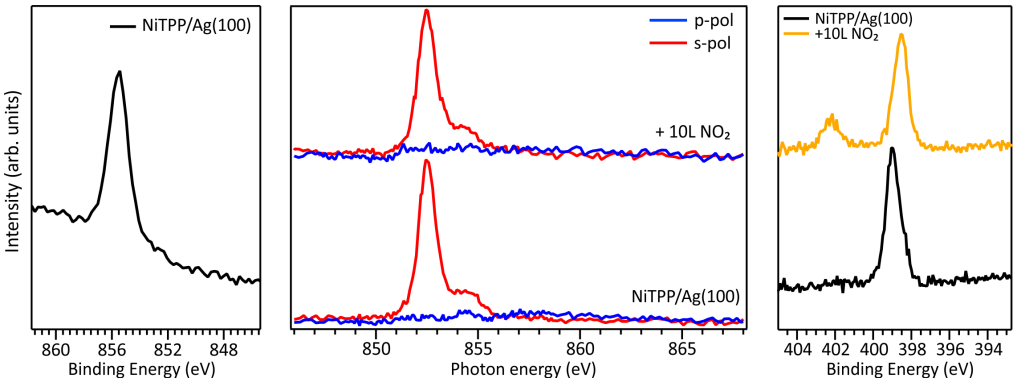

Figure 3.33: (a) Ni $2p_{3/2}$ XPS spectrum of NiTPP monolayer deposited on the Ag(100) surface. (b) Ni L_3-edge K-edge NEXAFS spectra and (c) N *1s* XPS spectra acquired at the NiTPP/Ag(100) interface before (bottom) and after (top) exposure to 10 L of NO_2.

Upon exposure of the NiTPP/Ag(100) interface to 10 L of NO_2 at RT, no changes are visible in the nickel oxidation state, despite the appearance of the component at 402.5 eV in the N *1s* XPS spectrum (see Figure 3.33), which can be attributed to the nitrogen dioxide interacting at the interface with the Ag(100) substrate, as previously observed in the case of the CoTPP/Ag(100) system.

By stabilizing NiTPP and CoTPP on Ag(100) and subsequently dosing NO_2 on the interface, we observed that the systems are not active towards functionalization, demonstrating the importance of the coupling to the copper surface in order to increase the catalytic reactivity of the molecular overlayer.

3.6 Conformation-dependent charge donation to the chelated metal ion: NiTPP and CoTPP on Au(111)

To fully exploit the potential of these interfaces, the understanding and capability to tune the physical, chemical, and transport properties of organic semiconductor components is critical [203, 204]. Within this framework, the capacity of controlling the metal charge and spin states in the organic array is a step towards molecular spintronics realization, and it has been shown that single electron injection in the molecule can drastically change its properties. Along these lines, scanning tunneling microscopy (STM) investigations on a single-molecule junction have shown that electrons travel through the FePc molecule via two different 3*d* atomic orbitals (AOs), and the electron pathway within the tip-FePc-Au junction can be selected just by changing the magnetic field. Tunable giant magnetoresistance in this molecular device originates from the re-orientation

of the iron magnetic moment, which alters the electron distribution in the Fe 3*d* AOs [205]. As such, it has been recently reported that, under the force field of an STM tip, it is also possible to reversibly modify both the Fe oxidation and spin states of the Fe(III) octaethylporphyrin-chloride anchored on a Pb(111) substrate [206,207]. In addition, both transition metal porphyrins (TMPs) and TM phthalocyanines (TMPcs) can coordinate electron acceptor/donor ligands to the metal center, thus resulting in a change of the valence electrons number in the chelated metal, which induces a variation in its oxidation and spin state [12,62]. For instance, the spin state could be controlled even by coordinating single H atoms to the magnetic core of the adsorbed molecule [208–210].
It is also noteworthy that XMCD measurements have recently brought to light that the molecular properties of surface-supported TMPc can be also modified by the donation of a single electron provided by an alkali metal (AM), with final oxidation and spin states being strongly TM dependent. Specifically, the TM(II) species in CuPc, NiPc, and FePc molecular layers decrease their oxidation state upon alkali metal deposition, whereas MnPc preserves its formal oxidation state Mn(II), but the magnetic configuration switches from an intermediate to a high-spin (HS) state [66]. Besides the TM and AM nature, the electron donation is also influenced by the adsorption site, and TM reduction is observed only when the AM adsorbs in TM proximity [65].

Changes in the molecular properties of TMPcs and TMPs can be also induced by the coordination of polyatomic molecules to the TM. In this respect, in the previous sections, it has been shown that axial coordination may be exploited to modulate the TM oxidation and spin states [53,211,212]. In fact, the spin state of the Mn ion in the tetra-pyrrolic pocket may sweep across different configurations by subtle modification of the N ligand field, *e.g.* by changes of the Mn-ligand distance (HS in Mn-porphyrins [49], IS in Mn-Pc [66]) or of the ligand peripheral coordination (HS in Mn-$TCNQ_4$ metal-organic covalent networks [10]. Interestingly, it has been recently demonstrated that ruthenium tetraphenylporphyrin (RuTPP) on Ag(111) can be stabilized in two different conformations, saddle-shaped and planar, and only the former may axially interact with CO as a consequence of its greater molecular flexibility [213]. As such, the role played by the molecular flexibility in prompting the electronic and magnetic properties of TMTPP after electron doping is an essential aspect whose potential applications are not yet sufficiently investigated.

In this section, the influence of the molecular conformation in the metal reduction of AM-doped TMTPP is tackled by combining X-ray photoemission and absorption spectroscopies with photoemission tomography and density functional theory (DFT) calculations. The charge donation induced by the bonding of a single K atom to NiTPP, and determining the Ni reduction, is almost unaffected by the K adsorption site. However, for higher K doses and then larger electron donation, the charge transfer is not limited to the Ni-based 3*d* AOs, but it also involves the TPP-based lowermost unoccupied MOs. Two different adsorption configurations involving two K atoms per molecule are found to be energetically stable. In the flattest macrocycle, a Ni(II) + K $\rightarrow$ Ni(I) + K^+ redox reaction takes place, while the relaxation to the energetically-favored distorted form leads to a concomitant nickel re-oxidation and the macrocycle doping increase. Such a result demonstrates the pivotal role played by the macrocycle flatness of the K-doped NiTPP in stabilizing the Ni(I) species. In addition to that, the TM role has been studied by investigating the K doping of CoTPP. The susceptibility to molecular conformation decreases for CoTPP and, unlike NiTPP, the Co(II) $\rightarrow$ Co(I) reduction takes place in both energetically stable configurations involving two K atoms per molecule.

TM oxidation and spin state variations in TMPc and TMPs-based systems can be triggered by coordinating them to metal surfaces, and the charge transfer eventually taking place is strongly TM and substrate-dependent. Indeed, as underlined in Section 3.2 and 3.3, the adsorption on the highly reactive copper surface implies the filling of the adsorbate lowermost unoccupied MOs (up to the LUMO+3) and the concomitant TM(II) $\rightarrow$ TM(I) reduction [100,152,211,212]. Charge injection into the metal complex may be also induced by exploiting alternative pathways such as AM doping. Aimed to look into the TM reduction process, a NiTPP layer deposited on the Au(111) surface has been stepwise K doped. The chemical inertness of the substrate assures that any variation of the NiTPP molecular properties eventually revealed can be traced back to the K doping. Valence band (VB) and near-edge X-ray absorption fine structure (NEXAFS) spectra recorded at the N K-edge were used to track the progressive filling of TPP-based MOs as the K doping is increased. Moreover, the K doping effect on the Ni 3*d* AOs was studied by using Ni 2*p* photoemission spectroscopy and Ni $L_{2,3}$-edges NEXAFS measurements.

Work function changes, $\Delta\phi$ (a), the angle-integrated VB spectra (b) and the N K-edge spectra (d) of a single layer of NiTPP deposited on the Au(111) substrate as a function of the K doping dose are displayed in Figure 3.34. Spectra of the pristine NiTPP layer (0′) have been also recorded and added to the figure for comparison.

The VB spectrum of the pristine NiTPP layer deposited on Au(111) is consistent with a weak adsorbate-substrate interaction: no peak due to charge transfer phenomena, frequently present at strongly interacting adsorbate–substrate interfaces [100,195,214], is observed and only features determined by the ionization from the topmost occupied MOs (HOMO/HOMO-1) are detected (see Figure 3.34b-c) and assigned using the PT approach. The assignment is in agreement with Scudiero *et al.* [215], according to whom the topmost occupied MOs correspond to the quasi-degenerate TPP-based a_{2u} and a_{1u} π MOs, as corroborated by exploiting the Slater transition state (STS) approximation [216].

The weak interaction of NiTPP on Au(111) is confirmed by the shape of the N K-edge NEXAFS spectra (Figure 3.34d). The major characteristics of the N K-edge NEXAFS spectra pre-edge region, both in terms of energy position and line-shape, are comparable to those recorded for NiTPP deposited on an inert substrate [152,160] (see Section 3.1) either as multilayer or as a self-assembled monolayer. The sharp peak at 398.9 eV is associated with excitations from N *1s* into the doubly degenerate LUMO/LUMO+1 (e_g) and LUMO+3 (b_{2u}) levels having π^* character [39]. Excitations to higher-lying unoccupied π^* MOs lead to the spectral feature at 401.1 eV [217]. A σ^*-symmetry resonance observed in the spectra obtained with s-polarized light at a photon energy of 398.6 eV results from the N *1s* level to the nickel-based σ-type LUMO+2 (b_{1g}) transition [39,160]. The strong linear dichroism in the N K-edge spectra in the range of the π^*-symmetry resonances indicates that the porphyrin macrocycle adsorbs parallel to the surface plane. On metal substrates, extended π-conjugated molecules frequently adopt such a comparable flat-lying geometry [11,12,126].

The electron injection into low-lying empty MOs induced by the K doping should determine complementary changes in the NiTPP VB and NEXAFS spectra; specifically, the partial filling of TPP-based π^* MOs should be accompanied by the emergence of new features in the VB spectra and intensity decrease of the low-lying NEXAFS resonances. Indeed, there is a dramatic change in the N K-edge NEXAFS spectra with increasing K doping, where the lowest energy resonance significantly alters the intensity weight after the K dosage, as a result of the partial filling of the lowermost unoccupied MOs. The inspection of Figure 3.34b reveals that, at high K doses, new features enrich the VB spectrum around 0.7 and 1.4 eV. Theoretical and experimental

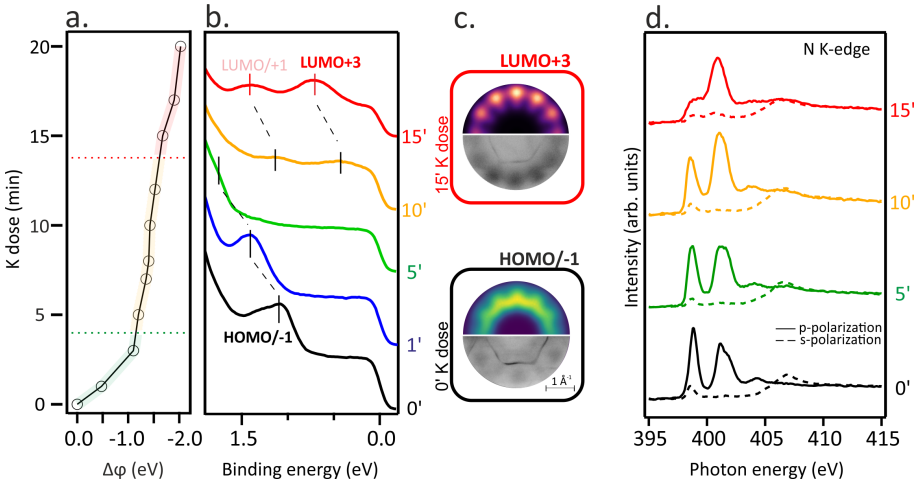

Figure 3.34: (a) Work function changes ($\Delta\phi$), (b) valence band spectra of NiTPP on Au(111) exposed to increasing K doses, (c) Simulated (top) and experimental (bottom) momentum maps identifying the last occupied molecular orbital before and after 15 min K dose, (d) N K-edge spectra of NiTPP on Au(111) exposed to increasing K doses (5, 10 and 15 minutes).

momentum maps at the corresponding peak maximum (Figure 3.34c top and bottom, respectively) provide information about the former empty MOs, now partially occupied by electron injection. In particular, simulated patterns are assigned to the LUMO/LUMO+1 and LUMO+3 levels, which is consistent with the NEXAFS results. Such a remarkable charge transfer (up to the LUMO+3) has been already revealed for the aforementioned NiTPP/Cu(100) and CoTPP/Cu(100) interfaces [100, 211, 212] (see Section 3.2 and 3.3).

As a final remark, the peculiar work function (WF) trend as a function of the K dose (see Figure 3.34a) deserves to be highlighted: (i) a significant WF drop, indicative of the formation of a new surface dipole induced by the adsorption of the K atoms at the interface, is present at the lower K doping level; such WF change is accompanied by a HOMO blue shift with respect to the Fermi level; (ii) a plateau region leading to the complete filling of the gas-phase unoccupied MOs up to LUMO+3 characterizes the intermediate K coverage; this range corresponds to the region of interest for the electron doping of the molecular layer; (iii) a further, less pronounced, WF drop determining a blue-shift of the low-lying empty MO (LUMO/+1 and LUMO+3) takes place at higher K doses, which corresponds to the appearance of neutral K species in the K 2*p* XPS spectrum (Figure 3.36). Similar effects on the VB spectra were previously reported for AM-doped TMPc layers [218–220].

So far, the effects associated with the filling of the low-lying empty TPP-based MOs have been discussed just by referring to the VB and N K-edge NEXAFS outcomes. Next, we look at the K doping effect on the nickel 3d levels. To that end, XPS spectra at the Ni 2*p* core levels and Ni L_3-edge NEXAFS measurements on the pristine NiTPP deposited on Au(111) have been recorded; their evolution as a function of the K doping has been then tracked (see Figure 3.35). The Ni 2*p* photoemission spectrum of the undoped NiTPP layer on Au(111) (see Figure 3.35a) shows a single and well-resolved peak at 855.1 eV accompanied by a satellite feature located at higher BE.

Such evidence indicates a Ni(II) oxidation state, which has been confirmed by the corresponding Ni L_3-edge spectrum (Figure 3.36). The L_3-spectra is characterized by a primary peak at 854.3 eV and the strong satellite A at higher photon energy (856.2 eV). The observed spectral shape is a fingerprint of a Ni(II) in a tetra-coordinated square-planar geometry [66, 152, 180, 181, 221]. Moreover, the presence of the extra satellite peak A in the spectra of NiTPP/Au(111) is indicative of a nickel in a LS $3d^8$ electronic configuration [66].

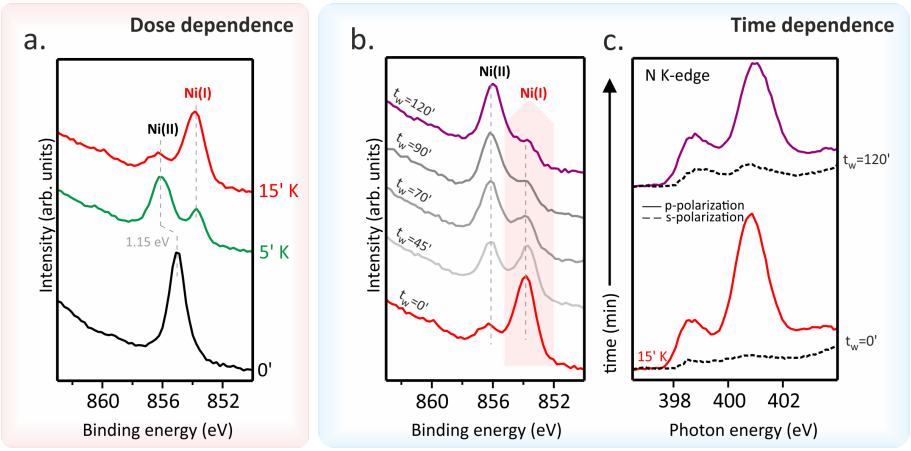

Figure 3.35: a) Ni $2p_{3/2}$ XPS spectra measured on the pristine NiTPP/Au(111) layer and after exposure to increasing K doses (5 and 15 minutes). Nickel oxidation states are evidenced in the spectra. Time dependent b) Ni $2p_{3/2}$ XPS and c) N K-edge NEXAFS spectra. The waiting time (t_w) after the dose is evidenced for every spectrum. The reference spectrum (t_w=0') is recorded immediately after the 15 minutes K dose on freshly prepared NiTPP/Au(111).

The K doping of the NiTPP monolayer significantly affects both XPS and NEXAFS spectra. In particular, the gradual Ni(II) $\rightarrow$ Ni(I) reduction induced by the electron injection due to the K adsorption on the NiTPP layer is well evident in the Ni $2p_{3/2}$ core-level spectra (Figure 3.35a) where a new, red-shifted feature with BE = 852.8 eV progressively increases its intensity with K doping. Likewise, in the Ni L_3-edge NEXAFS spectra (Figure 3.36), as the K concentration increases, a new peak emerges on the low-energy side of the original L_3 main peak. The shift to lower photon energies, as well as the energy position of the new resonance, is consistent with the Ni ion reduction [152] induced by the electron doping via AM. As such, it has to be noted that the intensity of the new Ni(I) peak increases at the expense of the Ni(II) resonance and its satellite A, whose drop in intensity implies a partial filling of the Ni $3d_{x^2-y^2}$-based b_{1g} MO. Filling one of the spin-paired holes in the $d_{x^2-y^2}$ orbitals results in a free spin 1/2, thus inducing a magnetic moment in the Ni ion. Current data reveal that NiTPP behaves similarly to NiPc, where magnetism is induced by the adsorption of Li atoms on top of the NiPc layer, as confirmed by XMCD measurements [66]. To investigate the stability of the Ni(I)TPP species, Ni $2p$ XPS spectra have been collected as a function of the time (t_w) after the 15 minutes K dose (see Figure 3.35b). To this end, the NiTPP/Au(111) interface has been freshly reprepared before the 15 minutes K doping. The main feature of the pristine Ni $2p_{3/2}$ core level spectrum has been assigned to Ni(I) which, after tens of minutes, re-oxidizes to Ni(II). Such a process takes a 90-minute t_w interval to complete at room temperature. This reconversion process is also observed on the same time

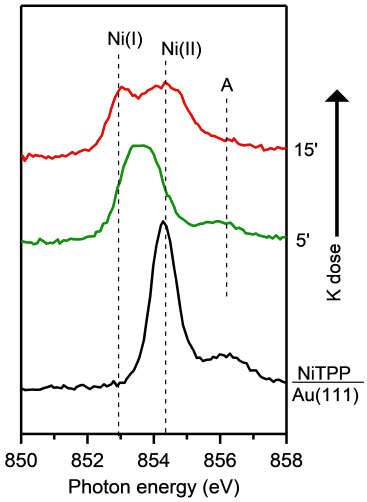

Figure 3.36: Ni L_3-edge NEXAFS spectrum acquired in s-polarization for the pristine NiTPP/Au(111) interface and after exposure to increasing K doses (5 and 15 minutes dose).

scale for smaller doses of K, namely 5 and 10 minutes, proving to be dose-independent. In addition, time-dependent N K-edge NEXAFS spectra (Figure 3.35c) show distinct changes when the Ni(I) to Ni(II) transition takes place. As such, it is noteworthy that the spectral linear dichroism at t_w = 0′ is perfectly consistent with a flat adsorption geometry of the porphyrin macrocycle, while the dichroic behavior of π* resonances in s-polarization at t_w=120′ suggests its distortion. Moreover, the different relative intensity of the two π* resonances in p-polarization at t_w=0′ and 120′ indicates an increase of the overall charge transfer on the macrocycle MOs, when observing the Ni(I) $\rightarrow$ Ni(II) conversion.

At this point, the question that spontaneously arises concerns the structure of the K doped NiTPP species, not only because it is probably related to the Ni(I) $\rightarrow$ Ni(II) conversion, but it also involves the bonding site of K atoms on NiTPP. In this case, DFT-based numerical experiments may provide insights into the electronic and geometrical structure of adsorbed species upon increasing the K dosing. DFT calculations reported in this section have been performed by Dr. Silvia Carlotto and Prof. Maurizio Casarin from the University of Padova, Italy.

As previously remarked, the NEXAFS measurements of the bare molecular adlayer reveal that its electronic structure is unaffected by the Au substrate, hence it may be regarded as a free standing layer. In this case, a molecular cluster approach provides a quantitative analysis of the atomic and molecular orbitals modification and corresponding charge exchange [10,66]. We tested different adsorption geometries by increasing the number of K atoms directly bonded to NiTPP.

Low K doses have been modeled by bonding a single K atom to NiTPP. Different stable K adsorption sites are found: i) K directly bonded to Ni in the top position, ii) K adsorbed in the hollow position, and iii) K adsorbed in the bridge position (see Figure 3.37). While the K atom has a single unpaired electron in its isolated electronic structure, the chelated TM ion in the NiTPP on the gold surface is stabilized in the Ni(II) LS $3d^8$ closed-shell configuration with no unpaired electron. A single unpaired electron is then assumed for the different K-NiTPP clusters.

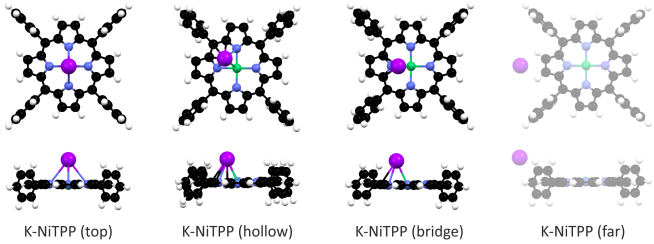

Figure 3.37: A schematic representation of the different K adsorption geometries calculated for the K-NiTPP complex. Black, white, blue, green, and violet spheres represent C, H, N, Ni, and K, respectively.

Table 3.3: Adsorption site-dependent DFT calculation for the K-NiTPP complex. K-NiTPP adsorption energies (E_{ads}), relative adsorption energies (ΔE_{ads}) with respect to the most favorable (hollow) one, number of unpaired electrons on the nickel ion, nominal Ni oxidation state, NM indexes for the Ni-N and Ni-K bond are reported.

	ΔE_{ads} eV	E_{ads} eV	Ni unpaired el.	Ni ox state	$^{NM}I_{Ni-N}$ avg	$^{NM}I_{Ni-K}$
K-NiTPP (top)	0.12	-1.24	0.88	Ni(I) d^9	0.380	0.136
K-NiTPP (hollow)	0.00	-1.37	0.75	Ni(I) d^9	0.387	0.095
K-NiTPP (bridge)	0.07	-1.30	0.86	Ni(I) d^9	0.383	0.115
K-NiTPP (far)	1.20	-0.16	0.32	Ni(II) d^8	0.416	//[1]

[a] In the K-NiTPP (far) complex, there is not a direct Ni-K bond.

The structure analysis (see Table 3.3) reveals that the hollow adsorption configuration is more stable than the top and bridge ones by 0.12 eV and 0.07 eV, respectively. The higher stability of the hollow configuration may be justified by the formation of a higher number of interactions between K and the TPP moiety, as can be appreciated in the structural models reported in Figure 3.37. Such small energy differences among the structures suggest that all absorption sites are accessible at room temperature. Data reported in Table 3.3 also point out that, independently of the assumed geometry, the Ni(II) + K $\rightarrow$ Ni(I) + K^+ redox reaction systematically takes place. It is of some interest to underline that, at large K$\cdots$NiTPP distances (see Figure 3.37 and Table 3.3), the Ni(II) reduction is inhibited and the K$\cdots$NiTPP system is destabilized by 1.20 eV with respect to the hollow geometry. In tune with the Ni–N antibonding character of the Ni $3d_{x2\text{-}y2}$-based MO, its partial filling induced by electron injection implies that the Ni–N Nalewajski–Mrozek index ($^{NM}I_{Ni-N}$ in Table 3.3) decreases upon K binding; the opposite is true for $^{NM}I_{Ni-K}$.

Higher K doses on the NiTPP/Au(111) interface, which retrace experimental data, have been modeled by bonding two K atoms to NiTPP. Numerical experiments' outcomes indicate that two stable structures are present, labeled as A and B in Figure 3.38.

The inspection of the results reported in Table 3.4 indicates that, both in A and B, the dopant species is present in its oxidized form. Interestingly, the porphyrin macrocycle in A is very flat, while it is significantly distorted in B (see Figure 3.38); in addition, the former conformation is less stable than the latter one by 0.23 eV (see Table 3.4). These conformational changes induce a different charge donation from K atoms to NiTPP. More specifically, the electron injection determined by the high K dosing involves both the Ni(II) $3d_{x2\text{-}y2}$-based MO and a TPP^{2-}-based MO in A, while in B the charge transfer does not involve the metal center, which maintains

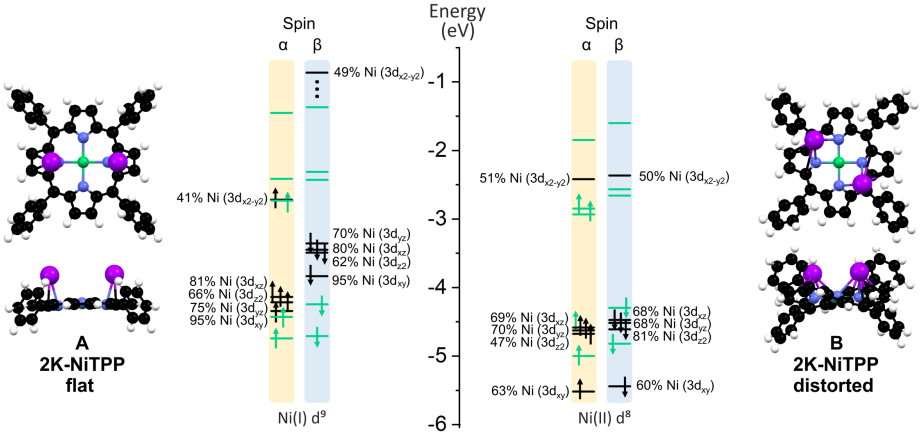

Figure 3.38: A schematic representation of the different conformations (A and B) calculated for the 2K-NiTPP complex. Color codes are the same adopted in Figure 3.37. On the right side of each configuration is reported the energy level diagram for selected MOs, Ni-based and TPP-based levels are highlighted in black and green, respectively. Both α and β spin are reported.

Table 3.4: Conformational-dependent DFT calculation for the 2K-NiTPP complex. 2K-NiTPP adsorption energies (E_{ads}), relative adsorption energies (ΔE_{ads}) with respect to the most favorable (B) one, number of unpaired electrons on the nickel ion, nominal Ni oxidation state, NM indexes for the Ni-N and Ni-K bond are reported.

	ΔE_{ads} eV	E_{ads} eV	Ni unpaired el.	Ni ox. state	$^{NM}I_{Ni-N}$ avg	$^{NM}I_{Ni-K}$ avg
A - 2K-NiTPP Flat	0.23	-2.19	1.00	Ni(I) d^9	0.384	0.075
B - 2K-NiTPP Distorted	0.00	-2.41	0.04	Ni(II) d^8	0.492	0.038

the same LS $3d^8$ configuration of the pristine NiTPP on Au(111). Similarly to K-NiTPP, the Ni(II)–N bond is stronger than the Ni(I)–N one (see the $^{NM}I_{Ni-N}$ in Table 3.4). As a whole, the DFT outcomes pertaining to the models adopted to mimic low and high K doping of the NiTPP/Au(111) interface agree well with experimental finding. In particular, they provide a rationale for the experimental temporal evolution from the flat conformation A, characterized by the presence of the paramagnetic Ni(I) species, to the thermodynamically most stable distorted geometry B typified by the occurrence of the diamagnetic Ni(II) species (see Figure 3.35b-c).

The interaction of NiTPP with three K atoms has been also considered and, in agreement with the experiment and 2K-NiTPP theoretical results, the 3K-NiTPP outcomes confirm that: i) once again the most stable species is associated with the Ni(II) presence (Table 3.5); ii) Ni(II) is always associated to the most distorted geometries (Figure 3.39), thus evidencing the relevant role played by the molecular distortion in determining the Ni oxidation state even in the presence of a large number of the electron donor K atoms.

Before proceeding with the discussion, it is necessary to spend a few words on the experimental estimation of the amounts of potassium involved in the various doping steps. Dose-dependent K

Table 3.5: Adsorption site-dependent DFT calculations for the 3K-NiTPP complexes. 3K-NiTPP adsorption energies E_{ads}, relative adsorption energy (ΔE_{ads}) with respect to the most favorable (A) one, number of unpaired electrons on the nickel ion, nominal Ni oxidation state, NM indexes for the Ni-N and Ni-K bond are reported. The A and B two structures are obtained with one unpaired electron, while C and D with 3 unpaired electrons. [a]Calculated with respect to 3 isolated K atoms; [b]Calculated with respect to a 3K cluster.

	ΔE_{ads} (eV)	E_{ads} (eV)	Ni unpaired el.	Ni ox. state	$^{NM}I_{Ni-N}$ avg	$^{NM}I_{Ni-K}$ avg	$^{NM}I_{Ni-K}$ TOT
A - 3K-NiTPP Distorted	0	-3.25[a]	0.04	Ni(II) d^8	0.483	0.042	0.084
B - 3K-NiTPP Distorted PY	0.24	-2.32[b]	0.00	Ni(II) d^8	0.488	0.029	0.057
C - 3K-NiTPP Flat	0.20	-2.35[b]	0.95	Ni(I) d^9	0.380	0.046	0.138
D - 3K-NiTPP Less Flat PY	0.30	-2.26[b]	0.95	Ni(I) d^9	0.378	0.043	0.130

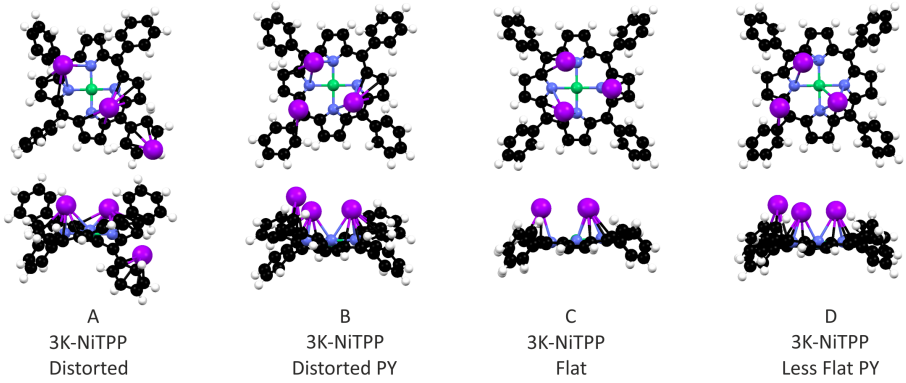

Figure 3.39: A schematic representation of the different K adsorption geometries calculated for the 3K-NiTPP complex. Black, white, blue, green, and violet spheres represent C, H, N, Ni, and K, respectively.

2p core-level spectra are reported in Figure 3.40, together with a semi-quantitative analysis of the K coverage with respect to the molecular layer.

Figure 3.40 shows the K *2p* core-level spectra of the NiTPP/Au(111) interface as a function of the potassium evaporation time. After the exposure of the bare NiTPP/Au(111) interface to a 5 minutes dose of K, new spectral features appear at binding energies of 293.70 and 296.51 eV, which are attributed to the potassium atoms co-adsorbed at the NiTPP/Au(111) interface. The energy difference of these features (ΔSOC = 2.8 eV) is in good agreement with the *2p* core-level spin-orbit splitting of K. The intensity of these features further increases for higher K doses, reaching saturation at a dose of about 15' K. At this coverage, we also observe the appearance of a new K *2p* component at higher BE, with the 3/2 and 1/2 spin-orbit levels located at 295.07 eV and 297.86 eV, respectively. This new component corresponds to the stabilization of a neutral K(0) species [222], while the features at lower BE are assigned to the ionized K species, suggesting the K oxidation to K^+ for low K doses at the NiTPP/Au(111) interface. This evidence couples well with the red-shifted features in the Ni *2p* spectra consistent with the reduction of the nickel

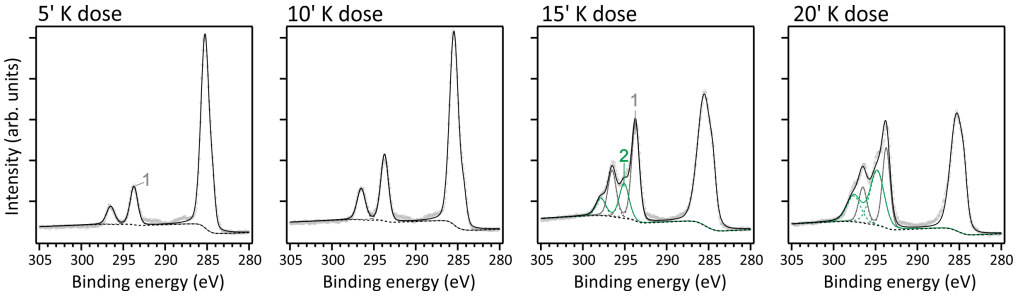

Figure 3.40: K *2p* and C *1s* XPS spectra acquired at the NiTPP/Au(111) interface as a function of the potassium evaporation time.

ion of the NiTPP molecule upon electron injection by K atoms. For an excess of potassium on the surface, the neutral alkali species rise in intensity, while the ionized component preserves the same intensity. We remark that the stabilization of the neutral species is observed only upon increasing the K doses, while no changes in the K *2p* spectral shape are observed as a function of the time. The Ni(I) to Ni(II) reconversion induced by the conformational change is taking place in the presence of the ionized K^+ species, leading, indeed, to the charge redistribution and to increased doping of the macrocycle. By combining the information provided by both C *1s* and K *2p* core-level spectra, a semi-quantitative analysis can be carried out to estimate the amount of deposited K atoms at NiTPP/Au(111) interface. In the analysis, we take into account the photo-ionization cross-sections at 515 eV photon energy for C *1s* and K *2p*, which correspond to 0.25 and 1.02 Mbarn [223], respectively. However, we neglect photoelectron diffraction effects and assume a constant transmission of the analyzer, as the corresponding kinetic energies are very close for these two core-level lines. With respect to the molecular monolayer (ML_{mol}), the 5′ dose of K leads to a K coverage of 0.04 ML_{mol}, which grows to 0.06 ML_{mol} when increasing the K dose to 10′. Co-deposition of 15′ of K leads to the appearance of a new component in the K *2p* spectrum, corresponding to a neutral species at the NiTPP/Au(111) interface. In this deposition step, the estimated K coverage is 0.14 ML_{mol}, with 0.09 ML_{mol} located on the low BE component (labeled as 1) corresponding to the ionized K^+ species. As evident from the 20′ dose spectrum, the 15′ dose corresponds to the saturation of the ionized K^+ species, in agreement with the valence band and nickel spectra reported in the main text. The semi-quantitative analysis performed for the 20′ K dose leads to 0.09 ML_{mol} coverage of ionized species, as in the 15′ dose, and a total K coverage of 0.19 ML_{mol}.

TMPcs with diverse TM act differently upon AM doping [66]; in the following section, we focused on CoTPP deposited on Au(111) to look into its eventually different behavior from NiTPP upon the AM dosing.

The Co $2p_{3/2}$ core level spectrum of CoTPP self-assembled on the Au(111) surface (see Figure 3.41a) is similar to the spectra reported in ref. [224], and analogously to the free molecule, CoTPP deposited on Au(111) has an LS $3d^7$ configuration with its single unpaired electron occupying the Co(II) $3d_{z^2}$-based MO [11,53,54,225]. The K binding to CoTPP red-shifts the spectrum main feature by 0.85 eV, a behavior tightly linked to the Co(II) → Co(I) reduction [212]. Moreover, the inspection of Figure 3.41b, where the N K-edge spectra of the pristine CoTPP/Au(111) and after 15 minutes K dosing in s- and p-polarization are compiled, clearly shows that the macrocycle

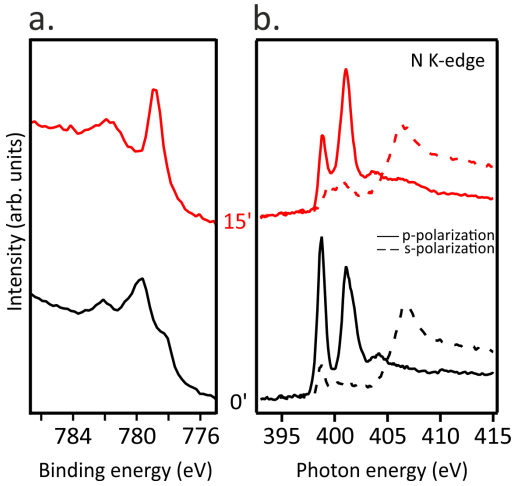

Figure 3.41: a) Co $2p_{3/2}$ core level and b) N K-edge NEXAFS spectra for pristine CoTPP/Au(111) (black curves) and after exposure to K for 15 minutes (red curves).

distortion takes place right after the K doping.

Similarly to NiTPP, different K doses have been modeled by directly bonding either one or two K atoms to CoTPP. K-NiTPP and K-CoTPP DFT results are very similar; specifically: i) three distinct adsorption sites are possible when a single K atom is considered (top, bridge, hollow position) (see Figure 3.42a), ii) the most stable configuration is the one with the K atom in the hollow site, iii) followed by the bridge (+0.05 eV) and the top (+0.11 eV) adsorption structures (see Table 3.6), closely spaced in energy. In addition, the bonding energy of the K-CoTPP cluster is tightly and directly related to the K–CoTPP bonding interaction, which determines the distortion of the macrocycle fragment. Indeed, the largest distortion is predicted for the most stable hollow configuration (see Figure 3.42), while an almost CoTPP flat geometry is foreseen for the top position. K–CoTPP adsorption energies are -1.76, -1.82 and -1.87 eV for top, bridge and hollow sites, respectively. Interestingly, the comparison of theoretical outcomes pertaining to K-CoTPP and K-NiTPP clearly indicates that the K-CoTPP interaction is stronger than the Ni-TPP one (see Tables 3.3 and 3.6).

Both the free CoTPP molecule and the K atom hold a single unpaired electron in their electronic structure hence two spin states are possible in the K-CoTPP complexes: zero or two unpaired electrons. The zero unpaired electron structure is more stable than the two unpaired electrons one by more than 1 eV. The detailed electronic analysis reveals that in all structures reported in Figure 3.42, the chelated Co ion gains an electron from K (see Table 3.6) and is stabilized in the closed-shell configuration with the empty $3d_{x^2-y^2}$ MO. This scenario is consistent with an electron transfer from K to Co and the stabilization of the Co(I) and K^+ ions in K-CoTPP complexes.

Analogously to NiTPP, higher K doses have been modeled by bonding two K atoms to CoTPP. Even though once again, LS (one unpaired electron) and HS (three unpaired electrons) states are possible, the LS one is always more stable than HS by 0.7 eV. Similarly to 2K-NiTPP, two different stable structures (see Figure 3.42) are obtained for LS; moreover, the B arrangement is more stable than the A one by 0.30 eV (see Table 3.6). Incidentally, the presence of two K atoms induces

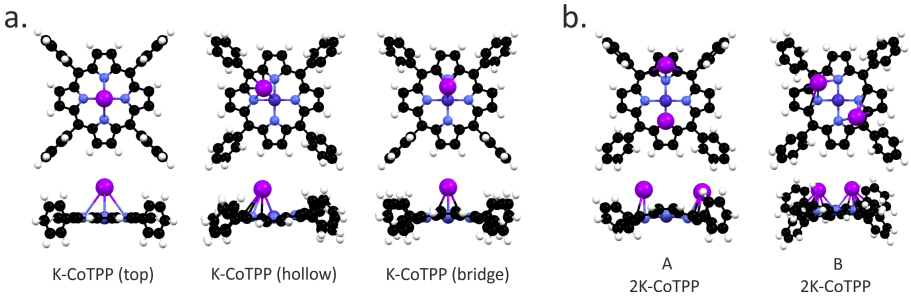

Figure 3.42: A schematic representation of the different K adsorption geometries calculated for the K-CoTPP (a) and 2K-CoTPP (b) complexes. Black, white, blue, light blue, and violet spheres represent C, H, N, Co, and K, respectively.

Table 3.6: Adsorption site-dependent DFT calculation for the K-CoTPP and 2K-CoTPP complexes. K-CoTPP and 2K-CoTPP adsorption energies (E_{ads}), relative adsorption energies (ΔE_{ads}) with respect to the most favorable (hollow and B) ones, number of unpaired electrons on the cobalt ion, nominal Co oxidation state, NM indexes for the Co-N and Co-K bond are reported.

	ΔE_{ads} eV	E_{ads} eV	Co unpaired el.	Co ox. state	$^{NM}I_{Co-N}$ avg	$^{NM}I_{Co-K}$
K-CoTPP (top)	0.11	-1.76	0.36	Co(I) d^8	0.659	0.253
K-CoTPP (hollow)	0.00	-1.87	0.42	Co(I) d^8	0.662	0.191
K-CoTPP (bridge)	0.05	-1.82	0.40	Co(I) d^8	0.662	0.210
A - 2K-CoTPP	0.30	-2.59	0.39	Co(I) d^8	0.644	0.142
B - 2K-CoTPP	0.00	-2.88	0.37	Co(I) d^8	0.636	0.158

significant structural perturbations both in A and B arrangements, but does not affect the Co(I) oxidation state. As such, the A and B spin population analysis indicates that, consistently with a Co(I) $3d^8$ configuration, Co has 0.39 unpaired electrons in A and 0.37 in B. Such a result clearly states that the two electrons transferred from K to CoTPP in 2K–CoTPP are used for inducing the Co(II) $\rightarrow$ Co(I) reduction and the partial occupation of a low-lying TPP-based empty MO. Differently from NiTPP, no stable structure with two K atoms and Co(II) is found.

DFT outcomes agree well with the experimental evidence. In particular, time-dependent Co $2p_{3/2}$ spectra on a freshly prepared K-doped CoTPP layer demonstrate, differently to NiTPP, the Co(I) high stability not only at room temperature, but also when annealed up to 500 K (see Figure 3.43). The charge donation from K atoms in both the CoTPP conformations stabilizes the chelated ion in the Co(I) oxidation state. Moreover, the time-dependent NEXAFS spectra measured at N K-edge, in particular the linear dichroic spectral behavior, show a strong distortion of the TPP macrocycle already in the as-deposited configuration and no significant time-dependent change is observed.

It has been demonstrated here that alkaline doping can be efficiently used for stabilizing desirable spin configurations in MTPP arrays supported by an inert substrate. However, the conformation changes of the organic system are of fundamental importance in defining charge distribution with both macrocycle and chelated metal ion.

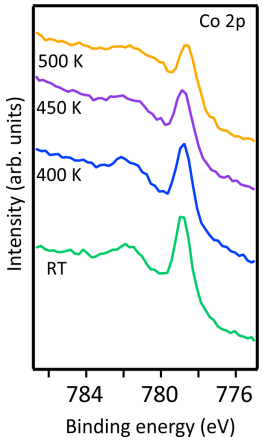

Figure 3.43: Co $2p_{3/2}$ core level of CoTPP/Au(111) after exposure to K for 15 minutes at room temperature (green curve) and for increasing annealing temperatures.

Chapter 4

The role of molecular conformation: temperature-induced planarization

In addition to the conformation adaptation that molecules spontaneously undergo on the surface, as discussed in the previous chapter, changes can also be induced by external *stimuli*. For example, well-known are the cyclodehydrogenation reactions that both octaethylporphyrins and tetraphenylporphyrins can undergo. Such reactions can be thermally activated and, for both classes of porphyrins mentioned here, lead to planarization of the molecule. The cyclodehydrogenation process consists of two steps, dehydrogenation of the peripheral substituents followed by cyclization, which implies a ring-closure reaction forcing the molecule into a planar structure. The modifications induced by these surface-assisted reactions can lead to major changes in the molecular properties. Next, such reactions will be induced on both less and more reactive substrates, Ag(100) and Cu(100), for both OEPs and TPPs. Having in mind the special properties exhibited by both OEPs and TPPs on copper, after inducing the ring-closure reaction, the reactivity towards further spin manipulation of the new planar system will be tested by exposing them to NO_2. The strong reactivity observed in the case of the pristine systems is not preserved upon planarization.

4.1 On-silver temperature-induced planarization

4.1.1 CoOEP annealing on Ag(100)

Surface-assisted chemistry is a promising way to create and modify organic systems suitable for functional materials in electronics. To date, STM is often used to follow thermally-induced on-surface reactions in molecular systems. While providing an excellent insight into the molecular backbone structural changes in planar molecules, STM is less conclusive in the case of molecules with peripheral ligands, which may induce collateral changes in the STM image. For such cases, here we show that photoemission tomography is an alternative efficient tool to directly probe on-surface reactions in molecular arrays. The photoemission tomography potential is tested with a cobalt octaethylporphyrin temperature-induced dehydrogenation reaction on Ag(100), which leads to the final product cobalt tetrabenzoporphyrin. Along with the ring-closure reaction, the changes in the electronic occupancy and energy level alignment of frontier orbitals and the

oxidation state of the metal ion in both molecular arrays are here elucidated.

Upon anchoring to a solid substrate, molecules can adapt their structural conformation to the local environment, deforming the macrocycle and/or reorienting the substituents (see Section 3.5)). Thereby, the peripheral ethyl groups of the adsorbed OEP molecule can point away from and towards to the substrate, allowing the metal ions in M-OEP to be closer to or farther from the metal substrate, respectively. Together with the surface-driven conformational changes, the porphyrin molecules may undergo on-surface temperature-induced chemical changes of their molecular structure [35,171,226–228]. A well-known surface-assisted ring-closure reaction in the case of metal-OEP involves the peripheral ethyl groups and results in the transformation of OEP into tetrabenzoporphyrin (TBP), which occurs via the dehydrogenation of two neighboring ethyl groups, followed by the formation of six-membered carbon rings (see Fig. 4.1) [227,229,230].

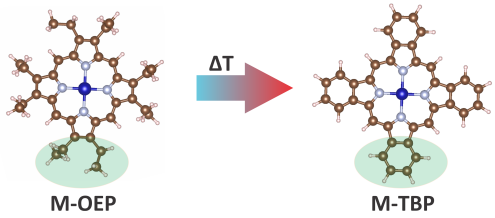

Figure 4.1: Schematic representation of the thermally-activated transformation from M-OEP to M-TBP.

The kinetics of the ring-closure reaction depends on the chemistry of the central ion and of the metal substrate [12]. This on-surface reaction can deeply alter the intriguing properties of the porphyrin array. For instance, a substantial increase in the effective spin moment has been reported in the case of iron(II)-TBP formed upon on-surface reaction on Au(111) from iron(II)-OEP [227]. In contrast to this system, CoOEP on Cu(100) has shown a sizable magnetic moment, while CoTBP displayed a quenched moment on this substrate [226]. Notably, the manipulation of the magnetic anisotropy in metal porphyrin molecules induced by ring-closure reactions is a key issue for the development of molecular-based spintronic devices. On silver, the M-OEP interaction with the surface leads to an electron charge transfer from the metal substrate to the molecule [12,231]. As a consequence, in the case of CoOEP deposited on silver, NEXAFS and UPS suggested the hybridization between the Co *d*-states and the Ag *sp*-band, resulting in a modification of the valence states of the adsorbed molecule with respect to the free OEP molecule [231,232]. In particular, the new state appearing at 0.65 eV below Fermi, in the monolayer phase of CoTPP on Ag(110) [232], CoOEP on Ag(111) [231], as well as FeTPP on Ag(111) [36], was unanimously assigned to the filling of the metal d_{z^2} unoccupied molecular orbital.

In the past, the PT approach [99] has already been employed to study the geometry and the electronic structure of the macrocycle in self-assembled porphyrin and its derivatives [100,161,233]. Additionally, this experimental method has been applied to study the pathway of thermally-activated on-surface intermolecular reactions [234]. But, could the PT approach also be extended to the study of surface-induced intramolecular modifications in single molecules self-assembled in molecular arrays? For instance, in the study of intramolecular temperature-induced reactions observed in metal porphyrin arrays where new irreversible covalent bonds are formed within the molecule. In the past, these reactions have been monitored by STM, temperature-programmed desorption (TPD), XPS and NEXAFS techniques [35,160,171,226–228,235], which do not always

allow the authoritative identification of an adsorbed species. For example, it is often difficult to identify the degree of (de)hydrogenation of a given molecule, as hydrogen is difficult to trace by surface sensitive techniques. Only indirect conclusions can be made from, *e.g.*, the presence or absence of specific vibrational modes in infrared spectroscopy or chemical shifts in core-level spectroscopy. Often, these data are ambiguous and leave room for alternative interpretations. Instead, while providing an excellent insight into the molecular backbone structure, STM is less conclusive about the molecular periphery, where adsorbates tend to react with the substrate, and the geometrical and chemical changes observed are convoluted with the substrate electron density changes [161]. In the present section, the possible on-surface chemical modification of CoOEP molecules assembled on a metal substrate is followed by PT and supported by DFT calculations. The reaction is activated by annealing the CoOEP/Ag(100) interface up to 600 K. The annealing treatment may result in the transformation from CoOEP to CoTBP via the dehydrogenation of the ethyl groups in the pristine porphyrin molecules, followed by the formation of six-membered carbon rings. The imaging of molecular orbitals in the reciprocal space, being extremely sensitive to the chemical structure, allows us to directly probe the ring-closure reaction (CoOEP $\rightarrow$ CoTBP) on the Ag(100) surface. We unequivocally determined the electronic occupancy and energy level alignment of the molecular frontier orbitals, *i.e.* the highest occupied (HOMOs) and lowest unoccupied molecular orbitals (LUMOs) of the as-deposited CoOEP array and the CoTBP adlayer formed by the on-surface reaction. Moreover, the reaction has been confirmed by x-ray photoemission spectroscopy and NEXAFS measured at the N K-edge. For both CoOEP and CoTBP molecular assemblies, the charge transfer at the organic/metal interface induces the reduction of the cobalt ion in the metal-organic arrays, as verified by Co *2p* core-level and Co L_3–edge NEXAFS measurements.

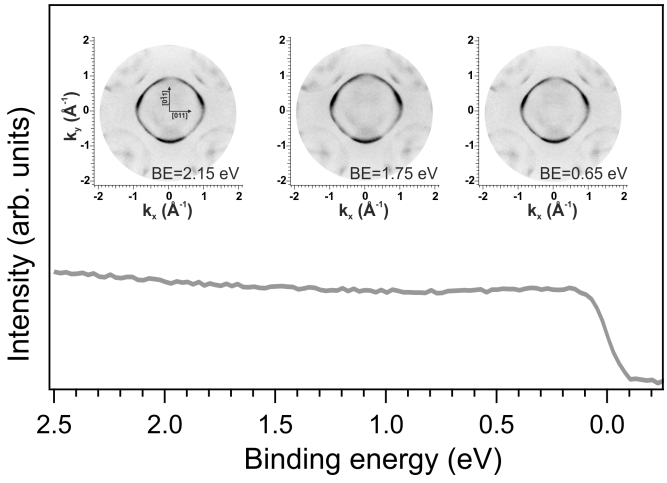

Figure 4.2: Angle-integrated valence band spectrum and momentum maps taken at the BE corresponding to the molecular features reported in Figure 4.3 of the clean Ag(100) substrate. The substrate orientation is indicated by the arrows.

Figure 4.3 presents the angle-integrated valence band spectra of pristine and annealed CoOEP/Ag(100) interfaces. While the valence band spectrum of the bare Ag(100) substrate

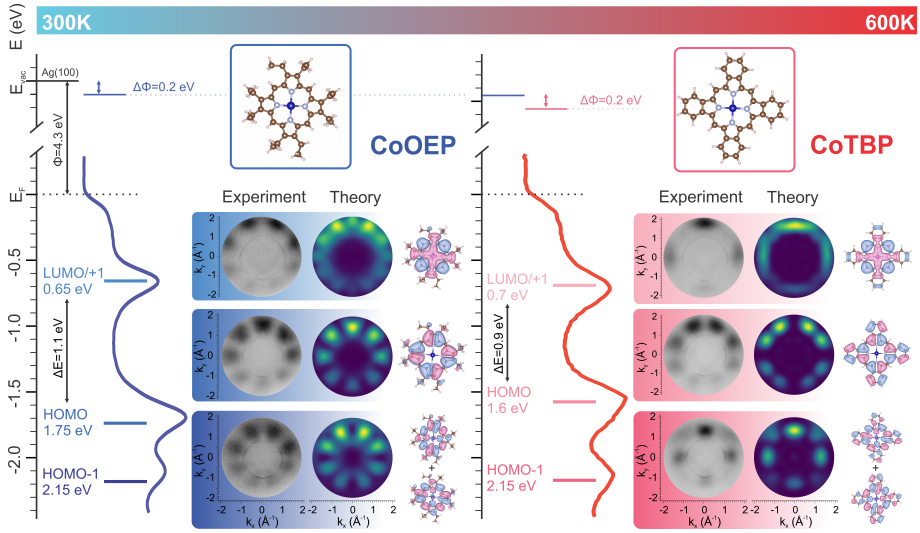

Figure 4.3: Angle-integrated valence band spectra and schematic energy diagrams of electronic levels of the CoOEP/Ag(100) and CoTBP/Ag(100) interfaces. Molecular orbitals of CoOEP and CoTBP, and corresponding experimental and theoretical momentum maps at the indicated BE, are shown.

has a rather featureless plateau associated with the *sp*-bands (see Figure 4.2), three prominent features can be recognized for the organic/metal interfaces, both before and after annealing. In particular, the feature peaked at higher binding energy (E_B = 2.15 eV) is present for both pristine and annealed samples, while the two low energy peaks undergo only minor changes in the energy position. While those energy shifts cannot reveal the nature of the chemical modifications, clear differences are observed in the measured momentum maps. To identify the origin of the features observed in the UPS spectra and test the possible CoOEP $\rightarrow$ CoTBP on-surface reaction, the experimental maps have been compared to the square modulus of the Fourier transform of the real space molecular orbitals, calculated for gas-phase CoOEP and CoTBP molecules. In that way, the features observed for the CoOEP/Ag(100) system can be unequivocally assigned to the molecular states simulated for the gas-phase CoOEP, where the states centered at BE 2.15 eV, 1.75 eV and 0.65 eV are due to the HOMO-1, HOMO and the degenerate LUMO/LUMO+1, respectively. No match for the annealed interface can be found between the measured maps and the CoOEP calculated maps, while the momentum maps simulated for CoTBP match very well the three measured patterns at 2.15 eV, 1.60 eV and 0.70 eV for the annealed interface, which according to the present calculation can be assigned to the HOMO-1, HOMO and LUMO/LUMO+1 molecular states of CoTBP, respectively. The excellent agreement between the measured and simulated maps using the PT approach is a direct proof that the annealing at 600 K on Ag(100) induces the chemical modification of CoOEP and leads to the formation of the tetrabenzoporphyrin array. The CoOEP $\rightarrow$ CoTBP transition in the molecular network upon annealing is also confirmed by XPS and NEXAFS measurements reported in Figure 4.4, where a clear chemical shift of the feature associated to the ethyl groups of pristine CoOEP is observed in the C *1s* spectra after the annealing treatment.

Indeed, in the C *1s* core level spectra reported on Figure 4.4 it is clearly visible that the feature at low binding energy (BE) of as-deposited CoOEP molecules at 284.1 eV, which is mainly associated with the ethyl groups, is shifted to higher BE upon formation of the six-membered carbon rings in CoTBP. The other features in the C *1s* spectrum of CoTBP on Ag(100) substrate undergo a shift to lower BE, consistent with the change in the work function (-0.2 eV). Complementary information of the molecular structural changes and formation of new bonds can be obtained by performing NEXAFS measurements. The sensitivity of NEXAFS transitions to the chemical nature and environment of the atoms present in a material provides a unique method to probe the molecular structure. In addition, NEXAFS can reveal molecular orientation and order by probing element-specific electronic transitions of core-level electrons to unoccupied molecular orbitals. The N K-edge spectra of as-deposited CoOEP onto Ag(100) surface and after annealing of the sample to the high temperature are reported in the right panel of Figure 4.4.

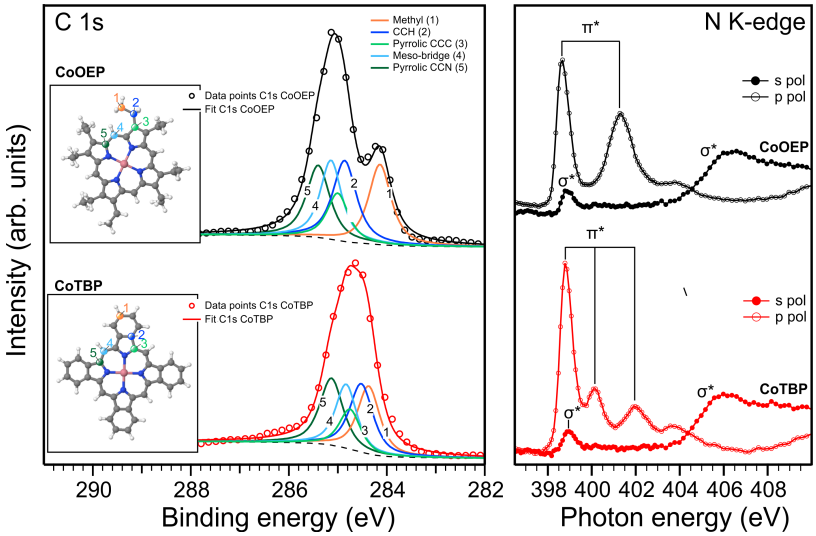

Figure 4.4: C *1s* XPS spectra and N K-edge NEXAFS of CoOEP and CoTBP on Ag(100).

The overall differences in the line shape and energy position of the observed resonances in the NEXAFS spectra measured in p-polarization across the N K-edge before and after the annealing process supports the changes in bonding environment in the adsorbed molecules. In particular, while the low energy peak at 398.8 eV display almost no change, the second main peak of the π^* orbital region in CoOEP, at $\sim$ 401.4 eV, is splitted after annealing in two features peaked at 400.15 and 402.0 eV photon energy. This spectral changes are a fingerprint of the on-surface ring-closure reaction, meaning that CoOEP transforms to CoTBP [99, 100]. Notably, both new resonances observed at higher photon energy for CoTBP maintain the π^*-symmetry character. As a rule of thumb, the N *1s* ionization threshold separates the region of π^*-symmetry resonance from that of σ^*-symmetry ones. Accordingly, the observed linear dichroism points to an adsorption orientation of the porphyrin macrocycle parallel or almost parallel to the surface in both CoOEP and CoTBP arrays supported by the Ag(100) substrate. Moreover, the low energy features in the N K-edge spectra measured in s-polarization at 399.0 eV observed for both CoOEP and CoTBP molecules

are associated with the transition from N *1s* to a mixed ligands $2p_{x,y}$- Co$3d_{x^2-y^2}$ orbital with σ^* symmetry [233].

For both systems, the HOMO-LUMO gaps are significantly lower than the calculated ones when deposited on the surface, from 3.0 eV to 1.1 eV (CoOEP) and from 2.5 eV to 0.9 eV (CoTBP), suggesting a strong molecule-surface interaction at both interfaces. Furthermore, the presence of the LUMOs for both the organic systems confirms the charge transfer effect for both metalorganic/Ag(100) systems. The occupation of the former π^* gas-phase LUMOs, delocalized over the entire molecular macrocycle, has been previously observed for metal porphyrin and phthalocyanine molecules on metal surfaces [100, 152, 161]. After the proof of the CoOEP $\rightarrow$ CoTBP on-surface reaction by PT, in the next section we shed light on the energy level alignment of CoOEP and CoTBP molecules assembled on Ag(100).

The adsorbate–induced work function changes of CoOEP and CoTBP are extracted from the shift of the secondary electron cut-offs. All changes are referred to the value for the bare Ag(100) work function (4.3 eV). Upon the adsorption of CoOEP, the WF of the metal substrate decreases by 0.2 eV, and it further decreases to 3.9 eV after the formation of CoTBP. The reduction of the WF of the metal substrate by adsorption of organic molecules has been frequently observed in the past and has been attributed to the push-back of electron spilling out from the metal substrate (Pauli repulsion) [236], which is partially compensated by a dipole of an opposite sign created by the charge transfer to the adsorbed molecule [100]. With the entire set of experimental data, we can now draw the energy level alignment picture for CoOEP and CoTBP molecular arrays on Ag(100) substrate (see Fig. 4.3). In the next step, the possible contribution of the atomic like d_{z^2} orbital to the lowest-in-energy peak (BE = 0.65 eV) in the valence band of CoOEP/Ag(100), discussed in previous works [231, 232], has been evaluated here. DFT simulations show that it is the molecular orbital LUMO+2 that has a strong atomic-like d_{z^2} character. Following the same procedure as for the molecular patterns reported in Fig. 4.3, we simulated the map for LUMO+2, shown in Fig. 4.5. Clearly, the present simulated pattern does not resemble the corresponding experimental map measured at BE 0.65 eV reported on Fig. 4.3, and, therefore, we can exclude the main contribution from the d_{z^2} state (LUMO+2) to the corresponding valence band feature, contrary to the expectation from previous reports for Co and Fe porphyrins on silver [36, 231, 232].

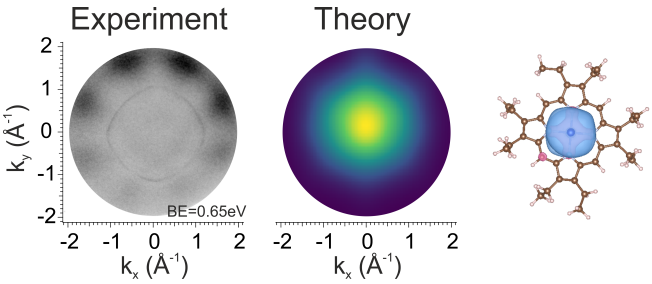

Figure 4.5: Comparison between the experimental feature peaked at 0.65 eV in BE and the charge plots of the atomic like d_{z^2} state (LUMO+2) and its corresponding FT.

The ring-closure reaction in the porphyrin array observed in the PT data can alter the oxidation state of the Co ion in the adsorbed CoOEP and CoTBP molecules and, as a consequence, modify the magnetic properties in the organic array. To investigate the Co oxidation state, we performed

XPS measurements of the Co $2p_{3/2}$ core-level, together with NEXAFS experiments at the Co L_3-edge.

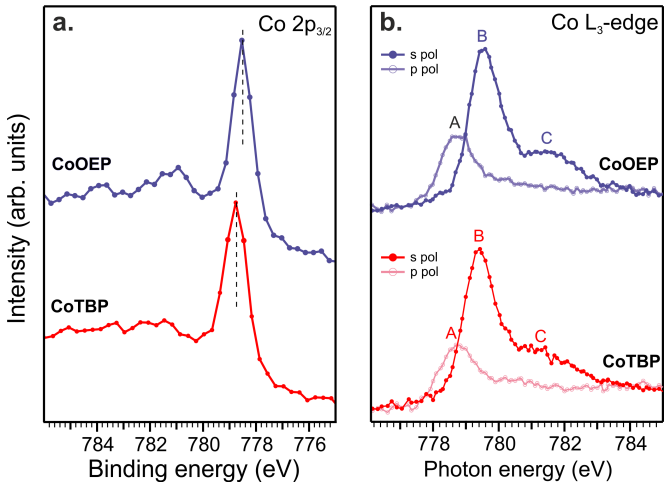

Figure 4.6: Co $2p_{3/2}$ and Co L_3-edge spectra of CoOEP and CoTBP on Ag(100)

In Figure 4.6, we compare the Co $2p_{3/2}$ core-level spectra of CoOEP and CoTBP adsorbed on the Ag(100) substrate. The XPS spectrum of CoOEP shows a main line peaked at 778.8 eV and a broad satellite at higher BE (with the maximum at 780.9 eV). Compared to the CoOEP multilayer phase reported in Ref. [231], we observe a significant shift of the Co $2p_{3/2}$ signal (-1.8 eV), as well as a notable change in the satellite features. This finding can be attributed to the reduction of the metal ion in the CoOEP monolayer phase [231] caused by strong charge transfer at the organic-metal interface, as observed in the UPS measurement reported in Figure 4.3. After annealing, the Co $2p$ spectrum of CoTBP shows the same spectral shape of the pristine layer, but a small energy shift ($\sim$ 0.2 eV) of the main peak to lower BE. This shift most likely reflects a shorter average distance between the Co ion and the metal substrate in case of CoTBP, which results in a more efficient screening of the core-level electrons. To get direct access to the oxidation state of the Co ion, we acquired the Co L_3-edge absorption spectra for both CoOEP and CoTBP (see Fig. 4.6b). and compared the results with the published NEXAFS and XMCD measurements reported by Arruda *et al.* [226] for CoOEP and CoTBP on copper. The NEXAFS spectra in Figure 4.6b show a similar shape and energy position of the resonances for both CoOEP and CoTBP, suggesting a similarity in the electronic structure, as well as in the oxidation and spin states of the Co ion in the two different metallorganic arrays. The NEXAFS spectra measured with s- and p-polarized light across the Co L_3-edge display a significant difference in the energy position of the resonances. While in the spectra measured in s-polarisation the main feature is peaked up at 779.5 eV (peak A), the spectra recorded with p-polarization show a peak at lower photon energy (778.7 eV, peak B). Both spectra show a pronounced shoulder (peak C) at higher photon energies (see Fig. 4.6b). The observed linear dichroism for the low energy feature in the Co L_3-edge spectra points to an out-of-plane component, which can be associated with the d_{z^2} orbital [226]. The full occupation of the d_{z^2} orbital would be reflected in the experimental data by the absence of the low energy feature in the absorption spectra. Notably, the full filling of this orbital in similar molecular compounds

on copper surfaces was responsible for the quenching of the spin moment, as evident from XMCD data [226]. On the contrary, the Co L_3-edge spectra of CoOEP and CoTBP on Ag(100) are similar to the published spectra of CoOEP on Cu(100) [226]. Following the XMCD measurement and theoretical calculation reported in Ref. [226], and the XPS and NEXAFS measurement showed here, we propose that the charge transfer at the organic/metal interface stabilizes the cobalt ion in CoOEP and CoTBP on Ag(100) in a non-integer valence state, with a formal oxidation state between +1 and +2.

In conclusion, PT is an efficient tool to probe on-surface reactions in self-assembled molecular arrays. This has been proved on the temperature-induced CoOEP → CoTBP transformation on Ag(100), which goes through the dehydrogenation of two neighboring ethyl groups in CoOEP followed by the formation of six-membered carbon ring. Combining different surface science techniques, accompanied by ab-initio DFT calculations, we show that the electronic structure and the energy alignment in both CoOEP and CoTBP arrays are very similar. In particular, the strong interaction of both organic molecules with the silver substrate at the interface causes charge transfer from the substrate to the molecule, as clearly identified by the PT method, resulting in the occupation of the gas-phase LUMO/+1 delocalized over the entire molecular macrocycle. Furthermore, the strong interaction at the metal-organic interface is also responsible for the reduction of the cobalt ion in both CoOEP and CoTBP to an oxidation state between +1 and +2, as found from Co L_3-edge NEXAFS measurements.

4.1.2 CoTPP and NiTPP annealing on Ag(100)

Not only octaethylporphyrins, but also tetraphenyl porphyrins can undergo on-surface dehydrogenation reaction. For both H_2TPP and MTPPs, annealing the intact monolayer above 550 K results in dehydrogenation of the *meso*-phenyl and pyrrole groups and subsequent C–C bond formation between the two [35,36,171,235,237]. This intramolecular rehybridization forces both the phenyls and the pyrroles to be co-planar with the porphyrin core, flattening the molecule. In earlier studies of this process, two types of dehydrogenation products were postulated, each with a different symmetry. One dehydrogenated TPP exhibits C_{4h} symmetry, often referred to as *spiral*, and involves one phenyl bonding to an adjacent pyrrole with two phenyls bonded to the same pyrrole, as shown in Figure 4.7. The spiral molecule exhibits clockwise C–C bonding between phenyls and pyrroles. The chiral counterpart of this molecule (*i.e.* counterclockwise C–C bonding) was also observed. The other exhibits D_{2h} symmetry, often referred to as *rectangle*, and involves two adjacent phenyls bonding to the same pyrrole, leaving two pyrroles devoid of phenyl bonding, as shown in Figure 4.7 [35]. In *hybrid 1*, the two leftmost phenyls bond to the same pyrrole, similarly to the rectangle molecule, whereas the two rightmost pyrroles bond clockwise to adjacent pyrroles, similarly to the clockwise spiral. In *hybrid 2*, the leftmost phenyls share the same characteristics as rectangle and hybrid 1; however, on the right side, one phenyl bonds to a counterclockwise pyrrole, whereas the other phenyl bonds to a clockwise pyrrole. It has been previously reported that the twofold symmetry of the H_2TPP's core, imposed by the two central hydrogens, drives the selectivity of a reaction at the periphery of the molecule towards a distinct product, namely the rectangular form. Such selectivity could not be observed when triggering the same ring-closing reaction in RuTPP or CoTPP species, where macrocycle core has a fourfold symmetry. Indeed, for RuTPP, species B and C amount to slightly more than 30% each and species A and D to less than 20% each. On the contrary, the reaction is very selective for H_2TPP, where

86% of the PPDs appear as species A, only 12% as species B and less than 3% as C or D.

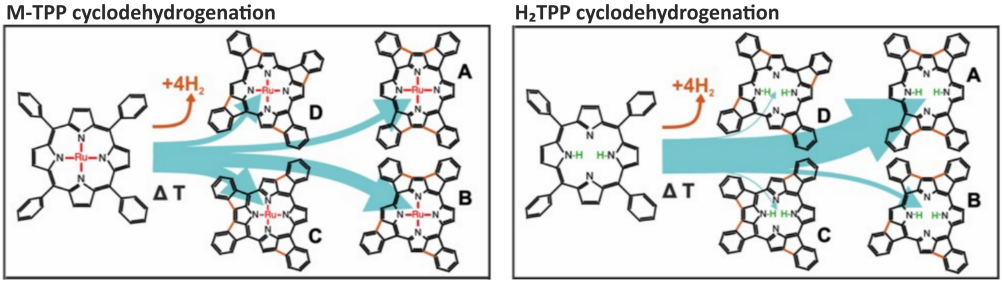

Figure 4.7: Schematic representation of the cyclodehydrogenation reaction which TPP can take part of. The possible products formed during post annealing are shown.

Having in mind the stereo-selectivity of the dehydrogenation reaction in the case of the metal-free TPP, in order to facilitate the discussion on the cyclodehydrogenation products of CoTPP on Ag(100), we will follow first the annealing of H_2TPP on Ag(100). The valence band spectrum of the as deposited H_2TPP on Ag(100) substrate manifests two main features at BEs of 2.05 eV and 2.40 eV. Similar to the case of CoTPP (see Section 3.5), we apply the PT approach to clarify the origin of these features. The measured momentum maps are compared with the square modulus of the FT of the real space MOs of H_2TPP provided by DFT calculation (Fig. 4.8). Based on the comparison and good match between the experimental and theoretical data, the features at 2.05 eV and 2.35 eV BE are assigned to the emissions from HOMO and the HOMO-1, respectively. While HOMO and HOMO-1 are quite close in energy for the gas-phase H_2TPP and CoTPP, this energy gap gets larger in the adsorbed molecules. We interpret this as a surface-induced change in the energy level alignment of the adsorbed molecular species. Moreover, upon adsorption, the frontier orbitals, *i.e.* HOMOs and HOMO-1 spread over a wide energy range [100], causing additional weak features in the valence band spectra on the molecular interfaces. The clear weak shoulder at 1.55 eV BE in the H_2TPP/Ag(100) interface is associated with such interface's phenomenon. The experimental pattern, in addition to the features originating from the molecular states, also contains sharp *sp*-band contributions from the silver surface, and this can be used to determine the rotation angle in the adsorbed molecular species with respect to the high-symmetry crystal axis. The data reveals that the H_2TPP molecules are perfectly aligned along the $[1\bar{1}0]$ high symmetry direction of the silver substrate.

Interestingly, the valence band spectra measured on the H_2TPP/Ag(100) interface shows the absence of the LUMOs features, similar to the saddle-shape conformation of CoTPP. Moreover, it has been reported that the deformation of the ring is much stronger for the MTPPs than for the free-base H_2TPP due to the higher intramolecular strain induced from the coordinated metal ion in the porphyrin core [173, 238]. In comparison with CoTPP on Ag(100), where the porphyrin's macrocycle experiences charge donation from the silver substrate in the planar conformational form of CoTPP, this phenomenon is not observed for metal-free H_2TPP as well as for the saddle-shaped CoTPP self-assembled on Ag(100). This evidence suggests that the central cobalt atom plays a minor role in the charge transfer between Ag(100) substrate and the porphyrin's macrocycle in its distorted form, while the planarization of the porphyrin's macrocycle can be a key issue in the observed charge transfer phenomenon. The role of the planarity of the porphyrin's macrocycle

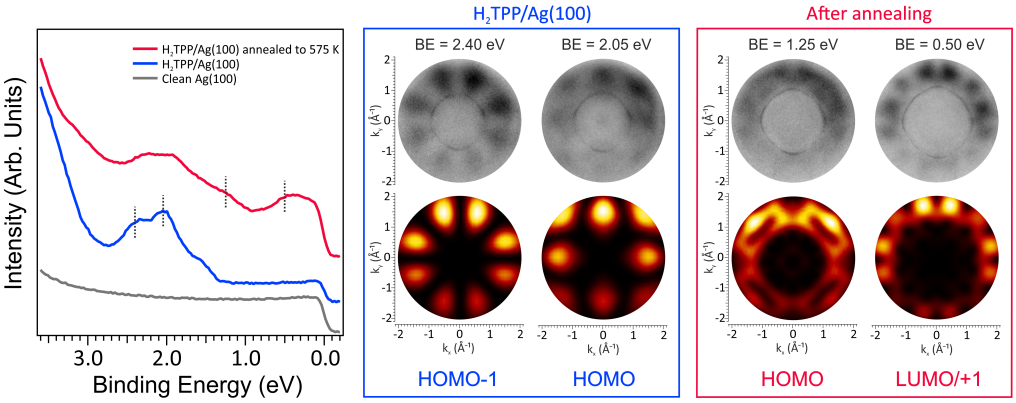

Figure 4.8: The valence band spectra and molecular maps of the as-deposited H_2TPP monolayer on Ag(100) surface and after annealing at 575 K.

in charge donation from the silver substrate, will be, in the next step, elucidated after inducing the planarization in both H_2TPP and CoTPP by the on-surface ring-closure reaction.

After annealing the H_2TPP/Ag(100) system to 575 K, a new peak located at Fermi appears in the angle-integrated valence band spectrum. By applying the PT approach, while having in mind that the dehydrogenation reaction is very selective in the case of H_2TPP, where the rectangular form is dominant, the peak at Fermi can be assigned to the degenerate LUMO/+1 levels of the rectangular species. In order to confirm the assignment, the PT approach has been applied also to the following-in-energy peak, which matches well with the HOMO of the rectangular form, confirming that the molecular products formed by the on-surface reaction are experiencing charge donation from the metal substrate to the porphyrin's macrocycle after planarization, which leads to the occupation of the LUMO level. The azimuthal angle derived for the rectangular dehydrogenation product of H_2TPP from the simulations is $\pm$ 15° with respect to the [1$\bar{1}$0] high symmetry direction of the silver substrate.

Upon annealing the CoTPP/Ag(100) interface to 575 K, cyclodehydrogenation can be induced also for the metal-porphyrin. The valence spectrum acquired at the interface after annealing (see Figure 4.9) suggests that the cyclodehydrogenation reaction has occurred; moreover, the similarity between momentum maps acquired in the vicinity of the Fermi, at BE 0.15 and 0.6 eV, and those observed after annealing of H_2TPP suggests they may be attributed to the LUMO of the dehydrogenated species. However, considering the coexistence of the four species in equal percentage and the very small differences in LUMO distribution and position in energy, it is difficult to define which species contributes to each peak. We have to also note the different intensity ratio in the LUMO features in the spectra measured for H_2TPP and CoTPP. This difference can be associated with the different occurrence of the four reaction products upon annealing in both molecules. As already mentioned, the reaction is very selective in the case of H_2TPP, where the rectangular dehydrogenation product is dominant, while for CoTPP the amount of the four products are almost equally distributed on the surface [239].

In order to follow in more detail the ring-closure reaction in the CoTPP/Ag(100) system, constant-current STM images have been acquired after annealing the interface to 575 K. The resulting data are shown in Figure 4.10.

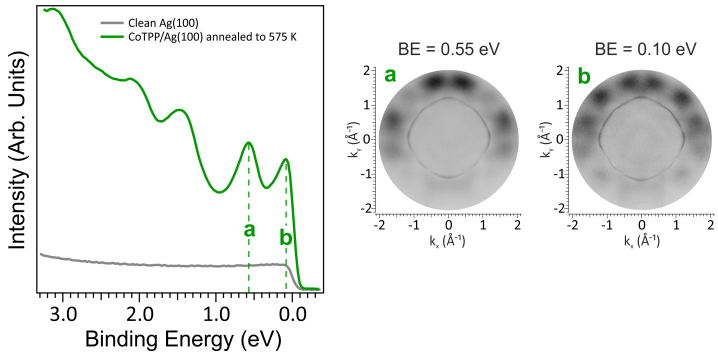

Figure 4.9: The valence band spectra and molecular maps of the CoTPP monolayer on Ag(100) surface after annealing at 575 K.

The result confirms that the annealing process flattens the CoTPP molecules by inducing the dehydrogenation followed by the surface-assisted reaction, giving rise to the four planar porphyrin (PP) species expected to form after metal-TPP cyclodehydrogenation, namely rectangular (A), spiral (B) hybrid 1 (C) and hybrid 2 (D). The chemical structures and appearances of the four PP products are determined by analogy to similar PP species synthesized on different metal surfaces [201]. Moreover, annealing at temperatures below 575 K allows us to observe various partially flattened intermediates in which one, two, or three phenyl units remain unreacted and show different brightness in the STM images. Similar behaviour has been previously observed for the H_2TPP and RuTPP deposited on Ag(111) substrate [239].

By exploiting STS (see Figure 4.11), it is possible to directly probe the electronic structure of the four distinct PP products here identified. While for A, B, and D PP species STS reveals a resonance close to the Fermi level located around 0.3 eV, for C (hybride 1) PP product this resonance is shifted to higher energy ($\sim$0.6 eV). On the other hand, the second strong peak in the STS spectra of the two hybrid forms, C and D, is situated at 1.5 eV; in contrast, the corresponding feature for the A and B forms, namely spiral and rectangular, appears at 2.0 eV (see Figure 4.11).

The occurrence of a LUMO peak in all the PP spectra strongly suggests that the molecular products formed by the on-surface reaction are experiencing charge donation from the metal substrate to the porphyrin's macrocycle for both flattened H_2TPP and CoTPP. These experimental evidences prove that the planarity of the macrocycle in both metal-free and metal TPP is a key factor in the observed charge transfer from the silver to the porphyrin's macrocycle, while the distortion of the macrocycle of TPP, *i.e.*, forming a saddle-shape conformation, quenches this phenomenon at the interface (see section 3.5)).

To monitor the ring closure reaction upon annealing of CoTPP on Ag(100) on a larger scale, NEXAFS spectra at the C and N K-edges were acquired. The occurrence of temperature-induced on-surface planarization of the TPP molecules can be unambiguously demonstrated by absorption spectra measured across the C K-edge region. The fingerprint of the ring closure reaction is, indeed, a change of the linear dichroism in the spectral feature at 285.05 eV associated with the π^* resonance of phenyl moieties in the TPP molecules. The C K-edges of pristine and up to 575 K annealed CoTPP/Ag(100) interface are shown in Figure 4.12.

While before annealing the average phenyl tilt-off angle was calculated to be $\sim$52°(see Section

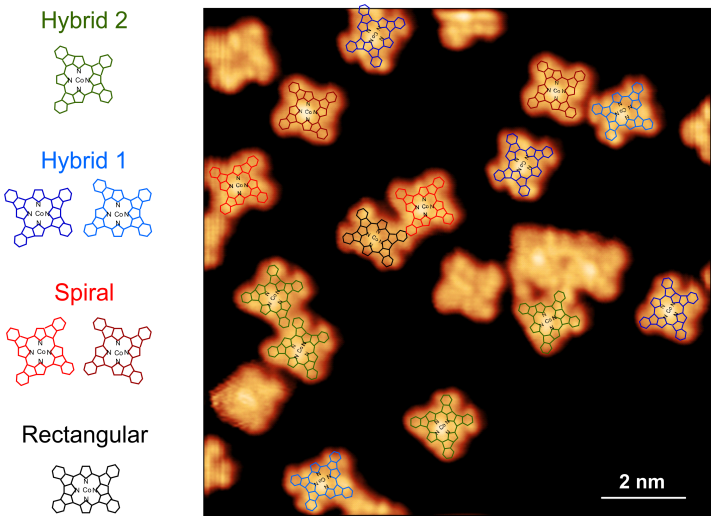

Figure 4.10: STM image of the CoTPP/Ag(100) interface after annealing. Images acquired at 77 K, tunneling parameters: U = -1.0 V, I = 0.5 nA.

3.5), after the annealing of the organic-metal interface, the dichroic behaviour in the spectra is drastically changing, *i.e.*, the π* resonances are now dominant only in the spectrum measured in p-polarization. This trend fully supports the temperature-induced planarization process in the adsorbed molecular species. Moreover, the differences in the energy position of the features in the C K-edge NEXAFS spectra, acquired before and after the annealing treatment, support the changes induced by the on-surface reaction on the bonding environment of the carbon atoms in the adsorbed molecules. In particular, while the low energy peak at 284.20 eV, associated with the macrocycle moiety, display almost no change, the higher energy peaks of the π* orbital region in CoTPP, located at 285.05, 287.30, and 288.70 eV, respectively, experience a change both in the relative intensities and in the energy positions after the annealing process. In agreement with the NEXAFS data, the C *1s* core-level spectra reported in the inset confirm the on-surface transformation of CoTPP upon annealing. Indeed, the feature at 284.45 eV binding energy of the as-deposited CoTPP molecules, which is mainly associated with the phenyl carbon atoms, is shifted by $\sim$0.5 eV to lower BE after heating the interface to 575 K. The chemical shift in the C *1s* spectrum is associated with chemical changes in the adsorbed molecules.

Planarization-induced changes are also observed in the N K-edge NEXAFS spectra. Indeed, the decrease in intensity of the π* resonance located at 398.5 eV in photon energy points towards an increasing charge transfer from the silver substrate to the molecular macrocycle, in agreement with the VB and STS results discussed previously.

As the ring-closure reaction could also alter the properties of the chelated metal ion in the adsorbed molecule and, as a consequence, modify the magnetic properties in the organic array, in order to investigate the possible changes in the Co oxidation state induced by annealing, we have performed XPS measurements at the Co $2p_{3/2}$ core-level and NEXAFS at the Co L_3-edge .

In Figure 4.13, the Co $2p_{3/2}$ core-level spectra of CoTPP self-assembled on the Ag(100) substrate and Co-PP molecules formed by on surface reaction upon high-temperature annealing are shown.

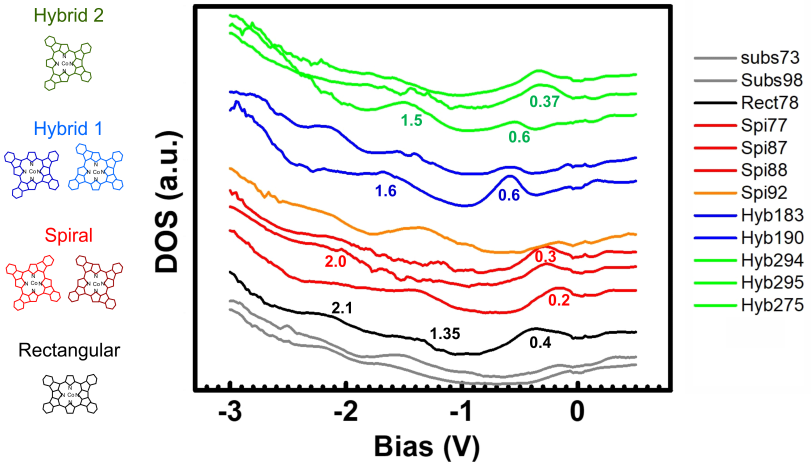

Figure 4.11: STS spectra of the dehydrogenation products formed after annealing at 575 K the CoTPP/Ag(100) system. The product on which the spectra were acquired are indicated with the same curve color. Setting parameters for STS: I_t = 0.5 nA.

The spectral shape and energy position of the main peak remains unaltered after the annealing of CoTPP. This evidence suggests that cobalt chelated ions in CoTPP deposited on the surface and its derivative molecules chemically modified by the on-surface reaction are stabilized in the same oxidation state, namely Co(I) state.

However, changes in the intensity of the spectrum acquired with s-polarized light can be observed in the spectrum of the CoTPP/Ag(100) after annealing to 575 K, suggesting that planarization in CoTPP induces changes in the in-plane delocalization of the Co *3d* electrons. The decreasing intensity suggests the presence of a stronger σ back-bonding donation from the ligand to the central metal, due to a more efficient overlap of the metallic d-orbitals with the N-ligand empty p-orbitals induced by the planarization. This interpretation is confirmed by the energy shift observed after annealing in both Co L_3-edge and N K-edge spectra.

The planarization reaction on Ag(100) is also possible in the case of NiTPP by annealing the system to 575 K. Figure 4.14 reports the C K-edge and N K-edge NEXAFS spectra of the NiTPP monolayer on Ag(100) before and after annealing to 575 K. A clear fingerprint of the planarization is visible by comparing the C K-edge spectra before and after annealing: the average tilt-off angle of the phenyls (γ) is varying from $\sim$58°(see section NiTPP on Ag(100)) to $\sim$0°, indeed no signal at 285.05 eV is visible in the s-polarized spectrum after annealing of the organic-metal interface. As discussed in Chapter 3, the NiTPP monolayer on Ag(100) shows, as in the case of the CoTPP, the co-existence of planar and saddle-shaped conformers. After annealing, the N K-edge NEXAFS spectrum shows a strong reduction of the intensity of the π^* transition located at 398.5 eV, suggesting that planarization is increasing the charge donation from the silver substrate to the molecular macrocycle.

The comparison between the Ni $2p_{3/2}$ XPS and Ni L_3-edge NEXAFS taken before and after annealing the NiTPP monolayer on Ag(100) to 575 K show that the nickel ion maintains the LS Ni(II) state. As discussed for the case of the CoTPP, the planarization induces a more efficient

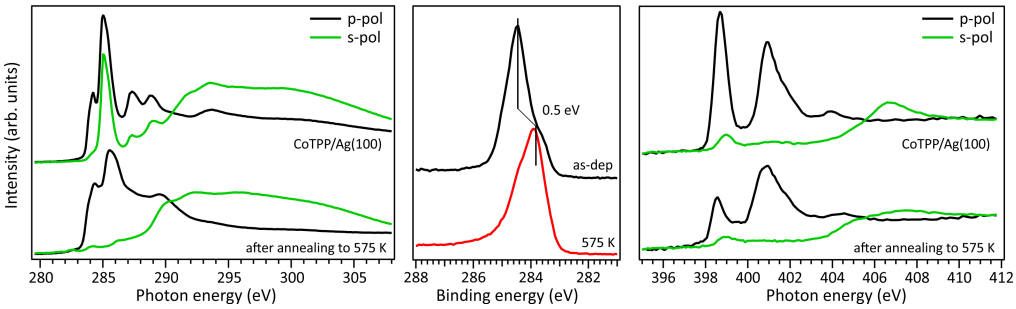

Figure 4.12: C K-edge, C *1s* XPS spectra and N K-edge NEXAFS spectra of CoTPP monolayer on Ag(100) before and after annealing to 575 K.

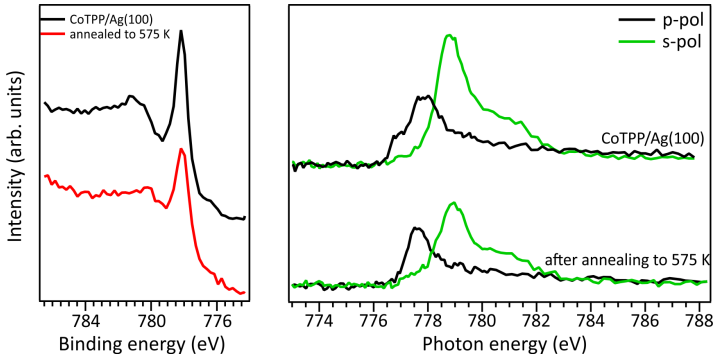

Figure 4.13: Co $2p_{3/2}$ XPS and Co L_3-edge NEXAFS spectra of CoTPP monolayer on Ag(100) before and after annealing to 575 K.

overlap between the central ion and the N-ligand which, ultimately, results in a decrease in the intensity of the Ni L_3-edge spectrum measured with s-polarized light.

4.2 On-copper temperature-induced planarization

Temperature-induced cyclodehydrogenation is strongly dependent on the substrate supporting the organic layer. Indeed, the more reactive the surface, the lower is the temperature required to induce the dehydrogenation process. Based on this, it is expected that on Cu(100) the ring-closure reactions investigated for the OEP and TPP on Ag(100) will be more favored. Moreover, since the molecular properties observed on copper are peculiar, special attention will be paid to how planarization modifies the properties previously discussed for pristine systems. In particular, the reactivity of the metal centers will be tested following the transformation by exposing the systems under consideration to NO_2.

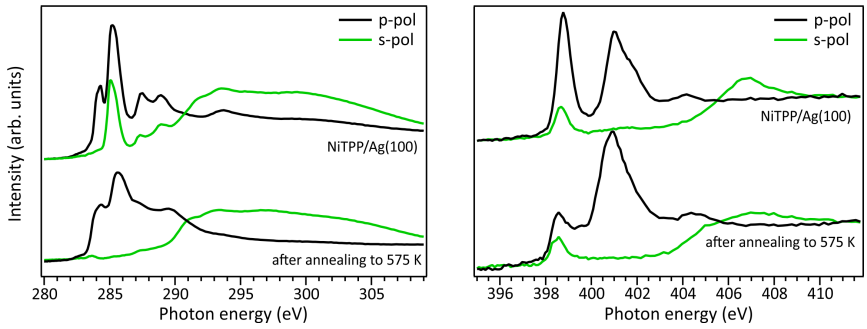

Figure 4.14: C K-edge and N K-edge NEXAFS spectra of NiTPP monolayer on Ag(100) before and after annealing to 575 K.

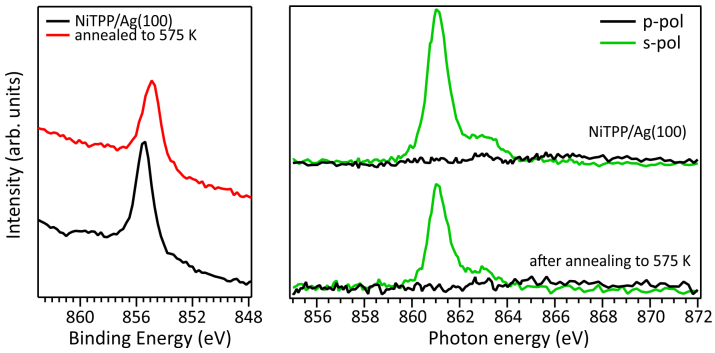

Figure 4.15: Ni $2p_{3/2}$ XPS and Ni L_3-edge NEXAFS spectra of NiTPP monolayer on Ag(100) before and after annealing to 575 K.

4.2.1 CoOEP annealing on Cu(100)

By annealing the CoOEP monolayer on Cu(100) to 500 K for 10 minutes, it is possible to induce the ring-closure reaction from CoOEP to cobalt tetrabenzoporphyrin (CoTBP) also on the Cu(100) substrate.

The characteristic changes in the electronic structure of the nitrogen atoms of the molecular macrocycle confirm that the reaction took place. The transformation from CoOEP to CoTBP induces strong chemical modifications within the molecule. Both N K-edge and C K-edge are very sensitive to the changes of the chemical environment and well-evident changes, arising from the ring-closure reaction of the peripheral ethyl groups and the flattening of the molecule, are observed after the formation of the CoTBP molecule (see Figure 4.16).

The dehydrogenation reaction induces remarkable difference also in the central cobalt ion. The 3d electronic configuration of the free CoTBP molecule is calculated to be $(d_{xy})^2$, $(d_{xz})^2$, $(d_{yz})^2$,$(d_{z^2})^1$, $(d_{x^2-y^2})^0$. This corresponds to a spin moment S = 1/2 for the free molecule, due to the half-filled d_{z^2} orbital. When the molecule is deposited on either substrate, the d_{z^2} orbital hybridizes and becomes filled with charge contributions from other d orbitals and from the copper surface, which occurs mainly through the out-of-plane orbitals. The full occupation of the d_{z^2}

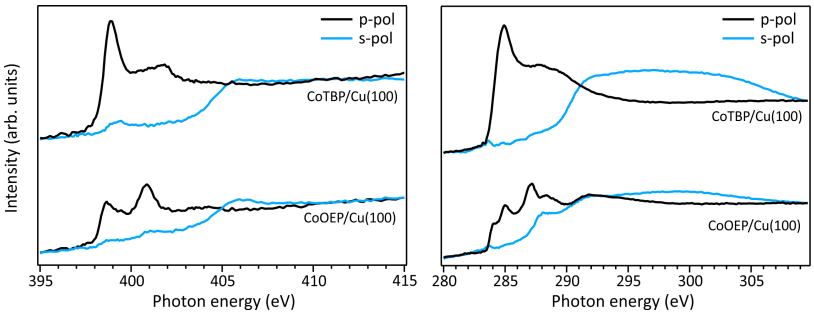

Figure 4.16: C K-edge, C *1s* XPS spectra (inset) and N K-edge NEXAFS spectra of CoOEP monolayer on Cu(100) before and after annealing to 500 K.

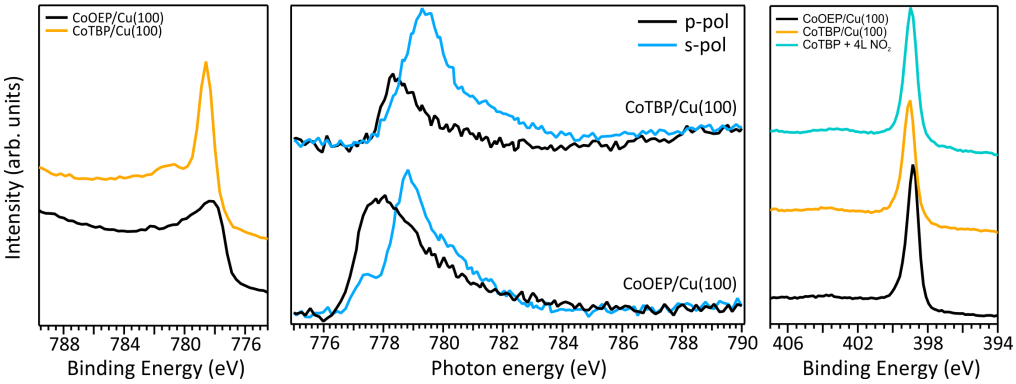

Figure 4.17: Co $2p_{3/2}$ XPS and Co L_3-edge NEXAFS spectra of CoOEP monolayer on Cu(100) before and after annealing to 500 K; N *1s* XPS spectra acquired for the CoOEP/Cu(100), CoTBP/Cu(100) and CoTBP/Cu(100) after 4 L dose of NO_2.

orbital is reflected in the experiment by the disappearing of the characteristic peak at around 778 eV in the Co L_3-edge NEXAFS spectrum (see Figure 4.17), and is the primary cause for the quench of the spin moment on Cu(100), still present in the CoOEP/Cu(100) system before annealing [226]. Does these changes in the central metal ion properties influence the molecular reactivity toward external ligands? In order to test this, the CoTBP/Cu(100) has been exposed to increasing doses of NO_2 at room temperature. No new component is visible in the N *1s* XPS spectrum after the dose of NO_2 suggesting that the CoTBP system does not interact with the NO_2 ligand. At the same time, no changes are detected neither in the Co $2p_{3/2}$ XPS spectrum.

The ring-closure reaction on Cu(100), leading from the CoOEP to the flat CoTBP molecule, de-activates the central metal ion not allowing any longer for the coordination of the external NO_2 axial ligand. Possible reasons leading to this effect will be discussed in Section 4.2.3.

4.2.2 NiTPP on Cu(100): post-deposition annealing

In the following, the possible temperature-induced changes will be investigated in the case of NiTPP monolayer deposited on the Cu(100) kept at RT.

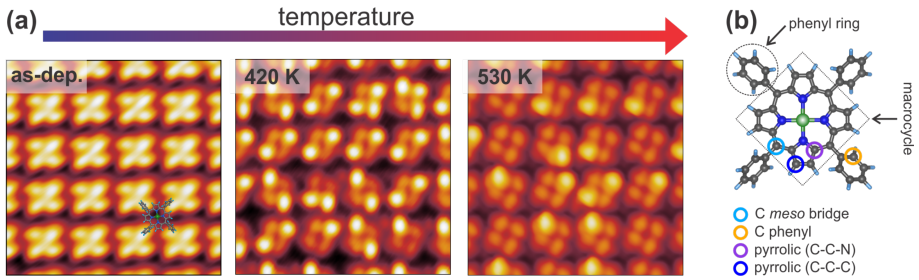

Figure 4.18: Temperature-dependent topographic STM images of the NiTPP film on Cu(100). (a) STM image parameters: lateral size 5.0x5.0 nm^2, tunneling parameters: left -1.5 V / 50 pA; center -0.8 V / 100 pA; right -0.5 V / 500 pA. A sketch of the NiTPP molecule is superimposed to the STM image of the as-deposited molecular film (left). (b) Ball-and-stick model of the gas-phase NiTPP molecule. Each atomic species is painted with a different color: Ni in green, N in blue, C in dark grey and H in light blue. The different carbon species and molecular moieties are labeled.

STM is a widely employed technique for studying the topography and electronic structure of molecular arrays supported by metal electrodes. Here, constant-current STM images of the NiTPP/Cu(100) interface were acquired at 77 K, starting from the as-deposited layer (room temperature) and after annealing at temperatures of 420 and 530 K. The resulting images are shown in Figure 4.18a. The STM appearance of the as-deposited (as-dep.) NiTPP molecule is dominated by four bright features and a dark depression in the center, associated with the four peripheral phenyl rings and with the macrocycle core, respectively [100]. This counter-intuitive appearance originates from the strong molecule-surface interaction. In fact, the macrocycle lies very close to the copper termination (2 Å), forcing the phenyl rings to point away from the surface. A ball-and-stick model of the gas-phase NiTPP molecule, indicating the different molecular moieties, is reported in Figure 4.18b.

Already after the first annealing step, the apparent height of some of the phenyl lobes decreases by several tenths of Å, and after annealing to 530 K, almost all the lobes display a dimmed contrast. The contrast polarity is independent of the bias and the tunneling current. A statistical analysis based on large-scale STM images revealed that, after annealing to 420 K, the height change involves 51 $\pm$ 7% of the phenyls, while at 530 K the percentage increases to 87 $\pm$ 9%. We did not notice any specific pattern in the propagation of phenyl flattening, *i.e.* random combinations of pristine bright and annealed dim phenyls within the molecule are observed in the STM images taken at different temperatures, ranging from all four phenyls in the as-deposited geometry to all four phenyls in the final configuration. We also observed that the dimming of one specific phenyl ring does not systematically influence the intensity/contrast of neighboring NiTPP molecules. From a comparison with former reports on silver [201,239,240] and copper [171,235,241,242] surfaces, one might tentatively associate the apparent decrease of the phenyl height with a molecular flattening due to partial cyclodehydrogenation and fusion of the phenyls with the tetrapyrrolic aromatic moiety. However, a complete flattening of the phenyls is not fully compatible with the topographic images on the basis of simple steric arguments, because we do not observe any change in the intermolecular distance or the positional alignment with respect to the substrate, whereas flattened TPPs would require a larger footprint area in either flat conformation (spiral, rectangular and hybrids as mapped on silver), [201,239,240] hence a change of surface phase density and symmetry. [228] In fact, not even the lattice phase symmetry is affected by the observed transition

and the NiTPP lattice can still be described using the (4,3/-3,4) and (3,4/-4,3) matrices reported in Ref. [100], as confirmed by the LEED patterns taken on the as-deposited film and after annealing to 520 K (see Figure 4.19).

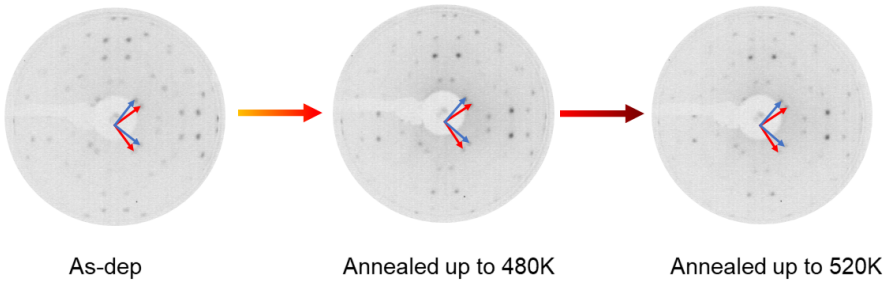

Figure 4.19: LEED images taken at an electron kinetic energy of 20 eV, for the as-deposited NiTPP/Cu(100) interface and after annealing up to 480 and 520 K. The unit cell basis of the two mirrored domains are indicated by the blue and red vectors, respectively.

Overall, the preservation of the phase symmetry, as well as of the local molecular arrangement across the transition, indicates that the porphyrin molecules are strongly anchored to the surface.

Nevertheless, at the present level of detail, the STM topography data cannot directly determine whether the transition is associated with a chemical reaction, a conformational change or a variation of the density of states in the phenyl moiety. From a chemical point of view, the most important evidence is the absence of any changes in the energy position and lineshape of the Ni *2p* core level after annealing at 470 K, as shown in the XPS spectra in Figure 4.21a. The binding energy of the Ni *2p* core level is 853.15 eV. This energy corresponds to the Ni(I) oxidation responsible for the catalytic activity of the metal porphyrin 2D layer. Even the N *1s* core level remains unchanged (see Figure 4.20), suggesting that also the overall reduction of the oxidation state of the tetra-pyrrolic pocket is not affected by the transition.

These observations prove the exceptional robustness of the present system against high temperatures as a consequence of the *surface trans-effect*, which is responsible for the charge injection on the macrocycle and its Ni center. As a consequence, we can confidently associate the local anchoring of the molecules to an effective chemical bond of the tetrapyrrolic pocket to Cu(100) through the nickel atom.

In contrast to the Ni *2p* and N *1s*, the C *1s* lineshape clearly changes after the annealing. The C *1s* core level spectra of the NiTPP/Cu(100) interface is reported in Figure 4.21b. The C *1s* spectrum of the as-deposited NiTPP monolayer at room temperature can be fitted using a multi-peak Voigt function, which accounts for the four different carbon species contained in the NiTPP molecule, as depicted in Figure 4.18b. The 44 C atoms are subdivided in 24 phenylic (binding energy 285.1 $\pm$ 0.1 eV), 4 meso-bridges (284.0 $\pm$ 0.1 eV), 8 C-C-N pyrrolic (285.2 $\pm$ 0.1 eV), and 8 C-C-C pyrrolic (284.6 $\pm$ 0.1 eV) carbon atoms (see Figure 4.21b). The overall energy alignment of the different components is in agreement with the results of a ZnTPP multilayer on Si(111) reported by Cudia *et al* [243].

Already after annealing to about 360 K, a new component arises at 284.4 $\pm$ 0.1 eV binding energy (BE), see Figure 4.21b.

For higher annealing temperatures, it becomes clear that, while the area of the new component

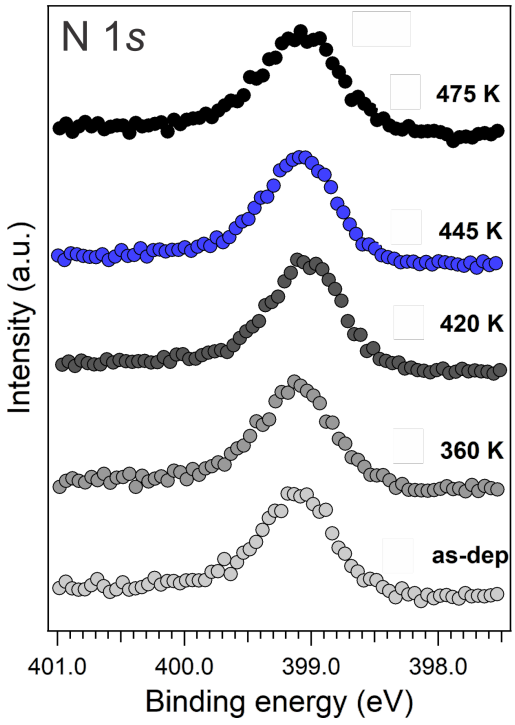

Figure 4.20: N *1s* XPS spectra of the NiTPP/Cu(100) interface taken after a stepwise annealing treatment up to 475 K. For each spectrum, the corresponding annealing temperature is indicated aside. All spectra were collected in normal emission geometry with a photon energy of 515 eV.

grows, the one associated with the phenyl moieties in the pristine layer decreases by the same amount, without appreciable changes of the total C *1s* area, hence the new feature can be confidently associated with the fraction of phenyl carbons undergoing a transformation across the temperature transition previously identified by STM. After annealing to 470 K, all of the pristine phenyl carbons have been transformed into the new state. Time dependence C *1s* XPS measurements show that the transformation is irreversible within our experimental time-scale (>24 hours).

The corresponding shift by $\sim$0.7 eV to lower binding energy appears to be too large for being attributed solely to a final state screening effect due to a smaller distance between the phenyls and the copper surface. Thus, these arguments do not allow us to discriminate between the case of a bare charge transfer to the phenyls or a more drastic chemical modification that would affect the aromatic structure of the whole molecular complex.

In order to shed light on this point, we exploited photoemission tomography to directly probe the electronic structure of the macrocycle. In Figure 4.22a, we compare the angle-integrated valence band spectrum of the clean substrate and of the as-deposited NiTPP film with those measured after a stepwise annealing of the sample up to 720 K. The spectra were obtained by integrating the intensity in the whole $k_{||}$ (k_x, k_y) range as a function of the electron binding

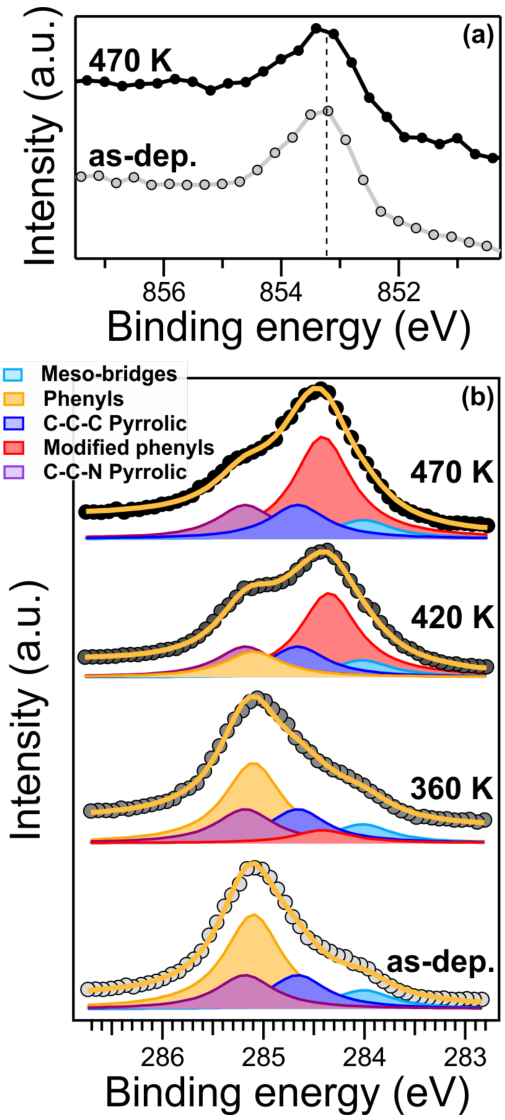

Figure 4.21: XPS spectra of NiTPP/Cu(100) interface at different core level shells. (a) Ni $2p_{3/2}$ spectra of as-deposited (bottom) and annealed up to 470 K (top) film. (b) C *1s* spectra (data and fit) of the NiTPP/Cu(100) interface taken after annealing treatment to the indicated temperature. All spectra were collected in normal emission geometry with a photon energy of 1020 (a) and 515 (b) eV, respectively.

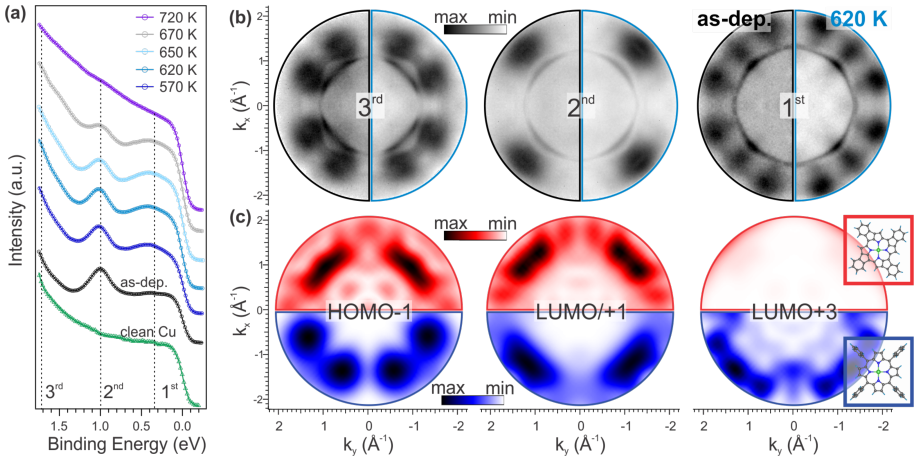

Figure 4.22: Angle-integrated valence band and photoemission tomography data of NiTPP/Cu(100) interface. (a) Valence band spectra acquired after annealing at the indicated temperatures. (b) Momentum patterns of pristine (left) and annealed (right) films, BE indicated on (a). (c) Calculated FTs of the molecular orbitals of NiTPP (bottom) and dh-NiTPP (top).

energy referred to the Fermi Level (E_F) of the copper substrate. The clean copper has a rather featureless spectrum between 0 and 1.8 eV BE, while after deposition of a saturated NiTPP ML, three new features (marked with dashed lines) appear in the spectrum. These features have a clear fingerprint in the momentum space, as will be discussed below. At first sight, the annealing treatment does not significantly affect the spectra: at a temperature of 570 K, we observed only a slight increase of the intensity of the VB region, in particular of the feature at 0.4 eV, while no shift in the energy position of the main molecular states is observed. Beyond 620 K, the VB spectrum starts to change. The two components at 0.4 and 1 eV gradually loose intensity, suggesting partial decomposition of the molecules in the layer that is completed at 720 K, where the molecular features are no longer visible. This provides a further indication of the thermal stability of the molecular film up to 620 K, in full agreement with the XPS C *1s* spectra taken in the 620-720 K temperature range.

Indeed, while up to 620 K we do not observe any modification of the C *1s* spectrum, at 650 K its lineshape starts to change (see the high binding energy shoulder in Figure 4.23, blue spectrum). At 720 K, we observe a very broad feature at 284.2 eV and another component growing on the low BE side.

In Figure 4.22b, we report the experimental momentum maps for both as-deposited (left half) and annealed (right half) porphyrin film, measured at the BEs marked in Figure 4.22a. Whereas the sharp states close to the Γ point are associated with the Cu(100) *sp*-bands, in all momentum maps the pattern related to the molecular overlayer is visible around $|k| \approx 1.5$ Å^{-1}, as described in Ref. [100] These molecular features are associated with the HOMO-1 (BE: 1.7 eV), the degenerate LUMO/LUMO+1 (BE: 1.0 eV) and LUMO+3 (BE: 0.4 eV) of the NiTPP molecule, respectively. Upon annealing up to 620 K, we do not observe any remarkable change in these molecular patterns. The increased intensity of the LUMO+3 peak in the valence band spectra (see Fig. 4.22a) after annealing to 620 K is consistent with an increase of the charge transfer from the substrate to

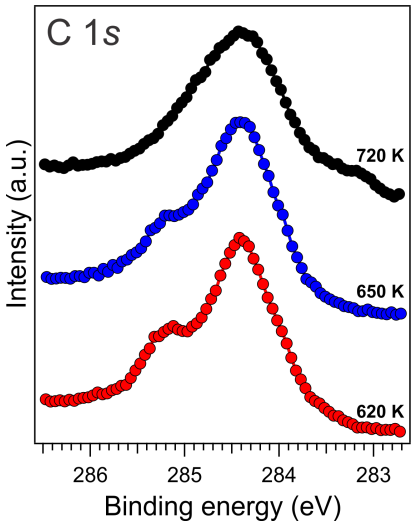

Figure 4.23: C *1s* XPS spectra of the NiTPP/Cu(100) interface taken after annealing, the corresponding temperature is indicated for each spectrum. The spectra are collected in normal emission geometry with a photon energy of 515 eV.

the molecule.

PT has already been proven to be a suitable tool for identifying possible reaction products, as demonstrated in the case of the thermally-induced reaction from CoOEP to CoTBP on Ag(100) (see Section 4.1.1). In our case, however, the one-to-one match between the momentum patterns of the as-deposited and the annealed molecular overlayers clearly shows that no rearrangement of the chemical bonds at the macrocycle rim takes place upon annealing, as otherwise the molecular symmetry would have been affected and the appearance in the reciprocal space of the corresponding molecular orbitals would have changed.

To confirm our interpretation, we performed DFT calculations for dehydrogenated NiTPP (dh-NiTPP) where the phenyl rings are fused with the macrocycle leading to benzotetracyclopenta[at,ef,jk,op] porphyrin, which is depicted in the inset in Figure 4.22c, bottom. It should be noted that such reaction product, as resulting from the NiTPP dehydrogenation, is the only possible form that is compatible with the fourfold symmetry observed in STM imaging.

The calculated momentum distributions of the frontier molecular orbitals of dh-NiTPP are reported in Figure 4.22c (top, red color scale) and compared to those of the pristine NiTPP (bottom, blue color scale). The resulting momentum patterns of dh-NiTPP, together with its overall electronic structure, significantly differ from the one of NiTPP and they do not resemble the measured maps in Figure 4.22b. As an example, the LUMO+3 changes its π character becoming a σ orbital, and at the same time, the HOMO-LUMO gap decreases due to the delocalization of the π electrons over the whole molecule. Thus, we can conclude that the ring-closing reaction between the phenyls and the macrocycle would lead to a completely different appearance of the molecular features in k-space, which do not match the experimental maps after annealing. Therefore, the PT experiment rules out chemical changes in the NiTPP array on Cu(100) across the thermal transition. In Figure 4.24, we compare the Fourier transforms of the frontier molecular orbitals of NiTPP and dh-NiTPP. Panel (a) shows a ball-and-stick model of the NiTPP molecule

and the corresponding momentum maps, which are azimuthally oriented such that the N-Ni-N axis is at 45° to the k_x direction. To directly compare the simulated maps to the angle-resolved photoemission data, the different azimuthal orientation of the molecule for each domain must be taken into account. In the present case, NiTPPs self-assemble in two mirrored domains with the N-Ni-N axis oriented ± 8° with respect to the [100] direction of Cu(100), respectively. The resulting momentum maps are shown in panel (b).

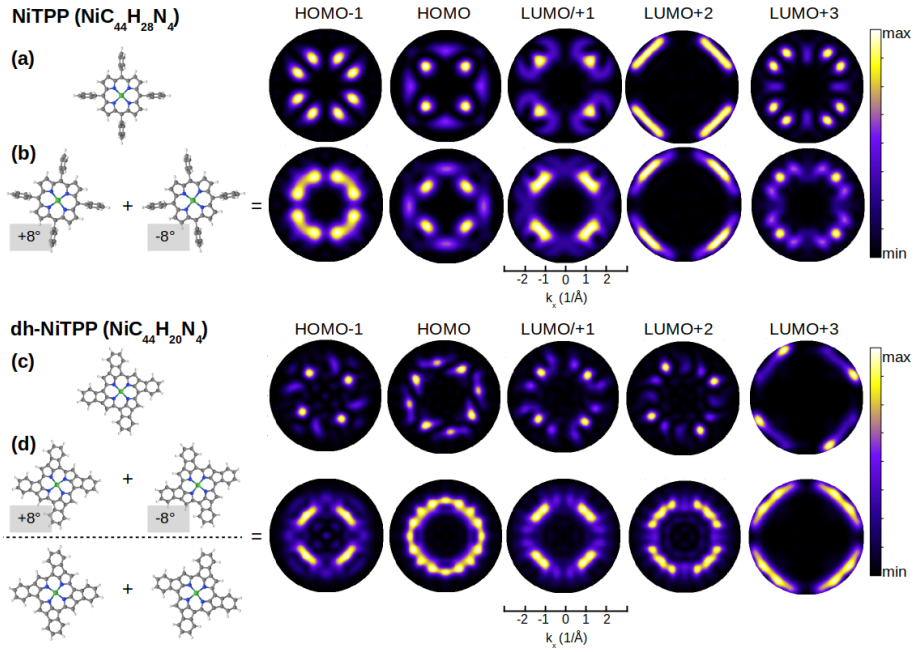

Figure 4.24: Simulation of the momentum space pattern of the frontier molecular orbitals of NiTPP and dh-NiTPP. Panels (a) and (c) depict the Fourier transforms of the molecular orbitals for a single molecular orientation, while panel (b) and (d) take into account the azimuthal alignment of the molecule upon adsorption and the symmetry of the substrate as detailed in the text.

The momentum patterns for the dehydrogenated molecule (dh-NiTPP) are displayed in panel (c). Here, the N-Ni-N axis of dh-NiTPP has the same orientation of the NiTPP one in panel (a). The resulting $|FT|^2$ of the dh-NiTPP frontier orbitals significantly differ from the ones of the NiTPP. In the case of the dh-NiTPP, we have to take into account that the molecule is chiral (see the ball-and-stick model in panel (c)), in order to compare the simulated and experimental momentum maps. Since the momentum maps are obtained averaging over a large surface area (several μm^2), we have to consider in the simulated momentum maps not only the azimuthal orientation of the molecule but also its chirality within the single domain. The results are reported in panel (d). The comparison of the simulated momentum maps of the frontier molecular orbitals for NiTPP and dh-NiTPP molecules reveals pronounced differences. Since the shape of the measured momentum patterns does not change upon annealing, this provides strong evidence that the cyclodehydrogenation does not take place during the annealing.

As depicted in Figure 4.25, dh-NiTPP has a completely different electronic structure compared

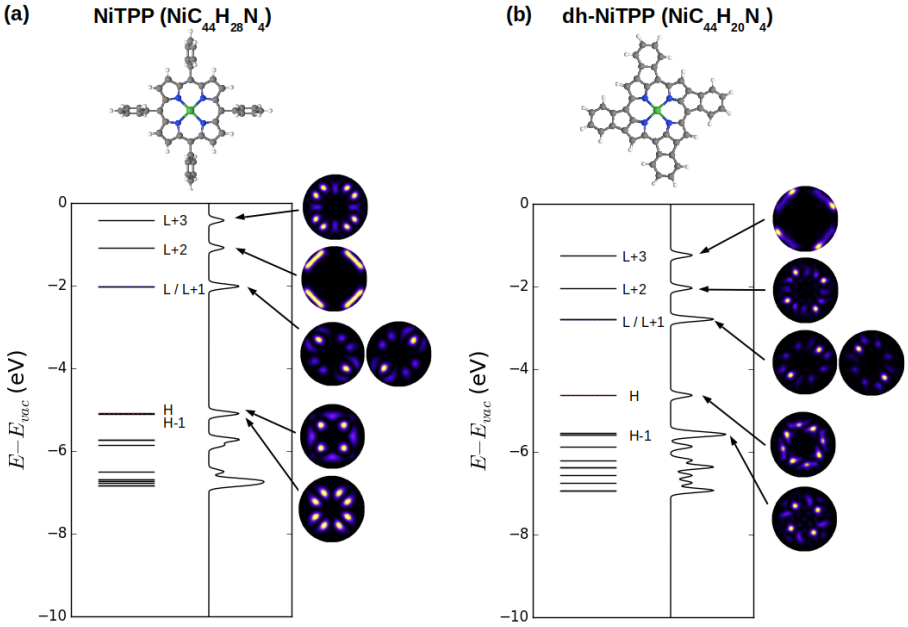

Figure 4.25: Orbital energies and momentum maps (a) NiTPP and (b) dh-NiTPP from a gas phase DFT calculation with the B3LYP exchange-correlation functional. The momentum space patterns corresponding to the HOMO-1, HOMO, LUMO/LUMO+1, LUMO+2 and LUMO+3 orbitals are displayed next to the orbital energy diagram.

to NiTPP. This results in a completely different alignment of the frontier orbitals, resulting in a smaller HOMO-LUMO gap, and in π- to σ-symmetry change the LUMO+2 (whose filling up, in the NiTPP/Cu(100), is responsible for the +1 oxidation state of the Ni atom).

What is the ultimate origin of the observed spectroscopic and topographic evolution with temperature? All the gathered experimental data suggest that, upon annealing, the molecules experience only a conformational change involving a downward bending of the phenyl moieties. In this regard, angular-dependent NEXAFS measurements can provide valuable information on the orientation of a specific moiety with respect to the copper surface plane. In Figure 4.26a, we compare the NEXAFS spectra acquired across the N K-edge with p and s linear polarized light, for the as-deposited (bottom) and annealed (top) NiTPP film up to 490 K. We observe that, upon annealing, the NEXAFS dichroism does not change, and, at the same time, the π-symmetry resonances at 398.7 and 401.5 eV witness an overall intensity decrease. The former evidence indicates that the macrocycle remains both flat and parallel to the surface. The latter points towards an overall enhancement of the charge transfer, from the substrate to the molecular film, in agreement with the trend in the VB spectra shown above.

In contrast to the N K-edge, the NEXAFS measurements at the C K-edge, reported in Figure 4.26b, show, after the annealing, a change of the linear dichroism in the spectral feature at 285.1 eV mainly associated with the π* resonance of phenyls in NEXAFS C K-edge spectrum [244]. In fact, by looking at the intensity ratio of these resonance in the two polarizations, it is possible to estimate the average angle between the direction of the π* orbitals of the phenyl moiety and

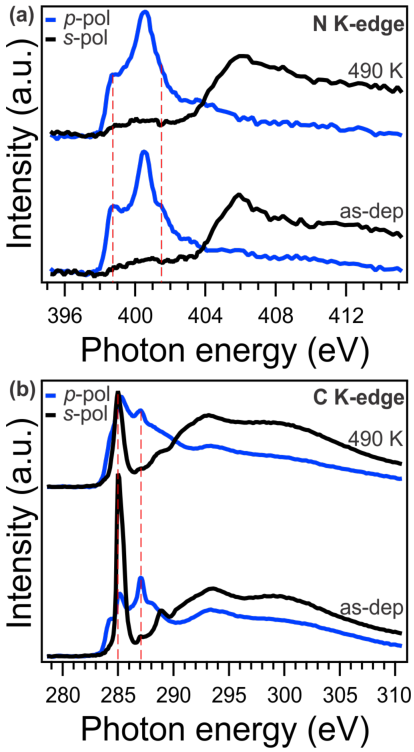

Figure 4.26: NEXAFS measurements of the NiTPP/Cu(100) interface. The spectra are acquired at the nitrogen (a) and carbon (b) K-edges for the as-deposited film (bottom panel) and after annealing up to 490 K (top panel).

the surface normal (tilt-off angle). While for the as-deposited NiTPP film the tilt-off angle of the phenyl results to be $70^{\circ} \pm 2^{\circ}$, it decreases up to $60^{\circ} \pm 3^{\circ}$ after the thermal transition. In the present case, it has to be noticed that this tilt-off angle results from the convolution of both twisting and tilting of the phenyl ligand [100] and the two contributions cannot be disentangled solely from the NEXAFS data. In any case, this small variation alone cannot fully explain the observed dimming of the phenyl features in STM images. The overall intensity decrease of the phenyl resonance at 285.1 eV indicates an increase of the charge transfer to the substituent, which, combined with the observed large core level shift of the phenyl C *1s* component, suggests also an electronic origin of the change of STM contrast.

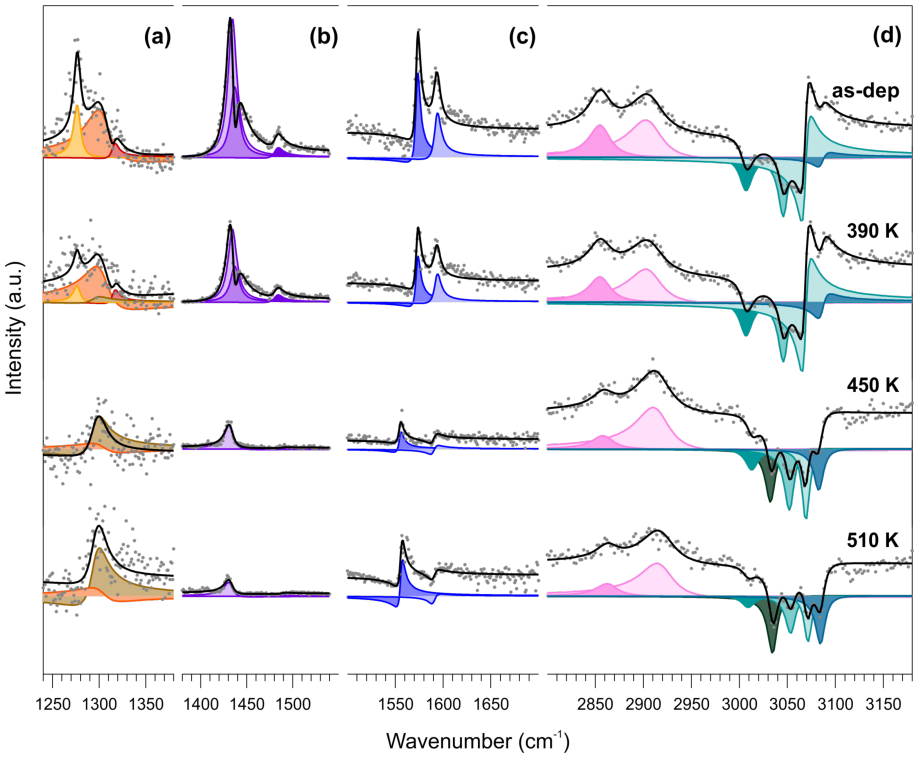

Figure 4.27: Temperature-dependent IR-Vis SFG spectra of 1 ML NiTPP/Cu(100). Spectra were acquired at room temperature after annealing the system to progressively higher temperatures (from top to bottom). Data were renormalized and split into four different energy windows (a-d) for best visualization. The normalized SFG signal (grey dots) is shown together with the best fit (black lines) and the deconvolution (color filled offset profiles), according to the model lineshape described in the text. Data rescaling factors are (a) 1, (b) 0.15, (c) 0.5, (d) 0.2.

Summarizing the topographic and X-ray spectroscopy data, we conclude that the Ni(I)TPP monolayer phase undergoes an irreversible thermally-activated transition resulting only in a change of the peripheral phenyls tilt, while the electronic structure of the macrocycle and its adsorption geometry are preserved. We suggest that the new conformation is stabilized by the enhancement of the charge transfer from the substrate to the organic film, preventing the system to return to its pristine adsorption geometry. Moreover, the molecular pinning, achieved by the

surface trans-effect and the corresponding charge transfer, is responsible for the molecular stability up to its final decomposition. A similar phenomenon was observed for porphyrins on the surface of rutile-TiO_2(110), [142] where the anchoring on TiO_2 was rather driven by a double chemical bond of the tetrapyrrolic pocket to the substrate, delaying the flattening by cyclodehydrogenation beyond up to 620 K. [228]

Infrared-Visible Sum-Frequency Generation (IR-Vis SFG) spectroscopy measurements endorse the conformational change model depicted above. In Figure 4.27, we report the vibronic spectra measured in the 1240-3180 cm^{-1} frequency region of the as-deposited monolayer at room temperature (top) and after stepwise annealing at progressively higher temperature values (from top to bottom). The NiTPP/Cu(100) system is characterized by a number of specific features that can be quantitatively determined by proper deconvolution of the experimental data according to the procedure described elsewhere. The best results of the fitting procedure are shown in the figure (black line and color-filled profiles). The assignment to the respective vibrational modes can be obtained with reference to literature data [165, 245–247].

The temperature-dependent evolution of the vibronic spectra in the 300-510 K range indicates substantial stability of the molecule for both the macrocycle and the phenyl moieties. An overall increase of planarity of the molecule is suggested by the general reduction of resonant amplitudes at increasing temperatures. More specifically, from the quantitative evolution of the resonant amplitudes, line positions, and relative phases, a number of conclusions can be drawn from the data. First, the feature growing with the temperature at 1296 cm^{-1} (Figure 4.27a) at the expense of the resonances at 1277, 1304, and 1316 cm^{-1} is associated with the orientational rearrangement of the out-of-plane modes of the phenyl rings. Second, the strong phase changes in the C-H high energy region (d), accompanied by the growth of a new resonance at 3034 cm^{-1}, indicate both reorientation of the phenyl rings and increase of their interaction with the underlying surface. Finally, the progressively increasing non-resonant amplitude (shown in Figure 4.28) indicates modifications of the surface electronic charge density within 2.3 eV from the Fermi level, due to a change of the molecule-surface interaction. Altogether, these observations exclude the fusion of the phenyl moieties with adjacent molecules or with the macrocycle and rather point in the direction of substantial temperature stability of the NiTPP monolayer, at least up to 510 K. The observed downward bending of the phenyl groups is associated with the opening of a new vibrational channel and corresponding increase of the phenyl interaction with the copper substrate, which finally determines also the large core level shift of the C *1s* phenyl component, as measured by XPS.

The *surface trans-effect* at the basis of the macrocycle reduction results in an effective pinning of the molecule to its adsorption site, thus preventing any molecular displacement in the overlayer lattice, which would eventually allow the normally observed molecular flattening by cyclodehydrogenation. The strong thermal stability of the Ni(I)TPP network supported by copper paves the way to the application of this reactive interface in the field of heterogeneous catalysis, gas sensing and surface magnetochemistry, where temperatures up to 620 K can be used to regenerate the pristine properties of the active molecular porphyrin layer.

4.2.3 NiTPP on Cu(100): during deposition annealing

The high thermal and chemical stability of the NiTPP/Cu(100) interface has been demonstrated by annealing it at up to 620 K. Indeed, the room temperature deposition of NiTPP on copper

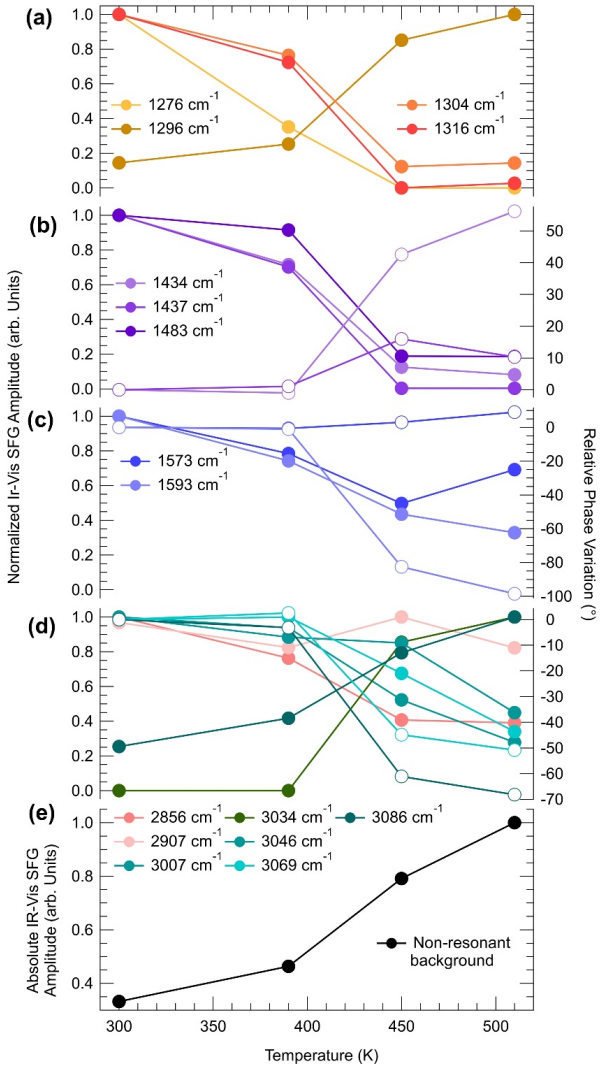

Figure 4.28: Temperature evolution of the IR-Vis SFG lineshapes as obtained from the best fits of the data reported in Figure 4.27: (a-d) resonant amplitude (left scales, filled circles) and relative phase (right scales, empty circles); (e) amplitude of the non-resonant background. For better clarity, the color code of the resonances reflects the deconvolutions plotted in Figure 4.27.

leads to the formation of a closed-packed monolayer phase with long-range order. In such a case, the strong interaction between the surface and the molecular layer, coexisting with a high charge transfer from the copper substrate to the NiTPP, leads to the pinning of the molecules to their own adsorption site, preventing possible displacement of the latter. This freedom is crucial to allow

This work			Phenyl Modes [8–10]		Macrocycle Modes [8–10]	
ω (cm^{-1})	$\Delta\varphi$ (°)	Γ (cm^{-1})	ω (cm^{-1})	*Assignment*	ω (cm^{-1})	*Assignment*
1277	288	5	1269	δ(CH)	1269	$\nu(C_m\text{-Ph})$, $\nu(NC_\alpha)$
1296	214	11	1283, 1285, 1289	Out-of-plane B_{1u}, A_{2u}, E_g		
1304	350	16			1302	ν(pyr half-ring), $\nu(NC_\alpha)$, $\nu(C_\alpha C_\beta)$
1316	224	6	1317, 1318	Out-of-plane B_{1u}, A_{2u}	1313	ν(pyr quarter-ring)
1434	246-314	6	1438	Out-of-plane B_{1u}		
1437	97-113	6	1440	Out-of-plane A_{2u}		
1483	215	6	1470	δ(CCH), ν(CC)	1470, 1473, 1485	$\nu(C_\alpha C_m)_{sym}$, $\nu(C_\beta C_\beta)$, $\nu(NC_\alpha)$, $\nu(C_\alpha C_\beta)$
1573	105-114	3	1576, 1583, 1586	ν(CC), out-of-plane E_g, B_{1u}, A_{2u}	1572	$\nu(C_\beta C_\beta)$, $\nu(C_\alpha C_m)$, $\delta(C_\alpha C_m)$
1590-1593	139-238	4	1586	out-of-plane A_{2u}	1586, 1594	$\nu(C_\alpha C_m)_{sym}$, $\nu(C_\alpha C_m)_{asym}$, $\delta(C_\alpha C_m Ph)$
2856	280	14	3039, 3047, 3063, 3068, 3069, 3071, 3073, 3075	Symm. and asymm. ν(CH), out-of-plane E_g, B_{1u}, A_{2u}		
2907	295	21				
3007	87	8				
3033-3035	97	6				
3046	97	6				
3069	90-131	5				
3086	97-155	6				

Figure 4.29: Lineshape parameters obtained from the best fit and deconvolution procedure of the IR-Vis SFG data shown in Figure 4.27. The assignment of the observed vibronic modes to local coordinates and skeletal modes for 1.0 ML NiTPP/Cu(100) is obtained through comparison with previous literature data. The frequency and phase ranges indicated in the table account for the temperature-dependent evolution reported in Figure 4.28.

the flattening of the phenyls and, consequently, the cyclodehydrogenation reaction to take place. To avoid the pinning effect, and to favor the temperature-induced cyclization reaction before the formation of closed-packed domains that would have inhibited it, the copper surface was kept at a temperature of 500 K during deposition, while the ML/min deposition rate was lowered. Comparing N and C K-edge NEXAFS spectra before and after the planarization reaction and, in particular, focusing on the spectral dichroic behavior, we demonstrate that this reaction is here taking place (see Figure 4.30).

Briefly, the π^* resonance related to the phenyl rings visible in the C K-edge spectrum measured using s-polarized light is now quenched, *i.e.*, the phenyl rings are now lying parallel to the copper surface and coplanar with the macrocycle moiety. The absence of the phenyl resonance in the spectrum is a clear fingerprint of the flattening of the adsorbed porphyrin molecules, as previously observed for NiTPP cyclodehydrogenation on Ag(100) (see Section 3.5).

These results show that a higher temperature of the substrate during the molecular deposition is a key factor for chemically transforming the NiTPP molecule to its flat derivatives (dh-NiTPP). This is an efficient method for inducing the ring-closure reaction in MTPPs anchored to strongly

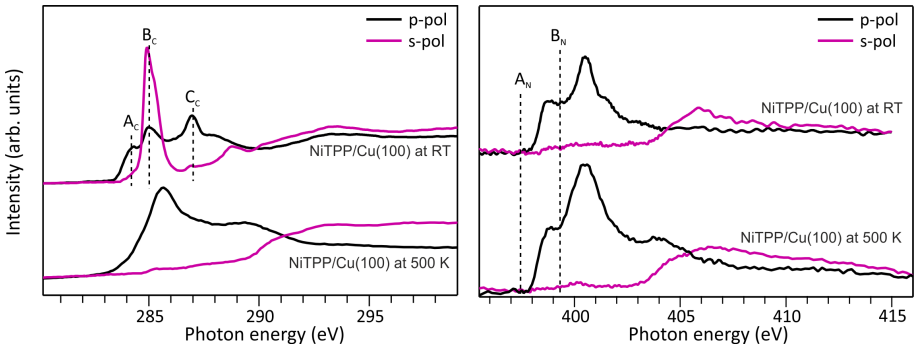

Figure 4.30: C K-edge and N K-edge NEXAFS spectra for the NiTPP monolayer deposited on Cu(100) substrate kept at room temperature and 500 K.

interacting substrates, where the post-annealing of the densely packed network formed upon room temperature molecule deposition has not shown any traces of such phenomenon (see Section 4.2.2). The conversion from NiTPP to dh-NiTPP molecules by the on-surface reaction is expected to be strongly dependent on the sublimation rate of the metalloporphyrin on the hot copper surface, being more efficient at lower deposition rates. This would be in line with previous coverage-dependence TPD studies on the TPP on-surface dehydrogenation reaction, which showed that the rate of dehydrogenation in TPP is lower at higher coverages because of the stabilizing effect of the higher molecular coordination [171,235].

The two low energy features A_N and B_N in the N K-edge NEXAFS spectra reported in Figure 4.30 originate from the four pyrrolic nitrogens of the macrocycle and are mainly related to the transition of N *1s* electron to the degenerate π^* unoccupied MO. The s/p dichroic trend in the spectra indicates a flat adsorption geometry of the porphyrin macrocycle on the copper substrate, in agreement with the previously discussed C K-edge NEXAFS data. Since the dichroic behavior in the N K-edge spectra of dh-MTPP molecules remains the same, we may conclude that the ring-closure reaction is not inducing any change in the adsorption geometry of the macrocycle moiety. The intensity reduction of the pre-edge resonances, especially of A_N, as well as an overall shift to lower energies of the whole spectrum (compared to the one measured for weakly interacting metal porphyrin molecules on oxygen-modified surface or in multilayer), relates to a partial filling of the unoccupied MOs. This means that charge transfer from the substrate to the organic system is taking place at both MTPP and dh-MTPP/metal interfaces. The charge transfer phenomenon has been already reported for both metalated and free-base porphyrins monolayers self-assembled on a copper substrate, and this effect is often observed in strongly interacting molecule-metal complexes [39].

During the process of cyclodehydrogenation between the macrocycle periphery and the phenyl substituents, different planarized NiTPP derivates can be formed. Among them, the spiral and the rectangular form. Optimization geometry calculations on the spiral and rectangle systems found that the spiral is more stable than the rectangle of -0.31 eV. These results agree with experimental data on supported metal-TPP, where in case of mixed metal-TPP and dehydrogenated metal-TPP, only the spiral planarized derivative is observed with STM measurements [248].

The presence of the sole spi-dh-NiTPP was confirmed in the present experiment by exploiting

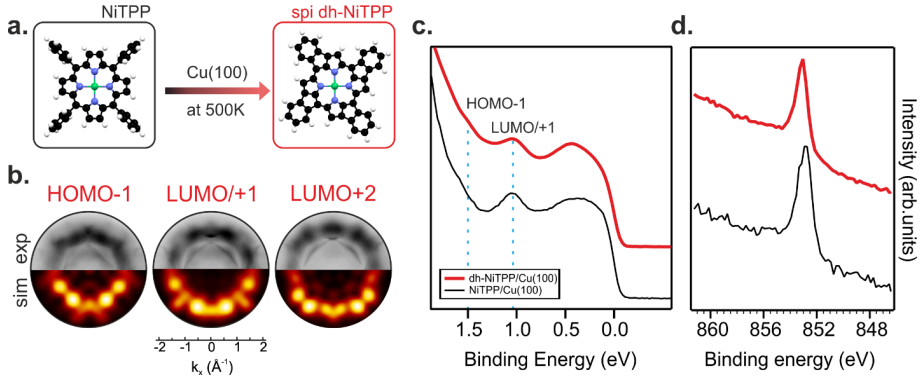

Figure 4.31: Schematic representation of the reaction taking place on the copper surface held at 500 K (a), PT-based attribution of the frontier orbitals of the spiral from of dh-NiTPP (b), valence band spectrum of NiTPP/Cu(100) and dh-NiTPP/Cu(100) (c) and corresponding Ni $2p_{3/2}$ spectra (d).

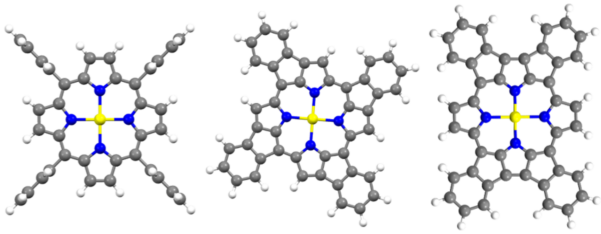

Figure 4.32: Optimized structures for NiTPP (left), NiTPP-spi (center) and NiTPP-rec (right). Grey, white, blue, and yellow spheres are C, H, N and Ni, respectively.

the photoemission tomography (PT) approach. Figure 4.31b shows the comparison between the experimental momentum maps acquired on the maximum of the three molecular peaks observed for the dh-NiTPP/Cu(100) interface and the simulated momentum maps obtained by considering only the spiral form. While a good agreement is found with the spiral form, this is not the case for the rectangular form (see Figure 4.33), pointing out that the deposition of NiTPP on the annealed copper surface leads to the formation of the spi-dh-NiTPP molecule. From here on only this form will be considered in the calculations.

Valence band spectra reported in Figure 4.31c compare the NiTPP/Cu(100) interface with the dh-NiTPP/Cu(100) one. The interaction of the macrocycle with the copper surface and the charge transfer to the molecular layer shows strong similarities for the two interfaces. Indeed, HOMO-1 and LUMO/+1 peaks are located at the same binding energy. The only difference observed between the two interfaces is the nature of the last MO occupied on the surface, which in the case of the NiTPP is the LUMO+3, located at 0.2 in BE, and for the dh-NiTPP the LUMO+2, located at 0.4 in BE. This difference arises from the intrinsically different distribution for the molecule before and after the temperature-induced ring-closure reaction.

Having thus demonstrated that the planarization of the molecule was obtained *via* this method of synthesis, we proceed to check the oxidation states of the central metal for both systems under consideration. Figure 4.31d reports the corresponding Ni $2p_{3/2}$ core-level spectra. The strong

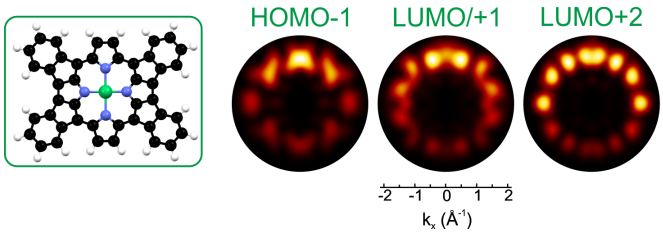

Figure 4.33: PT-based comparison of the frontier momentum maps acquired at the dh-NiTPP/Cu(100) interface with the maps of the rectangular dh-NiTPP form.

interaction between the NiTPP molecular layer and the copper substrate, accompanied by charge transfer from the substrate and hybridization, results in the reduction of the chelated ion, as previously discussed in Chapter 3. Indeed, the Ni $2p_{3/2}$ core-level spectra of the Ni-TPP molecules on Cu(100) substrate peak up at 852.7 eV of binding energy. By comparing the spectrum with the dh-NiTPP one, it is evident that the on-surface reaction does not influence the oxidation states of the metal ion in the flat-form of porphyrin derivatives, as the corresponding Ni $2p_{3/2}$ core-level spectra show a similar shape and peak up at almost the same BE. These values of BE display a significant shift to lower binding energies with respect to the values observed in the spectra of the metal porphyrin molecules adsorbed on inert substrates and in multilayer. Such significant chemical shifts in the core-level spectra are confirming the metal ion reduction (Ni(II) $\rightarrow$ Ni(I)) for both systems.

At this point, having proved the stabilization of nickel in its strongly interacting oxidation state in both TPP and its dehydrogenated form, we proceed to test its reactivity by exposing both systems to nitrogen dioxide. After exposing the dh-NiTPP/Cu(100) system to NO_2, no new bond formation is observed and there is no change in the XPS spectra acquired post-exposure (see Figure 4.34).

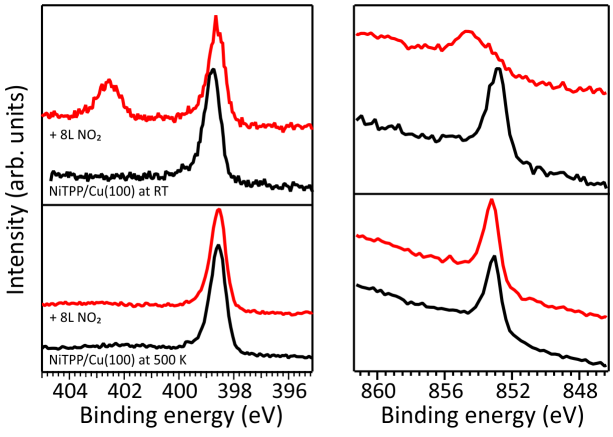

Figure 4.34: N *1s* and Ni $2p_{3/2}$ XPS spectra for the NiTPP monolayer deposited on Cu(100) substrate kept at RT, 500 K and after exposing to 8 L of NO_2 both porphyrin networks.

Let us therefore study in more detail why this experimental observation occurred. Further

information about the electronic structure of unoccupied *3d* states of NiTPP and its planarized form can be gained by the NEXAFS measurements across L_3-edge (see Figure 4.35a).

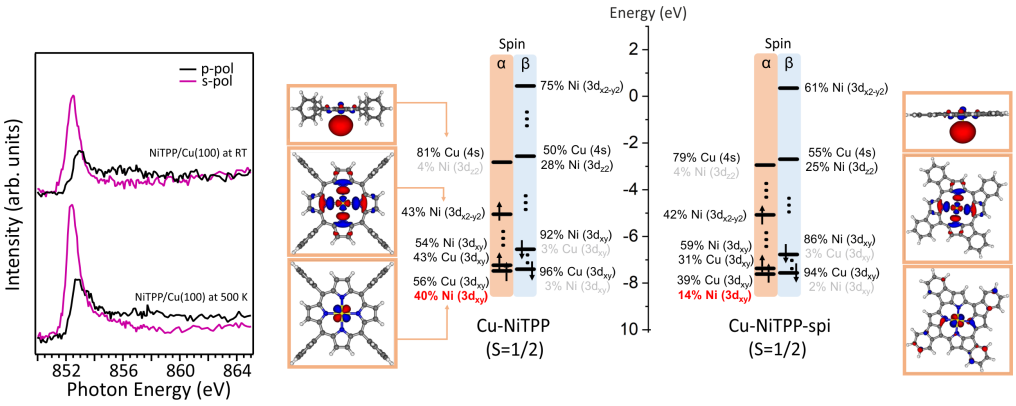

Figure 4.35: Ni L_3-edge NEXAFS spectra for the NiTPP deposited on Cu(100) substrate kept at room temperature and 500 K; energy level diagrams associated with the Cu-NiTPP (left) and Cu-NiTPP-spi (right) species with a fixed Ni-Cu distance at 2.1 Å and optimized structures. Both α and β spins are reported. Black arrows indicate the occupied Ni 3d-based α MOs. The relative percentage of MOs are also reported. 3D contour plots for α MOs are displayed in the insets. The comparison between α and β spin occupation shows that the single unpaired electron is localized on the α Ni $3d_{x^2-y^2}$ MO.

While the intensity of the transition from $2p_{3/2}$ to the out-of-the-plane Ni *3d* orbitals accessed with the p-polarized light for both nickel-containing molecules are similar, the intensity of the transition to the in-plane atomic orbitals measured with s-polarization in the planar dh-NiTPP derivatives is slightly enhanced compared to the NiTPP one. To get more insight in atomic orbitals and MOs of the metal-molecule complexes and relate this theoretical impute with the spectral behaviour in the next we perform the density functional theory (DFT) calculations using so-call molecular cluster approach in collaboration with Dr. Silvia Carlotto and Prof. Maurizio Casarin from the University of Padova, Italy.

According to the DFT/ROCIS calculations, the electronic ground states of the copper supported NiTPP and spi-dh-NiTPP correspond to a spin quantum number S = 1/2 (one unpaired electron). For the Cu-NiTPP, the s-polarization of the Ni L_3-edge spectrum (see Figure 4.35) has an asymmetric feature. The highest peak A_s feature lies at 852.4 eV is generated $\Delta S = 0$ state associated with the single Ni-based $2p \rightarrow 3d$ electronic excitation involving the Ni $3d_{x^2-y^2}$ singly occupied MO (SOMO). The shoulder B_s lies at 853.4 eV is almost equally associated with the single Ni-based $2p \rightarrow 3d$ electronic excitation involving virtual molecular orbitals (VMOs) Cu- and TPP-based. Also the highest intensity of the p-polarization B_p is associated to the same electronic transitions involved in the B_s, but the larger contribution is due to the Ni-based $2p \rightarrow$ Cu-based (VMO) electronic excitation. All Ni-, Cu- and TPP-based MOs (reported in Figure 4.35) are involved in the electronic excitation of the Ni L_3-edge spectrum. The s- and p-polarization of the Ni L_3-edge spectra for Cu-spi-dh-NiTPP (see Figure 4.35) are almost equal to the Cu-NiTPP ones. This is not surprising considering the similarity of the coordinative pocket of the Ni metal center. The single electronic transitions involved in these spectra are generated by the same SOMO and VMOs show in the Cu-NiTPP.

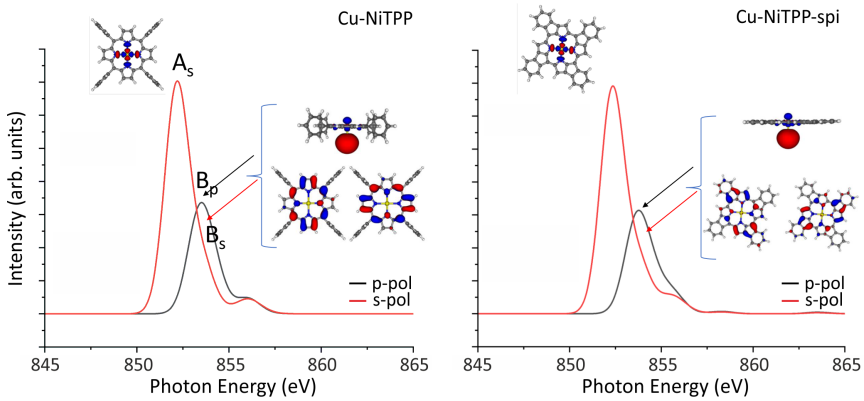

Figure 4.36: Ni L_3-edge NEXAFS spectra simulated for the NiTPP and spi-dh-NiTPP on Cu(100).

The square planar coordination of Ni(II) (D_{4h} symmetry) lifts the five-fold degeneracy of the Ni *3d* atomic orbitals (AOs) in a_{1g} (d_{z^2}), b_{1g} ($d_{x^2-y^2}$), b_{2g} (d_{xy}) and e_{1g} ($d_{xz,yz}$), while the NiTPP-spi system has a C_{4h} symmetry and the Ni *3d* atomic orbitals (AOs) are a_g (d_{z^2}), b_g ($d_{x^2-y^2}$), b_g (d_{xy}) and e_g ($d_{xz,yz}$). The Ni(II) chemical environmental is similar for NiTPP and NiTPP-spi systems and also the relative position of the molecular orbitals (MOs) mainly localized on the Ni *3d* AOs is the same (see Figure 4.35).

Also the absolute energies for the different levels are similar, except for the Ni *3d* AOs percentage on the double degenerate e_{1g}/e_g MOs, where in the NiTPP the Ni percentages on these MOs are sensitively higher (53%) with respect to the NiTPP-spi.

The similarity between the Ni chemical environmental in the NiTPP and NiTPP-spi systems is well highlighted by the Ni-N distances, which are very close (1.98 Å and 1.95 Å for NiTPP and NiTPP-spi, respectively). Further evidence is gained by the analysis of the Nalewajski-Mrozek bond multiplicity index (^{NM}I) [249], which provides a quantitative estimate of bond strengths: in both systems $^{NM}I_{Ni\text{-}N}$ values are similar (0.469 and 0.464 for NiTPP and NiTPP-spi, respectively).

Upon coordination of the Ni ion on copper, DFT calculations show that the Ni ion in the Cu-NiTPP and Cu-NiTPP-spi clusters has a single unpaired electron, while the copper atom becomes closed-shell. This confirms the on-surface redox reaction, where the Ni(II) is reduced to Ni(I), d^9, while the Cu(0) is oxidized to Cu(I). This is fully in agreement with the XPS data previously discussed. The single unpaired electron on Ni occupies the Ni $3d_{x^2-y^2}$-based MO (see Figure 4.35), while the Cu *4s* AOs are empty. In both molecular clusters, the Cu-Ni distance has been fixed to 2.1 Å, as previously reported for the Ni-TPP/Cu(100) interface. An optimization calculation on Cu-NiTPP-rec confirms the larger stability also of Cu-NiTPP-spi species (-0.31 eV). The oxidation state of Ni and Cu species as the charge transfer that causes the reduction of Ni is clearly visible from the analysis of MOs occupation and composition. In the Cu-NiTPP, the singly occupied MOs is manly localized on the Ni $3d_{x^2-y^2}$-based MO (43%) (spin α, while the spin β is empty) and no additional Ni 3d-based MOs are empty. This is compatible with a Ni(I), d^9 state. The lowest unoccupied MO (LUMO) is localized on Cu 4s MO (81%) in both α and β spin, hence the Cu has lost its electron and it is oxidized to Cu(I). The surface transfers its electron to the NiTPP. The situation is almost identical for the Cu-NiTPP-spi. The absolute energies are very

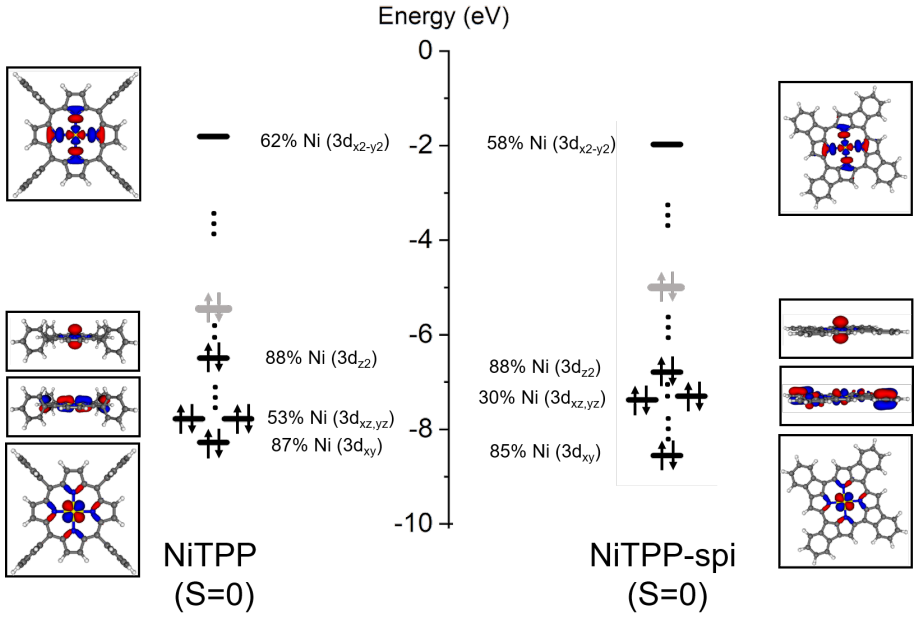

Figure 4.37: Energy level diagrams associated to the LS NiTPP (left) and LS NiTPP-spi (right) species and optimized structures. Black arrows indicate the occupied Ni *3d*-based MOs (the relative percentage is also reported), whose 3D contour plots are displayed in the insets. Grey arrows indicate the occupied TPP-based MOs. Vertical dots indicate that some levels, mainly localized on TPP fragment, are omitted.

similar, and the Ni/Cu undergoes the same redox reaction observed for Cu-NiTPP. The redox mechanism is proven for both systems, and a more detailed analysis on the net spin polarization, calculated as the number of α spin minus the β spin shows that the Ni in the Cu-NiTPP has a net spin population of 1.11, while the Cu-NiTPP-spi has 1.06, confirming that overall the system experiences very similar charge transfers.

The analysis of the geometrical parameters shows that in the supported systems, the Ni-N bond distances undergo a significant enlargement; in the Cu-NiTPP it increases from 1.98 Å to 2.04 Å, while in the Cu-NiTPP-spi the variation is from 1.95 Å to 2.01 Å. This is an expected result: the presence of a new bond (Ni-Cu) reduces the strength of the previous ones (Ni-N). The Cu-Ni binding energies are calculated -0.31 eV and -0.24 eV for Cu-NiTPP and Cu-NiTPP-spi, respectively. The calculated binding energies and geometrical structures are further supported by the analysis of the Nalewajski-Mrozek bond multiplicity indices. In both Cu-NiTPP and Cu-NiTPP-spi, the $^{NM}I_{Ni\text{-}N}$ values are reduced from 0.469 and 0.464 for NiTPP and NiTPP-spi to 0.307 and 0.309 for Cu-NiTPP and Cu-NiTPP-spi, respectively. The decrement of the $^{NM}I_{Ni\text{-}N}$ values suggests a weakening of the Ni-N bond in both supported systems. The $^{NM}I_{Ni\text{-}N}$ values are almost equal in both supported systems, while the results are different for the $^{NM}I_{Ni\text{-}Cu}$ values (0.572 and 0.534 for Cu-NiTPP and Cu-NiTPP-spi, respectively). The larger values for Cu-NiTPP indicate a larger bond strength and confirm the higher interaction (see higher binding energy).

The NO_2 interaction with the Ni(I)TPP or Ni(I)TPP-spi systems have been modeled considering

the Cu-NiTPP-NO_2 and Cu-NiTPP-spi-NO_2 clusters. The Ni-NO_2 bond is experimentally observed in the NiTPP supported systems, hence optimization calculations have been carried out by assuming either 0 or 2 unpaired electrons. Indeed, both the Cu-NiTPP cluster and isolated NO_2 molecule have an unpaired electron. Experimental and periodic calculations on metal-TPP systems show only a small increment of the TPP-surface distance (below the 0.2 Å) after coordination and the major effect is an increment of the metal-surface distance [54,213]. We tested different Ni-Cu fixed distances (from 2.2 to 3.0 Å) and selected the cluster that reproduced these behaviors. For all tests, the HS Cu-NiTPP-NO_2 cluster is more stable than the LS one and in the selected one, this stabilization is by -0.33 eV, thus only the HS state has been considered in the forthcoming discussion. Upon the Ni-NO_2 bond formation, the NiTPP conformation sensitively varies with respect to the Cu-NiTPP system (see Figure 4.38, left). The Cu-NiTPP-NO_2 structure assumes a non-planar conformation, while the planar one is observed for Cu-NiTPP. In more detail, the distance between the N (TPP) atoms and surface (Cu atom) remains the same (2.1 Å) of the non-coordinate system, but the carbon backbone assumes a bend conformation (see Figure 4.38, left, bottom). The other significant modification is found for the Ni ion: in the Cu-NiTPP it is in the same plane of the N (TPP) atoms, while in the Cu-NiTPP-NO_2 it arises from this plane of 0.61 Å, toward the NO_2 ligand. This behavior agrees with experimental and periodic calculations with metal-TPP, where the metal height after coordination arises up to 0.7 Å [54,213]. The Ni-NO_2 distance is 1.99 Å. In agreement with periodic calculations on the same system that obtained a value of 2.03 Å (see Section 3.2). The capability of the NO_2 to distort the TPP conformation is present also in the isolated NO_2 system, even if, due to the absence of the copper atom, the geometrical variations are different. The NO_2 binding energy is -0.93 eV in the Cu-NiTPP-NO_2 system, while in the isolated NiTPP-NO_2 is -0.38 eV. This trend is in perfect agreement with periodic calculations on the same system, where the binding NO_2 energy in the adsorbed systems is more than twice than the isolated one.

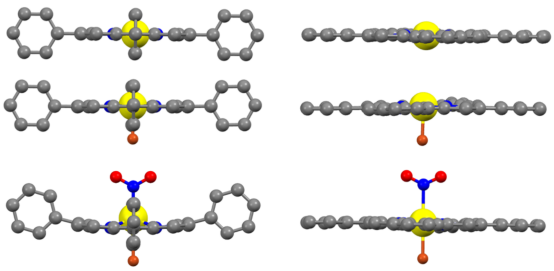

Figure 4.38: Optimized structures for left: NiTPP (top), Cu-NiTPP (center) and Cu-NiTPP-NO_2 (bottom); right: NiTPP-spi (top), Cu-NiTPP-spi (centre) and Cu-NiTPP-spi-NO_2 (bottom). Grey, red, blue, orange, and yellow spheres are C, O, N, Cu and Ni, respectively.

The detailed analysis of selected orbitals on Cu, Ni and NO_2 that mainly contribute to the Cu-NiTPP-NO_2 interaction reveals that: i) the two unpaired electrons are mainly localized on the Ni 3d AOs and in particulars the two single occupied MOs (SOMOs) are the Ni $3d_{x^2-y^2}$ and the Ni $3d_{z^2}$ AOs (see Figure 4.39); ii) the Cu *4s* AO are completely empty and (iii) the NO_2 π^* MOs are doubly occupied. These outcomes suggest that the *trans-effect* induced by the NO_2 coordination implies the oxidation of the Ni (from Ni(I) to Ni(II)), but the Ni(II) has an high spin state, different to the NiTPP, where the Ni(II) has a closed shell, hence a low spin state. The net spin polarization

calculated for Ni is 1.51, while it is 0.19 for NO_2 moiety. These results further support the oxidation of the Ni ion and its high spin state. Due to the large conformational rearrangement, there is the weakening of the direct Ni-Cu interaction, but there are new Cu-N(TPP) interactions. The Cu maintains the Cu(I) oxidation state which it had in the NiTPP-Cu system. The Ni(II) high spin oxidation state after NO_2 dosage is in prefect agreement with experiment data.

The crucial role of the copper surface to stabilize the Ni(II) high spin state becomes more clear if we compare the Cu-NiTPP-NO_2 system with the isolated NiTPP-NO_2. In the former systems, the net spin polarization is 1.51, while in the latter is 0.28. These results suggest that in the absence of the copper atom, the Ni has a +2 oxidation and low spin state (closed-shell). The value being slightly different from 0 shows a small interaction with NO_2, far from a complete transfer of one electron as in the Cu-NiTPP-NO_2 situation.

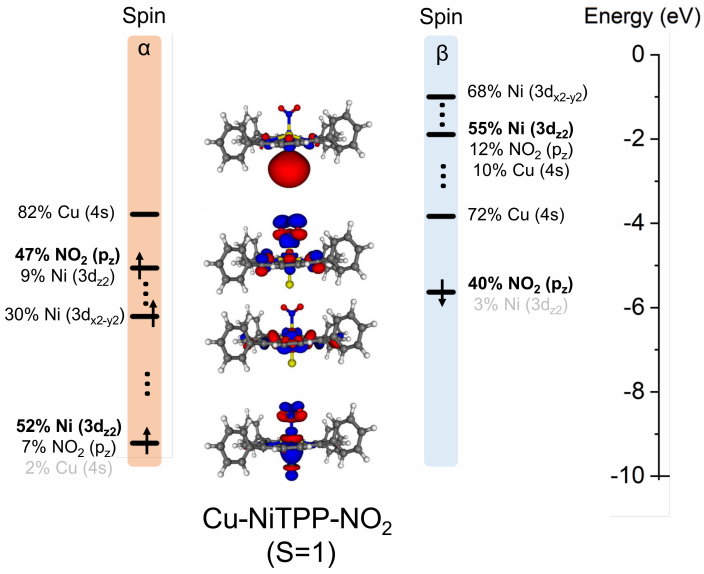

Figure 4.39: Energy level diagram associated to the Cu-NiTPP-NO_2 species at HS state. Both α and β spins are reported and black arrows indicate the occupied MOs. The relative percentage of MOs are also reported. 3D contour plots for α MOs are displayed in the insets. The comparison between α and β spin occupation shows that the two unpaired electrons are localized on the α Ni $3d_{x^2-y^2}$ and Ni $3d_{z^2}$ MOs.

The HS Cu-NiTPP-spi-NO_2 is optimized at different Ni-Cu fixed distances and we selected the cluster with the TPP-Cu distance closest to the Cu-NiTPP one, in accordance with periodic calculations on the metal-TPP system [248]. The NO_2 binding energy for the Cu-NiTPP-spi-NO_2 is -0.31 eV, which is very similar to the isolated NiTPP-spi-NO_2 one (-0.26 eV). The binding energy for the supported NiTPP-spi is sensitively lower with respect to the supported NiTPP one and the comparison between the two NO_2 binding energy values is in perfect agreement with the experimental spectra, where no NO_2 adsorption is observed for supported NiTPP-spi. The different capability to strongly adsorb the NO_2 in the supported NiTPP and NiTPP-spi can be due to the smaller conformation rearrangement of the TPP moieties (see Figure 4.38, right). Indeed, in the supported NiTPP, the large variation of the TPP conformation and the Ni chemical

coordination environment causes a larger binding energy. The larger capacity to bend the Ni coordinative environment in NiTPP can be ascribed to the difference between the NiTPP and NiTPP-spi moieties: the former has less geometrical constrains due to the absence of four indene moieties arising from the cyclodehydrogenation reaction.

For the Cu-NiTPP-spi-NO_2 system, the direct Ni-NO_2 bond, in accordance with the experimental N *1s* spectra is very weak. Indeed, the Ni-NO_2 distance found for the optimized Cu-NiTPP-spi-NO_2 geometry is sensitively higher (2.44 Å) with respect to the same distance in the Cu-NiTPP-NO_2 (1.99 Å) and ii) the N-O distance in the coordinate molecule is 1.216 Å, very similar to the isolated molecule (1.203 Å).

The analysis of the Nalewajski-Mrozek bond multiplicity indices for both the Cu-NiTPP-NO_2 and Cu-NiTPP-spi-NO_2 HS state can further support the catalytic properties. Due to the different capability to bond the NO_2 the $^{NM}I_{Ni\text{-}NO_2}$ values are the most important. In the Cu-NiTPP-NO_2 systems its value is 0.368 with a bond strength comparable with the Ni-N bond in the Cu-NiTPP system. This value dramatically decreases in the Cu-NiTPP-spi-NO_2, where $^{NM}I_{Ni\text{-}NO_2}$ in equal to 0.092. This very low bond strength can explain the incapacity of supported NiTPP-spi to bond NO_2. Also the other Nalewajski-Mrozek indices ($^{NM}I_{Ni\text{-}N}$ and $^{NM}I_{Ni\text{-}Cu}$) can be useful to better rationalize the different behavior between the two supported system with respect to the NO_2. The $^{NM}I_{Ni\text{-}Cu}$ indices in the supported systems after NO_2 adsorption are sensitively lower with respect the Cu-NiTPP and Cu-NiTPP-spi values (0.072 and 0.136 for Cu-NiTPP-NO_2 and Cu-NiTPP-spi-NO_2 respectively). This means that: i) the presence of the NO_2 strongly weakens the strength of the direct Ni-Cu bond and ii) this strength is very weak especially in Cu-NiTPP-NO_2. The influence of NO_2 is visible also on the $^{NM}I_{Ni\text{-}N}$ indexes. In particular, for the Cu-NiTPP-spi-NO_2 this value is 0.425, almost equal to the isolated NiTPP-spi-NO_2 one (0.427). This is compatible with the electronic analysis, where the presence of the NO_2, even if the interaction is weak, reduces the Ni-Cu interaction and favors the reduction of the Cu oxidation number to its original value (0). For the Cu-NiTPP-NO_2 system, the $^{NM}I_{Ni\text{-}N}$ is 0.255, lower with respect to the isolated NiTPP-NO_2 one (0.421). This low value can be explained with the strong conformational change of the TPP ring upon NO_2 ligation (see Figure 4.38). The structural variation avoids the Ni-N (TPP) direct bonds (see $^{NM}I_{Ni\text{-}N}$) and favors the Ni-NO_2 one (see $^{NM}I_{Ni\text{-}NO_2}$). The Cu-NiTPP-spi-NO_2 does not suffer a large conformation variation, hence the direct Ni-N (TPP) is still favored with respect to the Ni-NO_2 one.

The robustness of spin and oxidation states of the chelated metal ion upon thermal treatment and subsequent planarization is evidenced by spectroscopic measurements acquired on the systems before and after annealing. However, the thermally-induced planarization in NiTPP, which results in the formation of the flat NiTPP-spi, leads to the quenching of the molecular reactivity. Although, this change has been previously attributed to a different interaction between central metal and surface that would define a different occupancy of the d_{z^2} level, the results reported here do not seem to confirm this. Even though, in all likelihood, molecular flexibility plays an important role in the reactivity, also crucial is the redistribution of charge on the in-plane *3d* levels that occurs as a result of the planarization.

Chapter 5

Functionalization of NiPc and FePc

Metal–phthalocyanines (MPc) are a representative broad class of planar metal–organic complexes with several applications in organic-based electronics. They can be assumed as a good model system to investigate the interaction of metal-organic systems with a metal electrode, and its influence on the electronic structure of an anchored molecule. Owing to the chelated transition metal ion with its unique magnetic properties in the molecular structure, the MPc can be viewed as a potential candidate for building molecular magnets [250, 251]. By the on-surface coordination approach, the oxidation states of a metal ion can be modified, oxidized or reduced. This process can allow one to stabilize different spin configurations resulting in two magnetic states required to perform logic operations and to store information in molecule-based devices.

The reduction of a chelated metal ion in the tetrapyrrolic macrocycle can be achieved by anchoring of a metal porphyrin or phthalocyanine systems on a highly reactive substrate (see Chapter 3 and 4). Indeed, the charge transfer occurring at the interface between the Co- and Ni-tetraphenyl porphyrin and the copper substrate can change the oxidation state of the chelated ion and, at the same time, alter the magnetic properties of the metal-organic system. Moreover, the low valence state in the metal tetraphenyl porphyrins can be reactive to the axial ligand coordination inducing further changes in the oxidation state and in the spin configuration of the chelated ion.

The study previously done for the NiTPP and the flat form of the NiTPP, will hereafter be extended primarily to NiPc. NiPc is, like the dehydrogenated form of NiTPP, characterized by a flat structure with reduced flexibility compared to NiTPP, but with respect to NiTPP, there are differences in the electronic structure. How such differences influence molecular properties, *i.e.* oxidation and spin state and molecular reactivity toward external ligands, will then be investigated before proceeding with the functionalization of FePc on Cu(100).

5.1 NiPc on Cu(100) and O-Cu(100)

The molecular structure of NiPc is composed of four isoindole ligands bound to the nickel ion *via* pyrrole nitrogen atoms. The square planar coordination of the Ni(II) in the free (gas-phase) NiPc (D_{4h} symmetry) lifts the five-fold degeneracy of the Ni *3d* atomic orbitals (AOs) to generate b_{2g} (d_{xy}), b_{1g} ($d_{x^2-y^2}$), a_{1g} (d_{z^2}), and e_g ($d_{xz,yz}$) states. The highest occupied and lowest unoccupied molecular orbitals (HOMO and LUMO) are mainly delocalized in the Pc macrocycle forming a_{1u}

and $2e_g$ π molecular orbitals (MO). The same spin and oxidation state, namely low-spin Ni(II), can be maintained by depositing NiPc on the $\sqrt{2}$x2$\sqrt{2}$-R45°oxygen-reconstructed Cu(100) surface. Upon deposition on the oxygen-passivated copper surface, the Ni *2p* XPS spectrum shows a single peak situated at 855.5 eV BE, characteristic of the Ni(II) oxidation state. The LS Ni(II) state is further confirmed by the Ni L_3-edge NEXAFS, which displays the characteristic spectral shape and position (see Figure 5.2). The full decoupling between the molecule and the substrate for the NiPc/O-Cu(100) system is clearly visible also from the N *1s* and C *1s* XPS spectra, which present the shake-up structure typical of non-interacting molecules (see comparison with the multilayer spectra). This consideration is fully supported by the N K-edge spectrum, the strong transition intensity of which involving the LUMO shows that there is no interaction with the substrate such that leads to its occupancy.

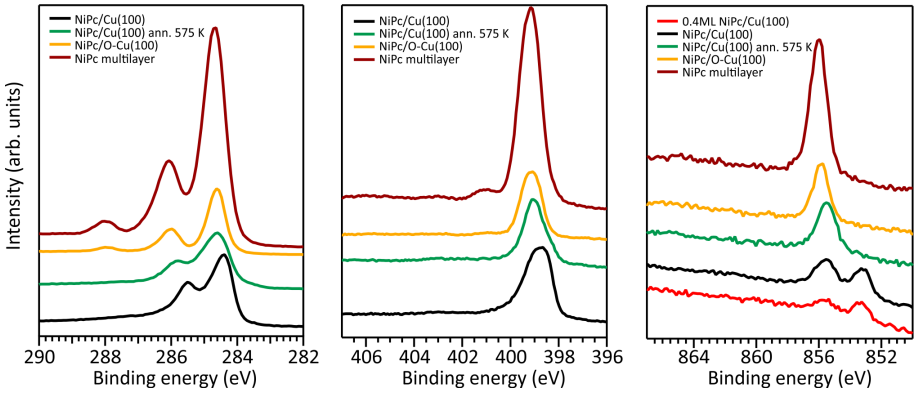

Figure 5.1: C *1s*, N *1s* and Ni *2p* XPS spectra of NiPc monolayer on Cu(100) before and after annealing to 575 K, on O-Cu(100), and in multilayer regime; Ni *2p* XPS is reported also in the sub-monolayer regime.

Upon deposition on copper, because of the strong reactivity of the substrate, one would expect a behavior similar to that previously observed for NiTPP and its dehydrogenated derivative (see Chapters 3 and 4), *i.e.*, that charge transfer from the substrate to the metal would lead to nickel reduction and its activation to the coordination of external ligands, like NO_2. However, the situation encountered after the deposition on Cu(100) is unexpectedly more complicated.

Even though the N K-edge NEXAFS suggests a flat-lying adsorption geometry upon deposition of NiPc on Cu(100), the multiplet structure observed in the Ni *2p* XPS spectra and the shape observed in the Ni L_3-edge NEXAFS point towards the stabilization of a high-spin Ni(II) state [181], which does not manifest any coverage-dependent behavior below the monolayer coverage (0.4, 0.75 and 1 ML coverages have been tested and for all of them the Ni L_3-edge manifest the same). The presence of such an oxidation state is unexpected, and before proceeding further in investigating its origin, its stability will be tested by stepwise annealing. Upon annealing to 575 K, the HS Ni(II) state switches to the gas-phase-like LS Ni(II) state. Indeed, after annealing the NiPc/Cu(100) interface the Ni *2p* XPS spectrum shows the presence of a single component peaked at 855.4 eV. The presence of the HS Ni(II) species is clearly visible also from the Ni L_3-edge NEXAFS, which manifest a narrower peak situated at 854.4 eV in photon energy. The nickel transition is accompanied by significant changes in the N K-edge NEXAFS spectra, suggesting variations in the nickel coordination sphere and in the coupling with the copper surface, which decrease together

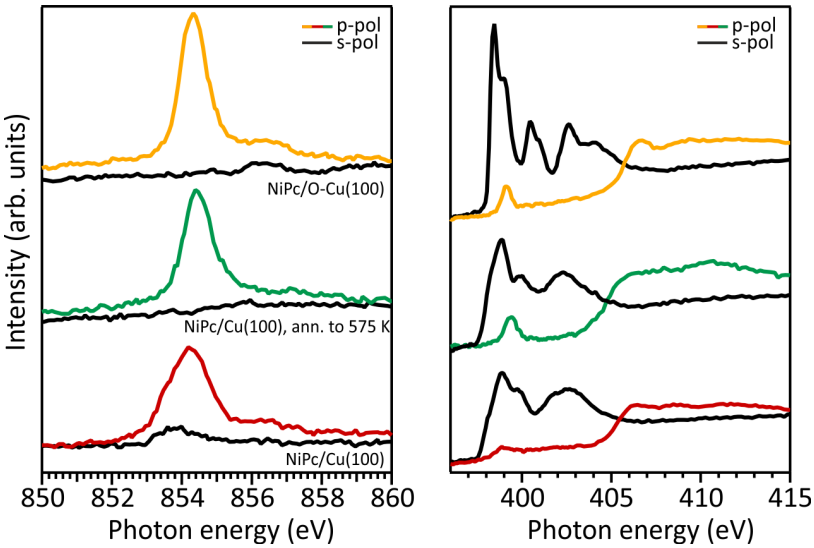

Figure 5.2: N K-edge and Ni L_3-edge NEXAFS spectra of NiPc monolayer on Cu(100) before and after annealing to 575 K, and on O-Cu(100).

with the switch from HS to LS Ni(II). The data interpretation is corroborated by the changes observed in the XMCD measured before and after annealing the NiPc/Cu(100) to 575 K. Indeed, the transition from HS to LS Ni(II) is confirmed by the quenching of the nickel magnetic moment (see Figure 5.3).

The new spin state induced by annealing remains stable over time, and no further changes are observed by annealing to higher temperatures. Based on these observations, we hypothesize the presence of two conformational minima, the first minimum stabilized by direct surface deposition and the second minimum reachable by temperature annealing. Since such changes could involve variations in the adsorption site and geometry, a direct visualization of the molecular arrangement on the surface, achievable *via* STM, is crucial for understanding what occurs at the interface.

Upon on-surface deposition, the NiPc molecules adsorb flat with respect to the surface, as had also been concluded from the analysis of the N K-edge spectrum. The NiPc molecules adsorb in the hollow position on the Cu(100) substrate with an azimuthal orientation of $\pm$ 30° with respect to the [110] crystal axis. No changes in the adsorption geometry are observed as a result of the annealing, ruling out that as the possible cause behind the spin switching [252].

Although being more common in the case of metal-phthalocyanines in which the central metal has a larger radius, it cannot be excluded that the reason for the high-to-low spin transition is maybe attributed to the vertical displacement of the central nickel, perhaps due to the strong interaction with the underlying copper in the pristine NiPc/Cu(100) system.

The DFT calculations presented in this section are performed in collaboration with Andreas Windischbacher and Peter Puschnig from the University of Graz, Austria. Theoretical outcomes show that this option is very probable. In fact, for the same Pc distance from the surface, while the displacement of nickel out of the plane of the molecule (0.27 Å toward the surface) would result in a Ni(II) HS state, the stabilization of the nickel atom in the molecular plane would coincide

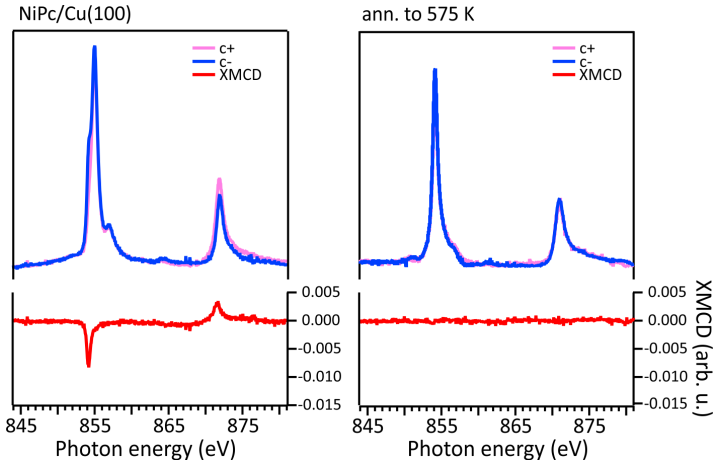

Figure 5.3: Ni $L_{3,2}$-edge NEXAFS and XMCD measurements of NiPc monolayer on Cu(100) before and after annealing to 575 K acquired at 3 K, while applying an external magnetic field of 6.8 T in normal incidence geometry.

with the stabilization of a Ni(II) LS. The two spin states are very close in energy using different functionals (PBE, PBE+U or HSE), with energy differences within 0.01-0.04 eV between the two states.

For the same distance between the macrocycle and the surface, the charge transfer from the surface to the molecule would remain unchanged, that is, occupancy of the molecular levels up to the LUMO occurs. The angle-integrated valence band acquired for the NiPc/Cu(100) system shows the presence of three peaks, located at 0.2, 1.0 and 1.6 eV in BE. While the first and the third correspond to the LUMO and HOMO of the NiPc molecule, respectively, the intermediate state (iS) rises from the superposition of the HOMO and LUMO state and is enhanced by the hybridization of the LUMO state with the surface.

Upon annealing to 575 K the NiPc/Cu(100) interface, the molecular features shift by 0.2 eV towards Fermi, while no significant variations on the azimuthal angle are observed, in agreement with the STM results commented previously. This effect is consistent with the shift of the whole molecule away from the surface, as also suggested by the N K-edge NEXAFS spectra after annealing, which shows less charge transfer on the LUMO level. DFT calculations show that already a shift upwards by 0.4 Å (height = 2.75 Å) leads to a shift of 0.2 eV on the HOMO, in perfect agreement with the experimental observations. This distancing leads also to a decrease of the DOS in the intermediate HOMO-LUMO region, which would be correlated with the lower intensity of the iS feature.

In summary, the NiPc has two accessible states, Ni(II) HS and Ni(II) LS, upon deposition on the Cu(100) substrate. Upon annealing the interface to 575 K, it is possible to switch from one to the other, inducing the high-to-low spin transition. However, despite the high reactivity of the copper surface, it is not possible to stabilize the NiPc in the Ni(I) state. As expected by analogy to Ni(II)TPP, exposing the interface to NO_2 results in no reaction with the gas.

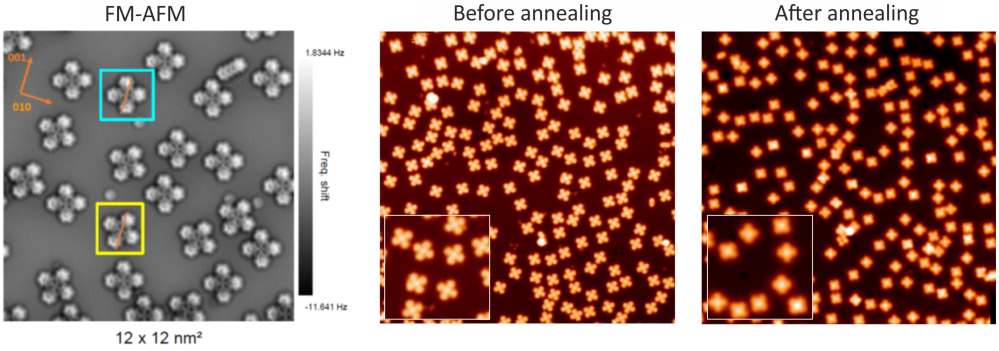

Figure 5.4: (a) AFM images acquired on the pristine NiPc/Cu(100) interface. (b-c) STM images acquired at the NiPc/Cu(100) interface before and after annealing to 575 K.

5.2 FePc on Cu(100) and O-Cu(100)

Among all the other metal phthalocyanines, the FePc molecules show a particular potential due to their unique magnetic properties as molecular magnets [250, 251].

In general, upon adsorption on a metal surface, the iron center of a tetrapyrrolic compound is expected to be subject to charge transfer, whose extent depends on both the nature of the chelated metal and the substrate reactivity. In particular, on coinage metals, the molecule-substrate interaction is weaker when the FePc is deposited on gold; it increases on silver, reaching its maximum on copper. No changes in the electronic structure of the FePc occur upon interaction with Au [126, 253], while in the case of Ag and Cu, the open Fe 3d shell hybridizes with the surface, leading to a charge transfer from the substrate to the molecular layer [126, 253, 254]. The coupling between the FePc and the substrate can alter or even completely quench the magnetic moment of the iron ion, because of the interaction occurring between the 3d shell and the substrate atoms [60, 255, 256]. In fact, the magnetic moment of the iron ion is retained upon the deposition of FePc on Au, whereas it almost vanishes when the molecule is deposited on Ag [66, 256] and it is completely quenched on Cu [254]. The introduction of a buffer layer at the organic-metal interface can be exploited to tune the molecular-surface interaction [147, 160], even for restoring the gas phase triplet spin state of the iron ion together with its net magnetic moment. The latter has been achieved on the oxygen-reconstructed copper surface, where the covalent nature of the Cu–O interaction yields a strong localization of the surface electrons inhibiting the charge transfer from the metal to the organic overlayer [147, 160]. Metal-phthalocyanines and metal-porphyrins exhibit two possible sites for axially binding ligands to the central metal ion [12] that can be used for spin manipulation, *i.e.* by changing the ligand field of the chelated ion. When these molecules are adsorbed on a surface, one of the two available binding sites is coordinated to the underlying substrate atom. The vacant site can be used both to influence the molecular-surface interaction via the so-called *surface trans-effect* [53, 62, 183, 257, 258], and to directly manipulate the spin and oxidation state of the ion within the tetrapyrrolic macrocycle. For instance, the local spin on the iron atom in FePc interfaced with the Au(111) substrate can be switched in a controlled way by ammonia and hydrogen adsorption [209, 259]. In some cases, the anchoring of atomic species to the metal ion in an organic array can switch-on or enhance the magnetic moment in the

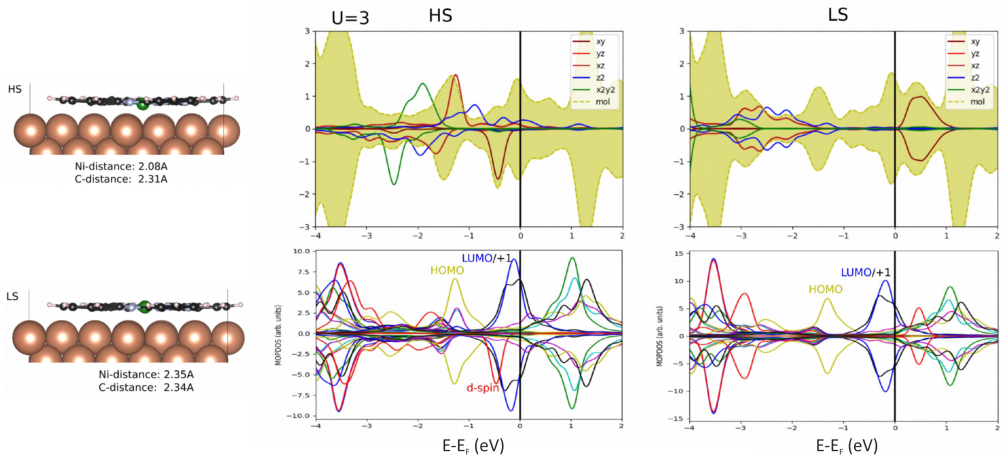

Figure 5.5: DFT simulations in dependence of the nickel position with respect to the Pc plane.

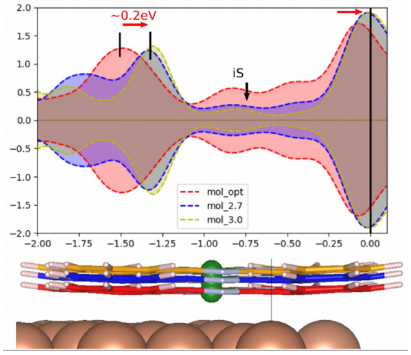

Figure 5.6: DFT simulations in dependence of the distance from the copper surface.

metalorganic layer [66, 183, 260]. In the following, by exploiting the FePc/Cu(100) interface, we will demonstrate the possibility to restore, *via* nitrogen dioxide (NO_2) dissociation at the interface, the magnetic moment of the metal ion of a Fe-phthalocyanine molecule, which is quenched when the molecule is adsorbed on the copper (100) surface.

Thanks to its relatively high reactivity, copper promotes a significant amount of charge to tetrapyrrolic compounds, as proved, for example, in the case of nickel-containing porphyrins, where the lowest unoccupied molecular orbitals (LUMOs) are filled up to the LUMO+3 and, at the same time, the molecule-substrate interaction stabilizes the Ni ion in the +1 oxidation state (see Chapter 3). To study the energy level alignment of the FePc frontier orbitals upon interaction with copper, followed by a possible charge transfer caused by the molecule-metal interaction, we performed photoemission tomography measurements combining momentum-resolved photoemission experiments and theoretical calculations [99].

Figure 5.8a shows the momentum integrated photoelectron spectrum of the FePc/Cu(100)

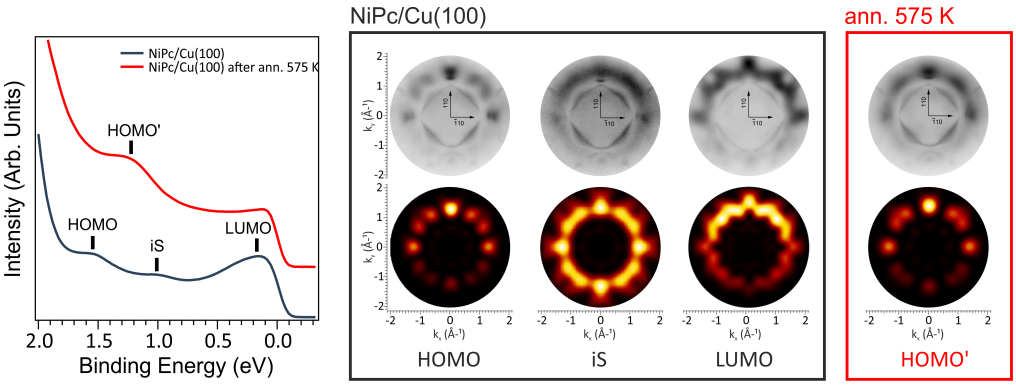

Figure 5.7: Angle-integrated valence band photoemission spectra and corresponding experimental (top) and theoretical (bottom) momentum maps acquired for the NiPc/Cu(100) before and after annealing to 575 K.

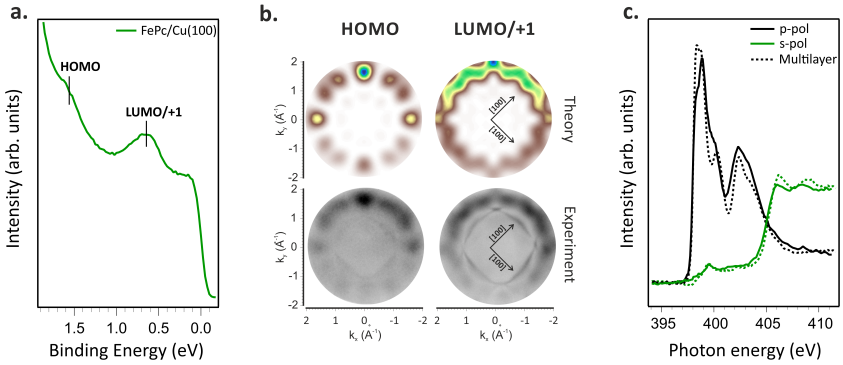

Figure 5.8: Valence band photoemission spectrum (a), and corresponding theoretical and experimental momentum maps (b) of a monolayer of FePc/Cu(100); N K-edge absorption spectra acquired in the mono- and multilayer regime (c).

interface measured at 30 eV using p-polarized synchrotron radiation. While the valence band spectrum of the bare copper substrate shows a rather featureless plateau associated with *sp*-bands [160], two prominent features are present in the FePc/Cu(100) spectrum, peaked at BEs 1.6 eV and 0.6 eV. To identify their origin, the momentum maps at corresponding BE were measured and the results are presented in the bottom row of Figure 5.8b. The experimental pattern, in addition to the features originating from the molecular states, also contains sharp *sp*-band contributions from the copper surface (visible at $|k| \approx 1.2$ Å^{-1}). The flat adsorption geometry of FePc, as determined from the N K-edge spectrum (Figure 5.8c), and the coexistence of two rotational domains due to the two-fold symmetry of the Cu(100) substrate have been taken into account in the simulated maps (see Figure 5.8b, top row). Furthermore, the intensity gradient along k_y, deriving from the experimental geometry (25° incidence angle with respect to the surface), is well-reproduced in the theoretical maps by including the $|A \cdot k|$ polarization factor [99]. The FePc molecules result to be 29 $\pm$ 5°mirrored with respect to the [100] high

symmetry direction of the substrate, in reasonable agreement with the data reported in Ref. [261]. Based on the excellent match between the experimental and theoretical data, the features at 1.6 eV and 0.6 eV BE, observed in the photoelectron spectrum of FePc/Cu(100) can be assigned to the emissions from the highest occupied molecular orbital (HOMO) of a_{1u} symmetry and the two degenerate LUMO/LUMO+1 of e_g symmetry of the FePc, respectively. Therefore the occupation of the former LUMOs is associated with a strong molecular-substrate interaction at the FePc/Cu(100) interface and these orbitals are populated due to charge donation from the metal substrate to the molecular system. FePc has previously shown a similar behavior when deposited on Ag(100) [262], but not on Au(100), suggesting a much weaker interaction of FePc with less reactive substrates and, as a consequence, no induced changes in the energy level alignment of the molecular electronic state upon adsorption [126]. Complementary information on the charge transfer mechanism can be obtained by performing NEXAFS spectroscopy [263].

Changes in the electronic structure can be determined using NEXAFS by comparing the absorption spectra measured in the monolayer and multilayer regime. The latter is used as a reference for the gas-phase like molecule and it is only weakly influenced by intermolecular and molecular-substrate interactions. While, in the monolayer regime, the intensity and energy position of the absorption resonances is strongly influenced by the latter. The NEXAFS spectra measured with p- and s-polarized light across the N K-edge, for both mono- and multilayer FePc deposited on Cu(100), are reported in Figure 5.8c. The intense spectral features observed in the photon energy range of 397-404 eV in the multilayer spectrum measured using p-polarisation are assigned to the transition of N *1s* electron to the π*-symmetry unoccupied molecular orbitals, while the resonances above the 404 eV are attributed to the $1s \rightarrow \sigma^*$ transitions [263]. The linear dichroism observed in the N K-edge spectra for the FePc monolayer on Cu surfaces, *i.e.*, the maximum intensity of the π^* transitions in p-polarisation and the almost vanishing intensity of these resonances in the spectra measured in s-polarisation, indicates that the FePc molecules are highly oriented on the copper surface, with the molecular plane lying parallel to the substrate [106]. Moreover, the decrease in intensity of the low energy π*-symmetry resonances around 399 eV, in the FePc/Cu(100) monolayer spectrum (compared to the multilayer) supports the filling of the low energy LUMOs via the charge donation from the substrate to the adsorbed layer. This agrees with the PT measurements discussed previously (see Figure 5.8a). Having studied the charge transfer taking place at the interface, in the following, we discuss how the charge transfer influences the electronic and magnetic properties of the iron ion in the adsorbed FePc. To address this point, we performed XPS measurements of the Fe $2p_{3/2}$ core level, together with NEXAFS and XMCD experiments at the Fe L-edge.

In Figure 5.9a, we compare the Fe $2p_{3/2}$ core level signals of FePc multilayer and monolayer adsorbed on the Cu(100) substrate. The monolayer spectrum, which consists of a main line peaked at 707.05 eV and a high-intensity satellite at higher BE (with the maximum at 708.8 eV), clearly resembles that of the FePc monolayer on the Cu(110) substrate [254]. The measurement of the Fe $2p_{3/2}$ core level of the multilayer phase (about 8 ML) displays a significant shift of the main peak to higher binding energies ($\sim$ 1.5 eV) with respect to the monolayer case, as well as a notable change in the satellite features (see Figure 5.9a). In the multilayer spectrum, a contribution from the first layer of FePc in direct contact with copper is still visible at 707.05 eV, suggesting that FePc deposition proceeds in a Stranski-Krastanov regime of growth. Notably, the energy shift between mono- and multilayer of the Fe $2p_{3/2}$ main line is much larger than the one observed for the peaks in the C *1s* and N *1s* spectra, namely 1.5 eV versus 0.1 eV (See Figure 5.10).

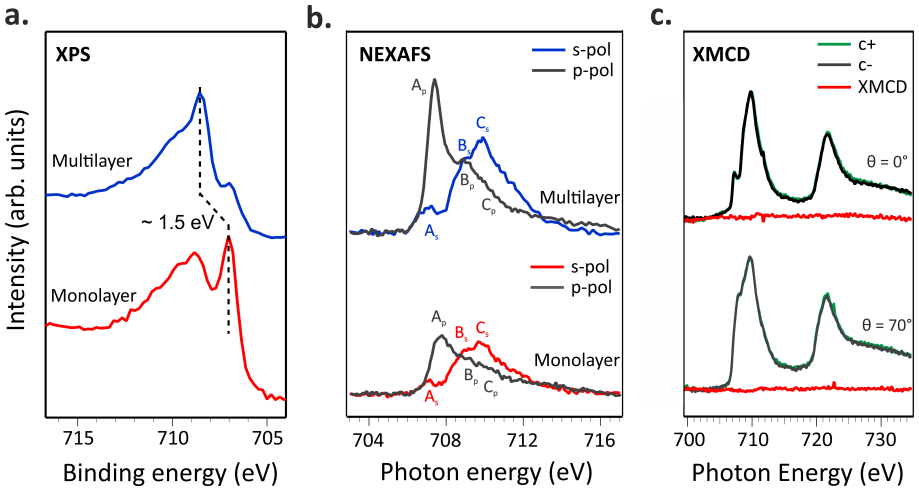

Figure 5.9: Fe $2p_{3/2}$ XPS (a) and Fe L_3-edge NEXAFS (b) spectra acquired at room temperature in the monolayer and multilayer regime; (c) Fe $L_{3,2}$-edge NEXAFS and XMCD measurements acquired at 3 K, while applying an external magnetic field of 4 T in the monolayer regime in grazing and normal incidence geometry.

Both initial and final state effects may contribute to this large energy shift at the Fe $2p_{3/2}$. From XPS measurements alone, we cannot disentangle these two contributions to the chemical shifts and the change of the spectral shape of the satellite features in the monolayer and multilayer spectra.

To get direct access to the oxidation and spin state states of the Fe ion, we acquired absorption spectra for both multi- and monolayer FePc coverages at the Fe L_3-edge (Figure 5.9b). Two groups of Fe $2p_{3/2}$ excitations with different polarization dependence are clearly visible from Figure 5.9b: in p-polarisation, the features at 707.4 and 708.9 eV (features A_p and B_p) are dominant in the spectra, whereas in s-polarisation the strongest peak C_s is observed at higher photon energy (709.8 eV). The Fe L_3-edge NEXAFS spectrum of the multilayer, as expected, resembles previously reported spectra for thin FePc films onto gold plated sapphire [251]. The Fe L_3-edges NEXAFS data of the free FePc molecule was recently analysed in great detail by Carlotto *et al.* [196]. Briefly, the 3d atomic orbitals of Fe ions transform as a_{1g} (d_{z^2}), b_{1g} ($d_{x^2-y^2}$), b_{2g} (d_{xy}) and e_g (d_{xz}, d_{yz}) in a D_{4h} symmetry.

According to the DFT/ROCIS calculations, performed in collaboration with Silvia Carlotto and Maurizio Casarin from the University of Padova, Italy, the electronic ground state (^3E_g) of free FePc corresponds to an intermediate state (IS) with a spin quantum number S = 1 and a $a_{1g}{}^1b_{2g}{}^1e_g{}^2b_{1g}{}^0$ spin up (α) and $b_{2g}{}^1e_g{}^1a_{1g}{}^0b_{1g}{}^0$ spin down (β) electronic configuration. We would like to point out that, despite the unanimous consensus about the number of unpaired electrons (two) and spin state (S = 1), different electronic terms and occupation numbers have been proposed in the literature [12, 66, 141, 250, 251, 264–267]. According to our calculations, the lowest-lying A_p and A_s features in the Fe L_3-edge multilayer spectra (see Figure 5.9b) are both generated by $\Delta S = 0$ states associated with single Fe-based 2p $\rightarrow$ 3d electronic excitations involving the a_{1g} and e_g singly occupied MOs (SOMOs). Notably, the intensity of A_p is significantly higher than that of A_s, clearly indicating that $(a_{2u} \rightarrow a_{1g})^{\perp}/(e_u \rightarrow e_g)^{\perp}$ excitations give a stronger contribution

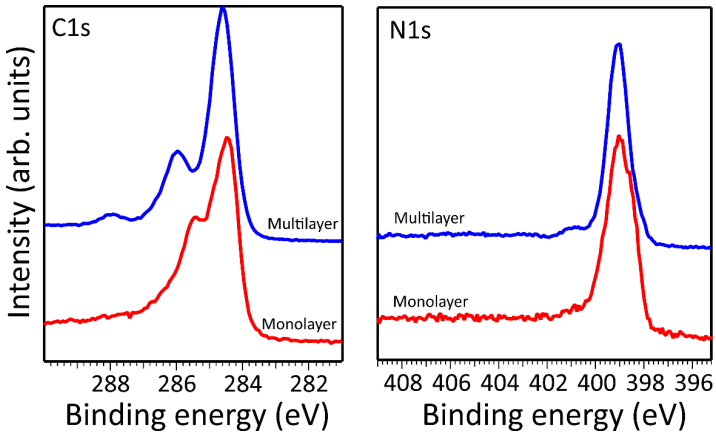

Figure 5.10: C *1s* and N *1s* (right) XPS spectra of FePc monolayer (red curve) and multilayer (blue curve) deposited on Cu(100) acquired at 515 eV.

to the spectra than the $(a_{2u} \rightarrow e_g)^{\parallel}/(e_u \rightarrow a_{1g})^{\parallel}$ ones. Regarding the B and C features at 708.9 and 709.7 eV, respectively, DFT/ROCIS results allowed us to conclude that they are associated with both single and coupled-single electronic excitations involving the $3d_{xy}$ virtual molecular orbitals (VMO) [196]. Comparing the multilayer to the monolayer spectra reported in Figure 5.9b (bottom), we notice a reduction in the intensity of the low energy resonances A_p and A_s. Notably, the excitations at high photon energy have not shown such strong changes. By referring at the theoretical predictions reported in Ref. [196], we can conclude that the transitions from the Fe $2p_{3/2}$ level to the a_{1g} and e_g molecular orbitals mainly contribute to the lower energy features in the spectra. The overall NEXAFS dichroism in the monolayer range is consistent with the expected out-of-plane-oriented d_{z^2} (a_{1g}) and d_{xz}/d_{yz} (e_g) molecular orbitals. These molecular orbitals have a stronger z-direction component, which is perpendicular to the copper surface, while the b_{1g} ($d_{x^2-y^2}$), b_{2g} (d_{xy}) orbitals lie mostly in the molecular plane parallel to the surface. Thus, the electrons of d_{z^2} and d_{xz}/d_{yz} orbitals can better couple with the electrons in the substrate than those of the b_{1g} and b_{2g} orbitals. Therefore, a_{1g} and e_g mainly participate in the molecule-surface interaction and they are partially occupied due to the charge transfer between the copper substrate and the FePc molecules at the interface.

The rearrangement of the electronic states at the Fe center, upon interaction with the Cu surface, is also expected to influence the magnetic properties of the chelated ion [66, 254, 256, 268]. Thus, the magnetic configuration of the iron atom was probed performing XMCD measurements. XMCD measurements were carried out at 3 K while applying an external magnetic field of 4 T, which ensures the saturation of the magnetic moments in the FePc thin film regime [251]. The magnetic moment of the Fe center ion is quenched on the Cu(100) surface, as evidenced by the absence of XMCD intensity both in in-plane and in out-of-plane directions indicating that the total magnetic moment of Fe is null ($\pm 0.05\ \mu_B$) (Figure 5.9c), supporting the stabilization of the Fe(II) singlet state (S = 0), in agreement with Ref. [254]. We suggest that this could be due to the enhanced coupling of the Fe d-states with the *sp*-band of copper substrate electrons. This is in clear contrast with the FePc multilayer [251] and FePc adsorbed on Au(111) [256], where an

XMCD signal is clearly visible. The change of the spin state in the adsorbed FePc molecule on a bare copper surface is also associated with the changes in energy position and shape of the Fe $2p_{3/2}$ core-level spectra discussed above.

To restore the magnetic moment of the ion, which is quenched by the molecule-surface interaction, two different approaches were previously proposed: electron doping [66, 190] or functionalization with an external ligand, *e.g.*, a small gaseous molecule [53, 62, 257, 258, 269]. Inspired by the latter, we exposed the FePc/Cu(100) interface to gaseous NO_2 to restore the magnetic moment of the iron ion. The interface was exposed to two different NO_2 doses, 30 and 100 L (referred to as low and high dose, respectively, from here on), and the changes at the Fe ion were followed by measuring the Fe $2p_{3/2}$ core-level at increasing NO_2 exposure (see Figure 5.11a). After the low dose, the Fe $2p_{3/2}$ spectrum resembles the one of the multilayer, showing the characteristic Fe(II) structures (see for comparison Figure 5.9a), *i.e.* a sharp peak at lower and broad satellite features at higher BE. However, after the high dose, we witness a quenching of the sharp line (see Figure 5.11a, top). At this point, two different scenarios regarding the interaction of NO_2 with the Fe ion have to be considered. i) The NO_2 molecules bind to the Fe center of the surface-anchored phthalocyanines in the *trans* position, decreasing the strength of the molecule-surface interaction *via* the *trans-effect* [12]. ii) The NO_2 molecules dissociate at the FePc/Cu(100) interface. In the latter scenario, the corresponding products can bind to the molecule in the trans position or intercalate between the substrate and the molecular overlayer. Further considerations on the dissociation at the interface will be discussed in the following.

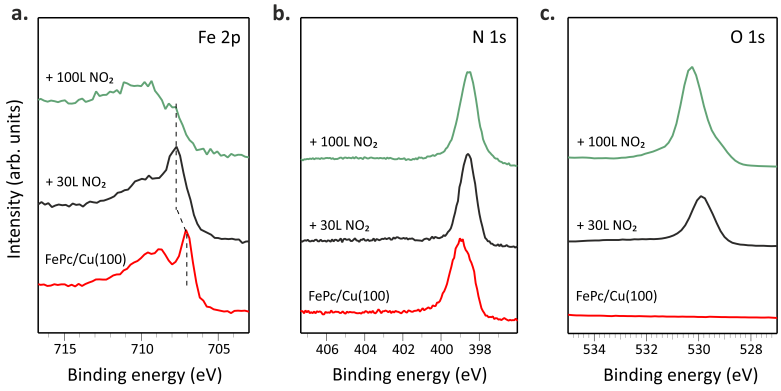

Figure 5.11: XPS spectra of FePc deposited on Cu(100) before and after exposure to increasing NO_2 doses acquired at the Fe $2p_{3/2}$ (a) and N *1s* (b) and O *1s* (c) level

The absence of a new component (expected to rise at higher binding energies) in the N *1s* spectra measured after both low and high dose of NO_2 (Figure 5.11b), as well as the conservation of the area below the peak related to the Pc nitrogen atoms, excludes the first scenario, in which intact NO_2 or other nitrogen-containing products bind to the coordinated iron atom. Therefore, the changes in the iron core-level spectra are likely caused by the oxygen atoms created at the interface by an on-surface reaction involving the dissociation of NO_2 molecules (the presence of oxygen at the FePc/Cu(100) interface is confirmed by the O *1s* spectra reported in Figure 5.11c). To elucidate whether oxygen atoms are anchored on top of the molecular layer (in *trans* position) or placed between the molecular layer and the copper substrate, the FePc molecules

have been sublimated on an oxygen pre-exposed copper surface (O-Cu(100)), which shows the $(\sqrt{2}\times 2\sqrt{2})$R45°reconstruction [270]. The Fe $2p_{3/2}$, O *1s*, N *1s*, C *1s* and Cu *3p* spectra of the FePc/O-Cu(100) interface are shown in Figure 5.12, and they very well resemble the corresponding spectra of FePc/Cu(100) after the exposure to the low NO_2 dose (see Figure 5.11a), supporting a similar chemical environment of iron in the two systems.

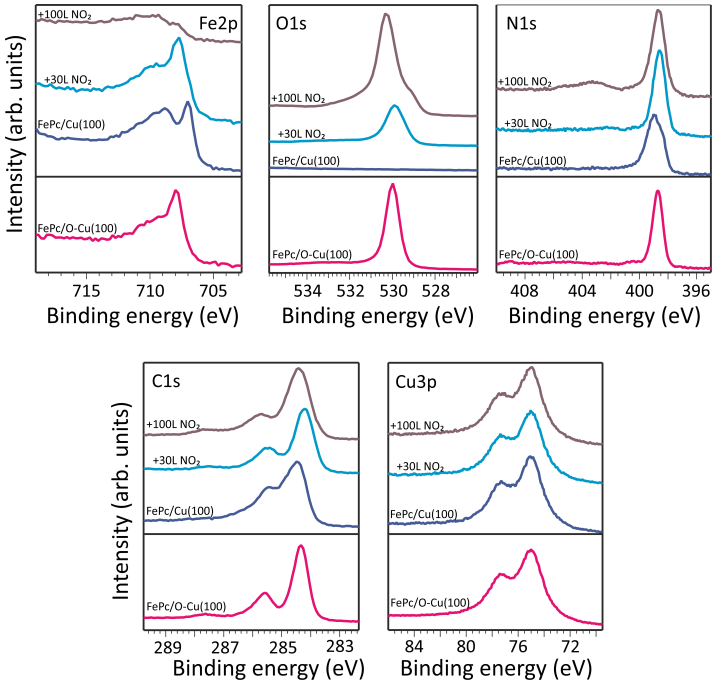

Figure 5.12: Fe $2p_{3/2}$, O *1s*, N *1s*, C *1s* and Cu *3p* XPS spectra of FePc monolayer deposited on bare Cu(100) (blue curve) and O-Cu(100) (pink curve) compared to the FePc/Cu(100) after 30L of NO_2 (light blue curve) and after 100L of NO_2 (purple curve). Fe *2p* acquired at 910 eV, O 1s at 650 eV and N *1s*, C *1s* and Cu *3p* at 515 eV.

This suggests that, upon the low NO_2 dose, oxygen atoms are formed after a dissociation reaction at the FePc/Cu(100) interface and are chemisorbed on the copper surface. This is well evident in the O *1s* spectra, where both core level spectra of O-Cu(100) and FePc/Cu(100) after the low dose are characterized by a similar BE (530.0 eV) and lineshape, *i.e.* a fingerprint of chemisorbed oxygen atoms on the copper surface. Instead, after dosing 100 L of NO_2 the O *1s* spectrum shows a clear chemical shift of the main feature to higher BE (530.3 eV) as well as the shoulder at lower BE (529.1 eV); associated with the oxidation of the copper substrate underneath the molecular layer (Cu_2O and CuO, respectively) [271]. Besides, the linear dichroism observed in the O K-edge NEXAFS spectra also confirms the presence of atomic oxygen chemisorbed on the copper surface, without further oxidation of the copper substrate. However, the clear changes in spectral shape and energy position in the O K-edge NEXAFS spectrum of FePc/O-Cu(100) as compared to the bare O-Cu(100) substrate spectrum (see Figure 5.13) suggest that FePc molecules are not fully decoupled electronically and physically from the chemisorbed oxygen, neither for FePc/O-Cu(100) nor the FePc/Cu(100) interface exposed to the low NO_2 dose.

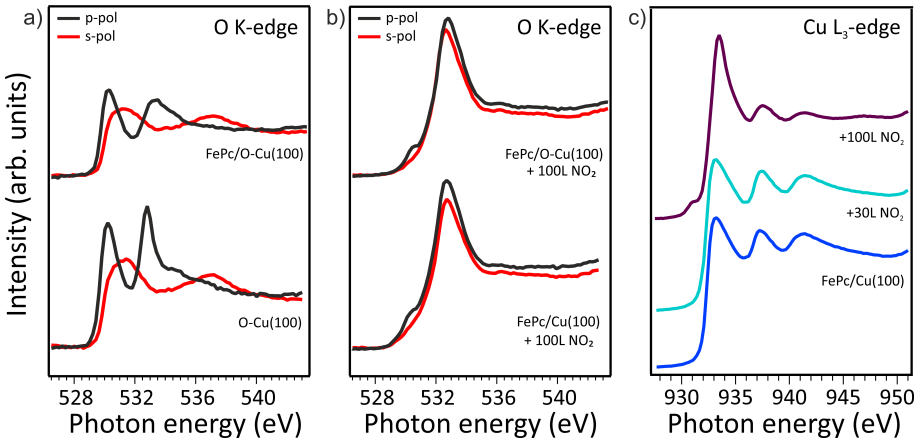

Figure 5.13: (a) O K-edge NEXAFS spectra acquired for O-Cu(100) and FePc/O-Cu(100) systems and (b) FePc/Cu(100) and FePc/O-Cu(100) after 100 L NO_2 dose; (c) Cu L_3-edge NEXAFS spectra collected at the magic angle of FePc monolayer deposited on bare Cu(100) (blue curve) and O-Cu(100) (pink curve) compared to the FePc/Cu(100) after 30 L of NO_2 (light blue curve) and after 100 L of NO_2 (purple curve).

To gain further insights into the low and high NO_2 dose trends, especially about the oxygen atoms coordination to the Fe ion, we simulated different structural arrangements for FePc on Cu(100). It is noteworthy that a leading role in determining the Fe L_3-edge NEXAFS spectrum [196] is played by the Fe nearest neighbours; thus, for the low NO_2 dose, the nature of the weakly interacting oxygen with FePc determined from the O K-edge NEXAFS data is critical, while the character of the O-Cu interaction is less relevant. The adoption of the molecular cluster approach to model a periodic system implies the saturation of the oxygen dangling bonds with hydrogen/pseudo-hydrogen atoms [272]. Therefore, the coordinated system resulting from low NO_2 dosing has been modelled by considering the free molecular complex I (see its optimized structure in Figure 5.14) characterized by the presence of a single oxygen atom of a water molecule placed at 1.8 Å from the Fe(II) ion [273]. The Fe L-edge NEXAFS modeling has been carried out for both s- and p-polarized excitation. The resulting good agreement between theory and experiment is a clear indication of the adopted model feasibility.

The comparison between theoretical results (see Figure 5.14, bottom row) and experimental evidence recorded at low (30 L) NO_2 dosing (see Figure 5.14, top row) encourages us to assess that NO_2 initially dissociates at the FePc/Cu(100) interface and generates single oxygen atoms, which intercalate between the FePc layer and chemisorb on the copper surface. The intercalation of the oxygen atoms results in the partial decoupling of the molecules from the substrate and the restoring of the original FePc gas-phase spin state (S = 1). As far as the detailed assignment of the L_3-edge spectrum of the decoupled FePc is concerned, the lowest-lying features in p (A_p) and s (A_s) polarization (see Figure 5.14, bottom row) are both associated with electronic states with $\Delta S = 0$, generated by single Fe $2p \rightarrow$ Fe $3d$ electronic excitations involving the $3d_{z^2}$ and $3d_{xz}$ singly occupied MOs (SOMOs). In contrast, $\Delta S = 0, \pm 1$ electronic states contribute to B_s. Single ($2p \rightarrow d_{z^2}/\pi^*$ Pc-based VMO) and coupled-single (Fe $2p \rightarrow 3d_{xz}$ and $3d_{xz} \rightarrow 3d_{xy}\pi^*$ Pc-based VMOs) electronic excitations generate $\Delta S = 0$ states, while the $\Delta S = \pm 1$ states are all associated to metal-to-ligand-charge-transfer (MLCT) single electronic transitions. Only electronic states with

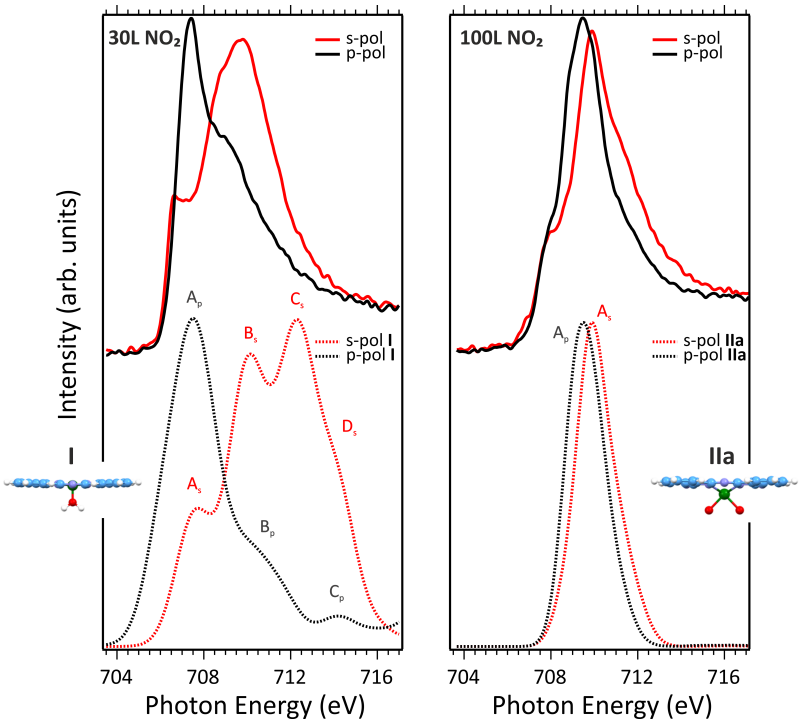

Figure 5.14: Top row: NEXAFS spectra of FePc/Cu(100) exposed to 30 L of NO_2 (left) and to 100 L of NO_2 (right). Bottom row: Fe L_3-edge NEXAFS spectra simulated for the s and p- polarized excitation. Normalized simulated spectra for **I** and **IIa** are shifted of 13.4 and 14.5 eV, respectively and have a Gaussian broadening of 2 and 1.3 eV, respectively; corresponding optimized structures for **I** and **IIa**. Blue, white, violet, red and green spheres are C, H, N, O and Fe atoms.

ΔS = 0, -1 contribute to B_p; both of them imply single electronic transitions, the former states have a Fe $2p \rightarrow 3d$ SOMOs nature; the latter ones, analogously to B_s, display an MLCT character. Finally, only ΔS = 0 electronic states contribute to C_s and D_s through single and coupled-single excitations having once again an MLCT character.

To get information about the most favourable adsorption structure formed after exposing FePc/Cu(100) to high NO_2 doses, we have examined different geometries considering two possible Fe oxidation states; *i.e.* Fe(III) and Fe(IV). The presence of the former has been modelled by considering two O atoms coordinated to FePc with a pseudo-peroxide coordination, the FePc(η^2-O_2) complex, (**IIa**, see Figure 5.14) whose electronic properties have been thoroughly described in Ref. [196]. As far as Fe^{IV} is concerned, two different models have been tested: the former implied the presence of two O atoms in a trans arrangement (**IIb**, Figure 5.15) with respect to FePc plane, while the latter involves the formation of an oxoiron(IV)Pc (**IIc**) (Figure 5.15) complex.

Among the different spin states considered for **IIb** and **IIc**, the most stable species corresponds to a triplet spin state with two unpaired electrons on the Fe=O fragment, in agreement with the literature [274]. As such, it is noteworthy that linear dichroism is well evident in the modeled spectra of **IIb** and **IIc** (see Figure 5.15), while it is absent in the spectra of **IIa** complex (see Figure

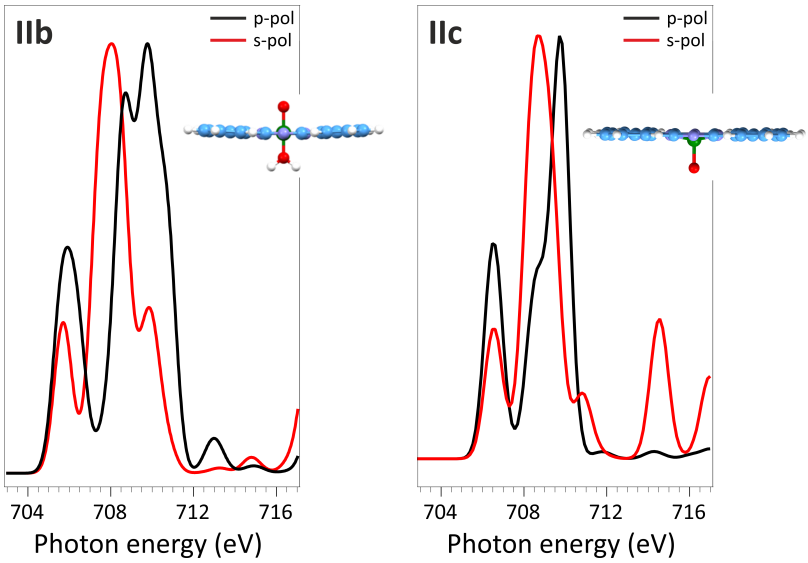

Figure 5.15: Fe L-edge NEXAFS spectra simulated for the s and p-polarized excitation. Normalized simulated spectra for **IIb** (O=Fe(OH_2)Pc) and **IIc** (O=FePc) are shifted of 9.6 eV and 10.1 eV, respectively. They have a Gaussian broadening of 1 eV. In the optimized structures for **IIb** and **IIc**, blue, white, violet, red and green spheres are C, H, N, O and Fe atoms.

5.14). As a whole, the comparison between simulated and experimental NEXAFS spectra at high (100 L) NO_2 dosage shows that **IIa** is the most favorable complex formed at the interface and rules out the presence of a relevant percentage of **IIb** or **IIc** species. A similar scenario has been observed for the FePc/Ag(110) interface exposed to oxygen [196, 275]. The use of the FePc(η^2-O_2) cluster shows a very good agreement between theory and experiment thus providing support to the presence of oxygen atoms lying in between FePc and the substrate and information about the relevant role of the substrate on the NO_2 dissociation. In detail, the single peak characterizing both the s- and p-polarized L_3-edge spectrum of the *cis* complex is mainly (80%) due to electronic states associated to transitions having $\Delta S = 0$ and corresponding to Fe(III) $2p$-based $\rightarrow$ $3d$-based single electronic excitations involving the d_{z^2}, d_{xz} and d_{xy} SOMOs. Interestingly, the MLCT electronic state generated by Fe(III) $2p \rightarrow \pi^*$ MLCT excitations with $\Delta S = -1$ significantly contributes to the higher excitation energy side of both peaks. Despite the overall agreement between experimental and simulated (see Figure 5.14, right) spectra, we have to point out that in the simulated spectrum **IIa** the evident shoulder on the lower excitation energy side of the s- and p-polarized spectra is not well reproduced. This feature is rather associated with the co-presence of residual molecules at the interface in the single-oxygen structure **I**. The NEXAFS spectra at O K-edge measured after the high dose (see Figure 5.13) are in good agreement with previous measurements for Cu_2O [271, 276], thus supporting the oxidation of the copper substrate after the exposure of FePc/Cu(100) interface to high NO_2 dose.

To summarize, the calculation shows that the **I** structure (low NO_2 dose) is associated with Fe(II) species with an intermediate spin state (S = 1), while binding of the second oxygen atom (**IIa** configuration) induces the oxidation of the iron ion (Fe(II) $\rightarrow$ Fe(III) transition). In agreement with

theoretical and experimental data, the *trans* adsorption configuration (**IIb** structure) is not formed at the present experimental condition. At this point, we can analyse the changes of the spin states and oxidation states in the **I** and **IIa** structures in comparison with XMCD data measured at Fe $L_{3,2}$-edge after stepwise increasing the dose of NO_2 (see Figure 5.16).

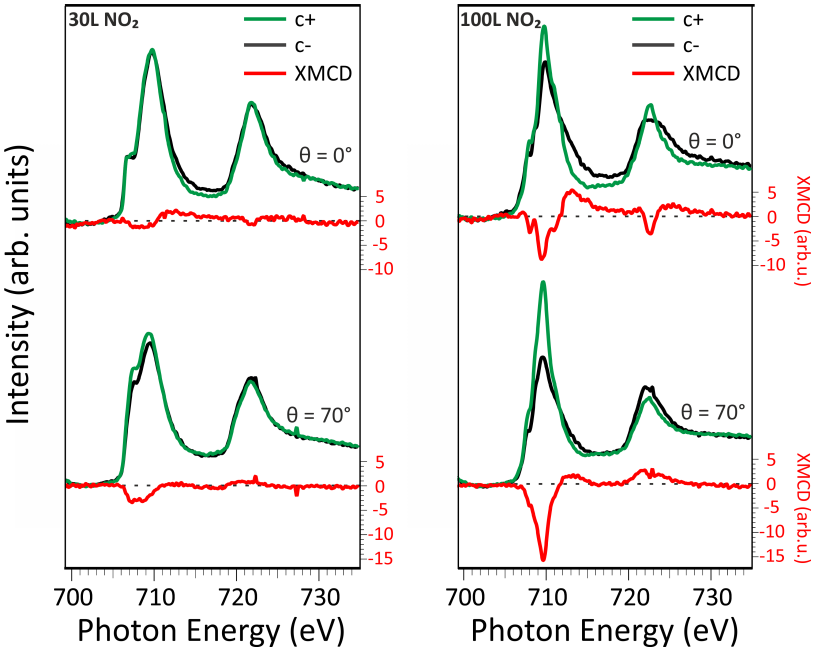

Figure 5.16: NEXAFS and XMCD spectra of FePc/Cu(100) exposed to 30 L of NO_2 (left) and to 100 L of NO_2 (right), acquired at 3 K, while applying an external magnetic field of 4 T.

As previously remarked, the Fe L-edge XMCD of the FePc is completely quenched on Cu(100). However, exposing the system to increasing NO_2 doses, the iron magnetic moment gradually increases and develops a sizable in-plane magnetic anisotropy. The orbital and spin components of the Fe magnetic moment projected along the field direction for a given incidence angle can be obtained from the sum rule analysis [110, 111]. We must point out that in the effective spin magnetic moment obtained from the sum rule analysis, the dipolar term T_z could induce big discrepancies between the effective $m_{S,eff}$ and m_S. To take this into account, based on previous multiplet calculations on the FePc system, we considered an error of 30% on m_S [277]. For calculating the magnetic moments, we have assumed 4 holes h_d for the intermediate dose and 5 holes for the higher dose, with the holes localized on the SOMO d_{z^2}, d_{xy} and d_{xz} and on the completely empty d_{yz} [196]. The XMCD measurements for the lower NO_2 dose confirm the recovery of the triplet spin state (S = 1). Indeed, the total magnetic moment m_{tot} in the molecular plane (0.46 μ_B, m_s and m_L values for the two doses are given in Table 5.1 for the in-plane direction) is comparable with the one reported for a film of 0.5 ML FePc deposited on a ferromagnetic Co(001) substrate (0.56 μ_B) [60]. Comparing the intermediate and high dose XMCD spectra, a strong increase of the m_{tot} to 2.14 μ_B (see Table 5.1) further confirms the change in the oxidation

state, as the transition from ferrous to ferric phthalocyanine is followed by the increasing of the number of unpaired electrons (from 2 to 3) that contribute to the organic layer magnetism.

As the XMCD intensity is proportional to the projection of the magnetic moment along the X-ray incidence direction, the higher intensity of the measured XMCD at grazing ($\theta = 70°$) rather than normal ($\theta = 0°$) incidence leads us to conclude that the system exhibits a preferential in-plane magnetic anisotropy at both low and high NO_2 dosing. The observed changes in the magnetic anisotropy induced by oxygen coordination are consistent with previous studies [251, 260].

FePc/Cu(100) + 30L NO_2	FePc/Cu(100) + 100L NO_2
m_L=0.08 $\pm$ 0.01 μ_B	m_L=0.17 $\pm$ 0.02 μ_B
m_S=0.38 $\pm$ 0.11 μ_B	m_S=1.97 $\pm$ 0.59 μ_B

Table 5.1: Resulting values for the effective spin moments and orbital moments of FePc/Cu(100) interface for 30 L and 100 L NO_2 doses in grazing incidence.

In summary, while the copper surface quenches the magnetic moment of the metal ion, the exposure to NO_2 and, consequently, the coordination with atomic oxygen formed due to the NO_2 dissociation at the interface gradually modifies the magnitude and orientation of the magnetization. For low NO_2 doses, FePc is decoupled from the copper substrate by the intercalation of atomic oxygen, and the molecular network recovers the typical gas-phase magnetic moment. In this regime, a single oxygen atom binds to the iron ion weakening the hybridization and the charge transfer effect at the interface, the two phenomena, which are responsible for the quenching of the magnetic moment at the FePc/Cu(100) interface. With increasing NO_2 doses, the central iron ion interacts with two oxygen atoms in a FePc(η^2-O_2) configuration, both transferred to the surface, and all the coordinated sites undergo the ferrous to ferric transition (from Fe(II) to Fe(III)), with a strong increase of the magnetic moment and the in-plane anisotropy. The FePc(η^2-O_2) complex, where two O atoms are coordinated to the Fe ion in a *pseudo*-peroxide geometry, appears to be most favorable among the different final structures considered.

Summary and conclusions

Organic electronics have increasingly found applications that were traditionally dominated by inorganic compounds, up to the extent of being incorporated into everyday objects, such as in the organic LEDs that are a built-in component of TVs and smartphones. Numerous are the advantages that organic compounds offer over their inorganic counterparts, first and foremost flexibility and adaptability.

Nevertheless, due to the vast amount of available organic compounds and combinations, fundamental material research becomes crucial in the understanding of the physical processes governing the molecular (opto-)electronic properties. This type of research is typically conducted on simple archetype samples rather than actual devices or prototypes. Among the plethora of available organic molecules, tetrapyrrolic compounds, *i.e.* porphyrins and phthalocyanines, are well suited for such studies due to their high stability and commercial availability. Instead of the circuits and mechanisms found in a performing device, their complexity can be reduced to the interface between molecules and a appropriate substrate. This intentional reduction in complexity allows to identify the material properties and their origin.

The properties to be taken into account at the interface are multiple, but with the goal of implementing the information obtained from this research in spintronic devices, special emphasis has been given to the definition of the oxidation state and spin, and, ultimately, molecular magnetism. Consequently, driven by the imperative to have metal centers having nonzero magnetic moment, the study was devoted to porphyrins and phthalocyanines containing the transition metals iron, cobalt and nickel.

Being interested not only in the presence of magnetism at the molecule-metal interface, but especially about the possibility of tuning spin properties via external *stimuli*, *i.e.*, functionalization with an axial ligand, the substrate choice becomes even more crucial.

Thus, the most common coinage metals, gold, silver and copper, characterized by increasing surface reactivity in combination with nickel and cobalt tetraphenylporphyrins were examined. From gold to copper, the changes induced by substrate interaction on the core metal are significant, and the associated effects are interesting.

In the case of nickel tetraphenylporphyrin, while on gold it retains the Ni(II) low spin state characteristic of the free-standing molecule, on copper it is subject to a strong charge transfer leading to the stabilization of the Ni(I) oxidation state possessing a nonzero magnetic moment. The reduction of the central metal also allows the molecule to be functionalized with an external ligand. The reactivity of Ni(I) was tested here by exposing the system to nitrogen dioxide, NO_2, a strongly oxidizing toxic gas, at room temperature. The surface trans effect observed in the interaction with NO_2 leads to oxidation of the central nickel and stabilization of a new spin state, Ni(II) high spin, which still possesses magnetism as demonstrated by XMCD measurements.

Also after the interaction with the ligand, the molecular macrocycle remains coupled to the copper surface and is still subject to charge transfer, maintaining the opto-electronic properties it possessed before ligand coordination.

Moreover, the strong molecule-substrate interaction at the basis of the macrocycle reduction results in effective pinning of the molecule to its adsorption site, thus preventing any molecular displacement in the overlayer lattice, which would eventually allow temperature-induced intramolecular modifications. The strong thermal stability of the Ni(I)TPP network supported by copper paves the way to the application of this reactive interface in the field of heterogeneous catalysis, gas sensing and surface magneto-chemistry, where temperatures up to 620 K can be used to regenerate the pristine properties of the active molecular layer. Annealing to 470 K is sufficient to desorb NO_2 from the NiTPP/Cu(100) system.

At this point, the comparison with the cobalt tetraphenylporphyrin is crucial for defining the influence of the metal ion and the importance of unpaired electrons in the molecular reactivity. Indeed, since NiTPP interacts with NO_2 in such a way that a reduced oxidation state and unpaired spin are present in the same system, it is not possible to understand which of the two factors plays a main role in the interaction. To answer this question, CoTPP was stabilized in two different states, closed-shell Co(I) on the bare and open-shell Co(II) on the oxygen-passivated copper surface, and exposed to increasing doses of NO_2. Experimental observations demonstrate that the on-surface reactivity of the metal tetraphenylporphyrin is driven by the oxidation state, rather than by the presence of an unpaired electron in the d_{z^2} atomic orbital. The interaction with NO_2 leads to the $\mathrm{Co(I)} \rightleftharpoons \mathrm{Co(III)}$ reversible reaction. This high catalytic activity derives only from the coupling to the copper surface, in fact no interaction with NO_2 has been detected on silver and gold.

Another factor that strongly influences molecular properties is the molecular flexibility. A first example of this is given by alkali metal doping. Thanks to their flexibility, metal tetraphenylporphyrins can assume different conformations in the complexes formed with the potassium atoms and, depending on molecular conformation and the planarity of the macrocycle, the reduction of the central metal takes place or not. Therefore, to study the effect of molecular conformation in the catalytic activity of the central metal, the planarization in porphyrins was induced by temperature annealing.

Considering that the strong pinning between the copper surface and the nickel tetraphenylporphyrin and the formation of a closed-packed layer inhibits the flattening of the molecule, the planarization reaction was first induced on silver. Both in the case of metal octaethylporphyrins and metal tetraphenylporphyrins it has been shown that it is possible to successfully induce the dehydrogenation reaction on silver and that photoemission tomography is an efficient method to follow this reaction. The planarization reaction on silver does not induce strong changes on the central metal for either of the two porphyrins, but in the case of tetraphenylporphyrins on silver, in which there is the coexistence of planar and saddle-shape conformations, it is observed that the planarization leads to a transfer of charge on all molecules, while prior to annealing the saddle form was not charged.

Since the molecular systems on silver did not show catalytic activity towards NO_2, they are not suitable for testing the role of planarization on reactivity. The cyclodehydrogenation reaction on copper was then induced, both for the octaethylporphyrins and for the tetraphenylporphyrins. While for octaethylporphyrins the planarization reaction proceeds easily, thanks to the flexibility of the ethyl substituents, a different planarization approach is required on copper for the

tetraphenylporphyrins. To inhibit the on-surface pinning and the formation of a closed-packed molecular overlayer prior to the transformation, metal tetraphenylporphyrin deposition has been performed while keeping the copper surface at 500 K. Both octaethyl and tetraphenylporphyrins were catalytically active towards nitrogen dioxide, but following the planarization reaction, both due to the lack of flexibility and to a redistribution of charge in the in-plane orbitals of the molecule, coordination no longer takes place, although the oxidation state of the central metal is formally maintained. This demonstrates the criticality of molecular flexibility in the interaction with NO_2.

When exposed to NO_2, even the planar metal phthalocyanines do not interact with the ligand. However, interesting observations have been made in the case of the FePc/Cu(100) interface. While the copper surface quenches the magnetic moment of the metal ion, the exposure to NO_2 and, consequently, the coordination with atomic oxygen, formed due to the NO_2 dissociation at the interface, gradually modifies the magnitude and orientation of the magnetization. For low NO_2 doses, FePc is decoupled from the copper substrate by the intercalation of atomic oxygen and the molecular network recovers the typical gas phase magnetic moment. In this regime, a single oxygen atom binds to the iron ion weakening the hybridization and the charge transfer effect at the interface, the two phenomena which are responsible for the quenching of the magnetic moment at the FePc/Cu(100) interface. With increasing NO_2 doses, the central iron ion interacts with two oxygen atoms, both transferred to the surface, and all the coordinated sites undergo the ferrous to ferric transition, with a strong increase of the magnetic moment and the in-plane anisotropy.

To conclude, in the present thesis, using a multi-technique approach, the possibility of obtaining magnetically and catalytically active molecular layers has been demonstrated by taking advantage of on-surface coordination processes. Of fundamental importance, also for future studies and possible applications, is the identification of new factors that guide the possibility of functionalizing the molecule-metal interfaces, in addition to those already known before this thesis work.

Appendix

A Highly oriented molecular p-n junctions

Metallic contacts in organic optoelectronic devices are extremely decisive for their ultimate performance [278]. In defining the properties of organic-based devices like light-emitting diodes (LEDs), photovoltaic (PV) cells and ambipolar field-effect transistors (FETs), one first has to take into account the intrinsic properties of the metal substrate, like transparency, reactivity, and especially for (opto)electronic applications, its work function. As demonstrated by several authors, tuning of the metal work function can be accomplished by using polar molecules that can self-assemble on the metal and form a highly-ordered, thin, two-dimensional (2D) layer that has an electric dipole in the desired direction [279–281]. As an example, alkanethiols and perfluorinated alkanethiols are known to form such self-assembled monolayers (SAMs) [279,282–284] on metals, and since they have opposite dipoles, they can be used to, respectively, decrease and increase [279] the work functions of metals (*i.e.* shift the vacuum energy levels [285]). Besides using the dipoles of SAMs to tune metal work functions, the interface dipole formed by SAMs can control the charge-carrier density in organic FETs [280,286]. For the realization of self-assembled monolayers, metal phthalocyanine (MPc) molecules are often used because of their stability and relatively high degree of commercialization. The controlled modification of peripheral substituents, *i.e.* the halogenation of Pcs, in particular fluorination, is a well-established method to tune electron transport. It is known that in order for a material to transport electrons (n-channel), it needs to have an accessible low-energy unoccupied molecular orbital (LUMO) level for electron injection, and sufficient π-overlap in order to achieve reasonable charge carrier mobilities [287]. Therefore, molecules with strong electron-withdrawing groups and extended π-systems are good candidates as n-channel semiconductors [288]. Besides this, a rectifying junction can be then formed with p-type unsubstituted MPcs [289–291].

Moreover, the Pc's central chelated metal ion can exhibit properties that are appealing for molecular spintronic applications [267]. In this respect, peripheral fluorination was demonstrated to induce strong changes also on the magnetic properties of the central metal ion [292]. In the past, FePc molecules and their derivatives, self-assembled in sub-monolayer and monolayer (ML) coverages on metal and oxide surfaces have been intensively studied by a variety of surface sensitive techniques, among them scanning tunneling microscopy (STM) [293], photoelectron spectroscopy (PES) [294], and near-edge X-ray absorption fine structure (NEXAFS) [265]. These experimental tools provide insight into the morphology and electronic structure of the molecules in the single adsorbed layers. Indeed, for FePc self-assembled on metal electrodes, a charge donation from the metal substrate to the molecular system influencing the electronic and magnetic properties of the iron ion in the adsorbed molecules has been observed, while the charge transfer

at the interface with and inert surface is quenched [195]. Despite their great potentialities, such high surface sensitive methods cannot be straightforwardly applied to study molecular multilayer systems and organic-organic interfaces, as often they are not capable of selectively probe each molecular layer. Therefore, a suitable technique for the investigation of these heterostacks is desirable, considering that such systems, and in particular phthalocyanine-based organic heterostructures, present a great potential for organic device applications [295]. In the present work, we have studied the influence of the degree of fluorination on electronic and structural properties in both monolayer and bilayer regimes for different FeF_xPc molecules. The use of photoemission tomography (PT), a technique that allows probing not only the on-top organic layer, but also the buried organic metal interface, gave us the means for probing, specifically, the layered molecular (p-n) heterojunctions.

In the homobilayered stacks of FePc/FePc, the lowest unoccupied molecular level in the first layer is fully filled by the charge transfer from the metal substrate, while the FePc in the second layer is decoupled from the substrate, and no charge transfer is manifested. Interestingly, fluorination has no influence on the charge transfer at the interface. However, in the homobilayered structure, the fluorinated molecules in the second layer show a different azimuthal orientation compared to the first one due to F-F repulsions. Such repulsion is completely suppressed in the heterojunctions. We underline that the strong molecular-substrate interaction in the first layer suppresses the intermixing in the bilayered heterostructures, allowing for a high stability of such interfaces. Indeed, depending on the stacking order of perhydrogenated and perfluorinated FePc, n-p and p-n junctions have been successfully designed.

Energy level alignment and molecular arrangement in FeF_xPc monolayers The molecule-substrate and intramolecular interactions in 2D monolayers define the arrangement of the molecular system and thus the interface properties can be distinctly affected by molecular orientation. Atomic substitution, such as fluorination, can be considered as a possibility to tune the interactions in the assembled molecular layer. Therefore, we first focus on the effect of fluorine substitution in iron phthalocyanine molecules self-assembled on the Ag(110) substrate on their electronic properties and adsorption geometry at the interface, *i.e.* in the first layer in direct contact with the metal electrode. Three different molecules, with increasing degree of fluorination, have been assembled on the metal electrode and, in the first place, characterized by means of XPS to prove the preservation of the stoichiometry upon surface deposition. In Figure 1a, we show the C *1s* core-level spectra of the FeF_xPc monolayers on Ag(110). Three main components are used to deconvolute the spectra, which correspond to carbon atoms bonded to other carbon atoms (C-C), carbon atoms bonded to nitrogen atoms (C-N) and carbon atoms bonded to fluorine atoms (C-F). For each component, a shake-up satellite peak was added at 1.2 ± 0.1 eV from the main component. The relative peak areas are in good agreement with the stoichiometry of the considered molecules. I_{CF}:I_{CN}:I_{CC} is 0:1:3, 1:1:2 and 2:1:1 for FePc, FeF_8Pc and $FeF_{16}Pc$, respectively.

Depending on the nature of the adsorbate and on the molecular ordering at the interface, drastic changes on the vacuum level alignment are observed. Experimentally these changes can be appreciated by measuring the variations of the metal work function ($\Delta\phi_{Ag}$) in the monolayer saturation regime, determined by measuring the secondary electron cutoff (see Figure A.1b). While a monolayer of FePc decreases the WF ($\Delta\phi_{Ag}$ = -0.2 eV), lowering the electron-injection barrier, $FeF_{16}Pc$ monolayer increases it ($\Delta\phi_{Ag}$ = +0.35 eV), leading to the lowering of the hole-injection barrier. FeF_8Pc substantially leaves the metal WF unchanged. The reduction of the WF of the

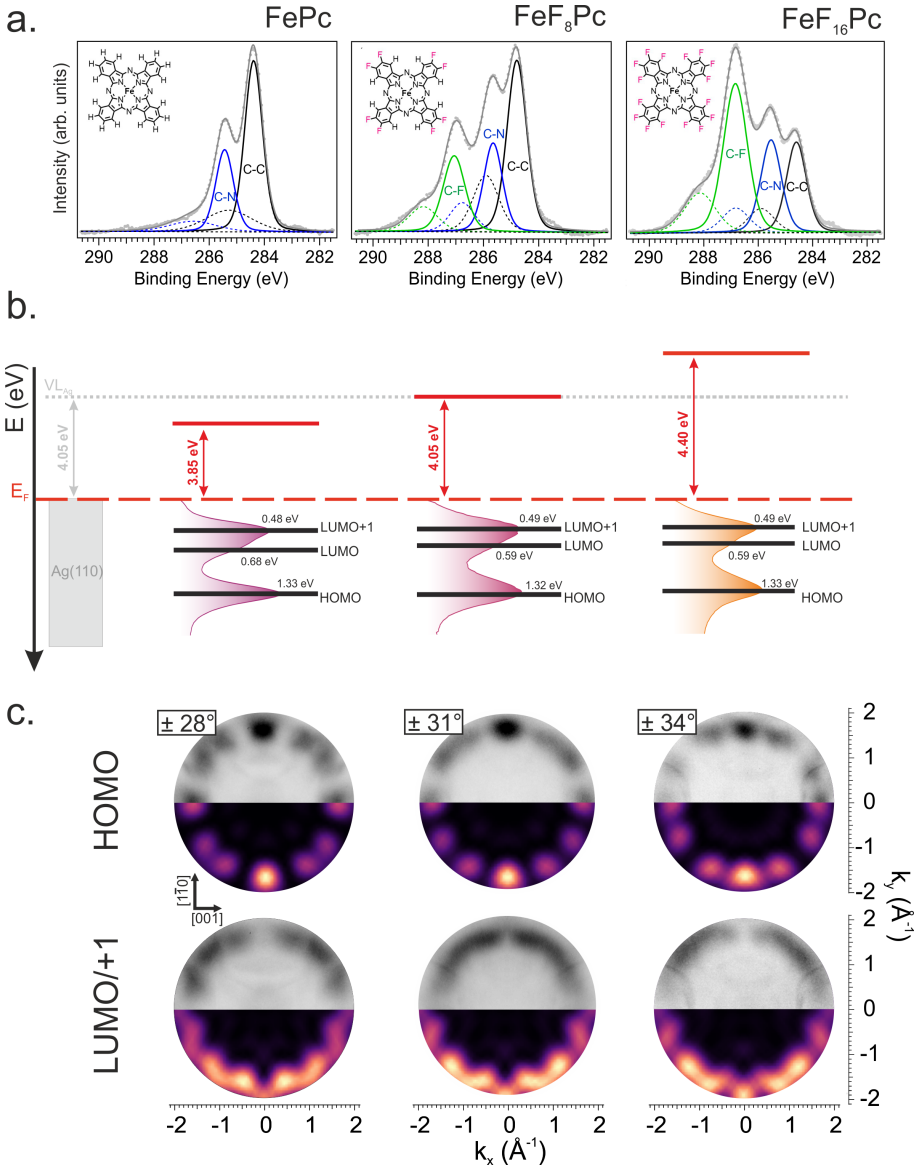

Figure A.1: C *1s* XPS core-level spectra, along with the deconvoluted components (a), energy level diagram referred to the clean Ag(110) substrate (b) and comparison between experimental (top half) and simulated (bottom half) momentum maps on the HOMO and LUMO/+1 levels (c) for FePc, FeF_8Pc and $FeF_{16}Pc$ monolayers deposited on Ag(110).

metal substrate by absorption of organic molecules has been frequently observed in the past and it has been attributed to the push-back of electrons spilling out from the metal substrate

(Pauli repulsion) [236]. The second phenomenon, which has to be considered, is the molecular dipole at the surface created due to the charge transfer effect at the organic/metal interface with positive or negative signs [100,236,296]. The molecular dipole at the organic/metal interface is localized foremost at the first molecular layer and the sign of the dipole moment of the fluorinated molecule is opposite to that of the non-fluorinated [296] one. This often causes the energy shift of former LUMOs below the Fermi level [262]. To probe this, we have measured the ultraviolet photoelectron spectra (UPS) of FePc/Ag(110), FeF_8Pc/Ag(110) and $FeF_{16}Pc$/Ag(110) interfaces as well as the bare Ag(110). While the valence band spectrum of the bare Ag(110) substrate shows a rather featureless plateau associated with the silver *sp*-bands, prominent molecular features appear for the three molecular/metal interfaces (see Figure A.1b). Interestingly, the spectra of the molecular films show two prominent features at 0.48 and 1.30 eV of BE. To identify the origin of these spectral features, we have measured 2D momentum maps at corresponding BE values for the three interfaces reported in Figure A.1c. Next, the experimental data have been compared to the square modulus of the Fourier transform (FT) of the real space molecular orbitals calculated for the gas-phase FePc, FeF_8Pc and $FeF_{16}Pc$ molecules. As this relation provides a one-to-one correspondence between the momentum distribution of the photocurrent and the molecular orbitals in the reciprocal space, it is an efficient way to assign the valence band features [99]. From Figure A.1c we note that the resemblance of simulated and measured HOMO states of a_{1u} symmetry (BE = 1.30 eV) and two degenerate LUMO/LUMO+1 states of e_g symmetry (BE = 0.48 eV) is clear, thus, the emissions are unequivocally assigned to the molecular states of metal phthalocyanine. The adsorption onto the silver substrate lowers the HOMO-LUMO energy gap in this case to 0.82 eV, substantially reduced compared to the isolated molecule, where theoretically a value of 1.58 eV has been reported [297].

Moreover, the detection of the LUMO confirms that electron donation from the metal to the LUMOs of FePc and $FeF_{16}Pc$ is independent of the molecular fluorination, while the WF shows a clear energy shift of about 0.45 eV for these two systems. The experimental pattern is shown in the top panels of Figure A.1c., in addition to the features originating from the molecular states, it also contains sharp *sp*-band contributions from the Ag(110) surface (visible at $|k| \approx 1.2$ Å^{-1}). Exploiting these features of the Ag substrate as a gauge in the momentum maps, the orientation of the molecule with respect to the substrate's high symmetry directions can be determined, allowing us to probe the effect of H-H and F-F steric repulsions at the monolayer/substrate interface. Indeed, the molecular azimuthal angles with respect to the substrate's high symmetry directions can be determined by comparison of the calculated FTs and the experimental momentum maps. Note, that the intensity gradient along k_y, deriving from the experimental geometry (25° incidence angle with respect to the surface), is well-reproduced in the theoretical maps by including the polarization factor [99]. In particular, the symmetry of the Ag(110) substrate leads to two mirror domains with oppositely tilted azimuthal angles of the molecules, and as a consequence, both of them must be taken into account for the simulated patterns. The best agreement between all experimental and corresponding simulated momentum maps is for an azimuthal orientation of FePc, FeF_8PC and $FeF_{16}Pc$ of $\pm 29°$, $\pm 31°$ and $\pm 34°$ with respect to the $[1\bar{1}0]$ direction of the substrate, respectively. The result depicted from molecular maps for FePc /Ag(110) interface agrees with the previous STM data [298]. Notably, the gradual increase of the degree of fluorination induces a continuous increment of the azimuthal angle (+3°) as an effort to minimize the intermolecular repulsions. After defining the azimuthal orientation of the two domains with respect to the high symmetry direction of the substrate, structural ordering

at the saturated monolayer regime has been evaluated by means of low energy electron diffraction (LEED) patterns acquired at a fixed incidence electron energy of 14 eV for the three systems. In all systems, the superstructure is commensurate and the relative matrices are reported in Figure A.2. The addition of fluorine atoms creates highly dipolar regions situated on the carbon-fluorine bonds. Consequently, the strong electrostatic interactions, arising from the accumulation of charge on the fluorine atoms and their increased steric repulsion, affect the molecular arrangement. The increased degree of fluorination leads to the increase of the azimuthal angle and area of the unit cells in order to minimize intermolecular steric repulsions. The expansion of the unit cell area with respect to the FePc (188.82 $Å^2$) is 12.5% (212.39 $Å^2$) and 25% (236.03 $Å^2$) for FeF_8Pc and $FeF_{16}Pc$, respectively. The area increment between the perhydrogenated system and the perfluorinated one is comparable to the increase in the van der Waals radius (1.20 Å for H and 1.47 Å for F) [299].

Layered homojunctions By contacting a second molecular layer of the same chemical nature to the first one, well-defined homobilayers on Ag(110) may be fabricated. The energy level realignment in the homojunction and the molecular ordering on the topmost layer are discussed in the following. To address these points, we performed valence band measurements, in particular PT mapping and WF determination, for FePc, FeF_8Pc and $FeF_{16}Pc$ molecules in the homobilayer film juncted on the Ag(110) surface (see Figure A.3). As mentioned above, the PT approach is one of the best-suited methods for determining the azimuthal angle and energy level alignment of molecules in the topmost as well as in the interfacial layer in the bilayer systems [300], with no erosion or other processes required unlike in the case of STM measurements [298]. Indeed, the features associated with the HOMOs of the first and second layer are well separated in energy (HOMO and $HOMO_{bil}$ in Figure A.3).

The formation of the bilayered homojunction induces a vacuum level realignment, as is well appreciable by the changes in the work function value, which increases concomitantly with the degree of halogenation; variations of 0.1 to 0.2 eV are observed going from FePc to $FeF_{16}Pc$ bilayer, respectively. The co-presence of the second layer also induces energy shifts on the molecular levels of the first layer, although being the underlying layer strongly interacting with the silver electrode. In the absence of fluorination, the bottom FePc layer exhibits the downshift in energy by 50 meV in the presence of the second layer. The trend is increasingly different when going to the fluorinated bilayers. On the other side, both FeF_8Pc and $FeF_{16}Pc$ exhibit an energy upshift of 100 meV of 150 meV, respectively.

At the same time, the first layer in direct contact with the metal electrode acts as a decoupling layer for the topmost layer, effectively screening it from the substrate. No occupation of the LUMO is observed on the second layer, and only the feature labelled as $HOMO_{bil}$ rises in the spectra as a consequence of the additional deposition. Moreover, the absence of the LUMO peak for the second layer clearly indicates that the HOMO-LUMO gap for both FePc and $FeF_{16}Pc$ systems in the topmost layer is larger than the underlying layer directly contacted with the metal substrate.

To determine the stacking geometry of the FeF_xPc bilayer systems, we have measured molecular maps of $HOMO_{bil}$ of the molecules in the topmost layer and determined the azimuthal angle in order to compare them with the ones obtained previously for the monolayer system (see Figure A.2). Substantial differences in the molecular arrangement are observed on the second layer. To minimize F-F interlayer steric repulsions, the azimuthal angles change drastically in the case of the fluorinated FeF_8Pc and $FeF_{16}Pc$ second layer, while the FePc second layer preserves the order register of the first underlying layer. Due to the hemifluorinated nature of FeF_8Pc, where the periphery is occupied by both hydrogens and fluorines, the second layer adsorbs in such a way as

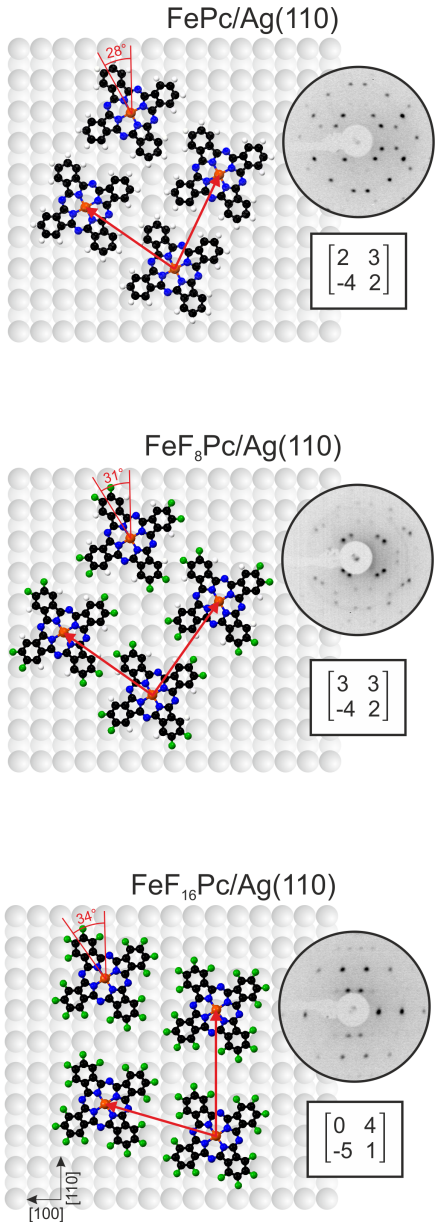

Figure A.2: Sketch of the superstructure ordering, relative LEED pattern acquired at 14 eV and derived superstructure matrix for the self-assembled monolayers of FePc, FeF_8FePC and FeF_{16}Pc on Ag(110).

to avoid any proximity between groups of the same nature, with the fluorine atoms sitting on top of the hydrogens present on the first layer and *vice versa*, as evidenced by the azimuthal angle of

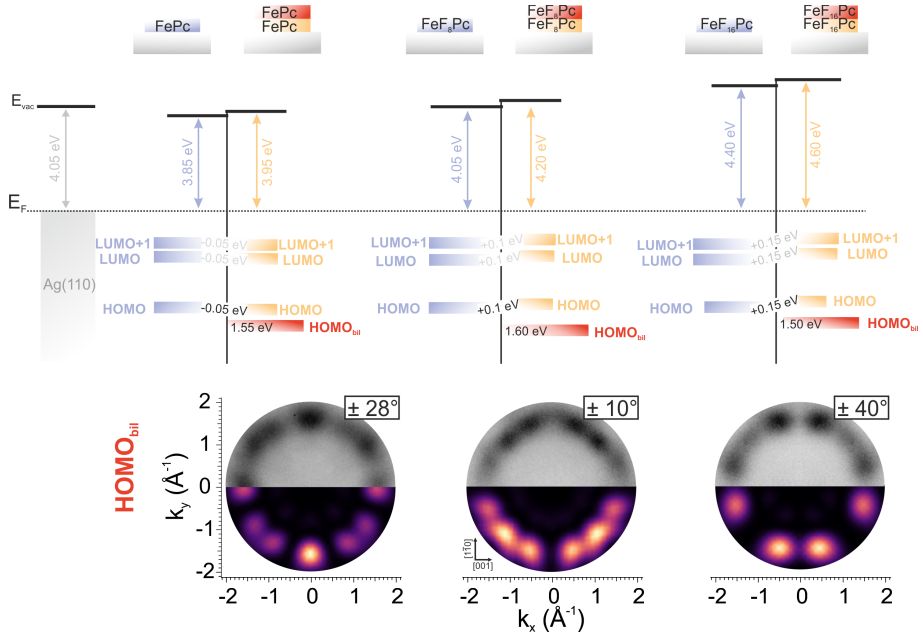

Figure A.3: Energy level diagram referred to the clean Ag(110) substrate (top) and comparison between experimental and simulated momentum maps on the $HOMO_{bil}$ level (bottom) for FePc, FeF_8Pc and $FeF_{16}Pc$ homobilayers deposited on Ag(110).

$\pm$ 10°.

Layered heterojunctions By contacting the layers of perhydrogenated FePc (p-type organic semiconductor) and perfluorinated $FeF_{16}Pc$ (n-type), it is possible to design donor-acceptor (D-A) junctions in heterobilayer systems. However, it is still a great challenge to form unary n and p-type organic semiconductor layers in the stacked molecular bilayers. Indeed, on weakly interacting substrates, where the molecules are only physisorbed, mixed phases are usually formed upon deposition of the second layer [301]. The choice of the silver substrate, where a strong molecular-substrate interaction is taking place at the interface, can allow avoiding possible intermixing effects between the two layers of the heterojunction. This strong interaction can suppress a re-ordering and yield a uniform bilayer stacked structure on the surface, allowing us to form a robust template with well distinct n/p type ($FeF_{16}Pc$/FePc) organic semiconductor layers. In the following, two different systems are investigated, namely $FeF_{16}Pc$/FePc/Ag(110) and FePc/ $FeF_{16}Pc$/Ag(110).

The second layer possesses a long-range order, which is testified by the quite sharp molecular momentum maps reported in Figure A.4 with well-defined molecular azimuthal angles in the topmost and interface layers. The adsorption geometry and azimuthal orientation are preserved from the first layer as no steric repulsion between the peripheral groups needs to be minimized due to their different nature in the heterojunctions. As in the case of the homobilayers, also here, the first layer decouples the second one from the substrate, resulting in the occupation of the sole HOMO (labelled as $HOMO_{bil}$ in Figure A.4) and leaving the LUMO of the second layer unoccupied. Interestingly, by assembling the n-type perfluorinated layer on top of the p-type

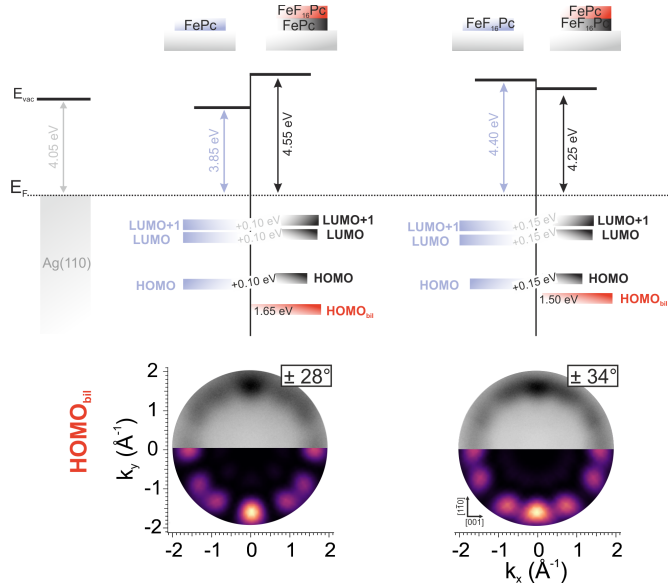

Figure A.4: Energy level diagram referred to the clean Ag(110) substrate (top) and comparison between experimental and simulated momentum maps on the $HOMO_{bil}$ level (bottom) for heterobilayers deposited on Ag(110).

FePc one, the work function of the system is significantly increased by 0.70 eV and the levels of the layer in direct contact with the electrode are upshifted by 100 meV; the $FeF_{16}Pc$ layer lowers the hole injection barrier, acting as the acceptor layer. The properties of this first heterojunction correspond to a donor-acceptor interface (n-p junction). The opposite is true when the order of the molecular layers is reversed. The deposition of a FePc layer on top of the perfluorinated first layer leads to the lowering of the work function by 0.15 eV, which corresponds to a donor character of the layer (p-n junction). The adsorption of the second layer still induces the up-shift in the energy of the levels of the first layer.

In summary, starting from the selection of a suitable substrate that allows the pinning of the layer in contact with it, we then studied in detail the electronic properties and structural order on the first layer as a function of the increasing degree of fluorination, FePc, FeF_8Pc and $FeF_{16}Pc$. Strong effects induced by fluorination are already observed in the molecular ordering, where perfluorinated FePc adopts a larger unit cell and optimizes the azimuthal angle in order to reduce F-F intermolecular steric repulsions. Significant are also the changes in the hole injection barrier, which is lowered as the degree of fluorination increases. The steric repulsions are crucial also in defining the adsorption geometry of the topmost layer in the homojunctions fabricated, where significant deviations of the azimuthal angles are observed for the fluorinated molecules. Such repulsions are completely suppressed in the layered heterojunctions. The strong molecule-substrate interaction at the interface can be used to design an organic semiconductor template for large-scale fabrication of well-defined layered p-n and n-p heterojunctions, depending on the stacking order.

Abbreviations

ARPES Angle Resolved Photoelectron Spectroscopy

ATR Attenuated Total Reflectance

BE Binding Energy

CoOEP Cobalt Octaethyl Porphyrin

CoTBP Cobalt Tetrabenzo Porphyrin

CoTPP Cobalt Tetraphenyl Porphyrin

DFT Density Functional Theory

DOS Density of States

EA Electron Affinity

FePc Iron Phthalocyanine

FT Fourier Transform

FWHM Full-width at Half-maximum

HOMO Highest Occupied Molecular Orbital

HS High Spin

IE Ionization Energy

IRAS Infrared Reflective Absorption Spectroscopy

KE Kinetic Energy

LEED Low Energy Electron Diffraction

LUMO Lowest Unoccupied Molecular Orbital

LS Low Spin

ML Monolayer

MO Molecular Orbital

MOT Molecular Orbital Tomography

MPc Metal Phthalocyanine

MSSR Metal Surface Selective Rule

MTPP Metal Tetraphenyl Porphyrin

NEXAFS Near Edge X-ray Absorption Fine Structure

NiOEP Nickel Octaethyl Porphyrin

NiPc Nickel Phthalocyanine

NiTPP Nickel Tetraphenyl Porphyrin

PDOS Projected Density of States

PEEM Photoemission Electron Microscopy

PES Photoemission Electron Spectroscopy

PT Photoemission Tomography

RT Room temperature

SFG Sum Frequency Generation

SOMO Singly Occupied Molecular Orbital

STM Scanning Tunnelling Microscopy

STS Scanning Tunneling Spectroscopy

SUMO Singly Unoccupied Molecular Orbital

TEY Total Electron Yield

UHV Ultra High Vacuum

UPS Ultraviolet Photoelectron Spectroscopy

VB Valence Band

VL Vacuum Level

WF Work Function

XAS X-ray Absorption Spectroscopy

XMCD X-ray Magnetic Circular Dichroism

XPS X-ray PhotoElectron Spectroscopy

Curriculum Vitae

Personal Data

Name	Iulia Cojocariu
Email	i.cojocariu@fz-juelich.de, iulia.cojocariu@elettra.eu
Date of Birth	14^{th} September 1993
Place of Birth	Dorohoi, Romania
Nationality	Italian

Education

12/2021-present	Research associate at Elettra Sincrotrone Trieste Supervisor: Prof. Dr. Claus Michael Schneider
10/2018-present	Ph.D. at Forschungszentrum Jülich (PGI-6) Advisor: Prof. Dr. Claus Michael Schneider
10/2016-07/2018	Master Degree in Inorganic-Physical Chemistry, Universita degli Studi di Roma "La Sapienza", Italy Thesis: "Electrosynthesis of nanostructured anodes for lithium-ion batteries for recovery of spent batteries" Advisor: Prof. Dr. Francesca Pagnanelli
10/2013-09/2016	Bachelor Degree in Chemistry, Universita degli Studi di Roma "La Sapienza", Italy Thesis: "Electrochemically reduced graphene oxide (erGO) onto n-Si(111)-H: preparation and XPS characterization" Advisor: Prof. Dr. Andrea Giacomo Marrani
2008-2013	Liceo Classico (Highschool diploma)

Publications and conference contributions

Publications related to the thesis

I. Cojocariu, S. Carlotto, M. Jugovac, L. Floreano, M. Casarin, V. Feyer, and C. M. Schneider.
Distortion-driven spin switching in electron-doped metal porphyrins
Journal of Materials Chemistry C (*Accepted for publication*).

M. Stredansky, S. Moro, M. Corva, H. Sturmeit, V. Mischke, D. Janas, **I. Cojocariu**, M. Jugovac, A. Cossaro, A. Verdini, L. Floreano, Z. Feng, A. Sala, G. Comelli, A. Windischbacher, P. Puschnig, C. Hohner, M. Kettner, J. Libuda, M. Cinchetti, C. M. Schneider, V. Feyer, E. Vesselli, and G. Zamborlini.
Disproportionation of Nitric Oxide at a Surface-Bound Nickel Porphyrinoid
Angewandte Chemie Int. Ed., **61** (2022) e202201916; Angewandte Chemie, **134** (2022), e202201916.

S. Carlotto, **I. Cojocariu**, V. Feyer, L. Floreano, and M. Casarin.
The Magnetic Behaviour of CoTPP Supported on Coinage Metal Surfaces in the Presence of Small Molecules: A Molecular Cluster Study of the Surface trans-Effect
Nanomaterials, **12** (2022) 218.

H. M. Sturmeit, **I. Cojocariu**, A. Windischbacher, P. Puschnig, C. Piamonteze, M. Jugovac, A. Sala, C. Africh, G. Comelli, A. Cossaro, A. Verdini, L. Floreano, M. Stredansky, E. Vesselli, C. Hohner, M. Kettner, J. Libuda, C. M. Schneider, G. Zamborlini, M. Cinchetti, and V. Feyer.
Room-Temperature On-Spin-Switching and Tuning in a Porphyrin-Based Multifunctional Interface
Small, (2021) 2104779.

I. Cojocariu, S. Carlotto, G. Zamborlini, M. Jugovac, L. Schio, L. Floreano, M. Casarin, V. Feyer, and C. M. Schneider.
Reversible redox reactions in metal-supported porphyrin: the role of spin and oxidation state
Journal of Material Chemistry C, **9** (2021) 12559-12565.

I. Cojocariu, F. Feyersinger, P. Puschnig, L. Schio, L. Floreano, V. Feyer, and C. M. Schneider.
Insight into intramolecular chemical structure modifications by on-surface reaction using photoemission

tomography
Chemical Communications, **57** (2021) 3050-3053.

I. Cojocariu, S. Carlotto, H. M. Sturmeit, G. Zamborlini, M. Cinchetti, A. Cossaro, A. Verdini, L. Floreano, M. Jugovac, P. Puschnig, C. Piamonteze, M. Casarin, V. Feyer, and C. M. Schneider.
Ferrous to ferric transition in Fe-phthalocyanine driven by NO_2 exposure
Chemistry - a European Journal, **27** (2021) 3526.

M. Stredansky, S. Moro, M. Corva, M. Jugovac, G. Zamborlini, V. Feyer, C. M. Schneider, **I. Cojocariu**, H. M. Sturmeit, M. Cinchetti, A. Verdini, A. Cossaro, L. Floreano, and E. Vesselli.
Vibronic Fingerprints of the Nickel Oxidation States in Surface-Supported Porphyrin Arrays
The Journal of Physical Chemistry C, **124** (2020) 6297-6303.

H. M. Sturmeit, **I. Cojocariu**, M. Jugovac, A. Cossaro, A. Verdini, L. Floreano, A. Sala, G. Comelli, S. Moro, M. Stredansky, M. Corva, E. Vesselli, P. Puschnig, C. M. Schneider, V. Feyer, G. Zamborlini, and M. Cinchetti.
Molecular anchoring stabilizes low valence Ni(I)TPP on copper against thermally induced chemical changes
Journal of Material Chemistry C, **8** (2020) 8876-8886.

I. Cojocariu, H. M. Sturmeit, G. Zamborlini, A. Cossaro, A. Verdini, L. Floreano, E. D'Incecco, M. Stredansky, E. Vesselli, M. Jugovac, V. Feyer, M. Cinchetti, and C. M. Schneider.
Evaluation of molecular orbital symmetry via oxygen-induced charge transfer quenching at a metal-organic interface
Applied Surface Science, **504** (2020) 144343.

Other publications

M. Jugovac, E. Donkor, P. Moras, **I. Cojocariu**, F. Genuzio, G. Zamborlini, G. Di Santo, L. Petaccia, N. Stojić, V. Feyer, C. M. Schneider, A. Locatelli, and T. O. Menteş.
Spin-polarized hybrid states in epitaxial and rotated graphene on cobalt
Submitted.

P. Sheverdyaeva, D. Pacile, D. Topwal, U. Manju, M. Papagno, V. Feyer, M. Jugovac, G. Zamborlini, **I. Cojocariu**, C. Tusche, X. Tan, K. Hagiwara, Y. Chen, J. Fujii, P. Moras, L Ferrari, E. Vescovo, G. Bihlmayer, and C. Carbone.
One-dimensional Rashba states with unconventional spin texture in Bi chains
Physical Review B, *In press*.

D. M. Janas, A. Droghetti, S. Ponzoni, **I. Cojocariu**, M. Jugovac, V. Feyer, M. M. Radonjić, I. Rungger, L. Chioncel, G. Zamborlini, and M. Cinchetti.
Breaking down of Stoner band ferromagnetism induced by interface formation
Submitted.

M. Jugovac, C. Tresca, **I. Cojocariu**, G. Di Santo, W. Zhao, L. Petaccia, P. Moras, G. Profeta,

and F. Bisti.
Clarifying the apparent flattening of the graphene band near the van Hove singularity
Physical Review B, **105** (2022) L241107.

E. Carrillo-Aravena, K. Finzel, R. Ray, M. Richter, T. Heider, **I. Cojocariu**, D. Baranowski, V. Feyer, L. Plucinski, M. Gruschwitz, C. Tegenkamp, and M. Ruck.
$Bi_{12}Rh_3Cu_2I_5$: A 3D Weak Topological Insulator with Monolayer Spacers and Independent Transport Channels
Physica Status Solidi B, **259** (2022) 2100447.

C.-I. Lu, C.-H. Huang, K.-H. Ou Yang, K. B. Simbulan, K.-S. Li, F. Li, J. Qi, M. Jugovac, **I. Cojocariu**, V. Feyer, C. Tusche, M.-T. Lin, T.-H. Chuang, Y.-W. Lan, and D.-H. Wei.
Spontaneously induced magnetic anisotropy in an ultrathin Co/MoS_2 heterojunction
Nanoscale Horizons, **5** (2020) 1058-1064.

P. G. Schiavi, L. Farina, R. Zanoni, P. Altimari, **I. Cojocariu**, A. Rubino, M. A. Navarra, S. Panero, and F. Pagnanelli.
Electrochemical synthesis of nanowire anodes from spent lithium ion batteries
Electrochimica Acta, **319** (2019) 481-489.

Talks

I. Cojocariu, S. Carlotto, H. M. Sturmeit, G. Zamborlini, M. Cinchetti, A. Cossaro, A. Verdini, L. Floreano, M. Jugovac, P. Puschnig, C. Piamonteze, M. Casarin, V. Feyer, and C. M. Schneider.
Ferrous to ferric transition in Fe-phthalocyanine driven by NO_2 exposure
International Conference of Young Scientists and Post-Graduate Students
Uzhorod (UA), May 26–28, 2021.

I. Cojocariu, M. Jugovac, V. Feyer, and C. M. Schneider.
Manipulation of charge donation in electron doped two-dimensional porphyrin arrays on Au(111)
EsMolNa 2019 - 12th European School on Molecular Nanoscience
Elche (ES), May 19-24, 2019.

I. Cojocariu, M. Jugovac, G. Zamborlini, V. Feyer, and C. M. Schneider.
Strong and weak interactions of metal organic networks with metal surface: adsorption geometry and electronic structure
DPG 2019 - Physik conference
Regensburg (DE) Mar 31-Apr 05, 2019.

Erklärung

Hiermit erkläre ich, dass ich die vorliegende Arbeit selbstständig und ohne fremde Hilfe verfasst habe. Ferner habe ich außer den angegebenen Quellen keine anderen Hilfsmittel benutzt. Die dem Sinn oder Wortlaut nach entnommenen Textpassagen oder Abbildungen habe ich in jedem Einzelfall kenntlich gemacht. Dieser Dissertation geht weder ein erfolgloser Promotionsversuch voraus, noch wurde sie in einem weiteren Promotionsverfahren eingereicht. Abgesehen von den angegebenen Publikationen sind die Ergebnisse dieser Dissertation unveröffentlicht.

Diese Dissertation, die den Doktorgrad "Dr. rer. nat." anstrebt, wurde von Prof. Dr. C. M. Schneider betreut.

Jülich, 28/06/2022

Iulia Cojocariu

Acknowledgments

At the end of every journey, there always comes a time to see what the adventure has enriched us with and which fellow travelers made it possible.

And that is where this section of the acknowledgments comes in.

I am deeply grateful to all the people I have met during these years and with whom I have had the pleasure of working for longer or shorter periods of time, for the opportunities I have had to learn, and for the growth you have all allowed by giving and not giving support. Each and every one of you has been fundamental for me to reach this milestone.

In a linear concept of time, there is always a before, a during and an after, and I want to start by thanking the people from before, my parents, Anisoara and Iuliu, my family, and my friends in Rome, those I have known since before I got involved in science and those I met during my studies. I thank you, who it is always nice to see on the way home, Chiara, Iulia, Giorgia, Djammo, Claudia.

I thank those who accompanied me during the process, my advisor, Prof. Claus Michael Schneider, for making this Ph.D. possible, through his advice and the trust he showed, and my supervisor, Dr. Vitaliy Feyer, who followed my progress day after day and eased what were very demanding days with his pleasant attitude. I thank my first colleague, Dr. Matteo Jugovac, for sharing his knowledge and being such a beautiful soul. I thank my bavarian colleague, Daniel Baranowski, for joining the NanoESCA team and for his good dose of veracity.

I thank all the people who played a part in this journey. I would like to thank the ALOISA beamline team, Prof. Albano Cossaro, Dr. Alberto Verdini, Dr. Luca Schio, and Dr. Luca Floreano, for their support on the beamline and helpful advice. To the latter I send my heartfelt thanks for the exchanges of opinions, for the suggestions, and for the professionalism and scientific passion shown in the projects on which we collaborated.

I would like to thank the people with whom this journey began and who allowed the first bricks of this work to be laid, Dr. Henning M. Sturmeit and Dr. Giovanni Zamborlini of the University of Dortmund. And I thank Prof. Mirko Cinchetti for making this fruitful collaboration possible.

I thank Dr. Silvia Carlotto and Prof. Maurizio Casarin of the University of Padova for the computational support given for some systems. Your enthusiasm and kind wisdom make you people with whom it is a pleasure to collaborate. I would like to thank Andreas Windischbacher, Florian Feyersinger and Prof. Peter Puschnig of the University of Graz for the other crucial part of the calculations supporting the experiments in this thesis. The computational support provided by all of you has added strength to many aspects presented here.

I would like to thank the STM groups with whom it was an honor to collaborate, Dr. Alessandro Sala and the TASC laboratory in Trieste where he works, and the group of Dr. Martin Svec at the Czech Academy of Sciences. I thank the vibrational spectroscopy groups I had the pleasure of working with: the group of Prof. Erik Vesselli of the University of Trieste and the group of Prof.

Jorge Libuda of the University of Erlangen. I would like to thank the staff of beamline X-Treme from Swiss Light Source in Switzerland, Dr. Jan Dreiser and Dr. Cinthia Piamonteze, for their help during beamtime. You have added richness in detail and quality to the work done.

I would like to thank the members of PGI-6 at the Forschungszentrum Jülich and the people working at the synchrotron in Trieste. In particular, I thank for their pleasant company and the helpful tips our neighbors, Dr. Francesca Genunzio, CarloAlberto Brondin, Dr. Andrea Locatelli, and the gentleman Dr. Onur T. Mentes.

And, finally, I thank those who will be part of the future.

Bibliography

[1] A. Wang, J. Li, and T. Zhang, "Heterogeneous single-atom catalysis," *Nature Reviews Chemistry*, vol. 2, no. 6, pp. 65–81, 2018.

[2] D. A. Reed, B. K. Keitz, J. Oktawiec, J. A. Mason, T. Runčevski, D. J. Xiao, L. E. Darago, V. Crocellà, S. Bordiga, and J. R. Long, "A spin transition mechanism for cooperative adsorption in metal-organic frameworks," *Nature*, vol. 550, no. 7674, pp. 96–100, 2017.

[3] F. D. Natterer, K. Yang, W. Paul, P. Willke, T. Choi, T. Greber, A. J. Heinrich, and C. P. Lutz, "Reading and writing single-atom magnets," *Nature*, vol. 543, no. 7644, pp. 226–228, 2017.

[4] A. A. Khajetoorians, J. Wiebe, B. Chilian, and R. Wiesendanger, "Realizing All-Spin-Based Logic Operations Atom by Atom," *Science*, vol. 332, no. 6033, pp. 1062–1064, 2011.

[5] P. Wahl, L. Diekhöner, G. Wittich, L. Vitali, M. A. Schneider, and K. Kern, "Kondo Effect of Molecular Complexes at Surfaces: Ligand Control of the Local Spin Coupling," *Physical Review Letters*, vol. 95, no. 16, p. 166601, 2005.

[6] P. Gambardella, S. Stepanow, A. Dmitriev, J. Honolka, F. M. F. de Groot, M. Lingenfelder, S. S. Gupta, D. D. Sarma, P. Bencok, S. Stanescu, S. Clair, S. Pons, N. Lin, A. P. Seitsonen, H. Brune, J. V. Barth, and K. Kern, "Supramolecular control of the magnetic anisotropy in two-dimensional high-spin Fe arrays at a metal interface," *Nature Materials*, vol. 8, no. 3, pp. 189–193, 2009.

[7] L. Giovanelli, A. Savoyant, M. Abel, F. Maccherozzi, Y. Ksari, M. Koudia, R. Hayn, F. Choueikani, E. Otero, P. Ohresser, J.-M. Themlin, S. S. Dhesi, and S. Clair, "Magnetic Coupling and Single-Ion Anisotropy in Surface-Supported Mn-Based Metal-Organic Networks," *The Journal of Physical Chemistry C*, vol. 118, no. 22, pp. 11738–11744, 2014.

[8] M. N. Faraggi, V. N. Golovach, S. Stepanow, T.-C. Tseng, N. Abdurakhmanova, C. S. Kley, A. Langner, V. Sessi, K. Kern, and A. Arnau, "Modeling Ferro- and Antiferromagnetic Interactions in Metal-Organic Coordination Networks," *The Journal of Physical Chemistry C*, vol. 119, no. 1, pp. 547–555, 2014.

[9] M. Blanco-Rey, A. Sarasola, C. Nistor, L. Persichetti, C. Stamm, C. Piamonteze, P. Gambardella, S. Stepanow, M. Otrokov, V. Golovach, and A. Arnau, "Magnetic Properties of Metal-Organic Coordination Networks Based on 3d Transition Metal Atoms," *Molecules*, vol. 23, no. 4, p. 964, 2018.

[10] S. Carlotto, M. Sambi, F. Sedona, A. Vittadini, and M. Casarin, "A Theoretical Study of the Occupied and Unoccupied Electronic Structure of High- and Intermediate-Spin Transition

Metal Phthalocyaninato (Pc) Complexes: VPc, CrPc, MnPc, and FePc," *Nanomaterials*, vol. 11, no. 1, p. 54, 2020.

[11] W. Auwärter, D. Écija, F. Klappenberger, and J. V. Barth, "Porphyrins at interfaces," *Nature Chemistry*, vol. 7, no. 2, pp. 105–120, 2015.

[12] J. M. Gottfried, "Surface chemistry of porphyrins and phthalocyanines," *Surface Science Reports*, vol. 70, no. 3, pp. 259–379, 2015.

[13] B. Cui, ed., *Recent Advances in Nanofabrication Techniques and Applications*. InTech, 2011.

[14] J. V. Barth, G. Costantini, and K. Kern, "Engineering atomic and molecular nanostructures at surfaces," *Nature*, vol. 437, no. 7059, pp. 671–679, 2005.

[15] K. Suto, S. Yoshimoto, and K. Itaya, "Two-Dimensional Self-Organization of Phthalocyanine and Porphyrin: Dependence on the Crystallographic Orientation of Au," *Journal of the American Chemical Society*, vol. 125, no. 49, pp. 14976–14977, 2003.

[16] D. Heim, D. Écija, K. Seufert, W. Auwärter, C. Aurisicchio, C. Fabbro, D. Bonifazi, and J. V. Barth, "Self-assembly of Flexible One-Dimensional Coordination Polymers on Metal Surfaces," *Journal of the American Chemical Society*, vol. 132, no. 19, pp. 6783–6790, 2010.

[17] J. V. Barth, "Molecular Architectonic on Metal Surfaces," *Annual Review of Physical Chemistry*, vol. 58, no. 1, pp. 375–407, 2007.

[18] L. Grill, M. Dyer, L. Lafferentz, M. Persson, M. V. Peters, and S. Hecht, "Nano-architectures by covalent assembly of molecular building blocks," *Nature Nanotechnology*, vol. 2, no. 11, pp. 687–691, 2007.

[19] B. D. Berezin, *Coordination compounds of porphyrins and phthalocyanines*. Wiley, 1981.

[20] C. Wöll, *Physical and Chemical Aspects of Organic Electronics From Fundamentals to Functioning Devices*. Wiley & Sons, Incorporated, John, 2009.

[21] J. V. Barth, "Fresh perspectives for surface coordination chemistry," *Surface Science*, vol. 603, no. 10-12, pp. 1533–1541, 2009.

[22] J. E. Falk, *Porphyrins and Metalloporphyrins - Their General, Physical and Coordination Chemistry and Laboratory Methods*. London: Elsevier 1964. (BBA Library), 1964.

[23] M. Bernien, J. Miguel, C. Weis, M. E. Ali, J. Kurde, B. Krumme, P. M. Panchmatia, B. Sanyal, M. Piantek, P. Srivastava, K. Baberschke, P. M. Oppeneer, O. Eriksson, W. Kuch, and H. Wende, "Tailoring the nature of magnetic coupling of Fe-porphyrin molecules to ferromagnetic substrates," *Physical Review Letters*, vol. 102, no. 4, p. 47202, 2009.

[24] X. Huang, K. Nakanishi, and N. Berova, "Porphyrins and metalloporphyrins: Versatile circular dichroic reporter groups for structural studies," *Chirality*, vol. 12, no. 4, pp. 237–255, 2000.

[25] J. Méndez, M. F. López, and J. A. Martín-Gago, "On-surface synthesis of cyclic organic molecules," *Chemical Society Reviews*, vol. 40, no. 9, p. 4578, 2011.

[26] M. Turner, O. P. H. Vaughan, G. Kyriakou, D. J. Watson, L. J. Scherer, A. C. Papageorgiou, J. K. M. Sanders, and R. M. Lambert, "Deprotection, Tethering, and Activation of a One-Legged Metalloporphyrin on a Chemically Active Metal Surface: NEXAFS, Synchrotron XPS, and STM Study of [SAc]P-Mn(III)Cl on Ag(100)," *Journal of the American Chemical Society*, vol. 131, no. 41, pp. 14913–14919, 2009.

[27] W. Auwärter, F. Klappenberger, A. Weber-Bargioni, A. Schiffrin, T. Strunskus, C. Wöll, Y. Pennec, A. Riemann, and J. V. Barth, "Conformational Adaptation and Selective Adatom Capturing of Tetrapyridyl-porphyrin Molecules on a Copper (111) Surface," *Journal of the American Chemical Society*, vol. 129, no. 36, pp. 11279–11285, 2007.

[28] F. Buchner, V. Schwald, K. Comanici, H.-P. Steinrück, and H. Marbach, "Microscopic Evidence of the Metalation of a Free-Base Porphyrin Monolayer with Iron," *ChemPhysChem*, vol. 8, no. 2, pp. 241–243, 2007.

[29] J. M. Gottfried, K. Flechtner, A. Kretschmann, T. Lukasczyk, and H.-P. Steinrück, "Direct Synthesis of a Metalloporphyrin Complex on a Surface," *Journal of the American Chemical Society*, vol. 128, no. 17, pp. 5644–5645, 2006.

[30] F. Buchner, K. Flechtner, Y. Bai, E. Zillner, I. Kellner, H.-P. Steinrück, H. Marbach, and J. M. Gottfried, "Coordination of Iron Atoms by Tetraphenylporphyrin Monolayers and Multilayers on Ag(111) and Formation of Iron-Tetraphenylporphyrin," *The Journal of Physical Chemistry C*, vol. 112, no. 39, pp. 15458–15465, 2008.

[31] T. Lukasczyk, K. Flechtner, L. R. Merte, N. Jux, F. Maier, J. M. Gottfried, and H. P. Steinrück, "Interaction of cobalt(II) tetraarylporphyrins with a Ag(111) surface studied with photoelectron spectroscopy," *Journal of Physical Chemistry C*, vol. 111, no. 7, pp. 3090–3098, 2007.

[32] W. Auwarter, A. Schiffrin, A. W. Bargioni, Y. Pennec, A. Riemann, and J. V. Barth, "Molecular nanoscience and engineering on surfaces," *International Journal of Nanotechnology*, vol. 5, no. 9/10/11/12, p. 1171, 2008.

[33] W. Auwärter, A. Weber-Bargioni, A. Riemann, A. Schiffrin, O. Gröning, R. Fasel, and J. V. Barth, "Self-assembly and conformation of tetrapyridyl-porphyrin molecules on Ag(111)," *The Journal of Chemical Physics*, vol. 124, no. 19, p. 194708, 2006.

[34] J. I. Urgel, M. Schwarz, M. Garnica, D. Stassen, D. Bonifazi, D. Ecija, J. V. Barth, and W. Auwärter, "Controlling Coordination Reactions and Assembly on a Cu(111) Supported Boron Nitride Monolayer," *Journal of the American Chemical Society*, vol. 137, no. 7, pp. 2420–2423, 2015.

[35] G. Di Santo, S. Blankenburg, C. Castellarin-Cudia, M. Fanetti, P. Borghetti, L. Sangaletti, L. Floreano, A. Verdini, E. Magnano, F. Bondino, C. A. Pignedoli, M. T. Nguyen, R. Gaspari, D. Passerone, and A. Goldoni, "Supramolecular engineering through temperature-induced chemical modification of 2H-tetraphenylporphyrin on Ag(111): Flat phenyl conformation and possible dehydrogenation reactions," *Chemistry - A European Journal*, vol. 17, no. 51, pp. 14354–14359, 2011.

[36] G. Di Santo, C. Sfiligoj, C. Castellarin-Cudia, A. Verdini, A. Cossaro, A. Morgante, L. Floreano, and A. Goldoni, "Changes of the molecule-substrate interaction upon metal inclusion into a porphyrin," *Chemistry - A European Journal*, vol. 18, no. 40, pp. 12619–12623, 2012.

[37] M. Chen, X. Feng, L. Zhang, H. Ju, Q. Xu, J. Zhu, J. M. Gottfried, K. Ibrahim, H. Qian, and J. Wang, "Direct synthesis of nickel(II) tetraphenylporphyrin and its interaction with a Au(111) surface: A comprehensive study," *Journal of Physical Chemistry C*, vol. 114, no. 21, pp. 9908–9916, 2010.

[38] A. Weber-Bargioni, W. Auwärter, F. Klappenberger, J. Reichert, S. Lefrançois, T. Strunskus, C. Wöll, A. Schiffrin, Y. Pennec, and J. V. Barth, "Visualizing the Frontier Orbitals of a Conformationally Adapted Metalloporphyrin," *ChemPhysChem*, vol. 9, no. 1, pp. 89–94, 2008.

[39] K. Diller, F. Klappenberger, M. Marschall, K. Hermann, A. Nefedov, C. Wöll, and J. V. Barth, "Self-metalation of 2H-tetraphenylporphyrin on Cu(111): An x-ray spectroscopy study," *The Journal of Chemical Physics*, vol. 136, no. 1, p. 014705, 2012.

[40] M. S. Dyer, A. Robin, S. Haq, R. Raval, M. Persson, and J. Klimeš, "Understanding the Interaction of the Porphyrin Macrocycle to Reactive Metal Substrates: Structure, Bonding, and Adatom Capture," *ACS Nano*, vol. 5, no. 3, pp. 1831–1838, 2011.

[41] K. Diller, F. Klappenberger, F. Allegretti, A. C. Papageorgiou, S. Fischer, A. Wiengarten, S. Joshi, K. Seufert, D. Écija, W. Auwärter, and J. V. Barth, "Investigating the molecule-substrate interaction of prototypic tetrapyrrole compounds: Adsorption and self-metalation of porphine on Cu(111)," *The Journal of Chemical Physics*, vol. 138, no. 15, p. 154710, 2013.

[42] F. Hanke, S. Haq, R. Raval, and M. Persson, "Heat-to-connect: Surface Commensurability Directs Organometallic One-Dimensional Self-Assembly," *ACS Nano*, vol. 5, no. 11, pp. 9093–9103, 2011.

[43] M. Affronte, "Molecular nanomagnets for information technologies," *J. Mater. Chem.*, vol. 19, no. 12, pp. 1731–1737, 2009.

[44] M. Affronte, F. Troiani, A. Ghirri, A. Candini, M. Evangelisti, V. Corradini, S. Carretta, P. Santini, G. Amoretti, F. Tuna, G. Timco, and R. E. P. Winpenny, "Single molecule magnets for quantum computation," *Journal of Physics D: Applied Physics*, vol. 40, no. 10, pp. 2999–3004, 2007.

[45] L. Bogani and W. Wernsdorfer, "Molecular spintronics using single-molecule magnets," *Nature Materials*, vol. 7, no. 3, pp. 179–186, 2008.

[46] A. L. Rizzini, C. Krull, T. Balashov, J. J. Kavich, A. Mugarza, P. S. Miedema, P. K. Thakur, V. Sessi, S. Klyatskaya, M. Ruben, S. Stepanow, and P. Gambardella, "Coupling Single Molecule Magnets to Ferromagnetic Substrates," *Physical Review Letters*, vol. 107, no. 17, p. 177205, 2011.

[47] K. Baberschke, "Magnetic switching of Fe-porphyrin molecules adsorbed on surfaces: An XAFS and XMCD study," *Journal of Physics: Conference Series*, vol. 190, p. 012012, 2009.

[48] M. Bernien, X. Xu, J. Miguel, M. Piantek, P. Eckhold, J. Luo, J. Kurde, W. Kuch, K. Baberschke, and H. Wende, "Fe-porphyrin monolayers on ferromagnetic substrates: Electronic structure and magnetic coupling strength," *Physical Review B*, vol. 76, no. 21, p. 214406, 2007.

[49] M. E. Ali, B. Sanyal, and P. M. Oppeneer, "Tuning the Magnetic Interaction between Manganese Porphyrins and Ferromagnetic Co Substrate through Dedicated Control of the Adsorption," *The Journal of Physical Chemistry C*, vol. 113, no. 32, pp. 14381–14383, 2009.

[50] A. Scheybal, T. Ramsvik, R. Bertschinger, M. Putero, F. Nolting, and T. Jung, "Induced magnetic ordering in a molecular monolayer," *Chemical Physics Letters*, vol. 411, no. 1-3, pp. 214–220, 2005.

[51] H. Wende, M. Bernien, J. Luo, C. Sorg, N. Ponpandian, J. Kurde, J. Miguel, M. Piantek, X. Xu, P. Eckhold, W. Kuch, K. Baberschke, P. M. Panchmatia, B. Sanyal, P. M. Oppeneer, and O. Eriksson, "Substrate-induced magnetic ordering and switching of iron porphyrin molecules," *Nature Materials*, vol. 6, no. 7, pp. 516–520, 2007.

[52] P. Oppeneer, P. Panchmatia, B. Sanyal, O. Eriksson, and M. Ali, "Nature of the magnetic interaction between Fe-porphyrin molecules and ferromagnetic surfaces," *Progress in Surface Science*, vol. 84, no. 1-2, pp. 18–29, 2009.

[53] C. Wäckerlin, D. Chylarecka, A. Kleibert, K. Müller, C. Iacovita, F. Nolting, T. A. Jung, and N. Ballav, "Controlling spins in adsorbed molecules by a chemical switch," *Nature Communications*, vol. 1, no. 1, p. 61, 2010.

[54] C. Wäckerlin, K. Tarafder, D. Siewert, J. Girovsky, T. Hählen, C. Iacovita, A. Kleibert, F. Nolting, T. A. Jung, P. M. Oppeneer, and N. Ballav, "On-surface coordination chemistry of planar molecular spin systems: novel magnetochemical effects induced by axial ligands," *Chem. Sci.*, vol. 3, pp. 3154–3160, 2012.

[55] D. Chylarecka, C. Wäckerlin, T. K. Kim, K. Müller, F. Nolting, A. Kleibert, N. Ballav, and T. A. Jung, "Self-Assembly and Superexchange Coupling of Magnetic Molecules on Oxygen-Reconstructed Ferromagnetic Thin Film," *The Journal of Physical Chemistry Letters*, vol. 1, no. 9, pp. 1408–1413, 2010.

[56] D. Chylarecka, T. K. Kim, K. Tarafder, K. Müller, K. Gödel, I. Czekaj, C. Wäckerlin, M. Cinchetti, M. E. Ali, C. Piamonteze, F. Schmitt, J.-P. Wüstenberg, C. Ziegler, F. Nolting, M. Aeschlimann, P. M. Oppeneer, N. Ballav, and T. A. Jung, "Indirect Magnetic Coupling of Manganese Porphyrin to a Ferromagnetic Cobalt Substrate," *The Journal of Physical Chemistry C*, vol. 115, no. 4, pp. 1295–1301, 2010.

[57] T. Suzuki, M. Kurahashi, and Y. Yamauchi, "Spin Polarization in Molecular Orbitals of Copper-Phthalocyanine Deposited on a Magnetized Fe(100) substrate," *The Journal of Physical Chemistry B*, vol. 106, no. 31, pp. 7643–7646, 2002.

[58] C. Iacovita, M. V. Rastei, B. W. Heinrich, T. Brumme, J. Kortus, L. Limot, and J. P. Bucher, "Visualizing the Spin of Individual Cobalt-Phthalocyanine Molecules," *Physical Review Letters*, vol. 101, no. 11, p. 116602, 2008.

[59] S. Javaid, M. Bowen, S. Boukari, L. Joly, J.-B. Beaufrand, X. Chen, Y. J. Dappe, F. Scheurer, J.-P. Kappler, J. Arabski, W. Wulfhekel, M. Alouani, and E. Beaurepaire, "Impact on Interface Spin Polarization of Molecular Bonding to Metallic Surfaces," *Physical Review Letters*, vol. 105, no. 7, p. 077201, 2010.

[60] E. Annese, F. Casolari, J. Fujii, and G. Rossi, "Interface magnetic coupling of Fe-phthalocyanine layers on a ferromagnetic surface," *Physical Review B*, vol. 87, no. 5, p. 54420, 2013.

[61] C. M. Drain, J. D. Batteas, G. W. Flynn, T. Milic, N. Chi, D. G. Yablon, and H. Sommers, "Designing supramolecular porphyrin arrays that self-organize into nanoscale optical and magnetic materials," *Proceedings of the National Academy of Sciences*, vol. 99, no. suppl_2, pp. 6498–6502, 2002.

[62] W. Hieringer, K. Flechtner, A. Kretschmann, K. Seufert, W. Auwärter, J. V. Barth, A. Görling, H.-P. Steinrück, and J. M. Gottfried, "The Surface Trans Effect: Influence of Axial Ligands on the Surface Chemical Bonds of Adsorbed Metalloporphyrins," *Journal of the American Chemical Society*, vol. 133, no. 16, pp. 6206–6222, 2011.

[63] K. Flechtner, A. Kretschmann, H.-P. Steinrück, and J. M. Gottfried, "NO-Induced Reversible Switching of the Electronic Interaction between a Porphyrin-Coordinated Cobalt Ion and a Silver Surface," *Journal of the American Chemical Society*, vol. 129, no. 40, pp. 12110–12111, 2007.

[64] K. Eguchi, Y. Takagi, T. Nakagawa, and T. Yokoyama, "Magnetic Interactions of Vanadyl Phthalocyanine with Ferromagnetic Iron, Cobalt, and Nickel Surfaces," *The Journal of Physical Chemistry C*, vol. 118, no. 31, pp. 17633–17637, 2014.

[65] C. Krull, R. Robles, A. Mugarza, and P. Gambardella, "Site- and orbital-dependent charge donation and spin manipulation in electron-doped metal phthalocyanines," *Nature Materials*, vol. 12, no. 4, pp. 337–343, 2013.

[66] S. Stepanow, A. Lodi Rizzini, C. Krull, J. Kavich, J. C. Cezar, F. Yakhou-Harris, P. M. Sheverdyaeva, P. Moras, C. Carbone, G. Ceballos, A. Mugarza, and P. Gambardella, "Spin Tuning of Electron-Doped Metal-Phthalocyanine Layers," *Journal of the American Chemical Society*, vol. 136, no. 14, pp. 5451–5459, 2014.

[67] A. P. Weber, A. N. Caruso, E. Vescovo, M. E. Ali, K. Tarafder, S. Z. Janjua, J. T. Sadowski, and P. M. Oppeneer, "Magnetic coupling of Fe-porphyrin molecules adsorbed on clean and c(2x2) oxygen-reconstructed Co(100) investigated by spin-polarized photoemission spectroscopy," *Physical Review B*, vol. 87, no. 18, p. 184411, 2013.

[68] M. Marks, A. Schöll, and U. Höfer, "Formation of metal-organic interface states studied with 2PPE," *Journal of Electron Spectroscopy and Related Phenomena*, vol. 195, pp. 263–271, 2014.

[69] J. C. Scott, "Metal-organic interface and charge injection in organic electronic devices," *Journal of Vacuum Science & Technology A: Vacuum, Surfaces, and Films*, vol. 21, no. 3, pp. 521–531, 2003.

[70] S. Braun, W. R. Salaneck, and M. Fahlman, "Energy-level Alignment at Organic/Metal and Organic/Organic Interfaces," *Advanced Materials*, vol. 21, no. 14-15, pp. 1450–1472, 2009.

[71] N. Koch, A. Kahn, J. Ghijsen, J.-J. Pireaux, J. Schwartz, R. L. Johnson, and A. Elschner, "Conjugated organic molecules on metal versus polymer electrodes: Demonstration of a key energy level alignment mechanism," *Applied Physics Letters*, vol. 82, no. 1, pp. 70–72, 2003.

[72] S. A. Krasnikov, N. N. Sergeeva, M. M. Brzhezinskaya, A. B. Preobrajenski, Y. N. Sergeeva, N. A. Vinogradov, A. A. Cafolla, M. O. Senge, and A. S. Vinogradov, "An x-ray absorption and photoemission study of the electronic structure of Ni porphyrins and Ni N-confused porphyrin," *Journal of Physics Condensed Matter*, 2008.

[73] R.-D. Guo, S.-Z. Yue, P. Wang, Y. Chen, Y. Zhao, and S.-Y. Liu, "Increased performance of an organic light-emitting diode by employing a zinc phthalocyanine based composite hole transport layer," *Chinese Physics B*, vol. 22, no. 12, p. 127304, 2013.

[74] K. Seufert, M.-L. Bocquet, W. Auwärter, A. Weber-Bargioni, J. Reichert, N. Lorente, and J. V. Barth, "Cis-dicarbonyl binding at cobalt and iron porphyrins with saddle-shape conformation," *Nature Chemistry*, vol. 3, no. 2, pp. 114–119, 2011.

[75] J. A. Shelnutt, X.-Z. Song, J.-G. Ma, S.-L. Jia, W. Jentzen, C. J. Medforth, and C. J. Medforth, "Nonplanar porphyrins and their significance in proteins," *Chemical Society Reviews*, vol. 27, no. 1, p. 31, 1998.

[76] P. Borghetti, G. D. Santo, C. Castellarin-Cudia, M. Fanetti, L. Sangaletti, E. Magnano, F. Bondino, and A. Goldoni, "Adsorption geometry, conformation, and electronic structure of 2H-octaethylporphyrin on Ag(111) and Fe metalation in ultra high vacuum," *The Journal of Chemical Physics*, vol. 138, no. 14, p. 144702, 2013.

[77] P. Gargiani, M. Angelucci, C. Mariani, and M. G. Betti, "Metal-phthalocyanine chains on the Au(110) surface: Interaction states versus d-metal states occupancy," *Physical Review B*, vol. 81, no. 8, p. 085412, 2010.

[78] I. Mochida, T. Miyaishi, H. Goshi, H. Fujitsu, and K. Takeshita, "Catalytic activity of nickel polyphthalocyanine in the reduction of nitric oxide with hydrogen," *Applied Catalysis*, vol. 7, no. 2, pp. 199–210, 1983.

[79] S. BERNER, S. BIELA, G. LEDUNG, A. GOGOLL, J. BACKVALL, C. PUGLIA, and S. OSCARSSON, "Activity boost of a biomimetic oxidation catalyst by immobilization onto a gold surface," *Journal of Catalysis*, vol. 244, no. 1, pp. 86–91, 2006.

[80] B. Hulsken, R. Van Hameren, J. W. Gerritsen, T. Khoury, P. Thordarson, M. J. Crossley, A. E. Rowan, R. J. Nolte, J. A. Elemans, and S. Speller, "Real-time single-molecule imaging of oxidation catalysis at a liquid-solid interface," *Nature Nanotechnology*, vol. 2, no. 5, pp. 285–289, 2007.

[81] G. Guillaud, J. Simon, and J. Germain, "Metallophthalocyanines," *Coordination Chemistry Reviews*, vol. 178-180, pp. 1433–1484, 1998.

[82] G. Ashkenasy, A. Ivanisevic, R. Cohen, C. E. Felder, D. Cahen, A. B. Ellis, and A. Shanzer, "Assemblies of "Hinged" Iron-Porphyrins as Potential Oxygen Sensors," *Journal of the American Chemical Society*, vol. 122, no. 6, pp. 1116–1122, 2000.

[83] N. A. Rakow and K. S. Suslick, "A colorimetric sensor array for odour visualization," *Nature*, vol. 406, no. 6797, pp. 710–713, 2000.

[84] K.-C. Ho and Y.-H. Tsou, "Chemiresistor-type NO gas sensor based on nickel phthalocyanine thin films," *Sensors and Actuators B: Chemical*, vol. 77, no. 1-2, pp. 253–259, 2001.

[85] A. Tibuzzi, F. Ficorella, R. Paolesse, G.-F. D. Betta, M. Boscardin, A. Macagnano, C. D. Natale, G. Soncini, and A. D'Amico, "Gas sensors based on high blue spectral responsivity photodiodes," *Sensors and Actuators B: Chemical*, vol. 111-112, pp. 242–246, 2005.

[86] R. Tongpool and S. Yoriya, "Kinetics of nitrogen dioxide exposure in lead phthalocyanine sensors," *Thin Solid Films*, vol. 477, no. 1-2, pp. 148–152, 2005.

[87] B. R. Takulapalli, G. M. Laws, P. A. Liddell, J. Andréasson, Z. Erno, D. Gust, and T. J. Thornton, "Electrical Detection of Amine Ligation to a Metalloporphyrin via a Hybrid SOI-MOSFET," *Journal of the American Chemical Society*, vol. 130, no. 7, pp. 2226–2233, 2008.

[88] I. Mochida, "A kinetic study on reduction of nitric oxide over cobalt tetraphenylporphyrin supported on titanium dioxide," *Journal of Catalysis*, vol. 77, no. 2, pp. 519–526, 1982.

[89] I. Mochida, K. Suetsugu, H. Fujitsu, and K. Takeshita, "Unusual activity of carbon monoxide on Co-tetraphenylporphyrin supported by TiO_2 for the reduction of nitric oxide," *Journal of the Chemical Society, Chemical Communications*, no. 3, p. 166, 1982.

[90] H. Hertz, "Ueber einen Einfluss des ultravioletten Lichtes auf die electrische Entladung," *Annalen der Physik und Chemie*, vol. 267, no. 8, pp. 983–1000, 1887.

[91] A. Einstein, "Über einen die Erzeugung und Verwandlung des Lichtes betreffenden heuristischen Gesichtspunkt," *Annalen der Physik*, vol. 322, no. 6, pp. 132–148, 1905.

[92] C. N. Berglund and W. E. Spicer, "Photoemission Studies of Copper and Silver: Theory," *Physical Review*, vol. 136, no. 4A, pp. A1030–A1044, 1964.

[93] S. Hüfner, *Photoelectron Spectroscopy*. Springer Berlin Heidelberg, 2003.

[94] A. Damascelli, "Probing the Electronic Structure of Complex Systems by ARPES," *Physica Scripta*, vol. T109, p. 61, 2004.

[95] W. Schattke, "PHOTOEMISSION WITHIN AND BEYOND THE ONE-STEP MODEL," *Progress in Surface Science*, vol. 54, no. 3-4, pp. 211–227, 1997.

[96] J. B. Pendry, "Theory of photoemission," *Surface Science*, vol. 57, no. 2, pp. 679–705, 1976.

[97] J. F. Watts and J. Wolstenholme, *An Introduction to Surface Analysis by XPS and AES*. John Wiley & Sons, Ltd, 2003.

[98] P. J. Cumpson and M. P. Seah, "Elastic Scattering Corrections in AES and XPS. II. Estimating Attenuation Lengths and Conditions Required for their Valid Use in Overlayer/Substrate Experiments," *Surface and Interface Analysis*, vol. 25, no. 6, pp. 430–446, 1997.

[99] P. Puschnig, S. Berkebile, A. J. Fleming, G. Koller, K. Emtsev, T. Seyller, J. D. Riley, C. Ambrosch-Draxl, F. P. Netzer, and M. G. Ramsey, "Reconstruction of Molecular Orbital Densities from Photoemission Data," *Science*, vol. 326, no. 5953, pp. 702–706, 2009.

[100] G. Zamborlini, Z. Lüftner, Danieland Feng, B. Kollmann, P. Puschnig, C. Dri, M. Panighel, G. Di Santo, A. Goldoni, G. Comelli, M. Jugovac, V. Feyer, and C. M. Schneider, "Multi-orbital charge transfer at highly oriented organic/metal interfaces," *Nature Communications*, vol. 8, no. 1, p. 335, 2017.

[101] A. M. Bradshaw and D. P. Woodruff, "Molecular orbital tomography for adsorbed molecules: is a correct description of the final state really unimportant?," *New Journal of Physics*, vol. 17, no. 1, p. 013033, 2015.

[102] P. Puschnig, G. Koller, C. Draxl, and M. G. Ramsey, "The Structure of Molecular Orbitals Investigated by Angle-Resolved Photoemission," in *Small Organic Molecules on Surfaces*, pp. 3–23, Springer Berlin Heidelberg, 2013.

[103] C. Schneider, C. Wiemann, M. Patt, V. Feyer, L. Plucinski, I. Krug, M. Escher, N. Weber, M. Merkel, O. Renault, and N. Barrett, "Expanding the view into complex material systems: From micro-ARPES to nanoscale HAXPES," *Journal of Electron Spectroscopy and Related Phenomena*, vol. 185, no. 10, pp. 330–339, 2012.

[104] J. Stöhr, *NEXAFS Spectroscopy*. Springer, 1992.

[105] L. Floreano, G. Naletto, D. Cvetko, R. Gotter, M. Malvezzi, L. Marassi, A. Morgante, A. Santaniello, A. Verdini, F. Tommasini, and G. Tondello, "Performance of the grating-crystal monochromator of the ALOISA beamline at the Elettra Synchrotron," *Review of Scientific Instruments*, vol. 70, no. 10, pp. 3855–3864, 1999.

[106] L. Floreano, A. Cossaro, R. Gotter, A. Verdini, G. Bavdek, F. Evangelista, A. Ruocco, A. Morgante, and D. Cvetko, "Periodic Arrays of Cu-Phthalocyanine Chains on Au(110)," *The Journal of Physical Chemistry C*, vol. 112, no. 29, pp. 10794–10802, 2008.

[107] G. Schütz, W. Wagner, W. Wilhelm, P. Kienle, R. Zeller, R. Frahm, and G. Materlik, "Absorption of circularly polarized x-rays in iron," *Physical Review Letters*, vol. 58, no. 7, pp. 737–740, 1987.

[108] Y. Wu, J. Stöhr, B. D. Hermsmeier, M. G. Samant, and D. Weller, "Enhanced orbital magnetic moment on Co atoms in Co/Pd multilayers: A magnetic circular x-ray dichroism study," *Physical Review Letters*, vol. 69, no. 15, pp. 2307–2310, 1992.

[109] M. Tischer, O. Hjortstam, D. Arvanitis, J. H. Dunn, F. May, K. Baberschke, J. Trygg, J. M. Wills, B. Johansson, and O. Eriksson, "Enhancement of Orbital Magnetism at Surfaces: Co on Cu(100)," *Physical Review Letters*, vol. 75, no. 8, pp. 1602–1605, 1995.

[110] B. T. Thole, P. Carra, F. Sette, and G. van der Laan, "X-ray circular dichroism as a probe of orbital magnetization," *Physical review letters*, vol. 68, no. 12, p. 1943, 1992.

[111] P. Carra, B. T. Thole, M. Altarelli, and X. Wang, "X-ray circular dichroism and local magnetic fields," *Physical Review Letters*, vol. 70, no. 5, pp. 694–697, 1993.

[112] W. L. O'Brien and B. P. Tonner, "Orbital and spin sum rules in x-ray magnetic circular dichroism," *Physical Review B*, vol. 50, no. 17, pp. 12672–12681, 1994.

[113] C. T. Chen, Y. U. Idzerda, H.-J. Lin, N. V. Smith, G. Meigs, E. Chaban, G. H. Ho, E. Pellegrin, and F. Sette, "Experimental Confirmation of the X-Ray Magnetic Circular Dichroism Sum Rules for Iron and Cobalt," *Physical Review Letters*, vol. 75, no. 1, pp. 152–155, 1995.

[114] J. P. Crocombette, B. T. Thole, and F. Jollet, "The importance of the magnetic dipole term in magneto-circular x-ray absorption dichroism for 3d transition metal compounds," *Journal of Physics: Condensed Matter*, vol. 8, no. 22, pp. 4095–4105, 1996.

[115] C. Piamonteze, U. Flechsig, S. Rusponi, J. Dreiser, J. Heidler, M. Schmidt, R. Wetter, M. Calvi, T. Schmidt, and H. Pruchova, "X-Treme beamline at SLS: X-ray magnetic circular and linear dichroism at high field and low temperature," *Journal of synchrotron radiation*, vol. 19, no. 5, pp. 661–674, 2012.

[116] F. Hoffmann, "Infrared reflection-absorption spectroscopy of adsorbed molecules," *Surface Science Reports*, vol. 3, no. 2-3, p. 107, 1983.

[117] J. T. Yates and T. E. Madey, eds., *Vibrational Spectroscopy of Molecules on Surfaces*. Springer US, 1987.

[118] A. A. Christy, Y. Ozaki, and V. G. Gregoriou, *Modern Fourier Transform Infrared Spectroscopy (Comprehensive Analytical Chemistry)*. Elsevier Science, 2001.

[119] C. Schuschke, C. Hohner, M. Jevric, A. Ugleholdt Petersen, Z. Wang, M. Schwarz, M. Kettner, F. Waidhas, L. Fromm, C. J. Sumby, A. Görling, O. Brummel, K. Moth-Poulsen, and J. Libuda, "Solar energy storage at an atomically defined organic-oxide hybrid interface," *Nature Communications*, vol. 10, no. 1, pp. 1–10, 2019.

[120] C. J. Chen, *Introduction to Scanning Tunneling Microscopy*. Oxford University Press, 2007.

[121] R. M. Feenstra, "Scanning tunneling spectroscopy," *Surface Science*, vol. 299-300, pp. 965–979, 1994.

[122] R. J. Hamers, "Atomic-resolution Surface Spectroscopy with the Scanning Tunneling Microscope," *Annual Review of Physical Chemistry*, vol. 40, no. 1, pp. 531–559, 1989.

[123] J. Bardeen, "Tunnelling from a Many-Particle Point of View," *Physical Review Letters*, vol. 6, no. 2, pp. 57–59, 1961.

[124] F. Bischoff, K. Seufert, W. Auwärter, S. Joshi, S. Vijayaraghavan, D. Écija, K. Diller, A. C. Papageorgiou, S. Fischer, F. Allegretti, D. A. Duncan, F. Klappenberger, F. Blobner, R. Han, and J. V. Barth, "How surface bonding and repulsive interactions cause phase transformations: Ordering of a prototype macrocyclic compound on Ag(111)," *ACS Nano*, vol. 7, no. 4, pp. 3139–3149, 2013.

[125] I. Bidermane, J. Lüder, R. Totani, C. Grazioli, M. de Simone, M. Coreno, A. Kivimäki, J. Åhlund, L. Lozzi, B. Brena, and C. Puglia, "Characterization of gas phase iron phthalocyanine with X-ray photoelectron and absorption spectroscopies," *Physica Status Solidi (B) Basic Research*, 2015.

[126] F. Petraki, H. Peisert, U. Aygül, F. Latteyer, J. Uihlein, A. Vollmer, and T. Chassé, "Electronic Structure of FePc and Interface Properties on Ag(111) and Au(100)," *The Journal of Physical Chemistry C*, vol. 116, no. 20, pp. 11110–11116, 2012.

[127] M. Corva, A. Ferrari, M. Rinaldi, Z. Feng, M. Roiaz, C. Rameshan, G. Rupprechter, R. Costantini, M. Dell'Angela, G. Pastore, G. Comelli, N. Seriani, and E. Vesselli, "Vibrational fingerprint of localized excitons in a two-dimensional metal-organic crystal," *Nature Communications*, 2018.

[128] S. Prato, L. Floreano, D. Cvetko, V. De Renzi, A. Morgante, S. Modesti, F. Biscarini, R. Zamboni, and C. Taliani, "Anisotropic ordered planar growth of α-sexithienyl thin films," *Journal of Physical Chemistry B*, vol. 103, no. 37, pp. 7788–7795, 1999.

[129] L. Casalis, M. F. Danisman, B. Nickel, G. Bracco, T. Toccoli, S. Iannotta, and G. Scoles, "Hyperthermal Molecular Beam Deposition of Highly Ordered Organic Thin Films," *Physical Review Letters*, 2003.

[130] S. Söhnchen, S. Lukas, and G. Witte, "Epitaxial growth of pentacene films on Cu(110)," *Journal of Chemical Physics*, vol. 121, no. 1, pp. 525–534, 2004.

[131] V. Lanzilotto, C. Sanchez-Sanchez, G. Bavdek, D. Cvetko, M. F. Lopez, J. A. Martin-Gago, and L. Floreano, "Planar growth of pentacene on the dielectric TiO_2(110) surface," *Journal of Physical Chemistry C*, vol. 115, no. 11, pp. 4664–4672, 2011.

[132] V. Lanzilotto, G. Lovat, G. Otero, L. Sanchez, M. F. López, J. Méndez, J. A. Martín-Gago, G. Bavdek, and L. Floreano, "Commensurate growth of densely packed PTCDI islands on the rutile TiO_2(110) surface," *Journal of Physical Chemistry C*, vol. 117, no. 24, pp. 12639–12647, 2013.

[133] G. Fratesi, V. Lanzilotto, S. Stranges, M. Alagia, G. P. Brivio, and L. Floreano, "High resolution NEXAFS of perylene and PTCDI: A surface science approach to molecular orbital analysis," *Physical Chemistry Chemical Physics*, vol. 16, no. 28, pp. 14834–14844, 2014.

[134] L. Cao, Y. Z. Wang, J. Q. Zhong, Y. Y. Han, W. H. Zhang, X. J. Yu, F. Q. Xu, D. C. Qi, and A. T. Wee, "Molecular orientation and site dependent charge transfer dynamics at PTCDA/TiO_2(110) interface revealed by resonant photoemission spectroscopy," *Journal of Physical Chemistry C*, 2014.

[135] G. Otero-Irurueta, J. I. Martínez, G. Lovat, V. Lanzilotto, J. Méndez, M. F. López, L. Floreano, and J. A. Martín-Gago, "Densely packed perylene layers on the rutile TiO_2(110)-(1×1) surface," *Journal of Physical Chemistry C*, vol. 119, no. 14, pp. 7809–7816, 2015.

[136] S. Rangan, C. Ruggieri, R. Bartynski, J. I. Martínez, F. Flores, and J. Ortega, "Adsorption Geometry and Energy Level Alignment at the PTCDA/TiO_2(110) Interface," *Journal of Physical Chemistry B*, 2018.

[137] L. Zajac, P. Olszowski, S. Godlewski, L. Bodek, B. Such, R. Jöhr, R. Pawlak, A. Hinaut, T. Glatzel, E. Meyer, and M. Szymonski, "Self-assembling of Zn porphyrins on a (110) face of rutile TiO_2 -The anchoring role of carboxyl groups," *Applied Surface Science*, vol. 379, pp. 277–281, 2016.

[138] C. Wang, Q. Fan, Y. Han, J. I. Martínez, J. A. Martín-Gago, W. Wang, H. Ju, J. M. Gottfried, and J. Zhu, "Metalation of tetraphenylporphyrin with nickel on a TiO_2(110)-1×2 surface," *Nanoscale*, vol. 8, no. 2, pp. 1123–1132, 2016.

[139] S. Rangan, C. Ruggieri, R. Bartynski, J. I. Martínez, F. Flores, and J. Ortega, "Densely Packed ZnTPPs Monolayer on the Rutile TiO_2(110)-(1×1) Surface: Adsorption Behavior and Energy Level Alignment," *Journal of Physical Chemistry C*, 2016.

[140] L. Zajac, L. Bodek, and B. Such, "Adsorption behavior of Zn porphyrins on a (101) face of anatase TiO_2," *Applied Surface Science*, vol. 443, pp. 452–457, 2018.

[141] V. Lanzilotto, G. Lovat, G. Fratesi, G. Bavdek, G. P. Brivio, and L. Floreano, "TiO_2(110) Charge Donation to an Extended π-Conjugated Molecule," *Journal of Physical Chemistry Letters*, vol. 6, no. 2, pp. 308–313, 2015.

[142] G. Lovat, D. Forrer, M. Abadia, M. Dominguez, M. Casarin, C. Rogero, A. Vittadini, and L. Floreano, "On-Surface Synthesis of a Pure and Long-Range-Ordered Titanium(IV)-Porphyrin Contact Layer on Titanium Dioxide," *Journal of Physical Chemistry C*, vol. 121, no. 25, pp. 13738–13746, 2017.

[143] J. Schneider, T. Berger, and O. Diwald, "Reactive Porphyrin Adsorption on TiO_2 Anatase Particles: Solvent Assistance and the Effect of Water Addition," *ACS Applied Materials and Interfaces*, 2018.

[144] J. Repp, G. Meyer, S. M. Stojković, A. Gourdon, and C. Joachim, "Molecules on insulating films: Scanning-tunneling microscopy imaging of individual molecular orbitals," *Physical Review Letters*, 2005.

[145] M. Corva, F. Mohamed, E. Tomsic, M. Rinaldi, C. Cepek, N. Seriani, M. Peressi, and E. Vesselli, "Learning from Nature: Charge Transfer and Carbon Dioxide Activation at Single, Biomimetic Fe Sites in Tetrapyrroles on Graphene," *Journal of Physical Chemistry C*, 2019.

[146] A. Carrera, L. J. Cristina, S. Bengió, A. Cossaro, A. Verdini, L. Floreano, J. D. Fuhr, J. E. Gayone, and H. Ascolani, "Controlling carboxyl deprotonation on Cu(001) by surface Sn alloying," *Journal of Physical Chemistry C*, vol. 117, no. 33, pp. 17058–17065, 2013.

[147] X. Yang, I. Krieger, D. Lüftner, S. Weiß, T. Heepenstrick, M. Hollerer, P. Hurdax, G. Koller, M. Sokolowski, P. Puschnig, M. G. Ramsey, F. S. Tautz, and S. Soubatch, "On the decoupling of molecules at metal surfaces," *Chemical Communications*, vol. 54, no. 65, pp. 9039–9042, 2018.

[148] A. Picone, D. Giannotti, A. Brambilla, G. Bussetti, A. Calloni, R. Yivlialin, M. Finazzi, L. Duò, F. Ciccacci, A. Goldoni, A. Verdini, and L. Floreano, "Local structure and morphological evolution of ZnTPP molecules grown on Fe(001)-p(1x1)O studied by STM and NEXAFS," *Applied Surface Science*, vol. 435, pp. 841–847, 2018.

[149] L. Sun, G. Weidlinger, M. Denk, R. Denk, M. Hohage, and P. Zeppenfeld, "Stranski-Krastanov growth of para-sexiphenyl on Cu(110)-(2×1)O revealed by optical spectroscopy," *Physical Chemistry Chemical Physics*, vol. 12, no. 44, pp. 14706–14709, 2010.

[150] J. Gall, P. Zeppenfeld, L. Sun, L. Zhang, Y. Luo, Z. Dong, C. Hu, and P. Puschnig, "Spectroscopic STM studies of single pentacene molecules on Cu(110)-c(6×2)O," *Physical Review B*, 2016.

[151] O. Plekan, V. Feyer, R. Richter, M. Coreno, M. de Simone, K. C. Prince, A. B. Trofimov, E. V. Gromov, I. L. Zaytseva, and J. Schirmer, "A theoretical and experimental study of the near edge X-ray absorption fine structure (NEXAFS) and X-ray photoelectron spectra (XPS) of nucleobases: Thymine and adenine," *Chemical Physics*, vol. 347, no. 1-3, pp. 360–375, 2008.

[152] G. Zamborlini, M. Jugovac, A. Cossaro, A. Verdini, L. Floreano, D. Lüftner, P. Puschnig, V. Feyer, and C. M. Schneider, "On-surface nickel porphyrin mimics the reactive center of an enzyme cofactor," *Chem. Commun.*, vol. 54, pp. 13423–13426, 2018.

[153] D. G. De Oteyza, A. Sakko, A. El-Sayed, E. Goiri, L. Floreano, A. Cossaro, J. M. Garcia-Lastra, A. Rubio, and J. E. Ortega, "Inversed linear dichroism in F K-edge NEXAFS spectra of fluorinated planar aromatic molecules," *Physical Review B - Condensed Matter and Materials Physics*, vol. 86, no. 7, 2012.

[154] M. G. Betti, P. Gargiani, R. Frisenda, R. Biagi, A. Cossaro, A. Verdini, L. Floreano, and C. Mariani, "Localized and dispersive electronic states at ordered FePc and CoPc chains on Au(110)," *Journal of Physical Chemistry C*, vol. 114, no. 49, pp. 21638–21644, 2010.

[155] R. De Francesco, M. Stener, and G. Fronzoni, "Theoretical study of near-edge X-ray absorption fine structure spectra of metal phthalocyanines at C and N K-edges," in *Journal of Physical Chemistry A*, 2012.

[156] M. V. Nardi, F. Detto, L. Aversa, R. Verucchi, G. Salviati, S. Iannotta, and M. Casarin, "Electronic properties of CuPc and H_2Pc: An experimental and theoretical study," *Physical Chemistry Chemical Physics*, vol. 15, no. 31, pp. 12864–12881, 2013.

[157] I. Reid, Y. Zhang, A. Demasi, A. Blueser, L. Piper, J. E. Downes, A. Matsuura, G. Hughes, and K. E. Smith, "Electronic structure of the organic semiconductor copper tetraphenylporphyrin (CuTPP)," *Applied Surface Science*, 2009.

[158] S. Grimme, J. Antony, S. Ehrlich, and H. Krieg, "A consistent and accurate ab initio parametrization of density functional dispersion correction (DFT-D) for the 94 elements H-Pu," *Journal of Chemical Physics*, vol. 132, no. 15, 2010.

[159] S. Stepanow, A. Mugarza, G. Ceballos, P. Moras, J. C. Cezar, C. Carbone, and P. Gambardella, "Giant spin and orbital moment anisotropies of a Cu-phthalocyanine monolayer," *Physical Review B*, vol. 82, no. 1, p. 14405, 2010.

[160] I. Cojocariu, H. M. Sturmeit, G. Zamborlini, A. Cossaro, A. Verdini, L. Floreano, E. D'Incecco, M. Stredansky, E. Vesselli, M. Jugovac, M. Cinchetti, V. Feyer, and C. M. Schneider, "Evaluation of molecular orbital symmetry via oxygen-induced charge transfer quenching at a metal-organic interface," *Applied Surface Science*, vol. 504, p. 144343, 2020.

[161] H. M. Sturmeit, I. Cojocariu, M. Jugovac, A. Cossaro, A. Verdini, L. Floreano, A. Sala, G. Comelli, S. Moro, M. Stredansky, M. Corva, E. Vesselli, P. Puschnig, C. M. Schneider, V. Feyer, G. Zamborlini, and M. Cinchetti, "Molecular anchoring stabilizes low valence Ni(I)TPP on copper against thermally induced chemical changes," *Journal of Materials Chemistry C*, vol. 8, no. 26, pp. 8876–8886, 2020.

[162] H. Geisler, G. Odörfer, G. Illing, R. Jaeger, H. J. Freund, G. Watson, E. W. Plummer, M. Neuber, and M. Neumann, "NO_2 adsorption on Ni(100): A comparison of NO_2 with CO_2 adsorption," *Surface Science*, vol. 234, no. 3, pp. 237–250, 1990.

[163] W. H. E. Schwarz, T. C. Chang, and J. P. Connerade, "Core-electron excitation in NO_2," *Chemical Physics Letters*, vol. 49, no. 2, pp. 207–212, 1977.

[164] K. Werner, S. Mohr, M. Schwarz, T. Xu, M. Amende, T. Döpper, A. Görling, and J. Libuda, "Functionalized Porphyrins on an Atomically Defined Oxide Surface: Anchoring and Coverage-Dependent Reorientation of MCTPP on Co_3O_4(111)," *Journal of Physical Chemistry Letters*, vol. 7, no. 3, pp. 555–560, 2016.

[165] X. Y. Li, R. S. Czernuszewicz, J. R. Kincaid, Y. O. Su, and T. G. Spiro, "Consistent porphyrin force field. 1. Normal-mode analysis for nickel porphine and nickel tetraphenylporphine from resonance Raman and infrared spectra and isotope shifts," *Journal of Physical Chemistry*, vol. 94, no. 1, pp. 31–47, 1990.

[166] S. Mishra, S. Kaur, S. K. Tripathi, C. G. Mahajan, and G. S. Saini, "Fourier-transform infrared spectroscopic studies of dithia tetraphenylporphine," *Journal of Chemical Sciences*, vol. 118, no. 4, pp. 361–369, 2006.

[167] T. Wähler, R. Schuster, and J. Libuda, "Self-Metalation of Anchored Porphyrins on Atomically Defined Cobalt Oxide Surfaces: In situ Studies by Surface Vibrational Spectroscopy," *Chemistry - A European Journal*, vol. 26, no. 54, pp. 12445–12453, 2020.

[168] H. Ogoshi, Y. Saito, and K. Nakamoto, "Infrared spectra and normal coordinate analysis of metalloporphins," *The Journal of Chemical Physics*, vol. 57, no. 10, pp. 4194–4202, 1972.

[169] J. O. Alben, S. S. Choi, A. D. Adler, and W. S. Caughey, "Infrared Spectroscopy of Porphyrins," *Annals of the New York Academy of Sciences*, vol. 206, no. 1, pp. 278–295, 1973.

[170] J. Brede, M. Linares, R. Lensen, A. E. Rowan, M. Funk, M. Broöring, G. Hoffmann, and R. Wiesendanger, "Adsorption and conformation of porphyrins on metallic surfaces," *Journal of Vacuum Science and Technology B: Microelectronics and Nanometer Structures*, vol. 27, no. 2, p. 799, 2009.

[171] J. Xiao, S. Ditze, M. Chen, F. Buchner, M. Stark, M. Drost, H. P. Steinrück, J. M. Gottfried, and H. Marbach, "Temperature-dependent chemical and structural transformations from 2H-tetraphenylporphyrin to copper(II)-tetraphenylporphyrin on Cu(111)," *Journal of Physical Chemistry C*, vol. 116, no. 22, pp. 12275–12282, 2012.

[172] D. Wechsler, M. Franke, Q. Tariq, L. Zhang, T. L. Lee, P. K. Thakur, N. Tsud, S. Bercha, K. C. Prince, H. P. Steinrück, and O. Lytken, "Adsorption Structure of Cobalt Tetraphenylporphyrin on Ag(100)," *Journal of Physical Chemistry C*, vol. 121, no. 10, pp. 5667–5674, 2017.

[173] F. Buchner, I. Kellner, W. Hieringer, A. Görling, H. P. Steinrück, and H. Marbach, "Ordering aspects and intramolecular conformation of tetraphenylporphyrins on Ag(111)," *Physical Chemistry Chemical Physics*, vol. 12, no. 40, pp. 13082–13090, 2010.

[174] M. E. Bartram and B. E. Koel, "The molecular adsorption of NO_2 and the formation of N_2O_3 on Au(111)," *Surface Science*, vol. 213, no. 1, pp. 137–156, 1989.

[175] T. J. Dines, C. H. Rochester, and A. M. Ward, "Infrared and Raman study of the adsorption of nitrogen oxides on titania-supported vanadia catalysts," *Journal of the Chemical Society, Faraday Transactions*, vol. 87, no. 10, pp. 1617–1622, 1991.

[176] J. Wang and B. E. Koel, "IRAS studies of NO_2, N_2O_3, and N_2O_4 adsorbed on Au(111) surfaces and reactions with coadsorbed H_2O," *Journal of Physical Chemistry A*, vol. 102, no. 44, pp. 8573–8579, 1998.

[177] R. V. St. Louis and B. Crawford, "Infrared Spectrum of Matrix-Isolated NO_2," *The Journal of Chemical Physics*, vol. 42, no. 3, pp. 857–864, 1965.

[178] M. H. Chang, N. Y. Kim, Y. H. Chang, Y. Lee, U. S. Jeon, H. Kim, Y. H. Kim, and S. J. Kahng, "O_2 , NO_2 and NH_3 coordination to Co-porphyrin studied with scanning tunneling microscopy on Au(111)," *Nanoscale*, vol. 11, no. 17, pp. 8510–8517, 2019.

[179] H. Wang, S. M. Butorin, A. T. Young, and J. Guo, "Nickel Oxidation States and Spin States of Bioinorganic Complexes from Nickel L-edge X-ray Absorption and Resonant Inelastic X-ray Scattering," *The Journal of Physical Chemistry C*, vol. 117, no. 47, pp. 24767–24772, 2013.

[180] H. Wang, P. Ge, C. G. Riordan, S. Brooker, C. G. Woomer, T. Collins, C. A. Melendres, O. Graudejus, N. Bartlett, and S. P. Cramer, "Integrated X-ray L absorption spectra. Counting Holes in Ni Complexes," *The Journal of Physical Chemistry B*, vol. 102, no. 42, pp. 8343–8346, 1998.

[181] H. Wang, C. Y. Ralston, D. S. Patil, R. M. Jones, W. Gu, M. Verhagen, M. Adams, P. Ge, C. Riordan, C. A. Marganian, P. Mascharak, J. Kovacs, C. G. Miller, T. J. Collins, S. Brooker, P. D. Croucher, K. Wang, E. I. Stiefel, and S. P. Cramer, "Nickel L-Edge Soft X-ray Spectroscopy of Nickel-Iron Hydrogenases and Model Compounds: Evidence for High-Spin Nickel(II) in the Active Enzyme," *Journal of the American Chemical Society*, vol. 122, no. 43, pp. 10544–10552, 2000.

[182] H. Wang, D. S. Patil, C. Y. Ralston, C. Bryant, and S. P. Cramer, "L-Edge X-ray magnetic circular dichroism of Ni enzymes : direct probe of Ni spin states," *Journal of Electron Spectroscopy and Related Phenomena*, vol. 116, pp. 865–871, 2001.

[183] C. Wäckerlin, K. Tarafder, J. Girovsky, J. Nowakowski, T. Hählen, A. Shchyrba, D. Siewert, A. Kleibert, F. Nolting, P. M. Oppeneer, T. A. Jung, and N. Ballav, "Ammonia coordination introducing a magnetic moment in an on-surface low-spin porphyrin," *Angewandte Chemie - International Edition*, vol. 52, no. 17, pp. 4568–4571, 2013.

[184] P. S. Deimel, R. M. Bababrik, B. Wang, P. J. Blowey, L. A. Rochford, P. K. Thakur, T.-L. Lee, M.-L. Bocquet, J. V. Barth, D. P. Woodruff, D. A. Duncan, and F. Allegretti, "Direct quantitative identification of the "surface trans-effect"," *Chemical Science*, vol. 7, no. 9, pp. 5647–5656, 2016.

[185] S. S. Eaton and G. R. Eaton, "Magnetic Susceptibility of Porphyrins," *Inorganic Chemistry*, vol. 19, no. 4, pp. 1095–1096, 1980.

[186] Y. H. Chang, H. Kim, S. J. Kahng, and Y. H. Kim, "Axial coordination and electronic structure of diatomic NO, CO, and O_2 molecules adsorbed onto Co-tetraphenylporphyrin on Au(111), Ag(111), and Cu(111): A density-functional theory study," *Dalton Transactions*, vol. 45, no. 42, pp. 16673–16681, 2016.

[187] S. Scheller, M. Goenrich, R. Boecher, R. K. Thauer, and B. Jaun, "The key nickel enzyme of methanogenesis catalyses the anaerobic oxidation of methane," *Nature*, vol. 465, no. 7298, pp. 606–608, 2010.

[188] T. Wagner, J. Kahnt, U. Ermler, and S. Shima, "Didehydroaspartate Modification in Methyl-Coenzyme M Reductase Catalyzing Methane Formation," *Angewandte Chemie - International Edition*, vol. 55, no. 36, pp. 10630–10633, 2016.

[189] P. Donovan, A. Robin, M. S. Dyer, M. Persson, and R. Raval, "Unexpected Deformations Induced by Surface Interaction and Chiral Self-Assembly of Co(II)-Tetraphenylporphyrin (Co-TPP) Adsorbed on Cu(110): A Combined STM and Periodic DFT Study," *Chemistry – A European Journal*, vol. 16, no. 38, pp. 11641–11652, 2010.

[190] S. Vijayaraghavan, W. Auwärter, D. Ecija, K. Seufert, S. Rusponi, T. Houwaart, P. Sautet, M. L. Bocquet, P. Thakur, S. Stepanow, U. Schlickum, M. Etzkorn, H. Brune, and J. V. Barth, "Restoring the Co magnetic moments at interfacial Co-porphyrin arrays by site-selective uptake of iron," *ACS Nano*, vol. 9, no. 4, pp. 3605–3616, 2015.

[191] B. W. Heinrich, C. Iacovita, T. Brumme, D. J. Choi, L. Limot, M. V. Rastei, W. A. Hofer, J. Kortus, and J. P. Bucher, "Direct observation of the tunneling channels of a chemisorbed molecule," *Journal of Physical Chemistry Letters*, vol. 1, no. 10, pp. 1517–1523, 2010.

[192] M. Casarin, F. Ferrigato, C. Maccato, and A. Vittadini, "So_2 on TiO_2(110) and Ti_2O_3(1012) nonpolar surfaces: A DFT study," *Journal of Physical Chemistry B*, vol. 109, no. 25, pp. 12596–12602, 2005.

[193] M. Casarin, C. Maccato, and A. Vittadini, "A Comparative Study of CO Chemisorption on Al_2O_3 and Ti_2O_3 Nonpolar Surfaces," *The Journal of Physical Chemistry B*, vol. 106, no. 4, pp. 795–802, 2002.

[194] S. Carlotto, M. Casarin, A. Lanza, F. Nestola, L. Pandolfo, C. Pettinari, and R. Scatena, "Reaction of Copper(II) Chloroacetate with Pyrazole. Synthesis of a One-Dimensional Coordination Polymer and Unexpected Dehydrochlorination Reaction," *Crystal Growth and Design*, vol. 15, no. 12, pp. 5910–5918, 2015.

[195] I. Cojocariu, S. Carlotto, H. M. Sturmeit, G. Zamborlini, M. Cinchetti, A. Cossaro, A. Verdini, L. Floreano, M. Jugovac, P. Puschnig, C. Piamonteze, M. Casarin, V. Feyer, and C. M. Schneider, "Ferrous to Ferric Transition in Fe-Phthalocyanine Driven by NO_2 Exposure," *Chemistry – A European Journal*, vol. 27, no. 10, pp. 3526–3535, 2021.

[196] S. Carlotto, M. Sambi, F. Sedona, A. Vittadini, J. Bartolomé, F. Bartolomé, and M. Casarin, "$L_{2,3}$-edges absorption spectra of a 2D complex system: A theoretical modelling," *Physical Chemistry Chemical Physics*, vol. 18, no. 40, pp. 28110–28116, 2016.

[197] T. Houwaart, T. Le Bahers, P. Sautet, W. Auwärter, K. Seufert, J. V. Barth, and M.-L. Bocquet, "Scrutinizing individual CoTPP molecule adsorbed on coinage metal surfaces from the interplay of STM experiment and theory," *Surface Science*, vol. 635, pp. 108–114, 2015.

[198] M. H. Chang, Y. H. Chang, N.-Y. Kim, H. Kim, S.-H. Lee, M.-S. Choi, Y.-H. Kim, and S.-J. Kahng, "Tuning and sensing spin interactions in Co-porphyrin/Au with NH_3 and NO_2 binding," *Phys. Rev. B*, vol. 100, p. 245406, 2019.

[199] P. Kumar, Y. M. Lee, Y. J. Park, M. A. Siegler, K. D. Karlin, and W. Nam, "Reactions of Co(III)-Nitrosyl Complexes with Superoxide and Their Mechanistic Insights," *Journal of the American Chemical Society*, vol. 137, no. 13, pp. 4284–4287, 2015.

[200] J. W. Lauher and J. A. Ibers, "Structure of octaethylporphyrin. Comparison with other free base porphyrins," *Journal of the American Chemical Society*, vol. 95, no. 16, pp. 5148–5152, 1973.

[201] C. Ruggieri, S. Rangan, R. A. Bartynski, and E. Galoppini, "Zinc(II) Tetraphenylporphyrin on Ag(100) and Ag(111): Multilayer Desorption and Dehydrogenation," *Journal of Physical Chemistry C*, vol. 120, pp. 7575–7585, 2016.

[202] X. Yang, L. Egger, J. Fuchsberger, M. Unzog, D. Lüftner, F. Hajek, P. Hurdax, M. Jugovac, G. Zamborlini, V. Feyer, G. Koller, P. Puschnig, F. S. Tautz, M. G. Ramsey, and S. Soubatch, "Coexisting Charge States in a Unary Organic Monolayer Film on a Metal," *The Journal of Physical Chemistry Letters*, vol. 10, pp. 6438–6445, 2019.

[203] V. A. Dediu, L. E. Hueso, I. Bergenti, and C. Taliani, "Spin routes in organic semiconductors," *Nature Materials*, vol. 8, no. 9, pp. 707–716, 2009.

[204] W. Xu, G. J. Szulczewski, P. LeClair, I. Navarrete, R. Schad, G. Miao, H. Guo, and A. Gupta, "Tunneling magnetoresistance observed in $La_{0.67}Sr_{0.33}MnO_3$/organic molecule/Co junctions," *Applied Physics Letters*, vol. 90, no. 7, p. 072506, 2007.

[205] K. Yang, H. Chen, T. Pope, Y. Hu, L. Liu, D. Wang, L. Tao, W. Xiao, X. Fei, Y.-Y. Zhang, H.-G. Luo, S. Du, T. Xiang, W. A. Hofer, and H.-J. Gao, "Tunable giant magnetoresistance in a single-molecule junction," *Nature Communications*, vol. 10, no. 1, p. 3599, 2019.

[206] B. W. Heinrich, L. Braun, J. I. Pascual, and K. J. Franke, "Tuning the Magnetic Anisotropy of Single Molecules," *Nano Letters*, vol. 15, no. 6, pp. 4024–4028, 2015.

[207] B. W. Heinrich, C. Ehlert, N. Hatter, L. Braun, C. Lotze, P. Saalfrank, and K. J. Franke, "Control of Oxidation and Spin State in a Single-Molecule Junction," *ACS Nano*, vol. 12, no. 4, pp. 3172–3177, 2018.

[208] L. Liu, K. Yang, Y. Jiang, B. Song, W. Xiao, L. Li, H. Zhou, Y. Wang, S. Du, M. Ouyang, W. A. Hofer, A. H. Castro Neto, and H.-J. Gao, "Reversible Single Spin Control of Individual Magnetic Molecule by Hydrogen Atom Adsorption," *Scientific Reports*, vol. 3, no. 1, p. 1210, 2013.

[209] Y. Wang, X. Li, X. Zheng, and J. Yang, "Spin switch in iron phthalocyanine on Au(111) surface by hydrogen adsorption," *The Journal of Chemical Physics*, vol. 147, no. 13, p. 134701, 2017.

[210] B. Liu, G. Miao, W. Zhong, X. Huang, N. Su, J. Guo, and W. Wang, "Manipulating the Electronic and Magnetic Properties of Coordinated Nickel Atoms in Metal-Organic Frameworks by Hydrogenation," *ACS Nano*, vol. 16, no. 2, pp. 2147–2153, 2022.

[211] H. M. Sturmeit, I. Cojocariu, A. Windischbacher, P. Puschnig, C. Piamonteze, M. Jugovac, A. Sala, C. Africh, G. Comelli, A. Cossaro, A. Verdini, L. Floreano, M. Stredansky, E. Vesselli, C. Hohner, M. Kettner, J. Libuda, C. M. Schneider, G. Zamborlini, M. Cinchetti, and V. Feyer, "Room-temperature On-Spin-Switching and Tuning in a Porphyrin-Based Multifunctional Interface," *Small*, vol. 17, no. 50, p. 2104779, 2021.

[212] I. Cojocariu, S. Carlotto, G. Zamborlini, M. Jugovac, L. Schio, L. Floreano, M. Casarin, V. Feyer, and C. M. Schneider, "Reversible redox reactions in metal-supported porphyrin: the role of spin and oxidation state," *J. Mater. Chem. C*, vol. 9, pp. 12559–12565, 2021.

[213] P. Knecht, J. Reichert, P. S. Deimel, P. Feulner, F. Haag, F. Allegretti, M. Garnica, M. Schwarz, W. Auwärter, P. T. P. Ryan, T.-L. Lee, D. A. Duncan, A. P. Seitsonen, J. V. Barth, and A. C. Papageorgiou, "Conformational Control of Chemical Reactivity for Surface-Confined Ru-Porphyrins," *Angewandte Chemie International Edition*, vol. 60, no. 30, pp. 16561–16567, 2021.

[214] M. Wießner, D. Hauschild, A. Schöll, F. Reinert, V. Feyer, K. Winkler, and B. Krömker, "Electronic and geometric structure of the PTCDA/Ag(110) interface probed by angle-resolved photoemission," *Phys. Rev. B*, vol. 86, p. 045417, 2012.

[215] L. Scudiero, D. E. Barlow, U. Mazur, and K. W. Hipps, "Scanning Tunneling Microscopy, Orbital-Mediated Tunneling Spectroscopy, and Ultraviolet Photoelectron Spectroscopy of Metal(II) Tetraphenylporphyrins Deposited from Vapor," *Journal of the American Chemical Society*, vol. 123, no. 17, pp. 4073–4080, 2001.

[216] J. C. Slater and J. C. Phillips, "Quantum Theory of Molecules and Solids Vol. 4: The Self-Consistent Field for Molecules and Solids," *Physics Today*, vol. 27, no. 12, pp. 49–50, 1974.

[217] G. Mangione, M. Sambi, S. Carlotto, A. Vittadini, G. Ligorio, M. Timpel, L. Pasquali, A. Giglia, M. V. Nardi, and M. Casarin, "Electronic structure of CuTPP and CuTPP(F) complexes: a combined experimental and theoretical study II," *Phys. Chem. Chem. Phys.*, vol. 18, pp. 24890–24904, 2016.

[218] M. G. Betti, F. Crispoldi, A. Ruocco, and C. Mariani, "Insulating state of electron-doped Cu-phthalocyanine layers," *Phys. Rev. B*, vol. 76, p. 125407, 2007.

[219] V. Y. Aristov, O. V. Molodtsova, V. V. Maslyuk, D. V. Vyalikh, T. Bredow, I. Mertig, A. B. Preobrajenski, and M. Knupfer, "Electronic properties of potassium-doped FePc," *Organic Electronics*, vol. 11, no. 8, pp. 1461–1468, 2010.

[220] A. Calabrese, L. Floreano, A. Verdini, C. Mariani, and M. G. Betti, "Filling empty states in a CuPc single layer on the Au(110) surface via electron injection," *Phys. Rev. B*, vol. 79, p. 115446, 2009.

[221] C. Y. Ralston, H. Wang, S. W. Ragsdale, M. Kumar, N. J. Spangler, P. W. Ludden, W. Gu, R. M. Jones, D. S. Patil, and S. P. Cramer, "Characterization of Heterogeneous Nickel Sites in CO Dehydrogenases from Clostridium thermoaceticum and Rhodospirillum rubrum by Nickel L-Edge X-ray Spectroscopy," *Journal of the American Chemical Society*, vol. 122, no. 43, pp. 10553–10560, 2000.

[222] G. Pirug, A. Winkler, and H. Bonzel, "Multilayer growth of potassium on a Pt(111) surface," *Surface Science*, vol. 163, no. 1, pp. 153–171, 1985.

[223] "Atomic calculation of photoionization cross-sections and asymmetry parameters." https://vuo.elettra.eu/services/elements/WebElements.html/. Online; accessed 20.10.2021.

[224] Y. Bai, M. Sekita, M. Schmid, T. Bischof, H.-P. Steinrück, and J. M. Gottfried, "Interfacial coordination interactions studied on cobalt octaethylporphyrin and cobalt tetraphenylporphyrin monolayers on Au(111)," *Phys. Chem. Chem. Phys.*, vol. 12, pp. 4336–4344, 2010.

[225] S. Carlotto, I. Cojocariu, V. Feyer, L. Floreano, and M. Casarin, "The Magnetic Behaviour of CoTPP Supported on Coinage Metal Surfaces in the Presence of Small Molecules: A Molecular Cluster Study of the Surface trans-Effect," *Nanomaterials*, vol. 12, no. 2, 2022.

[226] L. M. Arruda, M. E. Ali, M. Bernien, N. Hatter, F. Nickel, L. Kipgen, C. F. Hermanns, T. Bißwanger, P. Loche, B. W. Heinrich, K. J. Franke, P. M. Oppeneer, and W. Kuch, "Surface-orientation- and ligand-dependent quenching of the spin magnetic moment of Co porphyrins adsorbed on Cu substrates," *Physical Chemistry Chemical Physics*, vol. 22, no. 22, pp. 12688–12696, 2020.

[227] L. M. Arruda, M. E. Ali, M. Bernien, F. Nickel, J. Kopprasch, C. Czekelius, P. M. Oppeneer, and W. Kuch, "Modifying the Magnetic Anisotropy of an Iron Porphyrin Molecule by an on-Surface Ring-Closure Reaction," *Journal of Physical Chemistry C*, vol. 123, no. 23, pp. 14547–14555, 2019.

[228] G. Lovat, D. Forrer, M. Abadia, M. Dominguez, M. Casarin, C. Rogero, A. Vittadini, and L. Floreano, "Very high temperature tiling of tetraphenylporphyrin on rutile TiO_2(110)," *Nanoscale*, vol. 9, no. 32, pp. 11694–11704, 2017.

[229] B. W. Heinrich, G. Ahmadi, V. L. Müller, L. Braun, J. I. Pascual, and K. J. Franke, "Change of the magnetic coupling of a metal-organic complex with the substrate by a stepwise ligand reaction," *Nano Letters*, vol. 13, no. 10, pp. 4840–4843, 2013.

[230] D. Van Vörden, M. Lange, M. Schmuck, J. Schaffert, M. C. Cottin, C. A. Bobisch, and R. Möller, "Communication: Substrate induced dehydrogenation: Transformation of octaethyl-porphyrin into tetra-benzo-porphyrin," 2013.

[231] Y. Bai, F. Buchner, I. Kellner, M. Schmid, F. Vollnhals, H.-P. Steinrück, H. Marbach, and J. M. Gottfried, "Adsorption of cobalt (II) octaethylporphyrin and 2H-octaethylporphyrin on Ag(111): new insight into the surface coordinative bond," *New Journal of Physics*, vol. 11, no. 12, p. 125004, 2009.

[232] M. Fanetti, A. Calzolari, P. Vilmercati, C. Castellarin-Cudia, P. Borghetti, G. Di Santo, L. Floreano, A. Verdini, A. Cossaro, I. Vobornik, E. Annese, F. Bondino, S. Fabris, and A. Goldoni, "Structure and molecule-substrate interaction in a Co-octaethyl porphyrin monolayer on the Ag(110) surface," *Journal of Physical Chemistry C*, vol. 115, no. 23, pp. 11560–11568, 2011.

[233] P. Kliuiev, G. Zamborlini, M. Jugovac, Y. Gurdal, K. v. Arx, K. Waltar, S. Schnidrig, R. Alberto, M. Iannuzzi, V. Feyer, M. Hengsberger, J. Osterwalder, and L. Castiglioni, "Combined orbital tomography study of multi-configurational molecular adsorbate systems," *Nature Communications*, vol. 10, no. 1, p. 5255, 2019.

[234] X. Yang, L. Egger, P. Hurdax, H. Kaser, D. Lüftner, F. C. Bocquet, G. Koller, A. Gottwald, P. Tegeder, M. Richter, M. G. Ramsey, P. Puschnig, S. Soubatch, and F. S. Tautz, "Identifying surface reaction intermediates with photoemission tomography," *Nature Communications*, vol. 10, no. 1, p. 3189, 2019.

[235] M. Röckert, M. Franke, Q. Tariq, S. Ditze, M. Stark, P. Uffinger, D. Wechsler, U. Singh, J. Xiao, and H. Marbach, "Coverage-and Temperature-Dependent Metalation and Dehydrogenation of Tetraphenylporphyrin on Cu(111)," *Chemistry–A European Journal*, vol. 20, no. 29, pp. 8948–8953, 2014.

[236] P. C. Rusu, G. Giovannetti, C. Weijtens, R. Coehoorn, and G. Brocks, "Work function pinning at metal-organic interfaces," *Journal of Physical Chemistry C*, vol. 113, no. 23, pp. 9974–9977, 2009.

[237] G. Di Santo, C. Castellarin-Cudia, M. Fanetti, B. Taleatu, P. Borghetti, L. Sangaletti, L. Floreano, E. Magnano, F. Bondino, and A. Goldoni, "Conformational adaptation and electronic structure of 2H-tetraphenylporphyrin on Ag(111) during Fe metalation," *Journal of Physical Chemistry C*, vol. 115, no. 10, pp. 4155–4162, 2011.

[238] F. Albrecht, F. Bischoff, W. Auwärter, J. V. Barth, and J. Repp, "Direct Identification and Determination of Conformational Response in Adsorbed Individual Nonplanar Molecular Species Using Noncontact Atomic Force Microscopy," *Nano Letters*, vol. 16, no. 12, pp. 7703–7709, 2016.

[239] A. Wiengarten, J. A. Lloyd, K. Seufert, J. Reichert, W. Auwärter, R. Han, D. A. Duncan, F. Allegretti, S. Fischer, S. C. Oh, Özge Sağlam, L. Jiang, S. Vijayaraghavan, D. Écija, A. C. Papageorgiou, and J. V. Barth, "Surface-Assisted Cyclodehydrogenation; Break the Symmetry, Enhance the Selectivity," *Chemistry - A European Journal*, vol. 21, no. 35, pp. 12285–12290, 2015.

[240] A. C. Papageorgiou, K. Diller, S. Fischer, F. Allegretti, F. Klappenberger, S. C. Oh, Özge Sağlam, J. Reichert, A. Wiengarten, K. Seufert, W. Auwärter, and J. V. Barth, "In Vacuo Porphyrin Metalation on Ag(111) via Chemical Vapor Deposition of $Ru_3(CO)_{12}$: Mechanistic insights," *The Journal of Physical Chemistry C*, vol. 120, no. 16, pp. 8751–8758, 2016.

[241] C.-H. Shu, Y.-L. Xie, A. Wang, K.-J. Shi, W.-F. Zhang, D.-Y. Li, and P.-N. Liu, "On-surface reactions of aryl chloride and porphyrin macrocycles via merging two reactive sites into a single precursor," *Chemical Communications*, vol. 54, no. 89, pp. 12626–12629, 2018.

[242] A. C. Papageorgiou, S. Fischer, S. C. Oh, Özge Sağlam, J. Reichert, A. Wiengarten, K. Seufert, S. Vijayaraghavan, D. Écija, W. Auwärter, F. Allegretti, R. G. Acres, K. C. Prince, K. Diller, F. Klappenberger, and J. V. Barth, "Self-terminating Protocol for an Interfacial Complexation Reaction in Vacuo by Metal-Organic Chemical Vapor Deposition," *ACS Nano*, vol. 7, no. 5, pp. 4520–4526, 2013.

[243] C. C. Cudia, P. Vilmercati, R. Larciprete, C. Cepek, G. Zampieri, L. Sangaletti, S. Pagliara, A. Verdini, A. Cossaro, L. Floreano, A. Morgante, L. Petaccia, S. Lizzit, C. Battocchio, G. Polzonetti, and A. Goldoni, "Electronic structure and molecular orientation of a Zn-tetraphenyl porphyrin multilayer on Si(111)," *Surface Science*, vol. 600, no. 18, pp. 4013–4017, 2006.

[244] N. Schmidt, R. Fink, and W. Hieringer, "Assignment of near-edge x-ray absorption fine structure spectra of metalloporphyrins by means of time-dependent density-functional calculations," *The Journal of Chemical Physics*, vol. 133, no. 5, p. 054703, 2010.

[245] T. S. Rush, P. M. Kozlowski, C. A. Piffat, R. Kumble, M. Z. Zgierski, and T. G. Spiro, "Computational Modeling of Metalloporphyrin Structure and Vibrational Spectra: Porphyrin Ruffling in NiTPP," *The Journal of Physical Chemistry B*, vol. 104, no. 20, pp. 5020–5034, 2000.

[246] A. D. Procyk and D. F. Bocian, "Vibrational Characteristics of Tetrapyrrolic Macrocycles," *Annual Review of Physical Chemistry*, vol. 43, no. 1, pp. 465–496, 1992.

[247] L. Scudiero, D. E. Barlow, and K. W. Hipps, "Physical Properties and Metal Ion Specific Scanning Tunneling Microscopy Images of Metal(II) Tetraphenylporphyrins Deposited from Vapor onto Gold(111)," *The Journal of Physical Chemistry B*, vol. 104, no. 50, pp. 11899–11905, 2000.

[248] P. Knecht, J. Reichert, P. S. Deimel, P. Feulner, F. Haag, F. Allegretti, M. Garnica, M. Schwarz, W. Auwärter, P. T. P. Ryan, T.-L. Lee, D. A. Duncan, A. P. Seitsonen, J. V. Barth, and A. C. Papageorgiou, "Conformational Control of Chemical Reactivity for Surface-Confined Ru-Porphyrins," *Angewandte Chemie*, vol. 133, no. 30, pp. 16697–16703, 2021.

[249] R. F. Nalewajski and J. Mrozek, "Modified valence indices from the two-particle density matrix," *International Journal of Quantum Chemistry*, vol. 51, no. 4, pp. 187–200, 1994.

[250] M. Evangelisti, J. Bartolomé, L. J. de Jongh, and G. Filoti, "Magnetic properties of α-iron(II) phthalocyanine," *Physical Review B*, vol. 66, no. 14, p. 144410, 2002.

[251] J. Bartolomé, F. Bartolomé, L. M. García, G. Filoti, T. Gredig, C. N. Colesniuc, I. K. Schuller, and J. C. Cezar, "Highly unquenched orbital moment in textured Fe-phthalocyanine thin films," *Physical Review B*, vol. 81, no. 19, p. 195405, 2010.

[252] E. Salomon, D. Beato-Medina, A. Verdini, A. Cossaro, D. Cvetko, G. Kladnik, L. Floreano, and T. Angot, "Correlation between Charge Transfer and Adsorption Site in CoPc Overlayers Adsorbed on Ag(100)," *The Journal of Physical Chemistry C*, vol. 119, no. 41, pp. 23422–23429, 2015.

[253] H. Peisert, J. Uihlein, F. Petraki, and T. Chassé, "Charge transfer between transition metal phthalocyanines and metal substrates: The role of the transition metal," *Journal of Electron Spectroscopy and Related Phenomena*, vol. 204, pp. 49–60, 2015.

[254] N. Tsukahara, K.-i. Noto, M. Ohara, S. Shiraki, N. Takagi, Y. Takata, J. Miyawaki, M. Taguchi, A. Chainani, S. Shin, and M. Kawai, "Adsorption-Induced Switching of Magnetic Anisotropy in a Single Iron(II) Phthalocyanine Molecule on an Oxidized Cu(110) Surface," *Physical Review Letters*, vol. 102, no. 16, p. 167203, 2009.

[255] P. Gargiani, G. Rossi, R. Biagi, V. Corradini, M. Pedio, S. Fortuna, A. Calzolari, S. Fabris, J. C. Cezar, N. B. Brookes, and M. G. Betti, "Spin and orbital configuration of metal phthalocyanine chains assembled on the Au(110) surface," *Physical Review B*, vol. 87, no. 16, p. 165407, 2013.

[256] S. Stepanow, P. S. Miedema, A. Mugarza, G. Ceballos, P. Moras, J. C. Cezar, C. Carbone, F. M. F. de Groot, and P. Gambardella, "Mixed-valence behavior and strong correlation effects of metal phthalocyanines adsorbed on metals," *Physical Review B*, vol. 83, no. 22, p. 220401, 2011.

[257] L. S. Chia, Y. H. Du, S. Palale, and P. S. Lee, "Interaction of Copper Phthalocyanine with Nitrogen Dioxide and Ammonia Investigation Using X-ray Absorption Spectroscopy and Chemiresistive Gas Measurements," *ACS Omega*, vol. 4, no. 6, pp. 10388–10395, 2019.

[258] C. Isvoranu, B. Wang, K. Schulte, E. Ataman, J. Knudsen, J. N. Andersen, M. L. Bocquet, and J. Schnadt, "Tuning the spin state of iron phthalocyanine by ligand adsorption," *Journal of Physics: Condensed Matter*, vol. 22, no. 47, p. 472002, 2010.

[259] C. Isvoranu, B. Wang, E. Ataman, K. Schulte, J. Knudsen, J. N. Andersen, M.-L. Bocquet, and J. Schnadt, "Ammonia adsorption on iron phthalocyanine on Au(111): Influence on adsorbate-substrate coupling and molecular spin," *The Journal of Chemical Physics*, vol. 134, no. 11, p. 114710, 2011.

[260] J. Bartolomeé, F. Bartolomé, N. B. Brookes, F. Sedona, A. Basagni, D. Forrer, and M. Sambi, "Reversible Fe magnetic moment switching in catalytic oxygen reduction reaction of Fe-phthalocyanine adsorbed on Ag(110)," *The Journal of Physical Chemistry C*, vol. 119, no. 22, pp. 12488–12495, 2015.

[261] R. A. Rehman, Y. L. Cai, H. J. Zhang, K. Wu, W. D. Dou, H. Y. Li, P. M. He, and S. N. Bao, "Differences in the adsorption of FePc on coinage metal surfaces," *Chinese Physics B*, vol. 22, no. 6, p. 63101, 2013.

[262] V. Feyer, M. Graus, P. Nigge, M. Wießner, R. G. Acres, C. Wiemann, C. M. Schneider, A. Schöll, and F. Reinert, "Adsorption geometry and electronic structure of iron phthalocyanine on Ag surfaces: A LEED and photoelectron momentum mapping study," *Surface Science*, vol. 621, pp. 64–68, 2014.

[263] J. Åhlund, K. Nilson, J. Schiessling, L. Kjeldgaard, S. Berner, N. Mårtensson, C. Puglia, B. Brena, M. Nyberg, and Y. Luo, "The electronic structure of iron phthalocyanine probed by photoelectron and x-ray absorption spectroscopies and density functional theory calculations," *The Journal of Chemical Physics*, vol. 125, no. 3, p. 34709, 2006.

[264] P. A. Reynolds and B. N. Figgis, "Metal phthalocyanine ground states: covalence and ab initio calculation of spin and charge densities," *Inorganic Chemistry*, vol. 30, no. 10, pp. 2294–2300, 1991.

[265] T. Kroll, R. Kraus, R. Schönfelder, V. Y. Aristov, O. V. Molodtsova, P. Hoffmann, and M. Knupfer, "Transition metal phthalocyanines: Insight into the electronic structure from soft x-ray spectroscopy," *The Journal of chemical physics*, vol. 137, no. 5, p. 54306, 2012.

[266] X. Shen, L. Sun, Z. Yi, E. Benassi, R. Zhang, Z. Shen, S. Sanvito, and S. Hou, "Spin transport properties of 3d transition metal (II) phthalocyanines in contact with single-walled carbon nanotube electrodes," *Physical Chemistry Chemical Physics*, vol. 12, no. 36, pp. 10805–10811, 2010.

[267] A. Mugarza, R. Robles, C. Krull, R. Korytár, N. Lorente, and P. Gambardella, "Electronic and magnetic properties of molecule-metal interfaces: Transition-metal phthalocyanines adsorbed on Ag(100)," *Physical Review B*, vol. 85, no. 15, p. 155437, 2012.

[268] Z. Hu, B. Li, A. Zhao, J. Yang, and J. G. Hou, "Electronic and Magnetic Properties of Metal Phthalocyanines on Au(111) Surface: A First-Principles Study," *The Journal of Physical Chemistry C*, vol. 112, no. 35, pp. 13650–13655, 2008.

[269] C. Wäckerlin, D. Siewert, T. A. Jung, and N. Ballav, "On-surface coordination chemistry: Direct imaging of the conformational freedom of an axial ligand at room temperature," *Physical Chemistry Chemical Physics*, vol. 15, no. 39, pp. 16510–16514, 2013.

[270] M. Wuttig, R. Franchy, and H. Ibach, "Oxygen on Cu(100) - a case of an adsorbate induced reconstruction," *Surface Science*, vol. 213, no. 1, pp. 103–136, 1989.

[271] P. Jiang, D. Prendergast, F. Borondics, S. Porsgaard, L. Giovanetti, E. Pach, J. Newberg, H. Bluhm, F. Besenbacher, and M. Salmeron, "Experimental and theoretical investigation of the electronic structure of CuO and Cu_2O thin films on Cu(110) using x-ray photoelectron and absorption spectroscopy," *The Journal of Chemical Physics*, vol. 138, no. 2, p. 024704, 2013.

[272] M. Casarin, D. Falcomer, A. Glisenti, and A. Vittadini, "Experimental and Theoretical Study of the Interaction of CO_2 with α-Al_2O_3," *Inorganic Chemistry*, vol. 42, no. 2, pp. 436–445, 2002.

[273] S. Carlotto, M. Sambi, M. Rancan, and M. Casarin, "Theoretical Investigation of the Electronic Properties of Three Vanadium Phthalocyaninato (Pc) Based Complexes: PcV, PcVO, and PcVI," *Inorganic Chemistry*, vol. 57, no. 4, pp. 1859–1869, 2018.

[274] A. Rosa and G. Ricciardi, "Reactivity of Compound II: Electronic Structure Analysis of Methane Hydroxylation by Oxoiron(IV) Porphyrin Complexes," *Inorganic Chemistry*, vol. 51, no. 18, pp. 9833–9845, 2012.

[275] F. Sedona, M. Di Marino, D. Forrer, A. Vittadini, M. Casarin, A. Cossaro, L. Floreano, A. Verdini, and M. Sambi, "Tuning the catalytic activity of Ag(110)-supported Fe phthalocyanine in the oxygen reduction reaction," *Nature Materials*, vol. 11, no. 11, pp. 970–977, 2012.

[276] A. B. Gurevich, B. E. Bent, A. V. Teplyakov, and J. G. Chen, "A NEXAFS investigation of the formation and decomposition of CuO and Cu_2O thin films on Cu(100)," *Surface Science*, vol. 442, no. 1, pp. L971–L976, 1999.

[277] J. Fernández-Rodríguez, B. Toby, and M. van Veenendaal, "Mixed configuration ground state in iron(II) phthalocyanine," *Physical Review B*, vol. 91, no. 21, p. 214427, 2015.

[278] T. Van Woudenbergh, P. W. Blom, and J. N. Huiberts, "Electro-optical properties of a polymer light-emitting diode with an injection-limited hole contact," *Applied Physics Letters*, vol. 82, no. 6, pp. 985–987, 2003.

[279] I. H. Campbell, J. D. Kress, R. L. Martin, D. L. Smith, N. N. Barashkov, and J. P. Ferraris, "Controlling charge injection in organic electronic devices using self-assembled monolayers," *Applied Physics Letters*, vol. 71, no. 24, pp. 3528–3530, 1997.

[280] B. De Boer, A. Hadipour, M. M. Mandoc, and P. W. Blom, "Tuning of metal work function with self-assembled monolayers," *Materials Research Society Symposium Proceedings*, vol. 871, no. 1, pp. 189–196, 2005.

[281] G. Ashkenasy, D. Cahen, R. Cohen, A. Shanzer, and A. Vilan, "Molecular engineering of semiconductor surfaces and devices," *Accounts of Chemical Research*, vol. 35, no. 2, pp. 121–128, 2002.

[282] S. C. Veenstra, A. Heeres, G. Hadziioannou, G. A. Sawatzky, and H. T. Jonkman, "On interface dipole layers between C_{60} and Ag or Au," *Applied Physics A: Materials Science and Processing*, vol. 75, no. 6, pp. 661–666, 2002.

[283] J. Lü, E. Delamarche, L. Eng, R. Bennewitz, E. Meyer, and H. J. Güntherodt, "Kelvin probe force microscopy on surfaces: investigation of the surface potential of self-assembled monolayers on gold," *Langmuir*, vol. 15, no. 23, pp. 8184–8188, 1999.

[284] S. D. Evans, E. Urankar, A. Ulman, and N. Ferris, "Self-Assembled Monolayers of Alkanethiols Containing a Polar Aromatic Group: Effects of the Dipole Position on Molecular Packing, Orientation, and Surface Wetting Properties," *Journal of the American Chemical Society*, vol. 113, no. 11, pp. 4121–4131, 1991.

[285] H. Ishii, K. Sugiyama, E. Ito, and K. Seki, "Energy level alignment and interfacial electronic structures at organic/metal and organic/organic interfaces," *Advanced Materials*, vol. 11, no. 8, pp. 605–625, 1999.

[286] S. Kobayashi, T. Nishikawa, T. Takenobu, S. Mori, T. Shimoda, T. Mitani, H. Shimotani, N. Yoshimoto, S. Ogawa, and Y. Iwasa, "Control of carrier density by self-assembled monolayers in organic field-effect transistors," *Nature Materials*, vol. 3, no. 5, pp. 317–322, 2004.

[287] C. Reese and Z. Bao, "Organic single-crystal field-effect transistors," *Materials Today*, vol. 10, no. 3, pp. 20–27, 2007.

[288] X. Jiang, J. Dai, H. Wang, Y. Geng, and D. H. Yan, "Organic photovoltaic cells using hexadecafluorophthalocyaninatocopper (F_{16}CuPc) as electron acceptor material," *Chemical Physics Letters*, vol. 446, no. 4-6, pp. 329–332, 2007.

[289] T. L. Anderson, G. C. Komplin, and W. J. Pietro, "Rectifying junctions in peripherally-substituted metallophthalocyanine bilayer films," *Journal of Physical Chemistry*, vol. 97, no. 25, pp. 6577–6578, 1993.

[290] W. J. Pietro, "Rectifying junctions based on metallophthalocyanine thin films," *Advanced Materials*, vol. 6, no. 3, pp. 239–242, 1994.

[291] Y. Zhang, H. Dong, Q. Tang, S. Ferdous, F. Liu, S. C. Mannsfeld, W. Hu, and A. L. Briseno, "Organic single-crystalline p-n junction nanoribbons," *Journal of the American Chemical Society*, vol. 132, no. 33, pp. 11580–11584, 2010.

[292] K. Greulich, M. Trautmann, A. Belser, S. Bölke, R. Karstens, P. Nagel, S. Schuppler, M. Merz, A. Chassé, T. Chassé, and H. Peisert, "Influence of the Fluorination of Iron Phthalocyanine on the Electronic Structure of the Central Metal Atom," *Journal of Physical Chemistry C*, vol. 125, no. 12, pp. 6851–6861, 2021.

[293] Y. Bai, F. Buchner, M. T. Wendahl, I. Kellner, A. Bayer, H. P. Steinrück, H. Marbach, and J. M. Gottfried, "Direct metalation of a phthalocyanine monolayer on Ag(111) with coadsorbed iron atoms," *Journal of Physical Chemistry C*, vol. 112, no. 15, pp. 6087–6092, 2008.

[294] B. Brena, C. Puglia, M. De Simone, M. Coreno, K. Tarafder, V. Feyer, R. Banerjee, E. Göthelid, B. Sanyal, P. M. Oppeneer, and O. Eriksson, "Valence-band electronic structure of iron phthalocyanine: An experimental and theoretical photoelectron spectroscopy study," *Journal of Chemical Physics*, vol. 134, no. 7, p. 74312, 2011.

[295] P. F. Siles, T. Hahn, G. Salvan, M. Knupfer, F. Zhu, D. R. Zahn, and O. G. Schmidt, "Tunable charge transfer properties in metal-phthalocyanine heterojunctions," *Nanoscale*, vol. 8, no. 16, pp. 8607–8617, 2016.

[296] P. C. Rusu and G. Brocks, "Surface dipoles and work functions of alkylthiolates and fluorinated alkylthiolates on Au(111)," *Journal of Physical Chemistry B*, vol. 110, no. 45, pp. 22628–22634, 2006.

[297] "Organic molecules database." http://143.50.77.12:5000/. Online; accessed 29.01.2020.

[298] M. Casarin, M. Di Marino, D. Forrer, M. Sambi, F. Sedona, E. Tondello, A. Vittadini, V. Barone, and M. Pavone, "Coverage-dependent architectures of iron phthalocyanine on Ag(110): A comprehensive STM/DFT study," *Journal of Physical Chemistry C*, vol. 114, no. 5, pp. 2144–2153, 2010.

[299] M. Tredwell and V. Gouverneur, "1.5 Fluorine in Medicinal Chemistry: Importance of Chirality," *Comprehensive Chirality*, vol. 1, pp. 70–85, 2012.

[300] M. Grimm, C. Metzger, M. Graus, M. Jugovac, G. Zamborlini, V. Feyer, A. Schöll, and F. Reinert, "Molecular orbital imaging beyond the first monolayer: Insights into the pentacene/Ag(110) interface," *Phys. Rev. B*, vol. 98, p. 195412, 2018.

[301] Q. Wang, J. Yang, A. Franco-Cañellas, C. Bürker, J. Niederhausen, P. Dombrowski, F. Widdascheck, T. Breuer, G. Witte, A. Gerlach, S. Duhm, and F. Schreiber, "Pentacene/perfluoropentacene bilayers on Au(111) and Cu(111): Impact of organic-metal coupling strength on molecular structure formation," *Nanoscale Advances*, vol. 3, no. 9, pp. 2598–2606, 2021.

Band / Volume 77
Surface plasmon-enhanced molecular switching for optoelectronic applications
B. Lenyk (2021), x, 129 pp
ISBN: 978-3-95806-595-6

Band / Volume 78
Engineering neuronal networks in vitro: From single cells to population connectivity
I. Tihaa (2021), viii, 242 pp
ISBN: 978-3-95806-597-0

Band / Volume 79
Spectromicroscopic investigation of local redox processes in resistive switching transition metal oxides
T. Heisig (2022), vi, 186 pp
ISBN: 978-3-95806-609-0

Band / Volume 80
Integrated Control Electronics for Qubits at Ultra Low TemperatureD. Nielinger (2022), xviii, 94, xix-xxvi
ISBN: 978-3-95806-631-1

Band / Volume 81
Higher-order correlation analysis in massively parallel recordings in behaving monkey
A. Stella (2022), xiv, 184 pp
ISBN: 978-3-95806-640-3

Band / Volume 82
Denoising with Quantum Machine Learning
J. Pazem (2022), 106 pp
ISBN: 978-3-95806-641-0

Band / Volume 83
Hybrid hydrogels promote physiological functionality of long-term cultured primary neuronal cells in vitro
C. Meeßen (2022), x, 120 pp
ISBN: 978-3-95806-643-4

Band / Volume 84
Surface states and Fermi-level pinning on non-polar binary and ternary (Al,Ga)N surfaces
L. Freter (2022), 137 pp
ISBN: 978-3-95806-644-1

Band / Volume 85
Dynamical and statistical structure of spatially organized neuronal networks
M. Layer (2022), xiii, 167 pp
ISBN: 978-3-95806-651-9

Band / Volume 86
Persistent firing and oscillations in the septo-hippocampal system and their relation to locomotion
K. Korvasová (2022), 111 pp
ISBN: 978-3-95806-654-0

Band / Volume 87
Sol-Gel-Synthese, Tintenstrahldruck und Blitzlampentemperung von Tantaloxid-Dünnschichten zur pH-Messung
C. D. Beale (2022), xlix, 339 pp
ISBN: 978-3-95806-656-4

Band / Volume 88
Diversity of chiral magnetic solitons
V. Kuchkin (2022), xiv, 155 pp
ISBN: 978-3-95806-665-6

Band / Volume 89
Controlling the electrical properties of oxide heterointerfaces through their interface chemistry
M.-A. Rose (2022), vi, 162 pp
ISBN: 978-3-95806-667-0

Band / Volume 90
Modeling and Suppressing Unwanted Parasitic Interactions in Superconducting Circuits
X. Xu (2022), 123, XVIII pp
ISBN: 978-3-95806-671-7

Band / Volume 91
Activating molecular magnetism by controlled on-surface coordination
I. Cojocariu (2022), xi, 169 pp
ISBN: 978-3-95806-674-8

Information
Band / Volume 91
ISBN 978-3-95806-674-8

Mitglied der Helmholtz-Gemeinschaft

JÜLICH
Forschungszentrum